

DEVELOPMENT OF HIGH-ORDER DOUBLY  
ASYMPTOTIC OPEN BOUNDARIES FOR  
WAVE PROPAGATION IN UNBOUNDED  
DOMAINS BY EXTENDING THE SCALED  
BOUNDARY FINITE ELEMENT METHOD

By

SURIYON PREMPRAMOTE

A THESIS SUBMITTED IN FULFILLMENT OF  
THE REQUIREMENTS FOR THE DEGREE OF  
DOCTOR OF PHILOSOPHY



School of Civil and Environmental Engineering  
The University of New South Wales  
Sydney, Australia

March 2011

PLEASE TYPE

THE UNIVERSITY OF NEW SOUTH WALES  
Thesis/Dissertation Sheet

Surname or Family name: Prempramote

First name: Suriyon

Other name/s:

Abbreviation for degree as given in the University calendar: PhD

School: Civil and Environmental Engineering

Faculty: Engineering

Title: Development of High-Order Doubly Asymptotic Open  
Boundaries for Wave Propagation in Unbounded Domains by  
Extending the Scaled Boundary Finite Element Method

Abstract 350 words maximum: (PLEASE TYPE)

This thesis presents the development of high-order doubly asymptotic open boundaries used for the numerical simulation of wave propagation problems in unbounded domains, including homogeneous semi-infinite layers with a constant depth, homogeneous full-planes with a circular cavity and semi-infinite layered systems. The proposed open boundaries are necessary for dynamic and seismic analyses of large-scale structures such as dams, nuclear power plants etc. The theoretical framework of the research in the thesis is extended by employing the scaled boundary finite element method, which is a semi-analytical fundamental-solution-less boundary-element method based on finite elements.

To avoid the computationally expensive task of numerically integrating the scaled boundary finite element equation in dynamic stiffness, the doubly asymptotic continued fraction solution for dynamic stiffness matrices is developed in the frequency domain using the technique of continued fraction. Factor coefficients or matrices are introduced in the continued fraction solution to improve the stability of the solution. As the continued fraction orders increase, the doubly asymptotic continued fraction solution converges to the exactness at both high- and low-frequency limits.

By introducing auxiliary variables and the doubly asymptotic continued fraction solution to the force-displacement relationship in the frequency domain, a high-order doubly asymptotic open boundary condition is obtained. The open boundaries are expressed as systems of first-order ordinary differential equations in the time domain which are similar to the equation of motion with time-independent matrices in structural dynamics.

The high-order doubly asymptotic open boundaries can be coupled seamlessly with standard finite elements. The accuracy of the results in the frequency and time domains depends on the orders of continued fraction selected by the user. Standard time-step schemes e.g. the Newmark's method etc. in structural dynamics are directly applicable to the high-order doubly asymptotic open boundaries for the implementation in the time domain. No convolution integral, which is the expensive task in the time-domain analysis, is required.

Declaration relating to disposition of project thesis/dissertation

I hereby grant to the University of New South Wales or its agents the right to archive and to make available my thesis or dissertation in whole or in part in the University libraries in all forms of media, now or here after known, subject to the provisions of the Copyright Act 1968. I retain all property rights, such as patent rights. I also retain the right to use in future works (such as articles or books) all or part of this thesis or dissertation.

I also authorise University Microfilms to use the 350 word abstract of my thesis in Dissertation Abstracts International (this is applicable to doctoral theses only).

  
Signature

  
Witness

11/07/11  
Date

The University recognises that there may be exceptional circumstances requiring restrictions on copying or conditions on use. Requests for restriction for a period of up to 2 years must be made in writing. Requests for a longer period of restriction may be considered in exceptional circumstances and require the approval of the Dean of Graduate Research.

FOR OFFICE USE ONLY

Date of completion of requirements for Award:

THIS SHEET IS TO BE GLUED TO THE INSIDE FRONT COVER OF THE THESIS

**ORIGINALITY STATEMENT**

'I hereby declare that this submission is my own work and to the best of my knowledge it contains no materials previously published or written by another person, or substantial proportions of material which have been accepted for the award of any other degree or diploma at UNSW or any other educational institution, except where due acknowledgement is made in the thesis. Any contribution made to the research by others, with whom I have worked at UNSW or elsewhere, is explicitly acknowledged in the thesis. I also declare that the intellectual content of this thesis is the product of my own work, except to the extent that assistance from others in the project's design and conception or in style, presentation and linguistic expression is acknowledged.'

Signed .....  .....

Date ..... 11/07/11 .....

**COPYRIGHT STATEMENT**

'I hereby grant the University of New South Wales or its agents the right to archive and to make available my thesis or dissertation in whole or part in the University libraries in all forms of media, now or here after known, subject to the provisions of the Copyright Act 1968. I retain all proprietary rights, such as patent rights. I also retain the right to use in future works (such as articles or books) all or part of this thesis or dissertation.

I also authorise University Microfilms to use the 350 word abstract of my thesis in Dissertation Abstract International (this is applicable to doctoral theses only).

I have either used no substantial portions of copyright material in my thesis or I have obtained permission to use copyright material; where permission has not been granted I have applied/will apply for a partial restriction of the digital copy of my thesis or dissertation.'

Signed ..... *P. Sij* .....

Date ..... 11/07/11 .....

**AUTHENTICITY STATEMENT**

'I certify that the Library deposit digital copy is a direct equivalent of the final officially approved version of my thesis. No emendation of content has occurred and if there are any minor variations in formatting, they are the result of the conversion to digital format.'

Signed ..... *P. Sij* .....

Date ..... 11/07/11 .....

# Abstract

This thesis presents the development of high-order doubly asymptotic open boundaries used for the numerical simulation of wave propagation problems in unbounded domains, including homogeneous semi-infinite layers with a constant depth, homogeneous full-planes with a circular cavity and semi-infinite layered systems. The proposed open boundaries are necessary for dynamic and seismic analyses of large-scale structures such as dams, nuclear power plants etc. The theoretical framework of the research in the thesis is extended by employing the scaled boundary finite element method, which is a semi-analytical fundamental-solution-less boundary-element method based on finite elements.

To avoid the computationally expensive task of numerically integrating the scaled boundary finite element equation in dynamic stiffness, the doubly asymptotic continued fraction solution for dynamic stiffness matrices is developed in the frequency domain using the technique of continued fraction. Factor coefficients or matrices are introduced in the continued fraction solution to improve the stability of the solution. As the continued fraction orders increase, the doubly asymptotic continued fraction solution converges to the exactness at both high- and low-frequency limits.

By introducing auxiliary variables and the doubly asymptotic continued fraction solution to the force-displacement relationship in the frequency domain, a high-order doubly asymptotic open boundary condition is obtained. The open boundaries are expressed as systems of first-order ordinary differential equations in the time domain which are similar to the equation of motion with time-independent matrices in structural dynamics.

The high-order doubly asymptotic open boundaries can be coupled seamlessly with standard finite elements. The accuracy of the results in the frequency and time domains depends on the orders of continued fraction selected by the user. Standard time-step schemes e.g. the Newmark's method etc. in structural dynamics are directly applicable to the high-order doubly asymptotic open boundaries for the implementation in the time domain. No convolution integral, which is the expensive task in the time-domain analysis, is required.

*This thesis is dedicated to my late father, Chanchai Prempramote, my late sister, Suchada Prempramote, my late uncle, Thirachai Prempramote, and my late grandfather, Huikeng Pueng.*

*“Mystery has its own mysteries, and there are gods above gods. We have ours, they have theirs. That is what’s known as infinity.”*

*Jean Cocteau (1889-1963)*

# Acknowledgements

Firstly, I would like to express my deep gratitude and appreciation to my supervisor, Associate Professor Chongmin Song, for recruiting me as his second student. He is the one who laid the foundation of the scaled boundary finite element method. The source of his success is his mathematician's insight with his engineer's intuition. Without his timely support, encouragement and advice, this thesis would not have been completed. I would also like to thank my co-supervisor, Emeritus Professor Francis Tin-Loi, for his advice on the research and so on.

I would like to thank Australian Government and the Australian Research Council for providing the scholarships under the Commonwealth Government's Research Training Scheme (RTS) and the ARC Discovery Grant.

I would like to thank Emeritus Professor Thomas L. Geers (University of Colorado, U.S.A.), who established the theory of the doubly asymptotic approximations (DAAs), for his suggestion and discussion about the research in this area during his short visit at The University of New South Wales, and also Dr. Carolin Birk (Dresden University of Technology, Germany) and Dr. Xiang Wang (Tsinghua University, China) for the collaboration in the research on wave propagation in unbounded domains.

I am grateful to Dr. Wei Gao, Dr. Sawekchai Tangaramvong and Dr. Hou Man for exchanging research ideas, and to the computing and administrative staffs at School of Civil and Environmental Engineering for assisting me in many different ways. Kate Brown, Robert Hegedus, Patrick Vuong and Patricia McLaughlin deserve special mention. Many thanks also go to my friends in the office 613 for our friendship.

I wish to thank my mother, Aenghuang Prempramote, my aunt, Suwadee Prempramote, and my brother, Sampan Prempramote as well as the other members of my family for teaching, raising and supporting me, and also my nephew, Thanakrit Prempramote, who always makes me laugh even in the difficult times.

Lastly, and most importantly, I am deeply indebted to my late father, Chanchai Prempramote, who always encouraged and supported me in my studies.

# Publications

## Journal papers:

1. Prempramote, S., Song, C., Tin-Loi, F. and Lin, G. (2009). High-order doubly asymptotic open boundaries for scalar wave equation, *International Journal for Numerical Methods in Engineering*, 79:340-374.
2. Wang, X., Jin, F., Prempramote, S. and Song, C. (2011). Time-domain analysis of gravity dam-reservoir interaction using high-order doubly asymptotic open boundary, *Computers and Structures*, 89:668-680.
3. Birk, C., Prempramote, S. and Song, C. (2011). An improved continued-fraction-based high-order transmitting boundary for time-domain analyses in unbounded domains, *International Journal for Numerical Methods in Engineering*, (under review).

## Conference papers:

1. Prempramote, S., Bazyar, M. H. and Song, C. (2007). A direct procedure for the transient analysis of dynamic soil-structure interaction problems. *3rd Asian-Pacific Congress on Computational Mechanics (APCOM'07) in Conjunction with 11th International Conference on Enhancement and Promotion of Computational Methods in Engineering Science (EPMESC XI)*, 3-6 December 2007, Kyoto, Japan.
2. Prempramote, S. and Song, C. A high-order doubly asymptotic open boundary condition for scalar waves in a waveguide. *2nd International Conference on Computational Methods in Structural Dynamics and Earthquake Engineering (COMPdyn 2009)*, 22-24 June 2009, Island of Rhodes, Greece.
3. Prempramote, S., Birk, C. and Song, C. A high-order doubly asymptotic open boundary for scalar waves in semi-infinite layered systems. *9th World*

*Congress on Computational Mechanics and 4th Asian Pacific Congress on Computational Mechanics (WCCM/APCOM 2010)*, 19-23 July 2010, Sydney, Australia.

4. Birk, C., Prempramote, S., and Song, C. High-order doubly asymptotic absorbing boundaries for the acoustic wave equation. *20th International Congress on Acoustics (ICA 2010)*, 23-27 August 2010, Sydney, Australia.

# Contents

<b>Abstract</b>	<b>i</b>
<b>Acknowledgements</b>	<b>iv</b>
<b>Publications</b>	<b>v</b>
<b>Table of Contents</b>	<b>vii</b>
<b>1 Introduction</b>	<b>1</b>
1.1 Statement of problem . . . . .	1
1.2 Substructure and direct methods . . . . .	5
1.3 Global and local boundary conditions . . . . .	9
1.3.1 Global procedures . . . . .	10
1.3.2 Local procedures . . . . .	11
1.4 Objectives . . . . .	12
1.5 Thesis outline . . . . .	14
<b>2 Literature Review</b>	<b>16</b>
2.1 Introduction . . . . .	16
2.2 Global procedures . . . . .	16
2.2.1 Boundary element method . . . . .	17
2.2.2 Thin-layer method . . . . .	21
2.2.3 Scaled boundary finite element method . . . . .	24
2.2.4 Exact non-reflecting boundaries . . . . .	28
2.2.5 Temporally local exact non-reflecting boundaries . . . . .	31
2.2.5.1 Grote-Keller boundaries . . . . .	31
2.2.5.2 Boundary conditions of absolute transparency . . . . .	32
2.2.5.3 Residual-potential boundary . . . . .	32
2.3 Local procedures . . . . .	33
2.3.1 Low-order absorbing boundary conditions . . . . .	33
2.3.2 High-order absorbing boundary conditions . . . . .	35

2.3.2.1	Free-space boundary conditions . . . . .	35
2.3.2.2	Paraxial boundary conditions . . . . .	35
2.3.2.3	Bayliss-Turkel boundary conditions . . . . .	36
2.3.2.4	Extrapolation boundary conditions . . . . .	38
2.3.2.5	Higdon boundary conditions . . . . .	39
2.3.3	Local high-order absorbing boundary conditions . . . . .	39
2.3.4	Doubly asymptotic approximations . . . . .	43
2.3.5	Infinite elements . . . . .	45
2.3.6	Absorbing layers . . . . .	49
2.4	Capacity of commercial finite element packages for modeling unbounded domains . . . . .	53
2.5	Conclusions . . . . .	54

### **3 Doubly Asymptotic Open Boundaries for Modal Equations of Scalar Waves 56**

3.1	Introduction . . . . .	56
3.2	Dynamic stiffness of unbounded domains . . . . .	60
3.2.1	Semi-infinite layer with constant depth . . . . .	61
3.2.1.1	Analytical solution . . . . .	62
3.2.1.2	Equation of dynamic stiffness coefficient . . . . .	64
3.2.2	Circular cavity embedded in full-plane . . . . .	64
3.2.2.1	Analytical solution . . . . .	65
3.2.2.2	Equation of dynamic stiffness coefficient . . . . .	66
3.2.3	Comparison between dynamic stiffness coefficients of semi-infinite layer and circular cavity . . . . .	67
3.3	Doubly asymptotic continued fraction solution for dynamic stiffness . . . . .	68
3.3.1	Semi-infinite layer with constant depth . . . . .	69
3.3.1.1	High-frequency continued fraction . . . . .	69
3.3.1.2	Link with other absorbing boundaries for plane waves . . . . .	71
3.3.1.3	Doubly asymptotic continued fraction . . . . .	73
3.3.2	Circular cavity embedded in full-plane . . . . .	77
3.3.2.1	High-frequency continued fraction . . . . .	77
3.3.2.2	Doubly asymptotic continued fraction . . . . .	81
3.4	Doubly asymptotic open boundary condition . . . . .	85
3.5	Numerical examples . . . . .	88
3.5.1	Semi-infinite layer with constant depth . . . . .	90
3.5.2	Circular cavity embedded in full-plane . . . . .	97
3.6	Conclusions . . . . .	101

<b>4</b>	<b>Analysis of Gravity Dam-Reservoir Interaction Using Doubly Asymptotic Open Boundary</b>	<b>103</b>
4.1	Introduction . . . . .	103
4.2	Finite element model of dam-reservoir system . . . . .	107
4.3	Scaled boundary finite element method for semi-infinite reservoir with constant depth . . . . .	109
4.4	Modal decomposition of scaled boundary finite element equation . . .	114
4.5	Doubly asymptotic continued fraction solution for modal dynamic stiffness . . . . .	116
4.6	Doubly asymptotic open boundary condition . . . . .	120
4.7	Numerical implementation in time domain . . . . .	122
4.8	Numerical examples . . . . .	126
	4.8.1 Rigid dam . . . . .	126
	4.8.2 Flexible dam . . . . .	132
4.9	Conclusions . . . . .	135
<b>5</b>	<b>Improved Doubly Asymptotic Open Boundary for Scalar Wave Propagation in Full-Plane with Circular Cavity</b>	<b>136</b>
5.1	Introduction . . . . .	137
5.2	Governing differential equation of scalar waves . . . . .	140
5.3	Scaled boundary finite element method for full-plane with circular cavity . . . . .	142
5.4	Modal dynamic stiffness coefficients of full-plane with circular cavity .	145
5.5	Doubly asymptotic continued fraction solution for modal dynamic stiffness coefficients . . . . .	147
	5.5.1 Continued fraction solution at high frequency . . . . .	148
	5.5.2 Continued fraction solution at low frequency . . . . .	151
5.6	Doubly asymptotic open boundary condition . . . . .	156
5.7	Numerical examples . . . . .	159
	5.7.1 Illustration of robustness of improved doubly asymptotic open boundary for modal dynamic stiffness . . . . .	160
	5.7.2 Circular cavity subjected to transient surface traction on entire boundary . . . . .	165
	5.7.3 Circular cavity partially subjected to transient surface traction	168
	5.7.4 Circular cavity subjected to concentrated surface traction . . .	173
5.8	Conclusions . . . . .	177

<b>6</b>	<b>Doubly Asymptotic Open Boundary for Scalar Wave Propagation in Semi-Infinite Layered Systems</b>	<b>178</b>
6.1	Introduction . . . . .	179
6.2	Governing differential equation of scalar waves . . . . .	181
6.3	Scaled boundary finite element method for semi-infinite layered system	182
6.4	Dynamic stiffness matrix of semi-infinite layered systems . . . . .	187
6.5	Doubly asymptotic continued fraction solution for dynamic stiffness matrix . . . . .	189
6.5.1	Continued fraction solution at high frequency . . . . .	189
6.5.2	Continued fraction solution at low frequency . . . . .	192
6.6	Doubly asymptotic open boundary condition . . . . .	197
6.7	Numerical examples . . . . .	200
6.7.1	Semi-infinite layer . . . . .	200
6.7.2	Semi-infinite two-layered system . . . . .	205
6.7.3	Semi-infinite three-layered system . . . . .	209
6.8	Conclusions . . . . .	214
<b>7</b>	<b>Doubly Asymptotic Open Boundary for Vector Wave Propagation in Semi-Infinite Layer</b>	<b>216</b>
7.1	Introduction . . . . .	216
7.2	Governing differential equation of vector waves . . . . .	218
7.3	Scaled boundary finite element method of semi-infinite layer with constant depth . . . . .	221
7.4	Dynamic stiffness matrix of semi-infinite layer with constant depth .	227
7.5	Doubly asymptotic continued fraction solution for dynamic stiffness matrix . . . . .	229
7.5.1	Continued fraction solution at high frequency . . . . .	229
7.5.2	Continued fraction solution at low frequency . . . . .	233
7.6	Doubly asymptotic open boundary condition . . . . .	238
7.7	Numerical examples . . . . .	241
7.7.1	Illustration of robustness of doubly asymptotic open boundary for dynamic stiffness . . . . .	242
7.7.2	Semi-infinite layer subjected to horizontal surface traction . .	247
7.7.3	Semi-infinite layer subjected to vertical surface traction . . . .	251
7.7.4	Semi-infinite layer subjected to inclined surface traction . . . .	253
7.8	Conclusions . . . . .	256

<b>8</b>	<b>Conclusions</b>	<b>258</b>
8.1	Summary . . . . .	258
8.2	Recommendations for future research . . . . .	263
<b>A</b>	<b>Summary of Equations</b>	<b>265</b>
A.1	Ricker wavelet function . . . . .	265
A.2	Newmark's method . . . . .	265
A.3	Equivalent dynamic stiffness coefficient . . . . .	266
	<b>References</b>	<b>267</b>

# Chapter 1

## Introduction

### 1.1 Statement of problem

Today, millions of people throughout the world live with a significant risk to their lives and property from earthquakes. Earthquakes have occurred for millions of years and will occur in the future as they occurred in the past. Some may occur in remote or underdeveloped areas. Some may occur near densely populated areas in seismic regions. Therefore, the seismic safety of large-scale structures, for example, dams is a major concern, especially in such seismic regions. Hence, the performance of those structures during an earthquake must be analyzed in a realistic way and evaluated carefully in the time domain. The existing approaches used in the analyses and evaluations are based on the reliable research from the past to the present. Some provide accurate results but are inefficient. Some are efficient but yield low accurate results. Thus this research aims at developing an advanced numerical approach which is not only efficient, but can also provide accurate results of the seismic analysis and also the dynamic analysis of large-scale structures.

In this thesis, dams are used as examples to represent large-scale structures. An example is shown in Fig. 1.1.1. Apart from the dams, the so-called numerical approach is also applicable to other types of large-scale structures, such as long-span bridges, nuclear power plants, etc. Most of the pertinent research on the seismic analysis of structures (see Fig. 1.1.1) usually includes the following topics:

1. Modeling of the bounded domain (structure): the modeling must include non linearity and cracks since an earthquake can induce immense stresses in the dam body that may exceed the linear response range of the concrete and may cause cracking of the dam body (Chopra and Chakrabarti, 1972).

2. Modeling of the unbounded domains (in other words, the infinite regions or the far fields e.g. reservoirs and foundations): the modeling must satisfy the boundary condition at infinity or the radiation condition which states that no energy be radiated from infinity towards the structure (Wolf and Song, 1996). The energy carried by the waves is irreversibly transferred from the structure to the far field. The unbounded domain has an important consequence in wave propagation.
3. Hydrodynamic pressure: the hydrodynamic pressure acting on the dam is caused by the dam-reservoir interaction, which has considerable influence on the dynamic responses of the dam. The vibration of the dam body and the water pressure are dependent on each other (Chopra, 1968, 1970).
4. Soil-structure interaction: the movement of the dam body is induced by the ground motion caused by an earthquake. The actual seismic responses of the dam interact with the motion of the supporting foundation. This interaction is recognized as a significant effect (Tan and Chopra, 1996; Wolf, 1985, 1988).
5. Earthquake input model: the selecting input models in the analysis can affect the analysis results (Bayraktar *et al.*, 2005). The level of sophistication to be used in defining the seismic input is closely related to the degree of understanding of the dynamic behavior of the dam system and to capabilities for modeling such behavior. The progress in defining seismic input has, therefore, followed a long evolutionary process parallel to that of the dynamic analysis capability.

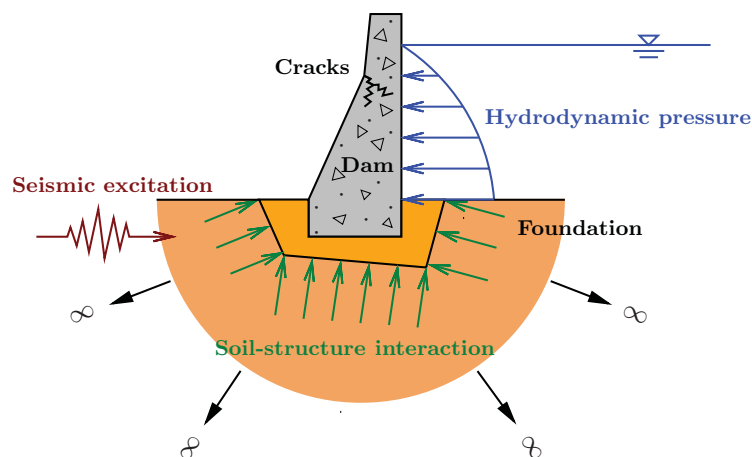


Figure 1.1.1: Seismic analysis system

One of the most difficult topics in the seismic analysis of structures is the modeling of the unbounded domains or the far fields. The infinite extend of the far field is of importance to wave propagation problems. Traveling or propagating in the unbounded direction towards infinity, waves are not reflected back to the near field from which they propagated. As a result, energy carried by the propagating waves is irreversibly transferred from the near field to the far field. This mechanism is called radiation damping. In the modeling of the far field, the boundary condition at infinity also known as the radiation condition must be satisfied.

As generally understood, imposing the condition of vanishing displacement amplitude at infinity is insufficient to seek a unique solution for a wave propagation problem. In 1949, Sommerfeld proposed the radiation condition in order to guarantee the uniqueness of solutions for boundary-value problems. The propagation of scalar waves described mathematically by the Helmholtz equation is addressed,

$$\nabla^2 U(\omega, r) + k^2 U(\omega, r) = 0 \quad (1.1.1)$$

where  $\nabla^2$  denotes the Laplace operator,  $k$  is the wave number,  $U(\omega, r)$  is the wave amplitude,  $r$  is the radial coordinate and  $\omega$  the excitation frequency. The radiation condition states that “sources are to be sources, not sinks of energy” i.e. if the energy radiated by a source, it must disperse at infinity and must not be radiated from infinity towards the source. Thus unbounded domains are regarded as energy sink, not energy source. The radiation condition applied at infinity is expressed in the frequency domain as

$$\lim_{r \rightarrow \infty} r^{\frac{(s-1)}{2}} (U(\omega, r)_{,r} + ikU(\omega, r)) = 0 \quad (1.1.2)$$

where  $s$  is the spatial dimension and  $i$  is the standard imaginary unit. It is obvious that only outgoing waves can satisfy Eq. (1.1.2) while incoming waves cannot.

One of the simplest approach to model an unbounded domain is the finite element method (FEM). The structure and a part of the unbounded domain adjacent to the structure is divided into finite elements. The finite element mesh has to terminate somewhere at a finite distance. In case of static analyses, only a simple boundary condition such as the Dirichlet boundary condition (fixed boundary) is enough for the analyses by enforcing the condition on the truncated boundary. This is because the displacements of the unbounded domain decrease with the increasing distance from the structure.

However, in case of dynamic analyses, such a simple boundary condition is not enough to satisfy the radiation condition because the waves propagating from the

source of excitation or the scatterer (where the load  $R$  is applied in Fig. 1.1.2) are still reflected at the truncated boundary, for example, the one-dimensional problem of an infinite bar as shown in Fig. 1.1.2. In Fig. 1.1.2(a), the bar is excited by a load  $R$  at the left end while the right end is fixed. When the load  $R$  is applied to the left end, a wave  $u$  propagates to the right-hand side at once. As soon as the propagating wave  $u$  impinges the truncated boundary or the fixed end (see Fig. 1.1.2(b)), it is reflected back toward the source of excitation or the left end (as shown in Fig. 1.1.2(c)). This means that the energy carried by the wave is still trapped in the computational domain.

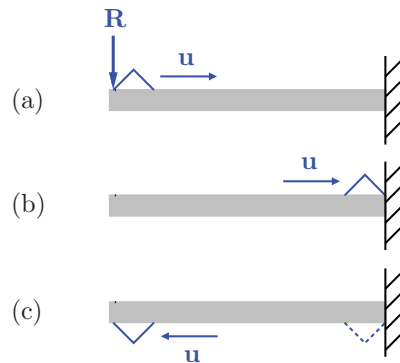


Figure 1.1.2: Wave reflection at truncated boundary

In contrast, in reality, the right end of the bar is at infinity as shown in Fig. 1.1.3. When the bar is excited by the load  $R$  at the left end (see Fig. 1.1.3(a)), a wave  $u$  propagates toward the right-hand side without any reflection as far as the impedance of the bar does not change (see Fig. 1.1.3(b)). Finally, the energy carried by the wave  $u$  must be lost at infinity while the left end still remains stationary as shown in Fig. 1.1.3(c).

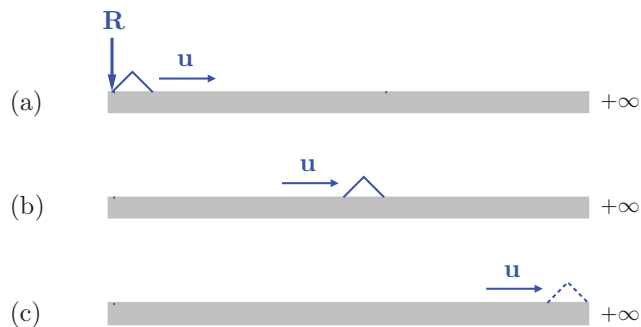


Figure 1.1.3: Wave satisfaction at infinity

To satisfy the radiation conditions is the most challenging task in the soil-structure interaction analyses of large-scale engineering problems. In the context

of dynamic soil-structure interaction, there are two main approaches used in analysis: the substructure method and the direct method as explained in Section 1.2 (Wolf, 1988; Aydinuđlu, 1993; Wolf and Song, 1996). They are employed in combination with global and local boundary conditions formulated at a finite distance from the structure (Section 1.3).

## 1.2 Substructure and direct methods

The fundamental concept of the substructure method is that a system is divided into two substructures, bounded and unbounded substructures as shown in Fig. 1.2.1. The bounded domain or the finite region is made up of the structure and the irregular soil adjacent to the structure. The unbounded domain or the infinite region includes only the regular soil extending to infinity. For the bounded domain, its behavior is assumed to be non-linear and usually modeled with finite elements. For the unbounded domain of infinite dimensions, its dynamic property is represented by a dynamic stiffness matrix on the soil-structure interface. Usually, the unbounded domain that is beyond the soil-structure interface is assumed to have regular properties e.g. isotropy, homogeneity, etc., behaving linearly. In the substructure method, the discretized boundary that encloses the bounded domain coincides with the soil-structure interface, and the rigorous boundary condition is enforced on it. The discretized boundary with the rigorous boundary condition is called a rigorous boundary. As shown in Fig. 1.2.1, a rigorous boundary is placed on the soil-structure interface, representing the whole unbounded domain.

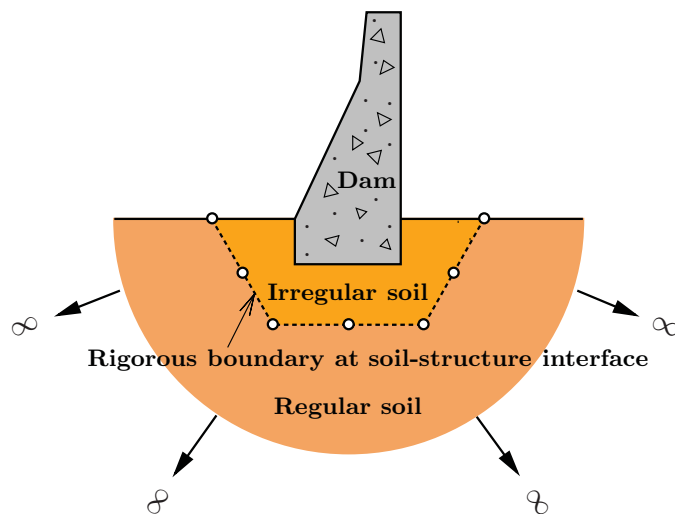


Figure 1.2.1: Substructure method

By combining the substructure method with a rigorous boundary, the relationship between force and displacement formulated on the soil-structure interface that satisfies the radiation condition is coupled with the substructure of the bounded domain. This leads to the governing equations of the total dynamic system, and can be regarded as a boundary condition which is generally rigorous. In the frequency domain, such a boundary condition is expressed as the following equation:

$$\{R(\omega)\} = [S^\infty(\omega)]\{U(\omega)\} \quad (1.2.1)$$

where  $\{R(\omega)\}$  is the interaction forces,  $[S^\infty(\omega)]$  the dynamic stiffness matrix of the interface, and  $\{U(\omega)\}$  the displacements of the nodes on the interface. The superscript  $\infty$  denotes the unbounded domain and  $\omega$  is the excitation frequency. Since this boundary condition is linear, when the non-linear behavior of the bounded domain is considered, the simulation has to be carried out in the time domain.

This can be done by transforming the boundary condition in the frequency domain (Eq. (1.2.1)) to the time domain using the inverse Fourier transform as expressed in

$$\{r(t)\} = \int_0^t [s^\infty(t - \tau)]\{u(\tau)\}d\tau \quad (1.2.2)$$

where  $\{r(t)\}$  is the interaction forces on the interface at a specific time  $t$  which is equal to the convolution integral of the unit-impulse response matrix of the unbounded domain  $[s^\infty(t)]$ , and  $\{u(\tau)\}$  the corresponding displacement vector (Wolf and Song, 1996). Equation (1.2.2) is similar to the Duhamel integral that is widely used in structural dynamics.

Usually, rigorous boundaries are defined by convolution integrals in the time domain. Thus they are non-local in time i.e. the present response depends on the previous time-history, and also non-local in space i.e. the future response of a degree of freedom depends not only on its own previous time-history but on the previous time-histories of all degrees of freedom on the boundary too. This can be described by Fig. 1.2.2 using the physics of wave propagation. When a force  $R$  is applied at node  $A$  on the discretized boundary, waves are generated, causing displacements ( $u_1, u_2, \dots, u_m$ , where  $m$  is the number of degrees of freedom) at all the other nodes on the boundary. The displacement response of a degree of freedom at time  $t_n$  (where  $n$  is the time step) depends on not only the force  $R_n$  at the same time but also on the forces at all previous time (i.e.  $t_1$  to  $t_{n-1}$ ).

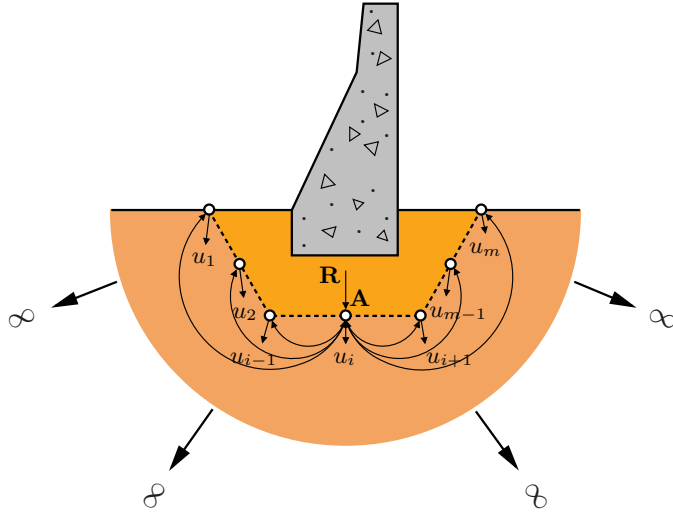


Figure 1.2.2: Spatial coupling of rigorous boundary

The non-locality in space leads to fully populated unit-impulse response matrices at each time step. This leads to immense storage consumption when the number of degrees of freedom is large. In addition, a convolution integral has to be evaluated at each time step which yields unacceptable storage requirements for a long-time simulation. Even though the substructure method usually provides high accuracy and robustness in a numerical implementation, it is often computationally expensive, especially for large-scale problems. This has led to the search of high quality approximations that are local in space and time, that is, approximations that involve only points in the neighborhood of the boundary point under consideration within a small time-window (Kausel, 1988).

In the direct method, the numerical discretization, e.g. by the finite element method, is truncated at a certain distance away from the structure (Fig. 1.2.3). To represent the unbounded domain outside of the boundary, a boundary condition formulated using local procedures has to be imposed on the discretized boundary. This boundary condition is formulated to absorb waves propagating across the boundary to the exterior unbounded domain. The discretized boundary with such a boundary condition is known in various names such as artificial boundary, transmitting boundary, absorbing boundary, non-reflecting boundary, open boundary etc. In this thesis, the term “artificial boundary” is chosen as the general term.

As shown in Fig. 1.2.3, the bounded domain, including the structure, the irregular soil and the part of the regular soil that is adjacent to the structure and enclosed by the artificial boundary, is normally modeled with standard finite elements as in the substructure method. In general, artificial boundaries are local in space and time, and thus approximate. They are less accurate than rigorous boundaries.

Nevertheless, they are numerically cheaper and more geometrically universal. In the time domain, they can be directly formulated with time-step integration schemes. Hence, the convolution integral, which is a computationally expensive task, is not required in the direct method.

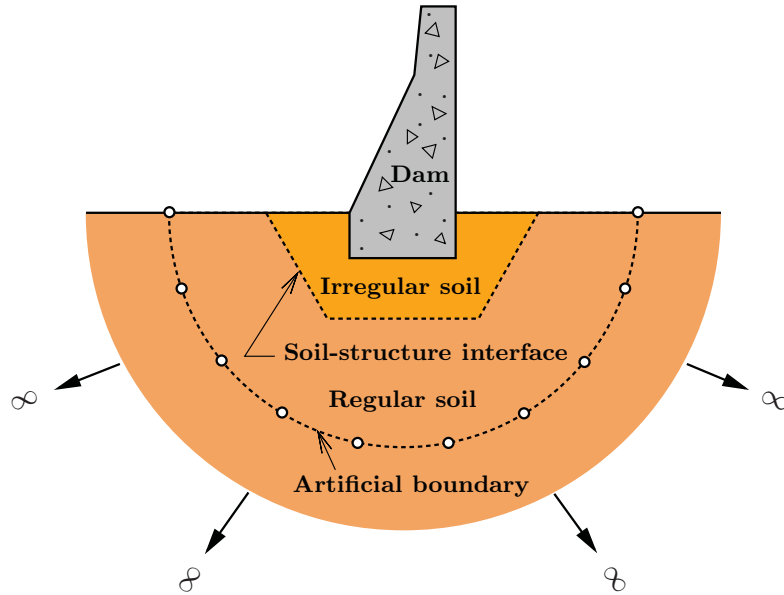


Figure 1.2.3: Direct method

An artificial boundary can be illustrated by using the physics of wave propagation in Fig. 1.2.4. When a force  $R$  is applied at node  $A$  on the boundary discretized with two-node elements, waves are generated. It is assumed that the waves cause displacements only within the elements connected to node  $A$ . The direct coupling of the degrees of freedom is limited to the portion of the boundary modeled by one element. To obtain the displacement response at a specified node at time  $t_n$ , the displacement responses of only nodes of the elements connected to it at only previous time steps ( $t_{n-1}$  or  $t_{n-2}$  depending on the formulation of the boundary) are used.

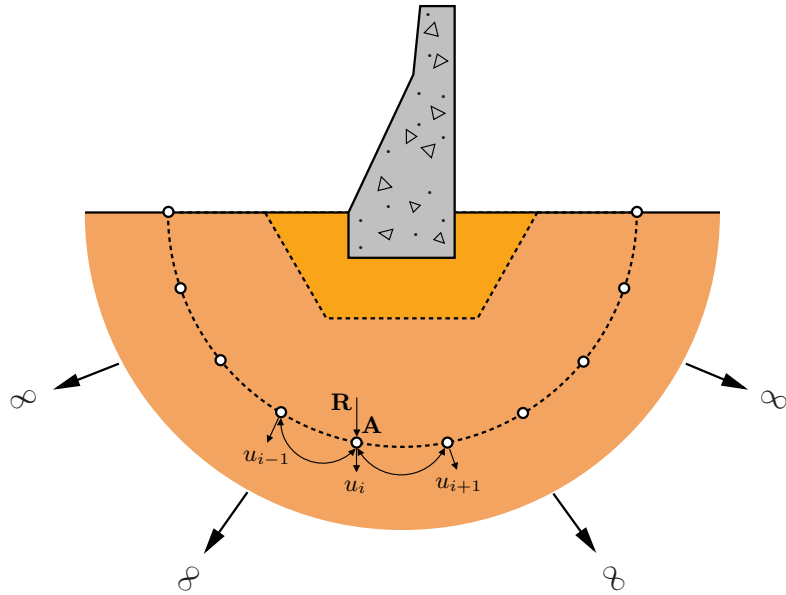


Figure 1.2.4: Spatial coupling of artificial boundary

The artificial boundaries do not perform well when they are placed too close to the structure due to the spurious reflections occurring at the truncated boundaries (Givoli, 1991). That means the radiation conditions are not satisfied. This is similar to the example of the one-dimensional bar as described earlier in Fig. 1.1.2. In order to avoid such a problem, those artificial boundaries must be placed sufficiently far from the scatterer. However, this would result in a large computational domain with a large number of degrees of freedom which increases the computational time. Thus, artificial boundaries, which may be placed relatively close to or directly on the embedded structure, are needed.

### 1.3 Global and local boundary conditions

Over the last four decades several approaches have been proposed formulating rigorous and artificial boundary conditions for wave propagation problems in unbounded domains. These approaches can basically be classified into two groups. The approaches in the first group are known as global procedures and those in the second group are local procedures. The first group is highly accurate but cumbersome while the second group is less accurate but algorithmically simple (Tsynkov, 1998).

### 1.3.1 Global procedures

Global procedures are rigorous. They are described through integral operators with respect to space or time. Due to their high accuracy, the rigorous boundaries constructed by these procedures can be placed as close as the structure. This leads to the reduction of the number of degrees of freedom in the unbounded domain which means the computational time also reduces due to the less amount of degrees of freedom. However, as they are spatially and temporally global, a great deal of data has to be processed. This results in an expensive computation, especially for large-scale problems and long-time calculations.

Among the global procedures, the boundary element method (BEM) is well-known as it has attracted a lot of attention from researchers for problems involving unbounded domains since 1970s (Brebbia, 1978; Dominguez, 1993; Hall and Oliveto, 2003). There are two distinct benefits when using the BEM for modeling unbounded domains. The former is that the radiation condition can be automatically satisfied by the fundamental solution, and the latter is that only the boundary of the soil-structure interface between the bounded domain (including the dam and irregular soil) and the unbounded domain is discretized, thereby reducing the spatial dimension by one. Even though the BEM is suited for modeling unbounded domains, fundamental solutions are sometimes much more complicated to achieve when anisotropic materials are used in the model. As a result, the BEM is unsuitable for many practical engineering problems owing to its reliance on the fundamental solution. Moreover, the coefficient matrices of the BEM are fully populated and unsymmetric. This leads to expensive computations.

The thin-layer method (TLM) or the consistent method that is also a global procedure. This approach was developed from the work of Lysmer in 1970 to solve wave propagation problems in layered media with a rigid base (Lysmer, 1970). Since then, this method has been developed continuously so that it can be applied to both frequency-domain analysis (Lysmer and Waas, 1972; Waas, 1972) and time-domain analysis (Kausel, 1994). The TLM is a semi-discrete numerical approach which is based on the finite element formulation. The rigorous boundary constructed from the TLM, also known as the consistent boundary, can be only applied on the vertical discretized boundary of a layered medium which is the restriction of the TLM.

The scaled boundary finite element method (SBFEM) is a novel approach used for modeling unbounded domains with arbitrary geometry (Wolf and Song, 1996; Song and Wolf, 1997). This approach is based on the finite element formulation but only the boundary is discretized. Thus the spatial dimension is reduced by one. Furthermore, It can be coupled seamlessly with standard finite elements. Therefore

it has the same advantages as similar as those of the BEM and the FEM. Moreover, in case of modeling unbounded domains, the SBFEM can automatically satisfy the radiation condition without any use of fundamental solution as required in the BEM.

Apart from these global procedures, there is another type of global procedures which is of interest. These global procedures are known as exact non-reflecting boundary conditions (exact NRBCs) which are based on analytical solutions for unbounded domains with simple geometry and material properties, for example, the exact NRBC of Keller and Givoli (1989) using the Dirichlet to Neumann (DtN) map and the exact NRBC of Alpert *et al.* (2000) using the non-reflecting boundary kernel.

These global procedures perform well in frequency-domain analyses, but in time-domain analyses, they always require convolution integrals which result in a large computational effort that is inappropriate for evaluating large practical problems. This issue led to the developments of local procedures which are spatially and temporally local.

### 1.3.2 Local procedures

Local procedures are formulated using differential operators with respect to space and time. The boundary conditions on the artificial boundaries formulated from the local procedures are generally approximate and based on the mathematical representation of wave propagation in order to absorb propagating waves. There have been several existing artificial boundaries for simulating wave propagation in unbounded domains developed by several researchers.

The first artificial boundary is the Lysmer-Kuhlemeyer boundary, which was invented in 1969 (Lysmer and Kuhlemeyer, 1969). It is generally known as the viscous boundary due to the viscous damping forces applied on the boundary. This viscous boundary is a low-order transmitting boundary. It is very low accurate since only first-order approximation is used in the formulation.

From the late 1970s to the mid-1980s, high-order absorbing boundary conditions (high-order ABCs) were proposed. The accuracy of the solution obtained from the high-order ABCs increases with increasing orders. Some of the high-order ABCs became well-known such as the paraxial boundary condition (Engquist and Majda, 1977), the Bayliss-Turkel boundary condition (Bayliss and Turkel, 1980). These two ABCs with second order became popular and are still commonly used today (Givoli, 2004).

However, from the implementation point of view, these high-order ABCs are impractical when their orders are beyond second-order (Givoli, 2004). Since the

mid-1990s, high-order local ABCs have been developed and overcome this problem by introducing auxiliary variables (Hagstrom and Hariharan, 1998; Givoli and Neta, 2003; Hagstrom and Warburton, 2004). These high-order local ABCs are spatially and temporally local. However, their applications are limited to unbounded domains with simple geometry. Moreover, the extension to elastic wave propagation in unbounded domains with arbitrary geometry is not straightforward since the method of separation of variables is not applicable.

In addition to these local procedures, there are three interesting local procedures that have been developed in different ways such as the doubly asymptotic approximations (DAAs) (Geers, 1978; Geers and Lewis, 1997; Geers and Tothaker, 2000), the infinite elements (Bettess, 1977; Astley and Eversman, 1983; Burnett, 1994) and the perfectly match layers (Berenger, 1994; Sacks *et al.*, 1995; Yu *et al.*, 2003). These local procedures are also used for absorbing propagating waves as well as the absorbing boundaries. They are temporally local and can be implemented with the finite element method or the finite difference method.

Recently, a new approach to constructing high-order transmitting boundary with arbitrary geometry has been proposed by Bazyar and Song (2008). The transmitting boundary is spatially and temporally local. The transmitting boundary condition is expressed as a system of first-order ordinary differential equations in time to which time-step integration schemes in structural dynamics are directly applicable. Most of the existing high-order ABCs are singly asymptotic at the high-frequency limit ( $\omega \rightarrow \infty$ ) and only propagating modes are embodied in the formulation (Hagstrom *et al.*, 2008). Therefore, they are suited for propagating waves not evanescent waves.

Today there are plenty of work and research on local procedures which relate to various fields such as acoustics, electrodynamics, hydrodynamics, geophysics, aerodynamics etc.

## 1.4 Objectives

As mentioned in the previous section, most of the existing artificial boundaries are singly asymptotic at the high-frequency limit ( $\omega \rightarrow \infty$ ) and applicable to scalar waves in homogeneous unbounded domains. To surpass these limitations, a new approach has been developed and proposed in this thesis. The term “open boundary” which means “free-space boundary” is chosen and used specifically for the artificial boundaries developed in this thesis. The main objectives of the present research in the thesis are as follows:

1. To develop the theory of doubly asymptotic continued fraction solutions for dynamic stiffness coefficients for the modal equations of scalar waves in a semi-infinite layer with a constant depth and a circular cavity in a full-plane.
2. To construct the high-order doubly asymptotic open boundaries for the modal equations of scalar waves in a semi-infinite layer with a constant depth and a circular cavity embedded in a full-plane.
3. To construct the high-order doubly asymptotic open boundary for two-dimensional acoustic wave propagation in a semi-infinite reservoir with a constant depth by extending the scaled boundary finite element method.
4. To develop the coupling scheme of the scaled boundary finite element method and the finite element method that is applicable to dynamic and seismic analyses of large-scale structures e.g. dams with a semi-infinite reservoir.
5. To develop the theory of doubly asymptotic continued fraction solutions for dynamic stiffness matrices for two-dimensional scalar wave propagation in a homogeneous full-plane with a circular cavity and in a semi-infinite layered system.
6. To construct the high-order doubly asymptotic open boundaries for two-dimensional scalar wave propagation in a homogeneous full-plane with a circular cavity and in a semi-infinite layered system by extending the scaled boundary finite element method.
7. To develop the theory of doubly asymptotic continued fraction solution for dynamic stiffness matrices for two-dimensional vector wave propagation in a homogeneous semi-infinite layer with a constant depth.
8. To construct the high-order doubly asymptotic open boundary for two-dimensional vector wave propagation in a homogeneous semi-infinite layer with a constant depth by extending the scaled boundary finite element method.

This thesis aims at developing the theory of the doubly asymptotic continued fraction solutions and also constructing the high-order doubly asymptotic open boundaries for unbounded domains which can improve the high-order singly asymptotic open boundary (the existing open boundary). The proposed open boundaries can be employed not only in the geotechnical engineering, but also in other disciplines such as acoustics, aeronautics, electromagnetics, hydrodynamics, etc. The proposed open boundaries are of the following characteristics and properties:

1. The open boundary conditions are based on high-order approximation, and developed from the extension of the scaled boundary finite element method.
2. The open boundaries are doubly asymptotic i.e. the approximation approaches the exactness at both high-frequency limit ( $\omega \rightarrow \infty$ ) and low-frequency limit ( $\omega \rightarrow 0$ ).
3. The approximation technique of continued fraction, which is similar to the rational function and the Padé expansion, is employed in the derivation of the continued fraction solution for dynamic stiffness since it has a large range of convergence, and also converge rapidly with high accuracy.
4. The open boundary conditions are constructed as systems of first-order ordinary differential equations in time by introducing auxiliary variables. Standard time-step integration schemes are applicable to transient analyses.
5. The open boundaries are applicable to wave propagation in homogeneous semi-infinite layers with a constant depth, semi-infinite layered systems and homogeneous full-planes with a circular cavity.
6. The open boundaries are practical in implementation, and can be coupled with finite element schemes in the time domain.
7. The open boundaries are temporally local.

## 1.5 Thesis outline

The outline of the thesis are as follows:

In Chapter 2, the literature review of the existing boundaries i.e. rigorous boundaries and artificial boundaries that are employed for wave propagation problems in unbounded domains are summarized. The key equations of the existing boundaries are expressed, and the key figures are shown. The history of development of each approach is described, and the advantages and disadvantages are also discussed.

In Chapter 3, the doubly asymptotic continued fraction solutions for modal dynamic stiffness coefficients are derived for a semi-infinite layer with constant depth and a circular cavity embedded in a full-plane. Also, the high-order doubly asymptotic open boundary conditions in the time domain for the modal equations of scalar waves are formulated. The accuracy of the doubly asymptotic open boundaries is evaluated and compared with that of the singly asymptotic open boundary in the numerical examples. The results are summarized in the conclusions.

In Chapter 4, the SBFEM is extended to acoustic wave propagation. The scaled boundary finite element equation in pressure is derived for the far-field water in the reservoir. The derivation of the doubly asymptotic continued fraction solution for modal dynamic stiffness coefficients is also described. The high-order doubly asymptotic open boundary condition in the time domain is then formulated and the coupling scheme with finite elements are established. Numerical examples are provided and the results are summarized in the conclusions.

In Chapter 5, the scaled boundary finite element equation in displacement of a full-plane with a circular cavity is derived for scalar wave propagation. The numerical stability of the doubly asymptotic continued fraction solution for modal dynamic stiffness coefficients is improved by introducing the factor coefficients to the continued fraction solution. The high-order doubly asymptotic open boundary condition in the time domain is formulated. Numerical examples are provided and the results are summarized in the conclusions.

In Chapter 6, the scaled boundary finite element equations in displacement and in dynamic stiffness of a semi-infinite layered system are derived for scalar wave propagation. The doubly asymptotic continued fraction solution for dynamic stiffness matrix is derived with the introduction of the factor matrices to improve the numerical stability of the solution. The high-order doubly asymptotic open boundary condition in the time domain is formulated. Numerical examples are provided and the results are summarized in the conclusions.

In Chapter 7, the scaled boundary finite element equations in displacement and in dynamic stiffness of a semi-infinite layer with a constant depth are derived for vector wave propagation. The doubly asymptotic continued fraction solution for dynamic stiffness matrix is derived with the introduction of the factor matrices to improve the numerical stability of the solution. The high-order doubly asymptotic open boundary condition in the time domain is formulated. Numerical examples are provided and the results are summarized in the conclusions.

In Chapter 8, all the works in the research are summarized, and the possible works in the future research are recommended.

# Chapter 2

## Literature Review

### 2.1 Introduction

As mentioned in Chapter 1, several approaches have been developed for modeling unbounded domains over the last four decades. They can be classified into two groups: global and local procedures. In this chapter, the literature review of the global and local procedures is presented. The history of development of both procedures is described. The advantages and disadvantages of the procedures are also discussed. Only the key equations and figures of the procedures are expressed and illustrated.

This chapter is organized as follows: in Section 2.2, the global procedures, including the boundary element method, the thin-layer method, the scaled boundary finite element method, exact non-reflecting boundaries and temporally local exact non-reflecting boundaries are summarized. In Section 2.3, the local procedures, including low-order, high-order and local high-order absorbing boundary conditions, doubly asymptotic approximations, infinite elements and absorbing layers are summarized. In Section 2.4, the capacity of commercial finite element packages used for modeling unbounded domains is discussed. In Section 2.5, the conclusions are presented.

### 2.2 Global procedures

Global procedures often lead to rigorous boundary conditions. The rigorous boundary condition can be placed very close to the structures. This leads to the reduction of the size of the bounded domain which is necessary to obtain accurate responses, and thereby the computational time. However, the rigorous boundaries obtained from the global procedures are spatially and temporally global. The amount of

data to be processed increases rapidly with the number of time steps due to the convolution integrals. This results in high computational cost for long-time analyses such as those required in earthquake engineering. Hence, the global procedures are impractical for large-scale structures subjected to earthquakes. Common global procedures include the boundary element method (see Section 2.2.1), the thin-layer method (see Section 2.2.2), the scaled boundary finite element method (see Section 2.2.3), exact non-reflecting boundaries (see Section 2.2.4) and temporally local exact non-reflecting boundaries (see Section 2.2.5).

## 2.2.1 Boundary element method

The boundary element method (BEM) is illustrated by its application to solve the Laplace equation, which is one of the best known partial differential equations in engineering.

$$\nabla^2\phi = 0 \tag{2.2.1}$$

where  $\phi$  is a potential function, the symbol  $\nabla$  called nabla denotes the gradient of a function in calculus. In the past, several mathematicians and scientists studied and performed their research on potential problems and established the potential theory (Kellogg, 1929). They solved the potential problems by posing them as boundary value problems i.e. imposing boundary conditions e.g. the Dirichlet boundary condition, the Neumann boundary condition, etc. on the boundary  $\Gamma$  enclosing a region  $\Omega$ . The solution of the governing differential equations (the Laplace equation in this case) of a free space under the action of a point source is called a fundamental solution.

The boundary element method (BEM) arises from the potential problems. The most important work presented by Green (1828) considerably contributed to the BEM at the early age. He proposed the three Green's identities. The first identity obtained from the divergence theorem is expressed as

$$\iiint_{\Omega} (\phi \nabla^2 \psi + \nabla \phi \cdot \nabla \psi) d\Omega = \iint_{\Gamma} \phi \frac{\partial \psi}{\partial n} d\Gamma \tag{2.2.2}$$

where  $\psi$  is also a potential function, and  $\frac{\partial \psi}{\partial n}$  is the directional derivative of  $\psi$  in the direction of the outward normal vector  $\vec{n}$  of the boundary  $\Gamma$ . The second identity

obtained from using the first identity is expressed as

$$\iint_{\Omega} (\phi \nabla^2 \psi - \psi \nabla^2 \phi) d\Omega = \iint_{\Gamma} \left( \phi \frac{\partial \psi}{\partial n} - \psi \frac{\partial \phi}{\partial n} \right) d\Gamma \quad (2.2.3)$$

By substituting the Green's function  $\frac{1}{r}$  which is a fundamental solution into  $\psi$  in the second identity, the third identity is obtained as

$$\phi = \frac{1}{4\pi} \iint_{\Gamma} \left[ \frac{1}{r} \frac{\partial \phi}{\partial n} - \phi \frac{\partial(1/r)}{\partial n} \right] d\Gamma \quad (2.2.4)$$

which is exactly the formulation of the present-day BEM for potential problems. A common feature of all BEMs is their use of fundamental solutions. The earliest fundamental solution for isotropic elastostatics was derived by Thomson (1848), later known as Lord Kelvin. It was used for solving the problem of a point force applied to the interior of an infinite isotropic solid. In elastodynamics, the first fundamental solution in the frequency domain was given by Stokes (1849), and in the time domain solution was presented by Eringen and Suhubi (1975). Besides the potential theory, the works of Betti (1873), Somigliana (1885), Kupradze (1963) and others in elasticity also contributed to the development of the BEM at its early age.

The works of Jaswon (1963) and Symm (1963) are considered as a very crucial contribution that inspired later researchers of the BEM. In their works, Jaswon and Symm have developed the direct boundary integral equation method (BIEM) using Green's boundary formula (or Green's third identity) as expressed in Eq. (2.2.5) for two-dimensional potential problems.

$$\frac{1}{2\pi} \int \ln|P - q| \phi'(q) dq - \frac{1}{2\pi} \int \ln|P - q| \phi(q) dq = \phi(P) \quad (2.2.5)$$

where  $P$  and  $q$  are the points on the boundary,  $\phi(P)$  a harmonic function throughout a domain  $D$ ,  $\phi(q)$  boundary values, and  $\phi'(q)$  boundary normal derivatives. Jaswon and Ponter (1963) and Symm (1963) solved the boundary integral equation (BIE) numerically and successfully. A few years later, Rizzo (1967) and Cruse (1969) developed BIE approaches for two- and three-dimensional elastostatic problems, and also extended the approaches to transient elastodynamics (Cruse and Rizzo, 1968; Cruse, 1968) using a fundamental solution and the vectorial form of Betti's theorem (the reciprocal work theorem). This yielded a vector identity in Laplace

transform domain,

$$u_j(p) = \int_{\Gamma} t_i(q)u_{ji}^*(q,p)d\Gamma - \int_{\Gamma} u_i(q)t_{ji}^*(q,p)d\Gamma + \int_{\Omega} F_i(q)u_{ji}^*(q,p)d\Omega \quad (2.2.6)$$

which corresponds to Somigliana's identity (in elastostatics) and Green's third identity (in potential theory), where  $p$  is an interior point or load point,  $q$  is any point on the boundary (field point),  $u_j(p)$  is the displacement,  $t_i(q)$  is the traction force,  $u_{ji}^*(q,p)$  is the fundamental solution,  $t_{ji}^*(q,p)$  is the boundary traction vector of the fundamental solution, and  $F_i(q)$  is the body load. In the time domain, they obtained the results by employing the numerical inversion technique of Papoulis (1957). Since the BIEM is derived in the Laplace transform domain, the drawback of this approach is the difficulty in transform inversion. If the BIEs are expressed in the time domain, they contain convolutions in time. The solution of geometrically complex problems through the use of time convolution is very computationally expensive. Therefore, neither Laplace-transformed nor time-convolved BIEs are suitable for use in practical transient elastodynamics analysis.

Lachat and Watson (1976) made a significant contribution to the numerical implementation of the BIEM by incorporating an isotropic formulation which was similar to that used in the FEM into the BIEM. The sub-regions were introduced to handle large-scale problems and algorithms were described for the computation of the weakly singular and quasi-singular integrals that appeared in the BIEs. This work was considered as the first-published work that incorporated the FEM idea into the BIEM.

An algorithm for the computation of the Cauchy principal value integrals resulting from the strong singularity of the traction fundamental solution was presented by Guiggiani and Gigante (1990). The term "boundary element method" was coined in 1977 in three publications (Banerjee and Butterfield, 1977; Brebbia and Dominguez, 1977; Dominguez, 1977), and in the following year, the first book on the BEM was released (Brebbia, 1978). The BEM presented by Brebbia and Dominguez (1977) is based on the weighted residual formulation. The weight function is assumed to be the fundamental solution. In the case of the Laplace equation, they used  $\frac{1}{4\pi r}$  as the weight function, and also imposed the Dirichlet boundary condition  $\phi = f(x)$  and the Neumann boundary condition  $\frac{\partial\phi}{\partial n} = g(x)$  on the boundaries  $\Gamma_1$  and  $\Gamma_2$ ,

respectively. This led to the weighted residual formulation,

$$\phi = \frac{1}{4\pi} \iint_{\Gamma_1} f(x) \frac{\partial(1/r)}{\partial n} d\Gamma - \frac{1}{4\pi} \iint_{\Gamma_1} \frac{1}{r} \frac{\partial\phi}{\partial n} d\Gamma + \frac{1}{4\pi} \iint_{\Gamma_2} \phi \frac{\partial(1/r)}{\partial n} d\Gamma - \frac{1}{4\pi} \iint_{\Gamma_2} \frac{1}{r} g(x) d\Gamma \quad (2.2.7)$$

Since the early 1980s, a surge in research activities on the BEM has occurred, and an increasing number of problems in structural mechanics including material and geometric non-linearities have been treated. Also, the range of applications was extended to other fields of mathematical physics such as electrodynamics and fluid mechanics. Today the BEM is known as one of the numerical methods based on the weighted residual formulation of which the weight function used is the fundamental solution (Green's function) of the governing equation. A key to the success of the BEM is the reduction of spatial dimension by one (i.e. transformation of the volume integrals into surface integrals for three-dimensional problems, or transformation of the surface integrals into line integrals for two-dimensional problems), thereby reducing the data preparation and computational time. Figure 2.2.1 illustrates the spatial discretization on the boundary  $\Gamma$  of the computational domain  $\Omega_i$  by the BEM to represent the unbounded domain  $\Omega_e$ .

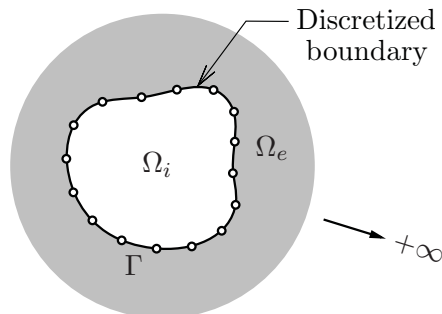


Figure 2.2.1: Spatial discretization by BEM for unbounded domain

Even though the BEM is a useful method for wave simulation in stratified media with irregular interfaces, the computational time increases exponentially as the number of layers increases. Hence, researchers proposed their own approaches to solve such a problem. For example, Bouchon *et al.* (1995) introduced a sparse method to reduce the numerical task. Fu (2002) proposed an improved block Gaussian elimination scheme to tackle the problems of wave propagation in a heterogeneous layered medium system. Fu and Bouchon (2004) also provided some approximation solutions. Ge and Chen (2008) employed an efficient approach to solve the global matrix propagators (introduced by Ge and Chen (2007) to improve the efficiency of

the BEM) directly, and the calculation of the matrix propagator of each single layer was omitted.

### 2.2.2 Thin-layer method

A well-known rigorous method apart from the BEM is the thin-layer method (TLM). The TLM is a semi-discrete numerical approach as it is based on a finite-element solution in the direction of layering (the vertical direction) while exact solutions are enforced on the remaining direction (the horizontal direction). The TLM requires relatively small computational effort in comparison with other full-discretization methods, such as the finite difference and finite element methods, provided that the medium is sufficiently regular in the horizontal direction that analytical solutions can be found. The vertical boundary discretized by the TLM is known as the consistent boundary as illustrated in Fig. 2.2.2. The consistent boundary represents the entire layered medium that extends to infinity in the horizontal direction.

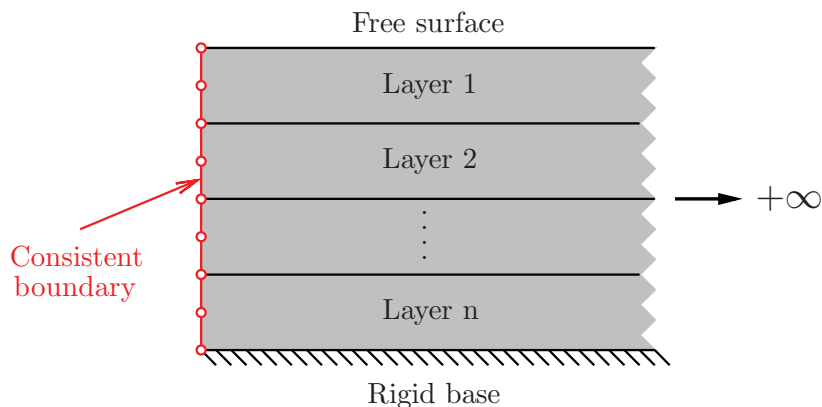


Figure 2.2.2: Consistent boundary generated by thin-layer method

The TLM was originally developed by Lysmer (1970) to study the propagation of seismic Rayleigh waves in layered earth strata. It was further substantially developed by Waas (1972). The characteristic equations (Eq. (2.2.8)) were obtained directly from a variational formulation, not from a limiting process to a finite element mesh as Lysmer had done. The original equation of the TLM was formulated in the frequency domain as

$$([A]k^2 + [B]k + [G] - \omega^2[M])\{U\} = \{P\} \quad (2.2.8)$$

where  $k$  denotes the wave number,  $\{U\}$  is the displacement vector,  $\{P\}$  is the prescribed load vector, and  $[A]$ ,  $[B]$ ,  $[G]$  and  $[M]$  are narrowly banded matrices that

depend on the material constants and layer thickness. Only  $[B]$  is skew-symmetric while the other matrices are symmetric. This  $[B]$  exists in the in-plane case ( $SV - P$  waves), but vanishes for the anti-plane case ( $SH$  waves).

The concept of a consistent energy transmitting boundary for layered strata proposed by Waas (1972) was extended by Kausel and Roesset (1977) in order to develop the hyperelement for plane-strain problems. The hyperelement is based on the same semi-analytical formulation of the TLM, and also known as the consistent boundary, representing a frequency-dependent force-displacement relation on the discretized boundary. Consequently, it can be used only in the frequency-domain computations. It is, therefore, restricted to the analysis of linear system and cannot be employed to study non-linear problems using time-step integration techniques.

In the early 1980s, Tajimi (1980), Waas (1980) and Kausel (1981) independently arrived at the closed-form solutions (Green's functions) for elastodynamic problems employing the TLM. Tajimi (1980) investigated the dynamic stiffness of surface foundations, considering only point loads. Waas (1980) considered point and ring loads, using cylindric expansions for the displacement field in the radial direction, and enforcing equilibrium and continuity conditions within the soil. Among these three, Kausel (1981) provided the most general framework for handling loads with arbitrary spatial-temporal characteristics via Fourier and Hankel transforms, and included detailed expressions on the consistent stresses and strains. Extending this work, Kausel and Peek (1982b) derived the Green's functions of point loads, which had become the core of several computer programs such as PUNCH, SASSI, SASW, etc, and also procedures for the analysis of wave propagation in layered media. These Green's functions allowed the application of the TLM to the BEM to study laminates with irregularities e.g. cavities or inclusions (Kausel and Peek, 1982a). Afterwards, Kausel (1999) presented the Green's functions for a class of dynamic point sources acting on, or within, laminated media. The set of the point sources that was considered included force dipoles (e.g. cracks, point moments, single and double couples), blast load and bimoments (or moment dipoles).

The Green's functions in the wavenumber domain are algebraic rather than transcendental. Therefore, the Hankel transforms required for an evaluation of the Green's functions in the spatial domain can be readily computed in closed forms. In the classical implementation, the Green's functions of layered media are obtained by the following steps: (1) formulating the equations of motion in the frequency-wavenumber domain, (2) solving a complex-valued quadratic eigenvalue problem in the wavenumbers, (3) integrating analytically over wavenumbers, and (4) integrating numerically over frequencies by means of the fast Fourier transform.

For the TLM formulated in the time domain, Kausel (1994) first succeeded in formulating it. This formulation is not only able to avoid the use of complex algebra and error-prone inverse Fourier transforms, but also allows the Green's functions to be obtained directly in the time domain. In this approach, a linear real-valued eigenvalue problem in the frequency variable is solved first, and then an analytical integration must be carried out over frequencies. Finally, a numerical transform is performed over wavenumbers.

Park and Kausel (2004) investigated the numerical dispersion of the TLM for both linear and quadratic expansions applying the exact solution to the spectrum equation for the discrete wave equation. Such a numerical dispersion occurs due to the spatial discretization when an elastic medium is modeled by the TLM. This numerical dispersion can slightly alter the paths and also the velocities of waves. This results in a discrepancy between the solutions for the discrete and continuous models. They first characterized the numerical dispersion for  $SH$  and  $SV - P$  waves in an unbounded domain. Then they developed optimal tuning factors used for minimizing the numerical dispersion error.

In case of anisotropic layered media, the TLM was also extended and studied by Kausel (1986). Within each sublayer, the material properties were assumed to be homogeneous, and would probably change from sublayer to sublayer. Waas and Hartmann (1988) also employed the TLM with explicit Green's functions for arbitrary ring loads to inhomogeneous layered media of which shear modulus increased linearly with depth. Apart from anisotropic and inhomogeneous layered media, the TLM formulated in the wavenumber-time domain was extended to inhomogeneous piezo-composite layered media (Chakraborty *et al.*, 2005). The material properties were allowed to vary in the depthwise direction only. Linear and exponential variations of elastic and electrical properties were both considered.

Park and Kausel (2006) employed the TLM formulated in the wavenumber-time domain to a homogeneous layer underlain by an elastic half-space in two dimensions. An impulsive, spatially harmonic  $SH$  source was considered in the homogeneous layer and the elastic half-space below the common interface independently. They proposed an approach which was based on combining the exact expressions for the response in the underlying half-space formulated in the wavenumber-time domain with a complete modal solution in that domain for the layers. The approach can avoid the computational problems associated with resonances in the layers. Kausel and Park (2006) also generalized the concept to two-dimensional  $SV - P$  line sources and to three-dimensional point sources, including seismic couples.

### 2.2.3 Scaled boundary finite element method

The novel scaled boundary finite element method is a fundamental solution-less boundary-element method based on finite elements, which combines the advantages of the boundary-element and finite element methods. This method was originally developed for two-dimensional scalar waves in unbounded domains (Song and Wolf, 1995), and was called the consistent infinitesimal finite-element cell method, reflecting the mechanically based derivation analogous to the early work in finite elements (Wolf and Song, 1996).

The concept is that a finite element cell with the exterior boundary similar to the interior one is introduced in the radial direction adjacent to the structure-medium interface. The relationship based on similarity and the limit of the infinitesimal cell width approaching zero leads to the consistent infinitesimal finite-element cell equation in dynamic stiffness of an unbounded domain in the frequency domain. For the consistent infinitesimal finite-element cell equation in acceleration unit-impulse response in the time domain, it is obtained from applying the inverse of Fourier transform to the equation in the frequency domain. This approach was later extended to two-dimensional vector waves (Wolf and Song, 1995) and three-dimensional vector waves (Song and Wolf, 1996).

Soon after, the procedure was rederived and renamed as the scaled boundary finite element method (SBFEM), starting from the governing partial differential equations of linear elastodynamics applying the weighted residual technique (Song and Wolf, 1997). The derivation is mathematically more appealing and is consistent with the finite element formulation. Only the boundary of the domain is discretized as surface finite elements, thereby reducing the spatial dimension by one. Although this method discretizes only the boundary as well as the BEM, it does not require fundamental solutions as the BEM does. This method is also a semi-analytical approach since the equilibrium equation is enforced exactly in the radial direction, and converges to the exact solution in the finite-element sense in the circumferential direction. In addition, the radiation condition or the boundary condition at infinity is satisfied rigorously.

The basic concept of employing the SBFEM for modeling an unbounded domain is illustrated in Fig. 2.2.3 i.e. a scaling center  $O$  must be chosen in a zone from which the total boundary  $S$  is visible. Without losing generality, the origin of the Cartesian coordinates  $(\hat{x}, \hat{y})$  is selected at the scaling center  $O$ . The boundary  $S$  is discretized into one-dimensional line elements. The geometry of an element on the boundary is interpolated using the shape functions formulated in the local coordinate  $\eta$  in the same way as that in the FEM. The geometry of the domain  $V$  is described by

scaling the boundary with the dimensionless radial coordinate  $\xi$  pointing from the scaling center  $O$  to a point on the boundary. The value of  $\xi$  is specified as 0 at the scaling center  $O$  and 1 at the boundary  $S$ . The unbounded domain is thus specified by  $1 \leq \xi \leq \infty$ . The radial coordinate  $\xi$  and the circumferential coordinate  $\eta$  form the scaled boundary coordinates.

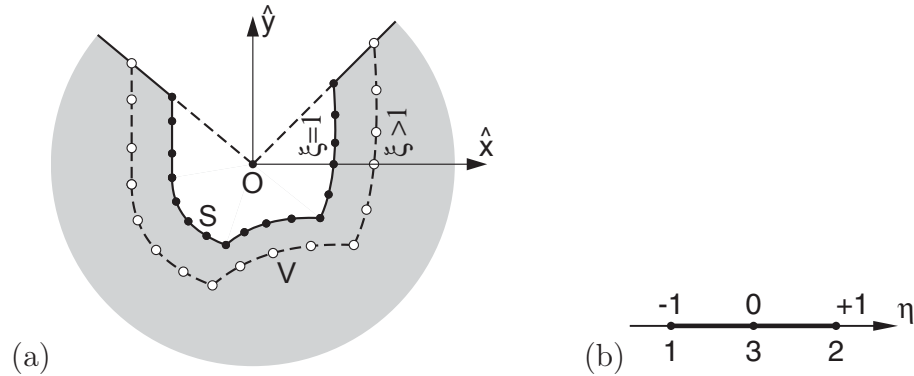


Figure 2.2.3: Scaled boundary finite element method: (a) spatial discretization of two-dimensional unbounded domain and (b) three-node line element

Along the radial lines passing through the scaling center  $O$  and a node on the boundary  $S$ , the nodal displacement functions are introduced. The shape functions are employed in the circumferential direction to interpolate the displacement functions piecewisely. The governing differential equations are expressed in the scaled boundary coordinates. The Galerkin's weighted residual method or the principle of virtual work is applied to the governing differential equations in the circumferential direction  $\eta$  to obtain the scaled boundary finite element equation in displacement (the Euler-Cauchy ordinary differential equation with the radial coordinate  $\xi$  as an independent variable).

The coefficient matrices of this scaled boundary finite element equation are calculated and assembled in the same way as the static-stiffness and mass matrices in the finite element method are. For a static analysis, the scaled boundary finite element equation is transformed into a system of first-order ordinary differential equations which can be solved as an eigenvalue problem. Thus, the displacement and stress fields are described by semi-analytical solutions permitting the boundary condition at infinity to be satisfied rigorously.

The scaled boundary finite element equation can also be expressed in dynamic stiffness with the frequency as the independent variable. It is a system of non-linear first-order ordinary differential equations to be solved numerically for the dynamic-stiffness matrix. The radiation condition at infinity is satisfied using an asymptotic expansion of the dynamic-stiffness matrix for high frequency. Applying the inverse

Fourier transform to the scaled boundary finite element equation in dynamic stiffness leads to the scaled boundary finite element equation in the time domain involving convolution integrals. The time-discretization method is used to solve the scaled boundary finite element equation in the time domain.

The original equation of the SBFEM is based on the Galerkin's weighted residual method which was later extended to model body loads (Song and Wolf, 1999). For certain distribution of body loads, the concentrated loads and loads varying as power function of radial coordinate, analytical solutions were derived. Deek and Wolf (2002b) rederived the scaled boundary finite element equations using the principle of virtual work. The original solution of the SBFEM for elastostatics uses eigen-decomposition which breaks down when problems involve logarithmic functions. To tackle this problem, Deek and Wolf (2002a, 2003) extended the SBFEM by adding the results of the eigen-decomposition with additional logarithmic terms associated with the translational motions.

Doherty and Deeks (2003c) presented an axisymmetric formulation of the SBFEM for the static analysis of a non-homogeneous elastic half-space. The Young's modulus was assumed to vary with depth. The rigid and flexible footings were tested on the elastic half-space under pure vertical load. Doherty and Deeks (2003b) presented a virtual work formulation of the SBFEM to elastostatic problems involving an axisymmetric domain subjected to a general load, extending the work of Deek and Wolf (2002b), and Doherty and Deeks (2003c). A Fourier series was used to model the variation of displacements in the circumferential direction of the cylindrical coordinates, and the non-homogeneous elasticity was included. Doherty and Deeks (2003a) determined the dependence of the dimensionless stiffness coefficients and the dimensionless torsional stiffness coefficient by evaluating the load-displacement response of rigid circular footings embedded in a non-homogeneous elastic half-space. The footings were subjected to vertical, horizontal, moment and torsion loads. The SBFEM for axisymmetric non-homogeneous unbounded domains presented by Doherty and Deeks (2003b) was adopted.

Song (2004a) developed a novel solution procedure for statics based on the theory of matrix power functions and block-diagonalized Schur decomposition. This Schur decomposition is more advantageous than the eigen-decomposition from the numerical and analytical point of view. Choosing the block-diagonalized Schur decomposition leads to well separated eigenvalues. This results in weighted orthogonal base functions. Song (2004a) used the scaling and squaring method based on Padé approximation to calculate the matrix power functions. The matrix power function solution is capable of accurately evaluating not only logarithmic functions but also the transition between the power functions and logarithmic functions.

Vu and Deeks (2006) investigated high-order elements in the SBFEM for statics. The spectral element and hierarchical approaches were examined. Lagrange shape functions were used in the spectral element approach. In the hierarchical approach, higher-derivative-based shape functions and Lobatto polynomials were adopted. They found that the spectral element approach performed better than the hierarchical approach.

The computational efficiency of static and dynamic analyses of large-scale unbounded domains using the SBFEM was increased significantly by adopting a technique called the reduced set of base functions in the frequency domain (Song, 2004b, 2006). Such base functions  $[\Psi]$  are weighted block-orthogonal and obtained from the Schur decomposition of the coefficient matrix  $[Z]$  of which the real Schur form matrix  $[S]$  is block-diagonal. The eigenvectors that correspond to the smallest absolute values of the real parts of the eigenvalues (the diagonals of the Schur form matrix) are selected as the reduced set of base functions. This technique approximates the degrees of freedom on the unbounded domains by using a smaller number of generalized coordinates. The scaled boundary finite element formulation with the reduced set of base functions is regarded as a spatially local formulation since the responses at different locations are coupled by the generalized coordinates only. The size of the system of equations is thus reduced to the number of the base functions retained in the reduced set.

Since the computational time and storage for calculating the reduced set of base functions is the most time-consuming part of a scaled boundary finite element analysis of wave propagation problems in large-scale unbounded domains, the sparsity of the coefficient matrices was explored by Song and Bazyar (2008) to reduce the computational time and storage. Moreover, Song and Bazyar (2008) developed an approach for lumped coefficient matrices for  $[E^0]$  and  $[M^0]$  using the Gauss-Lobatto-Legendre shape functions together with nodal quadrature for wave propagation problems in unbounded domains. This development leads to a formulation based on use of high-order elements. Earlier, this type of high-order element was successfully applied to the scaled boundary finite element method for statics by Vu and Deeks (2006).

Song and Bazyar (2007) proposed an approximate method of determining a dynamic stiffness matrix of an unbounded domain in the frequency domain. A Padé series is used for the regular term of the dynamic stiffness matrix due to its good properties: it converges more rapidly; it has a much larger range of convergence than the corresponding power series expansion does. The Padé series is constructed directly from the high-frequency expansion obtained from the scaled boundary finite element equation. Unlike the method proposed in Ruge *et al.* (2001) where a Padé

series or approximation is constructed by a least square approximation of the dynamic stiffness matrix pre-determined by other methods at discrete frequencies, this approach does not require the explicit evaluation of the dynamic stiffness matrix. Therefore, the computationally expensive task of calculating the dynamic stiffness matrix at discrete frequencies is avoided.

Recently, Bazyar and Song (2008) have developed a high-order transmitting boundary for wave propagation in unbounded domains by extending the SBFEM. The scaled boundary finite element equation in dynamic stiffness and the technique of continued fraction were used in the derivation of the continued fraction solution in the frequency domain. A continued fraction is closely related to a Padé series (Baker and Graves-Morris, 1996), having a large range of convergence and the higher rate of convergence compared to that of the corresponding power series.

#### 2.2.4 Exact non-reflecting boundaries

Another global procedure developed for wave propagation problems in unbounded domains is the exact non-reflecting boundaries. The boundary conditions of the exact non-reflecting boundaries are theoretically exact, and most of them involve integral transforms along the boundary and pseudo-differential operators. Ting and Miksis (1986) developed an exact boundary for scattering problems in uniform unbounded domains. The condition on the boundary is based on Kirchhoff's formula in the framework of time explicit integration. The integral in the formula is evaluated on the surface containing the scatterer, lying inside of the finite computational domain. Since the integrand only depends on the retarded values, the formula is exact and explicit. The non-reflecting boundary condition (NRBC) of Ting and Miksis was later implemented by Givoli and Cohen (1995). This approach is, however, computationally expensive since a convolution in space and time is required to update the solution at the points on the boundary.

Keller and Givoli (1989) and Givoli and Keller (1989) developed and proposed exact non-reflecting boundaries of simple shapes e.g. a circle in two dimensions, and a sphere in three dimensions for converting boundary-value problems defined over unbounded domains to formulations that are suitable for a numerical analysis. The boundary condition imposed on the truncated boundary is called the Dirichlet-to-Neumann (DtN) boundary condition, which is expressed as

$$u_v = -Mu \tag{2.2.9}$$

where  $u_v$  denotes the outward normal derivative of displacement,  $M$  is a non-local operator called the Dirichlet to Neumann (DtN) map, and  $u$  is the unknown displacement field. The way to find out the DtN boundary condition is to solve the Dirichlet problem in the external domain. For example, in case of a circle of radius  $R$ , the DtN boundary condition is expressed in terms of the following explicit equation:

$$u_v(R, \theta) = -\sum_{n=0}^{\infty} \int_0^{2\pi} m_n(\theta - \theta') u(R, \theta') d\theta' \quad (2.2.10)$$

which is an infinite series with the DtN kernels,

$$m_n(\theta - \theta') = -\frac{k}{\pi} \frac{H_n^{(1)'}(kR)}{\pi H_n^{(1)}(kR)} \cos(n(\theta - \theta')) \quad (2.2.11)$$

where  $k$  is the wave number in the Helmholtz equation, and  $H_n^{(1)}$  is the Hankel function of first kind. The prime after the sum indicates that the term with  $n = 0$  is multiplied by a factor of  $1/2$ . In the implementation with finite elements, the DtN boundary conditions converge at the convergence rate of the standard finite elements, and the non-locality of the boundary condition had no effect on the banded structure of the finite element matrix.

The DtN boundary condition was later extended to treat the hyperbolic linear wave equation by Givoli (1992b), and was further analyzed and improved by Harari and Hughes (1992a,b) for acoustics. For practical applications, the DtN map must be truncated, and only a specified number of leading terms of the infinite series are taken into account. Grote and Keller (1995b) modified the DtN boundary condition for the Helmholtz equation. Such modification was able to remove the difficulties caused by the real eigenvalues that occurred when the DtN boundary condition was truncated. They also proposed the DtN and the modified DtN boundary conditions of elliptic and spheroidal coordinates.

A few years later, Harari *et al.* (1998) derived the DtN boundary conditions for unbounded acoustic waveguides in two and three dimensions. The cross-sectional eigenvalues  $\mu_n^2$  and the orthogonal eigenfunctions  $Y_n(y)$  for two dimensions and  $Y_n(x, y)$  for three dimensions were introduced in the formulation of the DtN boundary condition. The eigenvalues and eigenfunctions were obtained from the method of separation of variables and modal decomposition techniques. To validate the performance of the DtN boundary conditions, they compared the numerical results obtained from the truncated DtN and modified DtN boundary conditions. They

concluded that the truncated and modified DtN boundary conditions performed similarly as long as there were sufficient terms for the truncated boundary condition to yield unique solutions, otherwise the modified boundary condition was superior to the truncated boundary condition.

Tsynkov (1998) also derived an exact non-reflecting boundary based on the application of the difference potential method (DPM) for steady-state flow computations. The boundary condition is not only geometrically universal, but also easy to incorporate into the structure of the existing flow solvers. However, the extension to the formulation in the time domain is not straightforward. Most of the exact non-reflecting boundaries were developed in the frequency domain. Only a few of them were formulated in the time domain. Guddati and Tassoulas (1998a,b) proposed the characteristic method for constructing exact non-reflecting boundaries for scalar wave propagation in homogeneous unbounded domains, including half space, full space and a layer. The method is based on the method of separation of variables, a dimensional reduction technique, involving the following three steps: (a) utilizing semidiscretization to reduce the governing partial differential equation (PDE) into a system of hyperbolic PDEs in a single spatial variable and time, (b) splitting the displacement vector into wave modes which satisfy the scalar dispersive wave equation, and (c) solving the resulting scalar equation on the characteristic grid. The third step is the key to the efficiency of this method. In the space-time domain, the solution facilitates an element-by-element solution, and the elements are processed in the order using a cell-centered finite-difference scheme. The boundary condition obtained from this method is spatially global but temporally pseudo-local as the past history is stored in a different form with the displacement vector that is stored along the characteristics.

Alpert *et al.* (2000) developed an exact non-reflecting boundary condition used for spherical and cylindrical boundaries, and two years later, the boundary condition was extended to planar boundaries (Alpert *et al.*, 2002). The boundary conditions are non-local in space and time due to the convolution term in the formulation. In the implementation, the boundary conditions can be coupled to finite-difference solvers for the scalar wave equation. The fundamental analytical tool that they employed is the non-reflecting boundary kernel, which is the inverse Laplace transform of the logarithmic derivative of a Hankel function. They adopted a ratio of polynomials of modest degree to approximate the logarithmic derivative of a Hankel function so that the inverse Laplace transform of the derivatives could be expressed as a sum of exponentials. The non-reflecting boundary kernel is similar to the non-dimensional residual function previously used by Geers (1969, 1971, 1972). In order to reduce the amount of work needed to apply the exact condition, the compression technique

was adopted to compress non-reflecting boundary kernels. The proposed approach is effective when long-time integrations are required. Nevertheless, the propagation media must be uniform at the boundary. The proposed technique is unable to treat wave problems in infinite-layered media.

From the viewpoint of practical computing, the exact non-reflecting boundaries may be cumbersome for implementation, and computationally expensive owing to their non-localities. In addition, they impose geometric restrictions that limit their practical use. However, some types of exact non-reflecting boundaries which are very rare for global procedures can be formulated in the time domain without any use of convolution integrals and can be implemented with finite elements. Those boundaries are thus local in time and reviewed in the next section.

## 2.2.5 Temporally local exact non-reflecting boundaries

### 2.2.5.1 Grote-Keller boundaries

The exact non-reflecting boundary condition (exact NRBC) developed by Grote and Keller (1995a) was formulated for the time-dependent wave equation in three dimensions. On a sphere of radius  $a$ , and the formulation is expressed as

$$\left(\frac{\partial}{\partial r} + \frac{\partial}{\partial t}\right)[ru] = -\frac{1}{a} \sum_{n=1}^{\infty} \sum_{m=-n}^n Y_{nm}(\theta, \varphi) \left\{ (-1)^n \sum_{j=1}^n \frac{j \gamma_{nj}}{a^j} \frac{d^{n-j} w_{nm}(t)}{dt^{n-j}} \right\} \quad (2.2.12)$$

where  $\gamma_{nj} = \frac{(n+j)!}{(n-j)!j!2^j}$  and  $Y_{nm}(\theta, \varphi)$  is the  $nm$ th spherical harmonic normalized over the unit sphere which is expressed as

$$Y_{nm}(\theta, \varphi) = [(2n+1)(n-|m|)!/4\pi(n+|m|)!]^{1/2} e^{im\varphi} P_n^{|m|}(\cos\theta) \quad (2.2.13)$$

where  $P_n^{|m|}$  is associated Legendre function and the auxiliary variable  $w_{nm}(t)$  is the solution of the ordinary differential equation,

$$\frac{d^n w_{nm}(t)}{dt^n} = (-1)^n a(U, Y_{nm})(a, t) - \sum_{j=1}^n \gamma_{nj} a^{-j} \frac{d^{n-j} w_{nm}(t)}{dt^{n-j}} \quad (2.2.14)$$

with the initial conditions,

$$w_{nm}(0) = \frac{dw_{nm}(0)}{dt} = \dots = \frac{d^{n-1} w_{nm}(0)}{dt^{n-1}} = 0 \quad (2.2.15)$$

This exact NRBC is local in time but non-local in space, having no high derivatives of  $u$  with respect to  $r$  due to the introduction of auxiliary variables (following the

method of Collino (Collino, 1993)). In the next year, Grote and Keller (1996) implemented the original boundary condition (Eq. (2.2.12)) and the modified boundary condition with the finite difference method and the finite element method. They showed that the boundary conditions were straightforward to implement and required little extra memory. Based on these boundary conditions, Grote and Keller (1998) presented an exact NRBC for time-dependent Maxwell's equations in three dimensions, which could be implemented with the finite difference method. This condition holds on a spherical surface, outside of which the medium is assumed to be homogeneous, isotropic, and source-free. The condition is local in time but global in space. Then Grote and Keller (2000) extended the concept to elastic waves in three dimensions. The exact NRBC that they proposed still holds on a spherical boundary, outside of which the medium is assumed to be linear, homogeneous, isotropic and source-free. The exact NRBC is local in time, but still global in space. Nevertheless, it can be combined easily with numerical methods for the interior region. By introducing a sequence of auxiliary variables, Grote (2006) derived an exact NRBC for the time-dependent Maxwell's equations in three dimensions, which is not only local in time but also local in space.

#### **2.2.5.2 Boundary conditions of absolute transparency**

Sofronov (1998) constructed exact NRBCs used for the scalar wave equations of circular and spherical boundaries. The boundary conditions were called the boundary conditions of absolute transparency (BCAT). The boundary conditions were formulated by using Fourier transform with respect to space variables and convolutions with respect to time. Instead of calculating the convolution integrals directly, Sofronov developed and used the recurrence formulae with respect to time to calculate them. In order to extend the BCAT to non-circular or non-spherical geometry, he first enclosed the actual non-reflecting boundary between two additional circular or spherical boundaries, and then used the interpolation. The BCAT is global in space but local in time.

#### **2.2.5.3 Residual-potential boundary**

Recently, Geers and Sprague (2010) have developed the residual-potential (RP) boundary, an exact non-reflecting boundary for time-dependent, infinite domain problems in computational acoustics. The RP boundary is based on the concept of the residual-potential, which has been previously used for solving a variety of canonical problems (Geers, 1969, 1971, 1972). In order to avoid ill-conditioning problems, a non-dimensional residual function  $r_n(t)$  was obtained from the inverse-transforming

$R(s)$  (the Laplace transform of  $r_n(t)$ ) which was expressed as a partial-fraction expansion. The solution obtained from the RP boundary is expressed in terms of a coupled equation of two sets of equations which is obtained from coupling them through nodal-modal transformation based on the orthogonal surface functions. The first set of equations is the set of first-order, uncoupled ordinary differential equations for nodal boundary responses, and the second one is the set of uncoupled time-stepping equations for modal boundary responses. The RP boundary is spherical, geometrically local for a compact body, spatially non-local but temporally local. However, the principal limitation of the RP boundary is that it loses geometric locality for non-compact bodies.

## 2.3 Local procedures

Local procedures are generally approximate. The resulting artificial boundary conditions usually have low accuracy. When artificial boundaries are placed close to the source of excitation, significant spurious reflections exist. To alleviate the loss of accuracy, the size of the bounded domain has to be increased. This leads to the increase of the computational time. However, in the time-domain analysis, the local procedures are rather computational efficient because convolution integrals are not required. Most of local procedures are local in space and time, and therefore, a less amount of data is processed compared to the global ones. Thus, the local procedures are practical for large-scale problems.

### 2.3.1 Low-order absorbing boundary conditions

Lysmer and Kuhlemeyer (1969) proposed the first local transmitting boundary and applied it to the FE analyses of infinite elastic media. Since this transmitting boundary is based on applying viscous damping forces along the boundary as shown in Fig. 2.3.1, it is always referred to as the viscous boundary. The viscous boundary is formulated for two-dimensional elastic media as the following two first-order differential equations:

$$\sigma = a \rho V_P \dot{w} \quad (2.3.1)$$

$$\tau = b \rho V_S \dot{u} \quad (2.3.2)$$

where  $a$  and  $b$  are the dimensionless parameters,  $\rho$  is the mass density,  $V_P$  is the velocity of  $P$ -waves,  $V_S$  is the velocity of  $S$ -waves,  $\sigma$  is a normal stress,  $\tau$  is a shear stress,  $\dot{w}$  is a normal velocity and  $\dot{u}$  is a tangential velocity.

The ability of the viscous boundary to absorb impinging elastic waves is evaluated by an energy ratio defined as the ratio of the energy transmitted by the reflected wave to the energy transmitted by the incident wave. A unit energy ratio corresponds to perfect reflection while a zero energy ratio corresponds to complete absorption. For a given choice of  $a$  and  $b$ , they found that the energy ratio depended only on the incident angle  $\theta$  and Poisson's ratio  $\mu$  of the medium. The parameters  $a$  and  $b$  were chosen to minimize the reflected energy for an incident plane wave hitting the boundary at a given angle of incidence.  $a = b = 1$  was recommended as a good choice in general. However, if the incident wave hits the boundary at a sharp angle, the boundary conditions will yield large spurious reflection.

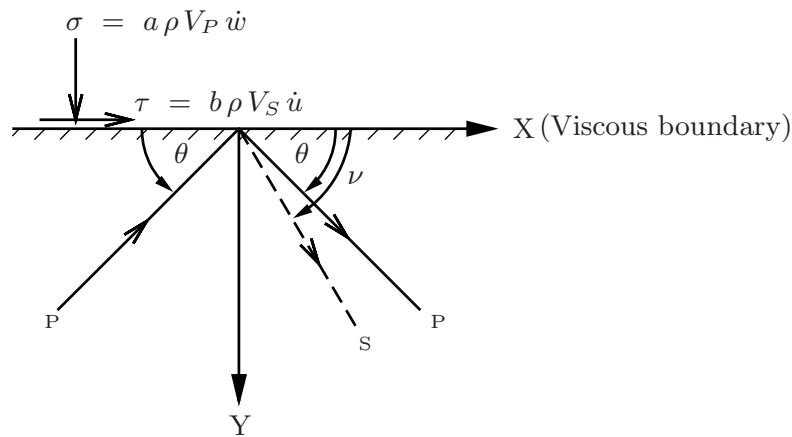


Figure 2.3.1: Incident  $P$ -wave at viscous boundary

The performance of the viscous boundary is known to deteriorate as the position approaches the source of scattering, especially in the low-frequency range. The great advantage of this boundary condition is that its absorption characteristics is independent of frequency and that it can be easily implemented in finite element codes for analyses in the time as well as frequency domain. The viscous boundary has no static stiffness and is erroneous at the low-frequency limit i.e. statics.

The viscous boundary was later generalized by White *et al.* (1977) as the unified boundary, which can be applied to anisotropic media with a certain choice of the parameters  $a$  and  $b$ . They obtained both parameters by first discretizing the domain with finite elements, and then determining the linear relationship between stresses and velocities on the boundary. Only the plane-strain and the axisymmetric conditions were considered in the formulations.

Akiyoshi (1978) developed the compatible viscous boundary for shear waves, which is a correction to the viscous boundary to account for the discretization scheme used for the domain. However, this approach has the disadvantage of involving a

convolution integral in the formulation, losing the local character of the boundary condition. Later Akiyoshi *et al.* (1994) presented absorbing boundary conditions in the time domain ( $u - w$ ,  $u - U$  and  $u - p$  formulations) for fluid-saturated porous media, based on Biot's two-phase mixture theory and the paraxial approximation. The absorbing boundary conditions are almost equivalent to the viscous boundary condition in the fundamental mode, focusing on the isotropic case. The concept of Akiyoshi *et al.* (1994) was then extended to transverse isotropic and anisotropic media (Akiyoshi *et al.*, 1998). They introduced the equivalent Lamé's constants under conditions of uniqueness to facilitate the analytical solutions.

The viscous boundary is regarded as a low-order transmitting boundary since the order of approximation is one. It has been implemented in commercial finite element packages such as ABAQUS, DIANA, etc.

## 2.3.2 High-order absorbing boundary conditions

### 2.3.2.1 Free-space boundary conditions

Lindman (1975) proposed the free-space boundary conditions for the time-dependent scalar wave equation. The boundary conditions are based on use of projection operators. The projection operators use past data on the boundary which are processed in the form of the updating of three to six wave equations. Lindman only determined reflection coefficients for the high-order boundary conditions to minimize reflection over a broad range of the angle of incidence for both propagating and evanescent waves. The minimum reflection coefficient of the free-space boundary conditions was found to be 1 percent or less while the maximum angle of incidence on the boundary could be up to 89 degrees, which is adequate for practical cases.

### 2.3.2.2 Paraxial boundary conditions

In 1977, Engquist and Majda proposed a hierarchy of high-order absorbing boundary conditions for scalar waves. The theoretical non-local boundary conditions of the scalar wave equation based on the theory of pseudodifferential operators is approximated by a Padé series (a rational function). The first three boundary conditions

are expressed in the Cartesian coordinates as

$$\text{A1:} \quad \left( \frac{\partial}{\partial x} + \frac{1}{c} \frac{\partial}{\partial t} \right) u = 0 \quad (2.3.3a)$$

$$\text{A2:} \quad \left( \frac{1}{c} \frac{\partial^2}{\partial x \partial t} + \frac{1}{c^2} \frac{\partial^2}{\partial t^2} - \frac{1}{2} \frac{\partial^2}{\partial y^2} \right) u = 0 \quad (2.3.3b)$$

$$\text{A3:} \quad \left( \frac{1}{c^2} \frac{\partial^3}{\partial t^2 \partial x} - \frac{1}{4} \frac{\partial^3}{\partial x \partial y^2} + \frac{1}{c^3} \frac{\partial^3}{\partial t^3} - \frac{3}{4} \frac{1}{c} \frac{\partial^3}{\partial t \partial y^2} \right) u = 0 \quad (2.3.3c)$$

Rational approximation is known to have better properties than polynomial approximation. This was the first time that the method of rational approximation was used as a tool to derive the absorbing boundary conditions (ABCs). These ABCs are known as the paraxial boundary conditions.

Clayton and Engquist (1977) further developed the paraxial boundary conditions for scalar and elastic wave equations, which were computationally inexpensive and simple to apply. The chief feature of the paraxial boundary conditions is that the outward-moving wave field can be separated from the inward-moving one. Engquist and Majda (1979) also further developed the theoretical and practical aspects of their paraxial boundary conditions proposed in 1977.

The paraxial boundary conditions are most convenient for finite difference applications. They appear as mathematical artifacts, being less supported by physical considerations when compared with the viscous boundary condition. The first approximation in Eq. (2.3.3a) is equivalent to the viscous boundary condition.

### 2.3.2.3 Bayliss-Turkel boundary conditions

Bayliss and Turkel (1980) proposed a sequence of ABCs for the three-dimensional wave equation in spherical or cylindrical coordinates. The ABCs are based on asymptotic expansions in  $1/r$  of the solution of the scalar wave equation where  $r$  is the distance from a fixed point. Such boundary conditions form a sequence of differential operators  $B_m$  which, for any  $m$ , annihilate the first  $m$  terms of the asymptotic expansion (based on the method of separation of variables) in Eq. (2.3.4),

$$p(t, r, \theta, \phi) = \sum_{j=1}^{\infty} \frac{f_j(t - r, \theta, \phi)}{r^j} \quad (2.3.4)$$

where  $\theta$  and  $\phi$  are the angular variables of the spherical coordinates centered at a fixed origin in space. A typical boundary condition is of the form,

$$B_m p = 0 \quad (2.3.5)$$

where  $p$  is the perturbation pressure, and the operator  $B_m$  is expressed as

$$B_m = \prod_{l=1}^m \left( \frac{\partial}{\partial t} + \frac{\partial}{\partial r} + \frac{2l-1}{r} \right) \quad (2.3.6)$$

Note that the  $m$ th-order condition involves a product of  $m$  first-order normal and time derivatives and thus leads to  $m$ th-order differential operators. When applied as an absorbing boundary of an increasing order, the operators in this sequence lead to improved accuracy but, at the same time, increasing difficulty of implementation (Givoli, 2004). Although  $m$  in Eq. (2.3.6) may be theoretically as large as desired, this ABC, at least in its original form (Eq. (2.3.6)), cannot be implemented up to an arbitrarily high-order due to the high derivatives appearing in it. For the 3D Helmholtz equation,

$$\Delta u + k^2 u = 0 \quad (2.3.7)$$

exterior to a sphere  $r = r_0$ , the solution based on the asymptotic expansion is expressed as

$$u = \frac{e^{ikr}}{kr} \sum_{j=0}^{\infty} \frac{F_j(\theta, \phi)}{(kr)^j} \quad (2.3.8)$$

By annihilating the first  $m$  terms in the expansion, the operator  $B_m$  is expressed as

$$B_m = \prod_{j=1}^m \left( \frac{\partial}{\partial r} - ik + \frac{(2j-1)}{r} \right) \quad (2.3.9)$$

For the 2D Helmholtz equation, the solution based on the asymptotic expansion is expressed as

$$u \approx \sqrt{\frac{2}{\pi kr}} e^{i(kr-\pi/2)} \sum_{j=0}^{\infty} \frac{f_j(\theta)}{r^j} \quad (2.3.10)$$

for simplicity, and the operator  $B_m$  is expressed as

$$B_m = \prod_{j=1}^m \left( \frac{\partial}{\partial r} + \frac{(2j-3/2)}{r} - ik \right) \quad (2.3.11)$$

For the 3D Laplace equation,

$$\Delta u = 0 \quad (2.3.12)$$

the solution based on the asymptotic expansion is expressed as

$$u = \frac{1}{r} \sum_{j=0}^{\infty} \frac{F_j(\theta, \phi)}{r^j} \quad (2.3.13)$$

By setting  $k = 0$  in Eq. (2.3.11), the operator  $B_m$  is expressed as

$$B_m = \prod_{j=1}^m \left( \frac{\partial}{\partial r} + \frac{(2j-1)}{r} \right) \quad (2.3.14)$$

Bayliss and Turkel (1982) further extended the sequence of ABCs they proposed earlier for far fields to fluid dynamics. They applied the sequence of ABCs to the non-linear compressible Navier-Stokes and Euler equations. These ABCs can be used at both subsonic outflow boundaries and at characteristic boundaries where the normal velocity is zero. In case of the subsonic flows, the equations of the ABCs are elliptic. The Sommerfeld-type radiation conditions for elliptic equations can be constructed from these ABCs.

The Bayliss-Turkel boundary conditions are perhaps the first operators providing a mechanism by which a finite-element mesh can be terminated without the necessity to include an excessively large number of elements in the region surrounding the structure. The operators became very popular because of their simplicity and good accuracy in comparison to the more primitive Sommerfeld radiation condition (Givoli, 1991).

#### 2.3.2.4 Extrapolation boundary conditions

Liao and Wong (1984) developed an extrapolation boundary condition for the numerical simulation of elastic wave propagation. It is a second-order ABC. The numerical scheme that they adopted is in the form of an extrapolation algorithm: the motion of the boundary at the current time step is predicted by extrapolating the past motion of the vicinity of the boundary, using backward temporal and spatial differences. The accuracy of results is controlled by the number of terms in the extrapolation series, and can be further improved by decreasing the size of the time step. The extrapolation boundary condition can be implemented easily in either the finite element method or the finite difference method. Later Liao (1996) generalized the extrapolation boundary condition of Liao and Wong (1984) by coupling a space-extrapolation to the space-time extrapolation and by introducing multiple artificial wave speeds. Only explicit time-integration schemes can be used for the generalized boundary condition in the time-domain analysis.

### 2.3.2.5 Higdon boundary conditions

Higdon (1986, 1987) developed the absorbing boundary conditions based on the dispersion relation for discrete problems. He first approximated the scalar wave equation using finite differences in both space and time, rather than finding analytical boundary conditions and then discretizing the analytical conditions. This approach yields some simple and effective discrete boundary conditions which are consistent with the analytical boundary conditions expressed in

$$H_m u = \left( \prod_{j=1}^m \left( (\cos \alpha_j) \frac{\partial}{\partial t} - c \frac{\partial}{\partial x} \right) \right) u = 0 \quad (2.3.15)$$

where  $\alpha_j$  denotes an angle of incidence and  $c$  is the wave speed. Equation (2.3.15) is known as the Higdon boundary condition. Higdon's numerical experiments showed that the amount of spurious reflections was not very sensitive to the choice of the  $\alpha_j$ . Also, a reasonably small value of  $m$  led to a boundary condition which absorbed waves very well for a wide range of angles of incidence.

Higdon later extended the boundary condition to acoustic and elastic waves in stratified media (Higdon, 1992) and also dispersive waves (Higdon, 1994). The Higdon boundary conditions are attractive because they are local and therefore relatively easy to use in a parallel finite difference code. The Higdon boundary conditions can be used not only for the scalar wave equation but also for the elastic case. These boundary conditions can be defined up to any desired order. However, the appearance of increasingly high order derivatives in the boundary renders it impractical beyond a certain order, typically two or three, which is similar to the Engquist-Majda ABCs (Engquist and Majda, 1977, 1979) and the Bayliss-Turkel ABCs (Bayliss and Turkel, 1980, 1982).

### 2.3.3 Local high-order absorbing boundary conditions

The local high-order ABCs are local in time and involve no high derivatives. The first local high-order ABC was devised by Collino (1993) for two-dimensional acoustic waves in rectangular domains. In theory, some of the classical ABCs, such as the Engquist-Majda ABC (Engquist and Majda, 1979), the Bayliss-Turkel ABC (Bayliss and Turkel, 1980) and the Higdon ABC (Higdon, 1987) can be defined up to any desired order. However, the appearance of increasingly high order derivatives in these ABCs renders them impractical beyond a certain order, typically two or three. For example, the  $P$ -order Higdon ABC involves  $P$ -order derivatives in space and time, and is thus very inconvenient for implementation when  $P$  becomes large. In

contrast, the Collino ABC involves no high-order derivatives owing to the use of auxiliary variables  $\phi_j$  on the artificial boundary. This development enables the implementation of ABCs of an arbitrarily high order. Equations (2.3.16) and (2.3.17) constitute the Collino ABC of order  $J$  in the time domain.

$$\frac{\partial u}{\partial x} + \frac{1}{c} \frac{\partial u}{\partial t} - \frac{1}{c} \sum_{j=1}^J \beta_j \frac{\partial \phi_j}{\partial t} = 0 \quad (2.3.16)$$

$$\frac{1}{c^2} \frac{\partial^2 \phi_j}{\partial t^2} - \alpha_j \frac{\partial^2 \phi_j}{\partial y^2} - \frac{\partial^2 u}{\partial y^2} = 0 \quad (2.3.17)$$

where  $j = 1, 2, \dots, J$ ,

$$\alpha_j = \cos^2 \left( \frac{j\pi}{2J+1} \right) \quad \text{and} \quad \beta_j = \frac{2\sin^2(j\pi/(2J+1))}{2J+1} \quad (2.3.18)$$

Other high-order ABCs that also use auxiliary variables in the time domain are, for example, the Hagstrom-Hariharan ABC (Hagstrom and Hariharan, 1998), the Givoli-Neta ABC (Givoli and Neta, 2003; Givoli *et al.*, 2003), and the Hagstrom-Warburton ABC (Hagstrom and Warburton, 2004).

Hagstrom and Hariharan (1998) presented a systematic approach for constructing asymptotic boundary conditions for the isotropic wave equations in two and three dimensions (i.e. polar and spherical coordinates) by direct applying the sequence of local boundary operators of Bayliss and Turkel (Bayliss and Turkel, 1980). The boundary conditions take a recursive form i.e. they are expressed recursively using auxiliary variables without any use of high-order derivatives. The key idea is to construct a sequence of operators which approximately annihilate the residual of the preceding element in the sequence, viewed as a function on the artificial boundary. For two-dimensional wave equation, the recursion leads to the sequence of the boundary conditions as summarized in the following equations:

$$\frac{1}{c} \partial_t u + \partial_r u + \frac{1}{2r} u = w_1 \quad (2.3.19a)$$

$$\frac{1}{c} \partial_t w_j + \frac{j}{r} w_j = \frac{(j-1/2)^2}{4r^2} w_{j-1} + \frac{1}{4r^2} \partial_\theta^2 w_{j-1} + w_{j+1} \quad (2.3.19b)$$

where  $p$  is the order of the ABC,  $j = 1, 2, \dots, p$ ,  $r$  is the radius of the circle, and  $w_j$  are unknown auxiliary variables. These boundary conditions are asymptotic and local in space and time. For three-dimensional wave equation, the sequence of the

boundary conditions are

$$\frac{1}{c}\partial_t u + \partial_r u + \frac{1}{r}u = w_1 \quad (2.3.20a)$$

$$\frac{1}{c}\partial_t w_j + \frac{j}{r}w_j = \frac{1}{4r^2}(\nabla_s^2 + j(j-1))w_{j-1} + w_{j+1} \quad (2.3.20b)$$

where  $p$  is the order of the ABC,  $j = 2, 3, \dots, p$ ,  $r$  is the radius of the sphere, and  $\nabla_s^2$  denotes the spherical Laplacian. This recursion can be truncated for finite spherical harmonic expansions and also can lead to an exact condition which is similar to those of Grote and Keller (1995a, 1996) but is somewhat easier and cheaper to use as it avoids spherical harmonic transformations. These boundary conditions are local in space and time.

The Givoli-Neta ABC developed by Givoli and Neta (2003) or by Givoli *et al.* (2003) is based on the same reformulation of the sequence of ABCs proposed by Higdon (Higdon, 1987, 1994), but no high-order derivatives beyond second order are involved in the formulation. The Givoli-Neta ABC was both constructed in the Cartesian coordinates  $(x, y)$  for the linear time-dependent wave equation (with or without a dispersive term). It can only be used for homogeneous semi-infinite layers (or waveguides). Compared to the auxiliary variables in the Hagstrom-Hariharan ABC (Hagstrom and Hariharan, 1998), the ones used in the Givoli-Neta ABC are less complicated since they are defined via simple recursive relations. The  $J$ th-order Givoli-Neta ABC is expressed as

$$\beta_0 u_{,t} + u_{,x} = \phi_1 \quad (2.3.21a)$$

$$\beta_j \phi_{j,t} - \alpha_j \phi_{j-1,tt} - \phi_{j-1,yy} + \lambda \phi_{j-1} = \phi_{j+1} \quad (2.3.21b)$$

$$\alpha_j = \frac{1}{C_j^2} - \frac{1}{C_0^2}, \quad \beta_0 = \frac{1}{C_1}, \quad \beta_j = \frac{1}{C_j} - \frac{1}{C_{j+1}}, \quad \lambda = \frac{f^2}{C_0^2} \quad (2.3.21c)$$

$$\phi_0 \equiv u, \quad \phi_J \equiv 0 \quad (2.3.21d)$$

where  $j = 1, 2, \dots, J-1$ ,  $C_0$  is the given reference wave speed,  $C_j$  are parameters signifying phase speeds in the  $x$ -direction which have to be chosen, and  $\phi_j$  are auxiliary variables. The Givoli-Neta ABC developed by Givoli and Neta (2003) was incorporated into a finite difference scheme while the other one (Givoli *et al.*, 2003) was incorporated into a finite element scheme.

The Hagstrom-Warburton ABC (Hagstrom and Warburton, 2004) is a modification of the Givoli-Neta ABC with enhanced stability. This leads to balanced systems

of wave equations on the boundaries. The Hagstrom-Warburton ABC of order  $P$  is expressed in the recursive relations as follows:

$$(a_0\partial_t + c\partial_x)u = a_0\partial_t\phi_1 \quad (2.3.22a)$$

$$(a_j\partial_t + c\partial_x)\phi_j = (a_j\partial_t - c\partial_x)\phi_{j+1} \quad (2.3.22b)$$

$$\phi_{P+1} = 0 \quad (2.3.22c)$$

where  $j = 1, 2, \dots, P$ ,  $c$  is the given wave speed,  $\phi_j$  are auxiliary variables, and  $a_j$  are free parameters signifying cosines of incidence angles which have to be chosen. Since the Hagstrom-Warburton ABC was developed for a full-space configuration of rectangles, special corner conditions were also devised. The ABC and the special corner conditions were incorporated into a finite difference scheme (Hagstrom and Warburton, 2004) and a finite element scheme (Givoli *et al.*, 2006). As compared with the Givoli-Neta ABC (Givoli and Neta, 2003), the Hagstrom-Warburton ABC has certain advantages over the Givoli-Neta ABC. For example, it has much lower reflection coefficients, involving derivatives of lower order which is expected to have a positive effect on the performance of the numerical scheme. Moreover, it lends itself easily to an adaptive update of the order  $P$ , and is more stable in long-time analysis.

Hagstrom *et al.* (2007) studied the free parameters  $0 < a_j \leq 1$ , for  $j = 0, 1, \dots, P$  in the Hagstrom-Warburton ABC (Hagstrom and Warburton, 2004) that had to be chosen. They suggested that the choice  $a_j = 1$  for all  $j$  was satisfactory in general although it was not necessary optimal. They also presented and tested an adaptive scheme which controlled the time-varying values of  $P$  and  $a_j$ . In the next year, Hagstrom *et al.* (2008) further developed and extended the Hagstrom-Warburton ABC in various ways. First, the ABC was analyzed in new ways and important information was extracted from the analysis. Second, it was extended to a dispersive medium for which the Klein-Gordon wave equation,

$$\partial_t^2 u - c^2 \nabla^2 u + f^2 u = s \quad (2.3.23)$$

governs (where  $c$  is the given wave speed,  $f$  is the given dispersion parameter, and  $s$  is the given wave source function). Third, it was also extended to a stratified medium. Fourth, the evanescent modes were introduced into the formulation of the ABC in order to improve the accuracy of the long-time behavior of the ABC. Hagstrom *et al.* (2008) also incorporated the ABC into finite difference and finite element schemes.

Recently, Bécache *et al.* (2010) have proposed a high-order ABC for scalar wave propagation in anisotropic and convective (non-dispersive isotropic) media. The ABC was still stemmed from the Hagstrom-Warburton ABC (Hagstrom and Warburton, 2004) used for isotropic media. They proved that the reflection coefficient of the ABC decreased exponentially as the order  $P$  of the ABC increased. The ABC was also proved to be well-posed using Kreiss criterion (Kreiss, 1970) instead of the energy method (Ha-Duong and Joly, 1994) which was much more difficult. In the implementation, only the ABC of the anisotropic medium was incorporated into a finite element scheme. In case of the convective medium, it was not incorporated into the finite element scheme because the formulation was still impossible for the convective medium due to the appearance of mixed space-time derivatives. This ABC is local in space and time and applicable to a full-space configuration of rectangles.

### 2.3.4 Doubly asymptotic approximations

The doubly asymptotic approximations (DAAs) are regarded as approximate impedance boundaries that match asymptotically the exact boundary integral representation for unbounded domains at both early time (high-frequency limit) and late time (low-frequency limit). The DAA boundaries were first developed to study the acoustic fluid-structure interaction in underwater shock problems in the 1970s (Geers, 1971, 1974, 1978). In the derivation, the Kirchhoff's integral equation (KIE) was used for an exact and integral-equation solution for the wave equation of a uniform acoustic fluid. It can be written for the pressure  $p$  at the position  $R$  on the boundary at the time  $t$  as the following equation:

$$2\pi p(R, t) = \int_{\Gamma}^{R' \neq R} \left\{ \rho \frac{\dot{v}(R', t_r)}{|R' - R|} - \frac{n' \cdot (R' - R)}{|R' - R|^3} \left[ p(R', t_r) + \frac{|R' - R|}{c} \dot{p}(R', t_r) \right] \right\} d\Gamma' \quad (2.3.24)$$

where  $v(R', t)$  is the normal fluid velocity at the boundary, the overdot denotes a temporal derivatives,  $t_r = t - \frac{|R' - R|}{c}$  is the retarded time,  $n'$  is the outward unit normal to the boundary at  $R'$ , and  $c$  is the sound speed. Geers took the Laplace transform of Eq. (2.3.24) to obtain

$$\int_{\Gamma} \frac{n' \cdot (R' - R)}{|R' - R|^3} \left( 1 + |R' - R| \frac{s}{c} \right) e^{-|R' - R| \frac{s}{c}} P(R', s) d\Gamma' = \rho s \int_{\Gamma} \frac{e^{-|R' - R| \frac{s}{c}}}{|R' - R|} V(R', s) d\Gamma' \quad (2.3.25)$$

where  $s$  is an excitation frequency. Equation (2.3.24) is used for constructing the early-time-approximation (ETA) boundaries while Eq. (2.3.25) is used for the late-time-approximation (LTA) boundaries.

The ETA boundaries are systematically expressed in the following equations:

$$\text{ETA}_1 : p(R, t) = \rho cv(R, t) \quad (2.3.26a)$$

$$\text{ETA}_2 : \dot{p}(R, t) + c\kappa(R)p(R, t) = \rho c\dot{v}(R, t) \quad (2.3.26b)$$

$$\text{ETA}_3 : \ddot{p}(R, t) + c\kappa(R)\dot{p}(R, t) = \rho c\ddot{v}(R, t) + \frac{1}{2}c^2[\kappa^2(R) - \tau(R) + \nabla_{\Gamma}^2]v(R, t) \quad (2.3.26c)$$

where  $\kappa$  and  $\tau$  are mean and total curvature. The ETA boundaries were systematically constructed by Felippa (1980) and Geers (1991). They parameterized the surface around a field point, noting the region of influence at a prescribed early time. Afterwards, they expanded the surface fields in Fourier series, and retained the terms of appropriate orders. The  $\text{ETA}_1$  is known as the plane-wave approximation (PWA). The  $\text{ETA}_2$  is known as the curved-wave approximation (CWA) as it introduces the effects of local curvature into the  $\text{ETA}_1$ . Both  $\text{ETA}_1$  and  $\text{ETA}_2$  are point relations. For the  $\text{ETA}_3$ , it includes additional curvature terms, as well as the surface Laplacian, which destroys the point-relation attribute but spatial locality is still maintained. These ETA boundaries are highly absorptive and spatially local.

For the LTA boundaries, they were constructed systematically from Eq. (2.3.25) by expanding the exponentials in Maclaren series, retaining terms of appropriate powers of  $s$ , and taking inverse-transform the results (Geers and Zhang, 1994; Geers and Toothaker, 2000) as expressed in the following equations:

$$\text{LTA}_1 : \gamma p(R, t) = \rho\beta\dot{v}(R, t) \quad (2.3.27a)$$

$$\text{LTA}_2 : \gamma p(R, t) = \rho[\beta\dot{v}(R, t) - \frac{1}{c}\alpha\ddot{v}(R, t)] \quad (2.3.27b)$$

$$\text{LTA}_3 : \gamma p(R, t) - \frac{1}{c^2}\eta\ddot{p}(R, t) = \rho[\beta\dot{v}(R, t) - \frac{1}{c}\alpha\ddot{v}(R, t) + \frac{1}{c^2}\mu\ddot{v}(R, t)] \quad (2.3.27c)$$

where  $\alpha$ ,  $\beta$ ,  $\gamma$ ,  $\eta$  and  $\mu$  are spatial integral operators which are spatially non-local. The  $\text{LTA}_1$  is known as added-mass or virtual-mass approximation, which governs hydrodynamic flow. The  $\text{LTA}_2$  introduces the first-order effects of compressibility, which are embodied in the second term on the right. The  $\text{LTA}_3$  includes both first- and second-order compressibility effects. The LTA boundaries are minimally absorptive, and spatially non-local due to the spatial integral operators.

The method of operator matching to early-time and late-time approximations was employed to obtain the doubly asymptotic approximations,

$$\text{DAA}_1 : \dot{p}(R, t) + c\beta^{-1}\gamma p(R, t) = \rho c\dot{v}(R, t) \quad (2.3.28a)$$

$$\begin{aligned} \text{DAA}_2 : \ddot{p}(R, t) + c(\chi + \kappa)\dot{p}(R, t) + c^2\chi\beta^{-1}\gamma p(R, t) \\ = \rho c[\ddot{v}(R, t) + c\chi\dot{v}(R, t)] \end{aligned} \quad (2.3.28b)$$

$$\begin{aligned} \text{DAA}_3 : \ddot{\ddot{p}}(R, t) + c(\lambda\beta^{-1}\alpha + \zeta + \kappa)\ddot{p}(R, t) \\ + c^2\zeta\beta^{-1}\gamma\dot{p}(R, t) + c^3\lambda\beta^{-1}\gamma p(R, t) \\ = \rho c[\ddot{\ddot{v}}(R, t) + c(\lambda\beta^{-1}\alpha + \zeta)\ddot{v}(R, t) + c^2\lambda\dot{v}(R, t)] \end{aligned} \quad (2.3.28c)$$

where  $\chi$  and  $\zeta$  are non-local spatial integral operators. The DAA boundaries are, therefore, spatially non-local. In a time-domain analysis, this is not a significant drawback unless the time increment is changed frequently.

In the 1980s, the acoustic DAA methodology was improved by Felippa (1980), Geers and Felippa (1983), and Nicolas-Vullierme (1991). The DAA boundaries were extended to other areas. The DAA<sub>1</sub> was also formulated heuristically by Underwood and Geers (1981) for elastodynamics, and further developed by Mathews and Geers (1987). In 1997, the DAA<sub>1</sub> and the DAA<sub>2</sub> were developed for transient elastodynamics by Geers and Lewis (1997), and in the same year, the DAA boundaries were extended to transient poroelastodynamics by Qi and Geers (1997). For electromagnetic scattering, the DAA<sub>1</sub> was developed by Geers and Zhang (1988).

The advantages of the DAA boundaries are their geometric versatility, temporal locality and ease of implementation. However, it is extremely difficult to construct a DAA formulation beyond DAA<sub>2</sub> (Geers and Sprague, 2010). The availability of high-order formulations limits the accuracy of DAA boundaries.

### 2.3.5 Infinite elements

The infinite element was introduced in the original work of Bettess (1977) for Laplace problems. The approach is very similar to the FEM except the shape function used for the elements extending to infinity. The shape function is based on Lagrange polynomials, including an exponential decay term as expressed in Eq. (2.3.29) for a one-dimensional problem,

$$N_j(r) = e^{(r_j-r)/L}l_j(r) \quad (2.3.29)$$

where  $l_j(r)$  is the Lagrange polynomial and  $L$  is an arbitrarily positive parameter. The accuracy of the infinite elements depends on the choice of the shape functions

towards infinity and on the order of approximation. The original infinite element of Bettess was used for a Laplace problem. The infinite elements are as spatially and temporally local as finite elements. They can be used for discretizing the entire unbounded domain without any use of ABCs. Therefore, infinite elements may be viewed as local ABCs. Figure 2.3.2 illustrates the infinite elements on the boundary  $\Gamma$  of the computational domain  $\Omega_i$  to represent the unbounded domain  $\Omega_e$ .

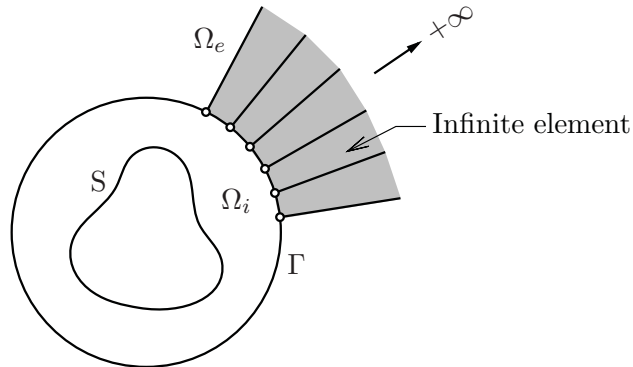


Figure 2.3.2: Infinite elements

Shortly thereafter, Bettess and Zienkiewicz (1977) extended the initial infinite element to the Helmholtz equation, using the same shape function (Eq. (2.3.29)) but introducing a complex-valued factor  $e^{(ikr)}$  in it as expressed in Eq. (2.3.30),

$$N_j(r) = e^{(ikr)} e^{(r_j - r)/L} l_j(r) \quad (2.3.30)$$

However, the infinite elements based on the shape functions in Eqs. (2.3.29) and (2.3.30) are unable to represent the correct asymptotic decay i.e.  $r^{-1/2}$  in two-dimensional problems. Thus, the solutions obtained from these two shape functions are not quite correct.

Zienkiewicz *et al.* (1983) further developed the infinite element by introducing a finite to infinite mapping so that the shape functions of infinite elements are constructed on a reference element spanning a finite interval. The mapping is of the form

$$x = \tilde{N}_0(\xi)x_0 + \tilde{N}_2(\xi)x_2 \quad (2.3.31)$$

where  $x_0$  and  $x_2$  are nodal coordinates, and  $\tilde{N}_0$  and  $\tilde{N}_2$  are expressed as  $\frac{-\xi}{1-\xi}$  and  $1 + \frac{\xi}{1-\xi}$ , respectively. It was further shown that polynomials defined on the reference

element were transformed by the mapping to functions with reciprocal powers of  $r$ . A polynomial  $p(\xi)$  was written as

$$p(\xi) = \sum_{i=0}^N \alpha_i \xi^i = \sum_{i=0}^N \beta_i r^{-i} \quad (2.3.32)$$

with  $r = x - x_0$ . By using this method, the previous restriction was completely removed and the correct decay was incorporated in the infinite element. Therefore, the solution of the Helmholtz problem obtained from using this mapped infinite element can represent the real behaviors of unbounded domains.

Another approach based on the use of wave envelope elements was first proposed by Astley (1983) and Astley and Eversman (1983) for acoustic problems. This approach incorporates the correct asymptotic behavior into the elements by using complex conjugates of wave-like functions as weight functions (i.e.  $r^{-1}e^{(-ikr)}$ ) in the Galerkin approach. This simplifies the element integration considerably due to the cancellation of the oscillatory terms in the weight function within the integrands. However, it results in unsymmetric matrices that destroy the symmetric structure of the semi-discretization of the bounded domains.

Burnett (1994) proposed the prolate spheroidal infinite element based on a multipole expansion in three-dimensional acoustic problems. This infinite element has symmetric matrices. The scattered or radiated pressure  $p$  exterior to the sphere is represented by the following multipole expansion in prolate spheroidal coordinates  $r, \theta, \phi$ ,

$$p = \frac{e^{-ikr}}{r} \sum_{n=0}^{\infty} \frac{G_n(\theta, \phi)}{r^n} \quad (2.3.33)$$

where  $G_n(\theta, \phi)$  denotes coefficients. The original formulation of Burnett was derived with unconjugated weight functions. Hence, the undefined oscillatory terms that comprise all terms containing the expression  $\lim_{\hat{r} \rightarrow \infty} e^{-i2k\hat{r}}$  exist in the formulation. This formulation was later known as the unconjugated Burnett formulation. The use of spheroidal coordinates ensures that the weight functions is complete as the radial order of the elements increases. Another formulation was proposed by Astley *et al.* (1994) using complex conjugate weight functions which were scaled by a geometric weight factor. It was later called the conjugated Astley-Leis formulation since the approach fit within the variational framework of Leis (1986).

The concept of Burnett (1994) was extended to the oblate spheroidal acoustic infinite element (Burnett and Holford, 1998) in three-dimensional acoustic problems, and also to the ellipsoidal infinite element which is the logical generalization

of the prolate and oblate elements. The three axes of an ellipsoid can be chosen independently. Therefore, the shapes of structures can be more circumscribed by an ellipsoid compared to those prolate and oblate spheroids. This results in the reduction in size of the computational domain, thereby increasing in the greater computational speeds.

Astley (1996) extended the conjugated Astley-Leis infinite element to the time-domain analysis by applying an inverse Fourier transform to a mapped wave envelop formulation in the frequency domain. This yields a discrete system of ordinary differential equations in time to which time-stepping schemes can be applied. Therefore, the coefficient matrices can be written in terms of frequency-independent mass, stiffness and damping matrices. This is opposite to the time-domain analysis using the unconjugated elements that leads to convolution integrals. Later Astley (1998b) extended this approach to oblate and prolate spheroidal elements for time-harmonic and transient wave problems in unbounded domains. Many examples were analyzed in order to study the required element orders, the effect of time step size and the performance of the iterative solutions. In the same year, Astley (1998a) formulated the conjugated Astley-Leis infinite element with a geometric weight factor based on Burnett's spheroidal trial solutions.

Shirron and Babuska (1998) compared the accuracy of approximate boundary conditions with the conjugated and unconjugated Burnett infinite elements for exterior Helmholtz problems. The test functions they used did not include any geometric factors. They found that the accuracy of the approximate boundary conditions decreased with increasing frequencies and was less than that of the infinite elements. Comparing those infinite elements, they also found that the rate of convergence of the conjugated infinite element was slower than that of the unconjugated one. In addition, the conjugated infinite element was more stable, converging to the exact solution in the far field, but being less accurate in the near field. On the contrary, the unconjugated infinite element diverged in the far field. This instability of the unconjugated infinite element was due to the bilinear form on which it was based.

Demkowicz and Gerdes (1998) analyzed the convergence properties of infinite elements which gave the first insight into the convergence mechanism behind infinite elements for separable geometry. Gerdes (1998) extended this work by performing numerical convergence studies on the conjugated and unconjugated infinite elements based on the Burnett and the Astley-Leis formulation. In conclusion, the unconjugated Burnett infinite element performed well for the near field while the conjugated Astley-Leis infinite element yielded the good result for the far field. For the conjugated Burnett and the unconjugated Astley-Leis infinite elements, they were the least accurate. Nevertheless, the study of Astley and Coyette (2001b) showed that

the performance of both infinite elements deteriorated at high frequencies and highly elongated artificial boundaries. The stability of infinite elements was also studied by Astley and Hamilton (2006) for transient acoustics. The conjugated Burnett and the mapped Bettes infinite elements were used in the study. From the study, it was shown that the stability of the infinite elements critically depended on the form of the inner surface of the infinite element domain.

Even though infinite elements are widely used today, they still have some limitations, for example, the geometry of the infinite-element mesh has to conform with a separable coordinate system for the wave equation, and increase of the order of elements to improve the accuracy of solutions may lead to ill-conditioning problems (Astley, 2000).

### 2.3.6 Absorbing layers

The perfectly matched layer (PML) is an absorbing layer which is a layer of artificial absorbing material. It is usually placed adjacent to the edges of the computational domain so that waves do not reflect at the interface. The PML was originally developed and implemented by Berenger (1994) for two-dimensional electromagnetic split fields as shown in Fig. 2.3.3. The computational domain is surrounded by a finite-thickness layer in which artificial attenuation of wave propagation in a pre-selected direction pointing to infinity is introduced to the governing equations for the unbounded domain. Later, Berenger extended the PML to three-dimensional electromagnetic waves (Berenger, 1996).

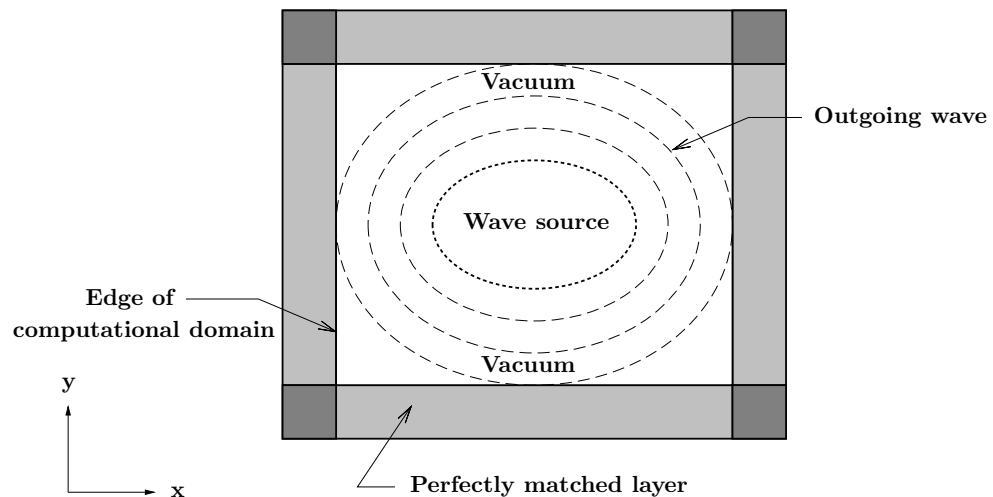


Figure 2.3.3: Perfectly matched layer

The PML is a hypothetical and nonphysical medium based on a mathematical model which is independent of the boundary condition. It was originally derived

for solving unbounded electromagnetic problems (Maxwell's equations) using the finite-difference time-domain technique (FDTD). Regardless of their frequency, angle of incidence and polarization, it can be implemented at the outer boundary of a FDTD grid to completely absorb outgoing waves. In a certain sense, the PML cannot exactly be called the boundary conditions because the layers always have finite thickness. Compared to transmitting boundaries based on asymptotic solutions, the PML equations can apply where an asymptotic solution is not available. Nevertheless, the PML requires more equations to solve for the solution.

The key concept is that the wave solutions are split artificially into the sum of two new artificial field components ( $E$  and  $H$  components) in the Cartesian coordinates, and the resulting field components are expressed as two coupled first-order partial differential equations. By choosing loss parameters consistent with a dispersionless medium, a perfectly matched planar interface is derived. Hence, Berenger's original formulation is called the split-field PML. The PML of Berenger had been paid attention until in 1997, Abarbanel and Gottlieb discovered one serious disadvantage of this PML, that is, the split set of partial differential equations was weakly well-posed. The derivations of the well-posed PMLs used for Maxwell's equations were proposed by Abarbanel and Gottlieb (1998).

Following the work of Berenger, many researchers verified his technique applying FDTD to the PML medium, but the first important advance was made by Chew and Weedon (1994). They restated the original split-field PML concept in a stretched-coordinate PML by viewing them as the result of a complex coordinate stretching. The use of stretched-coordinate PML allowed Teixeira and Chew (1997) to extend their PML to the cylindrical and spherical coordinates. The second important advance was firstly made by Sacks *et al.* (1995). They proposed the uniaxial PML or UPML based on a potentially and physically realization material formulation rather than the conventional PML (the non-physical PML of Berenger (1994)). The UPML is based on the use of anisotropic material properties to describe the absorbing layer. The material properties of the medium can be chosen such that a planar interface between the anisotropic medium and the free space is perfectly reflectionless. The UPML appears more attractive than the stretched-coordinate PML due to the fact that the Chew-Weedon modification of the spatial derivative operator via coordinate stretching is not required.

Unlike the conventional PML, the UPML no longer requires a modification of Maxwell's equations. Further, as summarized by Gedney and Taflove in Taflove and Hagness (2000), the UPML has capabilities exceeding the conventional PML by providing additional degrees of freedom which permit it to attenuate evanescent

waves and terminate conductive and dispersive materials. Nowadays, the more common formulation is the UPML, which is simpler and more efficient, and commonly implemented in commercial CEM (Computational Electromagnetic) software.

Besides the split-field PML, there is another PML approach that does not use the split-field components. Such an approach is known as the unsplit PML, which was firstly implemented in the time domain by Zhao and Cangellaris (1996) for Maxwell's equations in two-dimensional problems, and was subsequently done by Sullivan (1997) for Maxwell's equations in three-dimensional problems. The theory proposed earlier by Sacks *et al.* (1995) was used in the formulations of the unsplit PMLs. Yu *et al.* (2003) also developed an unsplit PML which was based on the conventional  $E - H$  algorithm but did not require the split  $E$  and  $H$  components. This unsplit PML is as memory-efficient as that using the theory of Sacks *et al.* (1995). The distinct advantage of using the unsplit PML is memory efficiency due to the less memory requirements of the FDTD procedure.

Apart from Maxwell's equations in electromagnetics, the PML approach was also studied and extended to the Euler equations linearized at constant flow in the Cartesian-coordinate system by Hu (1996). Hu considered only two-dimensional acoustic, vorticity and entropy waves, using the splitting technique introduced earlier by Berenger (1994). The detail of the split-field formulation is, however, different from Berenger's even though the general approach is the same. This led to a different PML scheme with different properties. In addition, the PML approach was extended to wave equations in elastodynamics by Chew and Liu (1996). The complex-valued coordinate stretching was introduced to obtain the governing equations of the PML, and a FDTD formulation was obtained through the splitting of the fields. In the same year, Hasting *et al.* (1996) performed the application of the PML for two-dimensional elastic wave propagation, using finite-difference formulation in the time domain analysis. The original split-field formulation of Berenger (1994) in the Cartesian-coordinate system was adopted and modified by adding loss terms to achieve more accurate results.

A few years later, Liu (1999) developed two PML schemes for elastic waves in the cylindrical and spherical coordinates. In the formulation, the integrated complex stretching variables were introduced to reduce the amount of unknown split field components. For two-dimensional elastic wave propagation in heterogeneous and anisotropic media, the PML approach was also developed by Collino and Tsogka (2001). The splitting technique was adapted in the velocity-stress formulation of elastodynamics. The finite-difference and finite-element schemes were employed in the implementation.

All the PMLs mentioned previously in the context of the elastodynamics are based on first-order system in velocity and stress. Such PMLs are regarded as classical PMLs and cannot be used in a straightforward manner for numerical schemes which are based on a second-order system in displacement, such as the finite element method, the finite difference method, etc. The first attempt to surpass this limitation was made by Komatitsch and Tromp (2003). They formulated a PML for the elastic wave equation written as a second-order system in displacement, and tested it on a two-dimensional elastic isotropic homogeneous medium.

Bécache *et al.* (2003) also investigated the numerical stability and well-posedness of the PMLs for isotropic and anisotropic elastodynamics thoroughly. In detail, a necessary condition for the stability of the PMLs in a general hyperbolic system was first derived in terms of the geometric properties of the slowness diagrams. This criterion was then used for explaining the instabilities observed with elastic waves, anisotropic Maxwell's equations and linearized Euler equations. Finally, a necessary stability condition and a sufficient stability condition for orthotropic elastic waves in terms of inequalities on the elasticity coefficients of the model were obtained separately.

Basu and Chopra (2003) developed a PML concept used for time-harmonic elastodynamics in the Cartesian coordinates, using insights obtained from the PMLs used in electromagnetics, and also presented a novel displacement-based, symmetric finite-element implementation of the PML for time-harmonic plane-strain or three-dimensional motion. The governing equations of the PML were defined in the frequency domain using complex-valued coordinate stretching, and only homogeneous and isotropic media were considered. For the PML concept, it was illustrated through a one-dimensional semi-infinite rod on an elastic foundation and a two-dimensional example of the anti-plane motion of a continuum governed by the Helmholtz equation. For the finite-element implementations, the PML was applied to the one-dimensional semi-infinite rod on elastic foundation, the anti-plane motion of a semi-infinite layer on a rigid base, and the classical plane-strain soil-structure interaction problems of a rigid strip-footing on a half-plane, on a layer which was on a half-plane and on a layer which was on a rigid base. Soon after Basu and Chopra (2003) proposed their PML concept. In the next year, they extended the same concept to transient elastodynamics for homogeneous and isotropic media in the Cartesian coordinates (Basu and Chopra, 2004).

In recent years, Harari and Albocher (2006) have formulated the equation of an absorbing layer for time-harmonic elastic waves, based on the PML concept. In the proposed approach, the layer was viewed as an anisotropic material with

continuously varying complex material properties. The effect of the PML parameters on its discrete representation was investigated through dispersion analyses.

## 2.4 Capacity of commercial finite element packages for modeling unbounded domains

Some of global and local procedures have been already implemented in commercial finite element packages in various applications in order to simulate wave propagation in unbounded domains. The commercial finite element packages being reviewed herein are, for example, FLUSH, ABAQUS, ANSYS, ADINA, DIANA and SOFiSTiK.

The TLM was implemented in the finite-element computer program FLUSH (Lysmer *et al.*, 1975). It has been widely used for seismic soil-structure interaction analysis for a long time. The plane strain quadrilateral elements for modeling soils and structures, the beam elements for modeling structures and multiple nonlinear soil properties for equivalent linear analysis which allows for different damping in each element were embodied in the program. Only semi-infinite layers with constant depth resting on a rigid base can be modeled by FLUSH.

The viscous boundary (Lysmer and Kuhlemeyer, 1969) was adopted in ABAQUS. Almost all of the energy of  $P$ - and  $S$ -waves can be absorbed by this viscous boundary. However, the viscous boundary is less efficient in absorbing Rayleigh wave energy (Ramshaw *et al.*, 1998). ABAQUS also provides the application of the impedance boundary which is based on the first-order Bayliss-Turkel absorbing boundary (ABAQUS, 2004).

The infinite acoustic elements (FLUID129 for a circular boundary and FLUID130 for a spherical boundary) are provided in ANSYS in order to absorb an outgoing pressure wave reaching the model boundary. These two elements provide second-order ABCs satisfying the Sommerfeld radiation condition and can be used in modal, harmonic and transient analyses (ANSYS, 2009a). The PML is also provided in ANSYS for electromagnetics and acoustics in order to absorb the outgoing waves in a modal or harmonic analysis (ANSYS, 2009b).

ADINA provides the potential-interface of type infinite for the time-domain analysis in acoustic or fluid problems. This potential-interface is based on the DAAs (Olson and Bathe, 1985), which can be applied on the truncated boundary to simulate infinite fluid regions. There are three types of the interface: planar, cylindrical and spherical interfaces. This potential-interface is also used associated with the

potential-based-fluid elements in the analysis of transient fluid-structure interactions.

DIANA (2010), which is a commercial finite element package, provides the spring / dashpot element for unbounded domains in elastodynamic problems (Ucci *et al.*, 2010). This element type actually is based on the viscous boundary (Lysmer and Kuhlemeyer, 1969) that can absorb outgoing waves.

ACTRAN is a general purpose finite element program for the modeling of sound propagation, transmission, absorption and for the coupled analysis of vibro-acoustic problems. The unconjugated and conjugated spheroidal elements were implemented in ACTRAN (Astley and Coyette, 2001b). The unconjugated element is similar to the original Burnett element (Burnett, 1994), and the conjugated element is the Astley-Leis type (Astley, 1998a). Both were implemented with Shifted Legendre polynomials as a radial basis to improve conditioning at high radial orders (Shirron and Babuska, 1998; Astley and Coyette, 2001a).

A recent development is the SBFEM (Wolf and Song, 1996; Wolf, 2003), which provides highly accurate impedance functions. The approach makes the rigid base mat assumption redundant. It will be commercially available for time domain analysis in a forthcoming release of SOFiSTiK (Nielsen, 2009). This could potentially lead to a revival of substructure methods in industry.

Most of the local procedures implemented in the commercial finite element packages as mentioned above are of low-order formulation, except those provided in ANSYS. However, these approaches are only applicable to isotropic and homogeneous unbounded domains with simple geometry. Therefore, such commercial finite element packages are unable to simulate wave propagation in unbounded domain with arbitrary geometry and material properties in an accurate and efficient way. Thus it is of interest to develop a local high-order artificial boundary which is applicable to arbitrary geometry and material properties, and also implemented easily with standard finite elements.

## 2.5 Conclusions

As summarized in the sections above, the global and local procedures have a long history of development. They both have advantages and disadvantages. However, for practical engineering problems, the local procedures have attracted more attention from researchers since they are more efficient owing to their locality in time. Among the local procedures, the local high-order ABCs are state-of-the-art. They are appropriate for simulating propagating scalar waves in homogeneous unbounded

domains with simple geometry. Nevertheless, almost all of them cannot simulate evanescent waves and are thus unsuitable for long-time analyses. Therefore, the future research on the local high-order ABCs should focus on the following topics:

- Inclusion of evanescent modes to improve the accuracy of the absorbing boundary condition for long-time analyses.
- Scalar wave propagation in non-homogeneous unbounded domains with simple and arbitrary geometry.
- Vector wave propagation in homogeneous unbounded domains with simple and arbitrary geometry.
- Vector wave propagation in non-homogeneous unbounded domains with simple and arbitrary geometry.

This thesis also focuses on these topics as clarified previously in the objectives of the thesis in Section 1.4 of Chapter 1. The high-order doubly asymptotic open boundaries proposed herein can simulate both propagating and evanescent waves and are thus suitable for long-time analyses as presented in Chapter 3 for the modal equations of scalar waves, and in Chapters 4 and 5 for scalar wave propagation in homogeneous unbounded domains with simple geometry. In Chapter 6, the high-order doubly asymptotic open boundary for scalar wave propagation in non-homogeneous unbounded domains with simple geometry is proposed. In Chapter 7, the high-order doubly asymptotic open boundary for vector wave propagation in a homogeneous unbounded domain with simple geometry is presented.

# Chapter 3

## Doubly Asymptotic Open Boundaries for Modal Equations of Scalar Waves

### Abstract

High-order doubly asymptotic open boundaries are developed for the modal equations of scalar wave equations for a semi-infinite layer with a constant depth and a circular cavity in a full-plane. The open boundaries are derived in the frequency domain as doubly asymptotic continued fraction solutions for the dynamic stiffness of the unbounded domains. Each term of the continued fraction is a linear function of the excitation frequency. The coefficients of the continued fraction solutions are determined recursively. The continued fraction solution is expressed in the time domain as ordinary differential equations, which can be solved by standard time-stepping schemes. No parameters other than the orders of the high- and low-frequency expansions need to be selected by the user. Numerical experiments demonstrate that evanescent waves and long-time (low frequency) responses are simulated accurately. In comparison with singly asymptotic open boundaries, significant gain in accuracy is achieved at no additional computational cost.

### 3.1 Introduction

When wave propagation problems are modeled, it is often necessary to introduce an artificial boundary around the region of interest so that the size of computational domain is limited to allow the application of well-established numerical methods such as the finite element method. The region exterior to the artificial boundary is regarded as an unbounded domain. A boundary condition mimicking the unbounded domain has to be enforced on the artificial boundary to prevent fictitious reflections

that pollute the solution. A direct time-domain formulation of the boundary condition is required when nonlinearities occur in the region of interest. Such a boundary condition is known by various names such as absorbing, non-reflecting, open, radiation, transmitting and transparent boundary conditions. Extensive literature on various artificial boundaries exists. Excellent literature reviews are available in papers (Luco, 1982; Kausel, 1988; Givoli, 1991; Tsynkov, 1998; Astley, 2000; Givoli, 2004) and books (Wolf, 1985, 1988; Givoli, 1992a; Wolf and Song, 1996).

In theory, an exact artificial boundary is global in space and time, i.e. the present response at a point on the boundary is a function of the response history at all boundary points up to the present time. When a rigorous method (for example, the boundary element method (Hall and Oliveto, 2003; Beskos, 1987), the thin-layer method (Kausel, 1994) or the scaled boundary finite element method (Wolf and Song, 1996; Song and Wolf, 1997) is employed to construct an artificial boundary, the formulation is global. The convolution integral and storage of the response history are computationally expensive for large-scale problems and long-time calculations.

Time realization techniques have been proposed to construct temporally local artificial boundaries from the dynamic stiffness matrices obtained at discrete frequencies from analytical solution or by a rigorous method. In Wolf (1991), Paronesso and Wolf (1995), and Alpert *et al.* (2002), a Padé approximation of the dynamic stiffness matrix is constructed by using a curve fitting technique based on the least-squares method. A temporally local artificial boundary is formulated after expressing the Padé approximation as unit fractions. In Ruge *et al.* (2001), the Padé approximation is expressed as a continued fraction leading to a mixed-variable method. In Paronesso and Wolf (1998), system theory is applied to construct a temporally local artificial boundary from the unit-impulse response obtained from the scaled boundary finite element method.

Moreover, a large number of approximate artificial boundary conditions have been developed. Well-known examples include the viscous boundary (Lysmer and Kuhlemeyer, 1969), the superposition boundary (Smith, 1974), the paraxial boundary (Engquist and Majda, 1979) and the extrapolation boundary (Liao and Wong, 1984). Generally speaking, they are spatially and temporally local, i.e. the response at a point is coupled with the response at a few adjacent points during a few previous time steps only. These local artificial boundaries are simple and computationally efficient by themselves, but have to be applied to an artificial boundary sufficiently away from the region of interest in order to obtain results of acceptable accuracy. This increases the total computational effort.

To increase the accuracy and efficiency of simple artificial boundaries, high-order local absorbing boundaries have been proposed. This type of absorbing boundary

has the potential of leading to accurate results as the order of approximation increases. At the same time, it is computationally efficient owing to its local formulation. Examples of early developments include the paraxial boundary (Engquist and Majda, 1979), the Bayliss, Gunzburger and Turkel (BGT) boundary (Bayliss *et al.*, 1982) and the multi-direction boundary (Higdon, 1986). However, the order of derivative in these formulations increases with the order of the absorbing boundary. Beyond the second order, the implementation in a finite-element computer program becomes complex and instability may occur (Wolf, 1988).

Researchers in several fields have shown their strong interest in developing absorbing boundaries of arbitrarily high order (see, e.g. Hagstrom and Hariharan (1998), Grote and Keller (2000), Guddati and Tassoulas (2000), Thompson *et al.* (2001), Krenk (2002), Givoli and Neta (2003), and Hagstrom and Warburton (2004)). Literature reviews are available, e.g., in Tsynkov (1998) and Givoli (2004). Most of the absorbing boundaries are, however, limited to straight, circular and spherical boundaries. Special corner conditions have to be devised for rectangular boundaries. Krenk (Krenk, 2002) showed that several of well-established absorbing boundaries can be formulated as a rational function approximation (Padé or continued fraction expansion) of the plane wave representation for scalar waves.

All the above high-order absorbing boundaries were constructed to absorb propagating waves radiating energy. As they are singly asymptotic at the high-frequency limit, these high-order absorbing boundaries are appropriate for radiative fields, i.e., virtually all of the field energy is propagating out to infinity (Geers, 1998). In some classes of applications, a part of the total energy may be trapped near the region of interest and may not propagate to infinity. The best-known example is probably the evanescent waves occurring in a semi-infinite layer with a constant depth (also known as a waveguide). It is explained in Hagstrom *et al.* (2008) that inclusion of evanescent modes improves the accuracy of the long-time behavior of a high-order absorbing boundary. Another example is the class of problems where the dimensionless frequency  $a_0 = \omega r_0 / c$  ( $\omega$  is the smallest excitation frequency of interest,  $r_0$  is a characteristic length of the region of interest,  $c$  is the wave velocity) is very low (statics can be regarded as the limiting case  $a_0 \rightarrow 0$ ). These wave fields are largely non-radiative. To achieve reasonably accurate results at low frequencies, i.e., over long time, the order of an absorbing boundary has to be very high, thereby leading to large computational cost. In most of the publications on high-order absorbing boundaries, the numerical results are shown for only the first few periods, and long-time responses are rarely reported.

From an application point of view, it is highly desirable to develop a temporally local absorbing boundary that is capable of accurately mimicking an unbounded

domain over the entire frequency range (i.e. from zero to infinity). One advance toward this objective is the introduction of the doubly asymptotic boundaries (Geers, 1978; Underwood and Geers, 1981; Geers and Zhang, 1994; Geers and Lewis, 1997; Geers, 1998). This formulation is spatially global as the dynamic stiffness is exact not only at the high-frequency limit but also at statics. To the knowledge of the authors, the highest order reported is three (Geers and Toothaker, 2000).

Recently, a new approach to construct temporally local transmitting boundaries of arbitrarily high order has been proposed in Bazzyar and Song (2008). It is applicable to both scalar and vector waves. The geometry of the boundary of the unbounded domain can be arbitrary as long as the scaling requirement (there exists a zone from where the whole boundary is visible) is satisfied. Anisotropic unbounded media are handled without additional computation cost. Different from most of existing approaches, it seeks a continued fraction solution for the equation of the dynamic stiffness matrix of an unbounded domain obtained in the scaled boundary finite element method (Song and Wolf, 1997). Each term of the continued fraction is a linear function of the excitation frequency  $\omega$ . The constant matrices in the continued fraction are determined recursively by satisfying the scaled boundary finite element equation at the high-frequency limit. No explicit solution of the dynamic stiffness matrix at discrete frequencies is required. By using the continued fraction solution, the force-displacement relationship of the unbounded domain is formulated as a temporally local transmitting boundary condition in the time domain. However, like other high-order absorbing boundaries, this transmitting boundary is inappropriate to model evanescent waves, and the convergence rate at low frequencies is much slower than that at high frequencies.

In this chapter, a technique for constructing a high-order doubly asymptotic open boundary is proposed by extending the work of Bazzyar and Song (2008). Only scalar waves and unbounded domains with simple geometry, namely a semi-infinite layer with a constant depth (a waveguide) and a circular cavity in a full-plane, are considered. Nevertheless, the artificial boundaries for these cases can be applied directly to solve practical problems by introducing straight or circular artificial boundaries (Hagstrom and Hariharan, 1998; Grote and Keller, 2000; Thompson *et al.*, 2001; Alpert *et al.*, 2002; Hagstrom *et al.*, 2008). The investigations into the simple cases also provide insights into the basic numerical phenomena involved in high-order absorbing boundaries such as the failure in representing evanescent waves and the relative poor performance at low frequencies. Furthermore, a novel approach to develop accuracy and efficient open boundaries is proposed.

This chapter is organized as follows: in Section 3.2, the scalar wave equation is decomposed into a series of one-dimensional wave equations by applying the method

of separation of variables. After the dynamic stiffness coefficient of a one-dimensional wave problem is introduced, an equation of the dynamic stiffness coefficient is derived. In Section 3.3, a doubly asymptotic continued fraction solution for the dynamic stiffness coefficient is determined recursively at the high- and low-frequency limits. The link between the singly asymptotic high-frequency solution for the semi-infinite layer and several other high-order absorbing boundaries based on Padé (or continued fraction) expansions is identified. In Section 3.4, an equation of motion of an unbounded domain is formulated on the boundary by using the doubly asymptotic continued fraction solution of dynamic stiffness. It leads to a temporally local open boundary expressed in time-independent stiffness and damping matrices. Well-established time-stepping schemes in structural dynamics are directly applicable. In Section 3.5, the high performance of the proposed high-order doubly asymptotic open boundaries is demonstrated with numerical examples. In Section 3.6, conclusions are presented.

## 3.2 Dynamic stiffness of unbounded domains

The linear homogeneous scalar wave equation is expressed as

$$\nabla^2 u = \frac{1}{c_s^2} \ddot{u} \quad (3.2.1)$$

where  $u = u(x, y, z, t)$  denotes the wave field,  $\nabla^2$  the Laplace operator and  $c_s$  the given wave speed. In this section, the arguments of functions are omitted for simplicity in the nomenclature. The initial conditions for an unbounded domain initially at rest are expressed as

$$u = \dot{u} = 0 \quad \text{at } t = 0 \quad (3.2.2)$$

The geometries and boundary conditions of the semi-infinite layer and the circular cavity are given in Sections 3.2.1 and 3.2.2, respectively. By employing the method of separation of variables, Eq. (3.2.1) can be transformed to a series of one-dimensional wave equations. From a one-dimensional wave equation and the definition of a dynamic stiffness coefficient, an equation of the dynamic stiffness coefficient is then derived.

### 3.2.1 Semi-infinite layer with constant depth

A semi-infinite layer with a constant depth  $h$  is shown in Fig. 3.2.1. For convenience, the  $x$ -axis of the coordinate system is chosen at the lower boundary of the layer. The formulation of the proposed open boundaries is based on the dynamic stiffness representing the property of the semi-infinite layer. It is independent of the coordinate system. The open boundaries are applicable to semi-infinite layers of any orientation. It is assumed that a distributed traction  $\tau_0(t)$  is applied to the vertical boundary  $\Gamma_V$  (at  $x = x_0$ ). The homogeneous boundary conditions prescribed on the parallel upper boundary  $\Gamma_U$  and lower boundary  $\Gamma_L$  are satisfied in the method of separation of variables by eigenfunctions. For example, when the upper boundary  $\Gamma_U$  is free (i.e.  $u_{,y}(y = h) = 0$ ) and the lower boundary  $\Gamma_L$  is fixed (i.e.  $u(y = 0) = 0$ ) the eigenfunctions are  $\sin(\lambda_i y/h)$  where the eigenvalues are equal to  $\lambda_i = (2i + 1)\pi/2$  for  $i = 0, 1, \dots$ . Note that as the eigenvalue  $\lambda_i$  increases, the eigenfunction varies more rapidly along the vertical boundary.

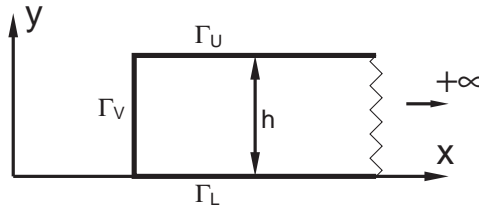


Figure 3.2.1: Semi-infinite layer with constant depth

For a mode with a modal eigenvalue  $\lambda$ , the one-dimensional wave equation is expressed as

$$\frac{\partial^2 \tilde{u}}{\partial x^2} - \left(\frac{\lambda}{h}\right)^2 \tilde{u} = \frac{1}{c_s^2} \ddot{\tilde{u}} \quad (3.2.3)$$

where  $\tilde{u} = \tilde{u}(x, t)$  is the modal displacement. The modal traction is denoted as  $\tilde{\tau}_0(t)$  at  $x = x_0$ . Once the solution of Eq. (3.2.3) satisfying both the boundary condition at  $x = x_0$  and the radiation condition at  $x \rightarrow +\infty$  is known, the solution for the wave propagation in the semi-infinite layer can be obtained by modal superposition. Hereafter, only the modal equation in Eq. (3.2.3) is addressed, and the word “modal” is omitted for the sake of simplicity except where confusion may arise.

By assuming the time-harmonic behavior  $\tilde{u} = \tilde{U}(\omega, x)e^{+i\omega t}$  and  $\tilde{\tau}_0(t) = \tilde{R}(\omega, x)e^{+i\omega t}$  ( $\omega$  is the excitation frequency), Eq. (3.2.3) is rewritten in the frequency domain as

$$\frac{d^2 \tilde{U}}{dx^2} + \frac{1}{h^2} (a_0^2 - \lambda^2) \tilde{U} = 0 \quad (3.2.4)$$

where  $\tilde{U} = \tilde{U}(\omega, x)$  is the displacement amplitude, and  $a_0$  is a dimensionless frequency

$$a_0 = \frac{\omega h}{c_s} \quad (3.2.5)$$

### 3.2.1.1 Analytical solution

The solution of Eq. (3.2.4) satisfying the radiation condition for the semi-infinite layer extending to  $x \rightarrow +\infty$  (Fig. 3.2.1) is

$$\tilde{U} = C e^{-\sqrt{\lambda^2 - a_0^2} x/h} \quad (3.2.6)$$

with the integration constant  $C$ . A cut-off frequency exists in Eq. (3.2.6) at the dimensionless frequency  $a_0 = \lambda$ . Below the cut-off frequency, i.e.  $a_0 < \lambda$ , the displacement decays exponentially. No propagating waves exist, in other words, evanescent waves are present. Above the cut-off frequency, i.e.  $a_0 > \lambda$ , Eq. (3.2.6) describes a wave propagating with a frequency-dependent phase velocity.

For the semi-infinite layer extending to the right-hand side, the force amplitude  $\tilde{R} = \tilde{R}(\omega, x)$  on a vertical boundary at arbitrary  $x$  is expressed as

$$\tilde{R} = -h \frac{d\tilde{U}}{dx} \quad (3.2.7)$$

Substituting Eq. (3.2.6) into Eq. (3.2.7) results in

$$\tilde{R} = -h \frac{d\tilde{U}}{dx} = C \sqrt{\lambda^2 - a_0^2} e^{-\sqrt{\lambda^2 - a_0^2} x/h} \quad (3.2.8)$$

The open boundary condition is represented as a force-displacement relationship. In the frequency domain, this relationship is defined by the dynamic stiffness coefficient  $S = S(\omega, x)$  at a vertical line with a constant  $x$ -coordinate

$$\tilde{R} = S\tilde{U} \quad (3.2.9)$$

It is analogous to the DtN operator (Givoli, 1999). The solution for the dynamic stiffness coefficient can be obtained from its definition in Eq. (3.2.9) with the substitution of Eqs. (3.2.6) and (3.2.8)

$$S(a_0) = \sqrt{\lambda^2 - a_0^2} \quad (3.2.10)$$

Note that the dynamic stiffness coefficient  $S(a_0)$  is only a function of the dimensionless frequency  $a_0$  and is independent of the value of the  $x$  coordinate (Eq. (3.2.5)). Below the cut-off frequency, i.e.  $a_0 < \lambda$ ,  $S(a_0)$  is a real number whereas the imaginary part representing radiation damping vanishes. At the cut-off frequency  $a_0 = \lambda$ ,  $S(a_0)$  is equal to zero representing the resonance of the semi-infinite layer. Above the cut-off frequency, i.e.  $a_0 > \lambda$ ,  $S(a_0)$  is pure imaginary. Equation (3.2.10) normalized by the modal eigenvalue  $\lambda$  is the square-root operator widely used in constructing open boundaries

$$\frac{S(a_0)}{\lambda} = \sqrt{1 - \left(\frac{a_0}{\lambda}\right)^2} \quad (3.2.11)$$

To obtain a reference solution to validate numerical results in the time domain, the response to a unit impulse of traction  $\tilde{\tau}_{0I}(t) = \delta(t)$  ( $\delta(t)$  represents the Dirac-delta function) applied at  $x = x_0$  is evaluated. The amplitude of the displacement response  $\tilde{U}_I$  is determined from Eqs. (3.2.10) and (3.2.9) with the Fourier transform of the unit impulse  $\tilde{R}_{0I} = 1$

$$\tilde{U}_I = \frac{1}{\sqrt{\lambda^2 - a_0^2}} \quad (3.2.12)$$

The unit-impulse response  $\tilde{u}_I(t)$  is equal to the inverse Fourier transform of  $\tilde{U}_I$  (Eq. (3.2.12))

$$\tilde{u}_I(t) = \frac{c}{h} J_0 \left( \lambda \frac{ct}{h} \right) H(t) \quad (3.2.13)$$

where  $J_0$  is the zero order first kind Bessel function,  $H(t)$  is the Heaviside-step function ( $H(t < 0) = 0$ ,  $H(t \geq 0) = 1$ ), and  $\bar{t} = ct/h$  represents the dimensionless time. At large time ( $\bar{t} \gg 1$ ), the asymptotic solution of the unit-impulse response is expressed as

$$\tilde{u}_I(t) \rightarrow \sqrt{\frac{2h}{\pi\lambda ct}} \cos \left( \lambda \frac{ct}{h} - \frac{\pi}{4} \right) \quad (3.2.14)$$

It oscillates at a period of  $T = 2\pi h/(\lambda c)$ . This period corresponds to the dimensionless cut-off frequency  $a_0 = \lambda$  where the dynamic stiffness coefficient is equal to zero. The unit-impulse response exhibits a long-lasting oscillation with a very slow decay rate of  $\sqrt{T/t}$  (see Fig. 3.5.7 in Section 3.5.1).

The displacement response to a prescribed traction  $\tilde{\tau}_0(t)$  is expressed as a convolution integral

$$\tilde{u}(t) = \frac{c}{h} \int_0^t J_0 \left( \lambda \frac{c(t-\tau)}{h} \right) \tilde{\tau}_0(\tau) d\tau \quad (3.2.15)$$

### 3.2.1.2 Equation of dynamic stiffness coefficient

An equation of the dynamic stiffness coefficient is derived from the wave equation and the definition of the dynamic stiffness coefficient. Eliminating the force amplitude  $\tilde{R}$  from Eqs. (3.2.7) and (3.2.9) leads to

$$h \frac{d\tilde{U}}{dx} = -S\tilde{U} \quad (3.2.16)$$

Differentiating Eq. (3.2.16) with respect to  $x$  and multiplying the result by  $h$  yield

$$h^2 \frac{d^2\tilde{U}}{dx^2} = -Sh \frac{d\tilde{U}}{dx} - h \frac{dS}{dx} \tilde{U} = \left( S^2 - h \frac{dS}{dx} \right) \tilde{U} \quad (3.2.17)$$

Substituting Eq. (3.2.17) into Eq. (3.2.4) multiplied by  $h^2$  results, for an arbitrary  $\tilde{U}$ , in

$$S^2 - \frac{dS}{dx} + a_0^2 - \lambda^2 = 0 \quad (3.2.18)$$

As both  $a_0$  (Eq. (3.2.5)) and the eigenvalue  $\lambda$  are independent of  $x$ , the dynamic stiffness coefficient is a function of  $a_0$  only, i.e.,  $dS/dx = 0$ . Equation (3.2.18) is, therefore, rewritten as

$$(S(a_0))^2 + a_0^2 - \lambda^2 = 0 \quad (3.2.19)$$

Its positive solution is given in Eq. (3.2.10).

## 3.2.2 Circular cavity embedded in full-plane

The scalar wave propagation in a full-plane with a circular cavity of radius  $r_0$  (Fig. 3.2.2) is addressed. A surface traction  $\tau_0(t)$  is applied on the boundary  $\Gamma$ . Applying the method of separation of variables to the scalar wave equation in polar coordinates  $r, \theta$  leads to a series of wave equations in the radial direction

$$r^2 \frac{d^2\tilde{u}}{dr^2} + r \frac{d\tilde{u}}{dr} - \lambda^2 \tilde{u} = \left( \frac{r}{c_s} \right)^2 \ddot{\tilde{u}} \quad (3.2.20)$$

where  $\tilde{u} = \tilde{u}(r, t)$  is the modal displacement,  $\lambda$  is the modal eigenvalue. The modal traction is denoted as  $\tilde{\tau}_0(t)$  at  $r = r_0$ . In the frequency domain ( $\tilde{U} = \tilde{U}(\omega, r)$  is the displacement amplitude), Eq. (3.2.20) is expressed as a Bessel equation of order  $\lambda$

$$r^2 \frac{d^2 \tilde{U}}{dr^2} + r \frac{d\tilde{U}}{dr} + \left( \left( \frac{\omega r}{c_s} \right)^2 - \lambda^2 \right) \tilde{U} = 0 \quad (3.2.21)$$

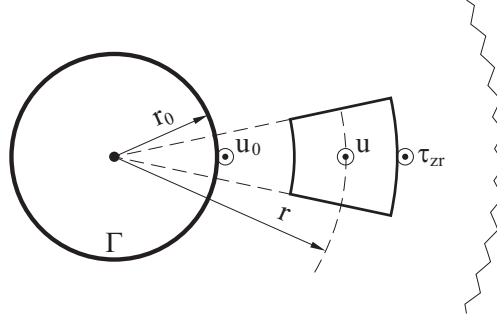


Figure 3.2.2: Circular cavity embedded in full-plane

### 3.2.2.1 Analytical solution

The solution of Eq. (3.2.21) satisfying the radiation condition is the second-kind Hankel function of order  $\lambda$

$$\tilde{U} = CH_\lambda^{(2)}(a) \quad (3.2.22)$$

with the dimensionless variable

$$a = a(\omega, r) = \frac{\omega r}{c_s} \quad (3.2.23)$$

and the integration constant  $C$ . The force amplitude  $\tilde{R} = \tilde{R}(\omega, r)$  on a circle of radius  $r$  is expressed as

$$\tilde{R} = -r \frac{d\tilde{U}}{dr} \quad (3.2.24)$$

Substituting Eq. (3.2.22) into Eq. (3.2.24) results in

$$\tilde{R} = -Cr \frac{dH_\lambda^{(2)}(a)}{dr} \quad (3.2.25)$$

The dynamic stiffness coefficient  $S = S(\omega, r)$  relating the force amplitude to the displacement amplitude on a circle of radius  $r$  is defined as

$$\tilde{R} = S\tilde{U} \quad (3.2.26)$$

It is obtained from Eqs. (3.2.26), (3.2.25) and (3.2.22) and expressed as

$$S(a) = -\frac{a}{H_\lambda^{(2)}(a)} \frac{dH_\lambda^{(2)}(a)}{da} = \lambda - \frac{H_{\lambda-1}^{(2)}(a)}{H_\lambda^{(2)}(a)} \quad (3.2.27)$$

Note that the only independent variable is the dimensionless variable  $a$ . The dynamic stiffness coefficient on the boundary  $\Gamma$  of the circular cavity is determined by evaluating  $S(a)$  at  $r = r_0$ .

### 3.2.2.2 Equation of dynamic stiffness coefficient

To derive an equation of the dynamic stiffness coefficient  $S = S(\omega, r)$ , the force amplitude  $\tilde{R}$  is eliminated from Eqs. (3.2.24) and (3.2.26). This leads to

$$r \frac{d\tilde{U}}{dr} = -S\tilde{U} \quad (3.2.28)$$

Differentiating Eq. (3.2.28) and multiplying the resulting expression by  $r$  result in

$$r^2 \frac{d^2\tilde{U}}{dr^2} + r \frac{d\tilde{U}}{dr} = -Sr \frac{d\tilde{U}}{dr} - r \frac{dS}{dr} \tilde{U} = \left( S^2 - r \frac{dS}{dr} \right) \tilde{U} \quad (3.2.29)$$

Substituting Eq. (3.2.29) into Eq. (3.2.21) and then eliminating  $\tilde{U}$  lead to an equation of the dynamic stiffness coefficient

$$S^2 - r \frac{dS}{dr} + \left( \frac{\omega r}{c} \right)^2 - \lambda^2 = 0 \quad (3.2.30)$$

Changing the independent variable from  $r$  to the dimensionless variable  $a$  (Eq. (3.2.23)) yields

$$(S(a))^2 - a \frac{dS(a)}{da} + a^2 - \lambda^2 = 0 \quad (3.2.31)$$

The number of independent variables is now reduced from two ( $\omega$  and  $r$ ) to one ( $a$ ). To construct an open boundary, it is sufficient to consider the dynamic stiffness

coefficient on the boundary  $\Gamma$ . Equation (3.2.31) is thus expressed at  $r = r_0$  as

$$(S(a_0))^2 - a_0 \frac{dS(a_0)}{da_0} + a_0^2 - \lambda^2 = 0 \quad (3.2.32)$$

with the dimensionless frequency

$$a_0 = \frac{\omega r_0}{c_s} \quad (3.2.33)$$

### 3.2.3 Comparison between dynamic stiffness coefficients of semi-infinite layer and circular cavity

The dynamic stiffness coefficients of the semi-infinite layer and the circular cavity are normalized with the eigenvalue  $\lambda$  to examine their interrelationship. Equation (3.2.19) is thus rewritten as

$$\left(\frac{S(a_0)}{\lambda}\right)^2 + \left(\frac{a_0}{\lambda}\right)^2 - 1 = 0 \quad (3.2.34)$$

and Eq. (3.2.32) as

$$\left(\frac{S(a_0)}{\lambda}\right)^2 - \frac{1}{\lambda} \left(\frac{a_0}{\lambda}\right) \frac{d}{d(a_0/\lambda)} \left(\frac{S(a_0)}{\lambda}\right) + \left(\frac{a_0}{\lambda}\right)^2 - 1 = 0 \quad (3.2.35)$$

Equation (3.2.35) can be regarded as an ordinary differential equation of  $S(a_0)/\lambda$  with the independent variable  $a_0/\lambda$ . The contribution of its second term decreases as  $\lambda$  increases. At the limit of  $\lambda \rightarrow \infty$ , the ordinary differential equation in Eq. (3.2.35) degenerates to the algebraic equation in Eq. (3.2.34). Therefore, the dynamic stiffness coefficient of a mode of the circular cavity tends to that of a mode of the semi-infinite layer with the same eigenvalue  $\lambda$  (Eq. (3.2.11)). This is illustrated in Fig. 3.2.3 by comparing the normalized dynamic stiffness coefficient  $S(a_0)/\lambda$  of the cylindrical cavity (Eq. (3.2.27) with  $a = a_0$  on boundary) for modes  $\lambda = 20, 200$  and  $2000$  with the dynamic stiffness coefficient of the semi-infinite layer (Eq. (3.2.11)). As  $\lambda$  increases, the dynamic stiffness coefficient of the cylindrical cavity approaches that of the semi-infinite layer ( $a_0 = \omega h/c_s$ ). At  $\lambda = 2000$ , the two dynamic stiffness coefficients become nearly indistinguishable.

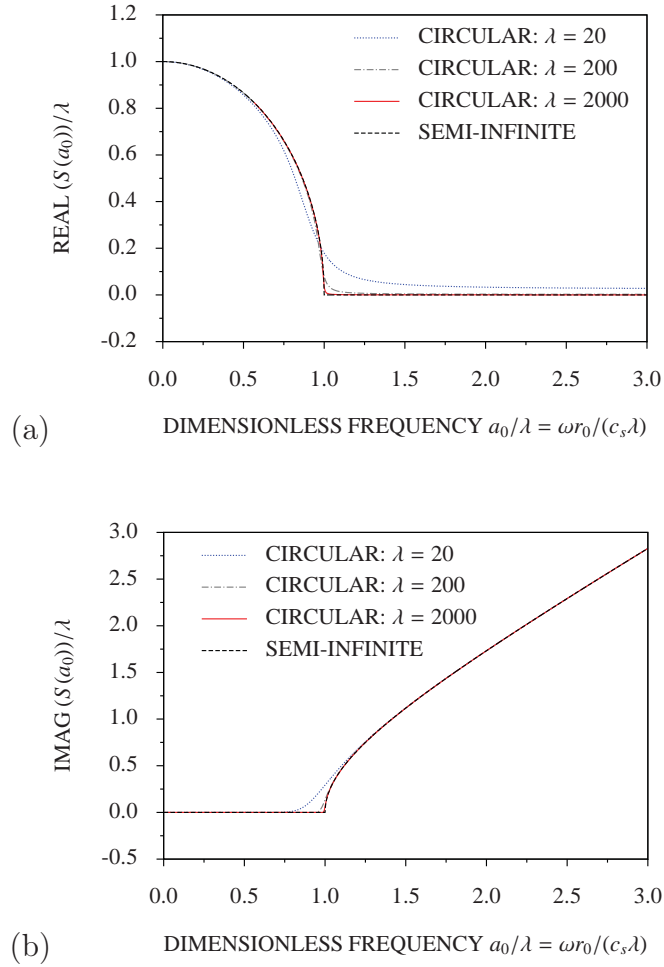


Figure 3.2.3: Comparison among dynamic stiffness coefficients of circular cavity and semi-infinite layer: (a) real part and (b) imaginary part

### 3.3 Doubly asymptotic continued fraction solution for dynamic stiffness

A continued fraction solution of the dynamic stiffness coefficient is obtained recursively in the work of Bazyar and Song (2008) as a singly asymptotic solution at the high-frequency limit ( $\omega \rightarrow +\infty$ ). It is shown for the circular cavity problem that the solution converges rapidly to the exact solution when the order of continued fraction increases and the dimensionless frequency is larger than the modal eigenvalue  $\lambda$ . At lower frequency range, the error increases significantly and the convergence is much slower. As it will be demonstrated in Section 3.5.1, the high-frequency continued fraction solution does not converge at all for the semi-infinite layer problem when the frequency is below the cut-off frequency.

A doubly asymptotic continued fraction solution is developed to improve the behavior of the singly asymptotic solution. After the high-frequency continued fraction solution is determined as in the work of Bazzyar and Song (2008) the differential equation of the residual term is solved again as a continued fraction, but the constants are determined at the low-frequency limit ( $\omega \rightarrow 0$ ).

Equation (3.2.19) for the semi-infinite layer is an algebraic equation, and Eq. (3.2.32) for the circular cavity is an ordinary differential equation. They are addressed in Sections 3.3.1 and 3.3.2, respectively.

### 3.3.1 Semi-infinite layer with constant depth

#### 3.3.1.1 High-frequency continued fraction

The construction of the high-frequency continued fraction solution for Eq. (3.2.19) follows the procedure in the work of Bazzyar and Song (2008). In this particular case, an order  $M_H$  continued fraction solution is expressed as

$$S(a_0) = (ia_0)C_\infty - \frac{\lambda^2}{(ia_0)Y_1^{(1)} - \frac{\lambda^2}{(ia_0)Y_1^{(2)} - \frac{\lambda^2}{\dots - \frac{\lambda^2}{(ia_0)Y_1^{(M_H)} - \frac{\lambda^2}{Y^{(M_H+1)}(a_0)}}}} \quad (3.3.1)$$

where the constants  $C_\infty$  and  $Y_1^{(i)}$  ( $i = 1, 2, \dots, M_H$ ) are determined by satisfying Eq. (3.2.19) at the high-frequency limit ( $a_0 \rightarrow +\infty$ ). The negative sign in front of each term is selected intentionally so that the open boundary can be easily expressed with symmetric coefficient matrices (see Section 3.4). Equation (3.3.1) is equivalent to

$$S(a_0) = (ia_0)C_\infty - \lambda^2(Y^{(1)}(a_0))^{-1} \quad (3.3.2a)$$

$$Y^{(i)}(a_0) = (ia_0)Y_1^{(i)} - \lambda^2(Y^{(i+1)}(a_0))^{-1} \quad (i = 1, 2, \dots, M_H) \quad (3.3.2b)$$

where  $Y^{(1)}(a_0)$  is of the order  $(ia_0)^{-1}$  as  $a_0 \rightarrow +\infty$ . When a singly asymptotic solution is considered, the residual term  $\lambda^2(Y^{(M_H+1)}(a_0))^{-1}$  is neglected.

Substituting Eq. (3.3.2a) into Eq. (3.2.19) results in an equation in terms of a power series of  $(ia_0)$

$$(ia_0)^2 (C_\infty^2 - 1) + \lambda^2 (-1 - 2(ia_0)C_\infty(Y^{(1)}(a_0))^{-1} + \lambda^2(Y^{(1)}(a_0))^{-2}) = 0 \quad (3.3.3)$$

This equation is satisfied by setting, in descending order, the two terms to zero. The first term is an equation for damping coefficient  $C_\infty$ . To satisfy the radiation condition, the positive solution is chosen

$$C_\infty = 1 \quad (3.3.4)$$

The second term of Eq. (3.3.3) is an equation of  $Y^{(1)}(a_0)$  as  $C_\infty$  is known (Eq. (3.3.4)). To derive a recursive formula for determining the constants of the continued fraction, it is rewritten as the  $i = 1$  case of

$$\lambda^2 - 2b_1^{(i)}(ia_0)Y^{(i)}(a_0) - (Y^{(i)}(a_0))^2 = 0 \quad (3.3.5)$$

with the constant

$$b_1^{(1)} = 1 \quad (3.3.6)$$

Substituting Eq. (3.3.2b) into Eq. (3.3.5) leads to an equation in terms of a power series of  $(ia_0)$

$$\begin{aligned} - (ia_0)^2 \left( (Y_1^{(i)})^2 + 2b_1^{(i)}Y_1^{(i)} \right) + \lambda^2 (1 + 2(ia_0)(Y_1^{(i)} + b_1^{(i)})(Y^{(i+1)}(a_0))^{-1} \\ - \lambda^2(Y^{(i+1)}(a_0))^{-2}) = 0 \end{aligned} \quad (3.3.7)$$

Again, this equation is satisfied by setting the two terms to zero. The non-zero solution of the  $(ia_0)^2$  term is equal to

$$Y_1^{(i)} = -2b_1^{(i)} \quad (3.3.8)$$

By using the solution of  $Y_1^{(i)}$  in Eq. (3.3.8), the second term of Eq. (3.3.7) is rearranged as

$$\lambda^2 + 2b_1^{(i)}(ia_0)Y^{(i+1)}(a_0) - (Y^{(i+1)}(a_0))^2 = 0 \quad (3.3.9)$$

Introducing the recursive formula for updating the constant

$$b_1^{(i+1)} = -b_1^{(i)} \quad (3.3.10)$$

Equation (3.3.9) is simply the  $(i + 1)$  case of Eq. (3.3.5). From Eqs. (3.3.6) and (3.3.10),

$$b_1^{(i)} = (-1)^{i+1} \quad (3.3.11)$$

applies.  $Y_1^{(i)}$  is obtained explicitly from Eq. (3.3.8) as

$$Y_1^{(i)} = (-1)^i 2 \quad (3.3.12)$$

The high-frequency continued fraction solution in Eq. (3.3.1) (or Eq. (3.3.2)) is constructed from the solutions of the constants  $C_\infty$  in Eq. (3.3.4) and  $Y_1^{(i)}$  in Eq. (3.3.12). For example, Eq. (3.3.1) is expressed for the order  $M_H = 2$  high-frequency continued fraction as

$$S(a_0) = (ia_0) - \frac{\lambda^2}{-2(ia_0) - \frac{\lambda^2}{2(ia_0) - \frac{\lambda^2}{Y^{(3)}(a_0)}}} \quad (3.3.13)$$

### 3.3.1.2 Link with other absorbing boundaries for plane waves

The singly asymptotic continued fraction solution in Eq. (3.3.1) is expressed by using Eqs. (3.3.4) and (3.3.12) as

$$\frac{S(a_0)}{(ia_0)} = 1 - \frac{(\lambda/(ia_0))^2}{-2 - \frac{(\lambda/(ia_0))^2}{2 - \frac{(\lambda/(ia_0))^2}{-2 - \dots}}} = 1 + \frac{(\lambda/(ia_0))^2}{2 + \frac{(\lambda/(ia_0))^2}{2 + \frac{(\lambda/(ia_0))^2}{2 + \dots}}} = 1 - \frac{(\lambda/a_0)^2}{2 - \frac{(\lambda/a_0)^2}{2 - \dots}} \quad (3.3.14)$$

Several absorbing boundaries have been constructed based on the continued fractions of the function  $\sqrt{1+x}$ , where  $x$  may represent the wave number, pseudo-differential operator or the angle of incidence of a plane wave depending on the particular formulation. For example, the third approximation expressed in Eq. 1.13 of Engquist and Majda (1977) is based on the continued fraction

$$\sqrt{1+x} = 1 + \frac{x}{2 + \frac{x}{2}} \quad (3.3.15)$$

When  $x = (\lambda/ia_0)^2 = -(\lambda/a_0)^2$  is assumed, Eq. (3.3.15) is equivalent to the second order singly asymptotic continued fraction in Eq. (3.3.14).

It has been shown by Krenk (2002) that, when all the angles of ideal transmission are selected as 0, the multi-directional absorbing boundary proposed by Higdon (1987) corresponds to the continued fraction of  $\cos \theta = \sqrt{1 - \sin^2 \theta}$  (Eq. 15 of Krenk (2002))

$$\cos \theta = 1 - \frac{\sin^2 \theta}{2 - \frac{\sin^2 \theta}{2 - \frac{\sin^2 \theta}{2 - \dots}}} \quad (3.3.16)$$

where  $\theta$  is the angle of incidence (the angle between the direction of propagation of a plane wave and the outward normal of the boundary). Equation (3.3.16) is equivalent to Eq. (3.3.15) for the same order of continued fraction when  $x = -\sin^2 \theta$  is assumed. By comparing Eq. (3.3.14) to Eq. (3.3.16), it can be identified that the two equations are identical when setting

$$\sin \theta = \lambda/a_0 \quad (3.3.17)$$

Equation (3.3.17) relates the dimensionless frequency  $a_0$  to the angle of incidence  $\theta$ .

As  $\sin \theta$  is bounded between 0 and 1, the performance of absorbing boundaries based on this continued fraction is controlled for  $a_0 \geq \lambda$ , i.e. above the cut-off frequency, only. Their accuracy below the cut-off frequency ( $a_0 < \lambda$ ), i.e. for the evanescent waves, is not guaranteed. This is illustrated in Fig. 3.3.1 by comparing the continued fraction solution with the exact solution (Eq. (3.2.10)). The dynamic stiffness coefficient and the dimensionless frequency are normalized as expressed in Eq. (3.2.11). When the frequency is slightly above the cut-off frequency ( $a_0/\lambda > 1.25$ ), the order  $M_H = 2$  continued fraction solution is already very accurate. However, the error below the cut-off frequency is very large. The imaginary part exhibits a discontinuous point. The real part of the continued fraction solution is always equal to zero independent of the order as expected from Eq. (3.3.13). As the order of the continued fraction increases to  $M_H = 5$  and  $M_H = 11$ , the accuracy of the results at frequencies immediately above the cut-off frequency improves. The result of  $M_H = 11$  is indistinguishable from the exact solution above the cut-off frequency. Below the cut-off frequency, the number of discontinuous points in the imaginary part increases and the accuracy does not improve. The error at the low-frequency range affects the accuracy of late-time response in the time domain as illustrated numerically in Section 3.5.1.

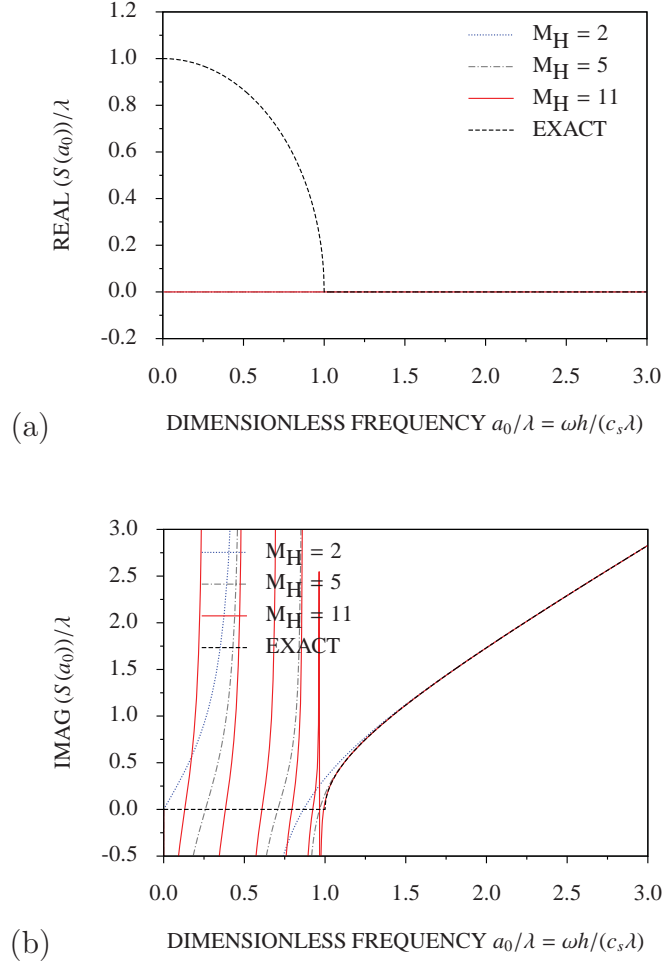


Figure 3.3.1: High-frequency continued fraction solution for dynamic stiffness coefficient of semi-infinite layer: (a) real part and (b) imaginary part

A reflection coefficient based on the angle of incidence of propagating plane waves is often derived in the literature to evaluate the performance of an absorbing boundary. It is meaningful for only  $0 \leq \sin \theta \leq 1$ , i.e., the frequency range  $a_0 \geq \lambda$ . As the order increases, the reflection coefficient becomes smaller but the accuracy below the cut-off frequency does not necessarily improve. This is consistent with the statement in Hagstrom *et al.* (2008) that: “a comparison of boundary conditions based solely on the magnitude of reflection coefficients for propagating modes is a poor predictor of actual performance, particularly as the order is increased”.

### 3.3.1.3 Doubly asymptotic continued fraction

The procedure in Section 3.3.1.1 leads to not only a high-frequency continued fraction solution for the dynamic stiffness coefficient but also an equation of the residual term  $Y^{(M_H+1)}(a_0)$ , i.e. the  $i = M_H + 1$  case of Eq. (3.3.5) with the constant  $b_1^{(M_H+1)}$

given in Eq. (3.3.11). To determine a solution that is valid over the whole frequency range, a low-frequency continued fraction solution for the residual term  $Y^{(M_H+1)}(a_0)$  is sought.

Denoting the residual term as

$$Y_L(a_0) = Y^{(M_H+1)}(a_0) \quad (3.3.18)$$

the  $i = M_H + 1$  case of Eq. (3.3.5) is expressed as

$$\lambda^2 - 2b_L(ia_0)Y_L(a_0) - (Y_L(a_0))^2 = 0 \quad (3.3.19)$$

with the constant

$$b_L = b_1^{(M_H+1)} = (-1)^{M_H} \quad (3.3.20)$$

given in Eq. (3.3.11). The continued fraction solution for  $Y_L(a_0)$  at the low-frequency limit is written as

$$Y_L(a_0) = Y_{L0}^{(0)} + (ia_0)Y_{L1}^{(0)} - \frac{(ia_0)^2}{Y_{L0}^{(1)} - \frac{(ia_0)^2}{Y_{L0}^{(2)} - \frac{(ia_0)^2}{\dots - \frac{(ia_0)^2}{Y_{L0}^{(M_L)}}}}} \quad (3.3.21)$$

It is equivalent to

$$Y_L(a_0) = Y_{L0}^{(0)} + (ia_0)Y_{L1}^{(0)} - (ia_0)^2(Y_L^{(1)}(a_0))^{-1} \quad (3.3.22a)$$

$$Y_L^{(i)}(a_0) = Y_{L0}^{(i)} - (ia_0)^2(Y_L^{(i+1)}(a_0))^{-1} \quad (i = 1, 2, \dots, M_L) \quad (3.3.22b)$$

where the constant term in Eq. (3.3.22b) is omitted as its solution is equal to zero. For an  $M_L$  order continued fraction, the residual  $(ia_0)^2/Y_L^{(i+1)}(a_0)$  is neglected. The constants  $Y_{L0}^{(i)}$  ( $i = 1, 2, \dots, M_L$ ) and  $Y_{L1}^{(0)}$  are determined by satisfying Eq. (3.3.19) at the low frequency limit ( $a_0 \rightarrow 0$ ).

Substituting Eq. (3.3.22a) into Eq. (3.3.19) leads to an equation in terms of a power series of  $(ia_0)$

$$\begin{aligned} & \left( \lambda^2 - (Y_{L0}^{(0)})^2 \right) - (ia_0) \left( 2b_L Y_{L0}^{(0)} + 2Y_{L0}^{(0)} Y_{L1}^{(0)} \right) + (ia_0)^2 \left( -2b_L Y_{L1}^{(0)} - (Y_{L1}^{(0)})^2 \right. \\ & \left. + 2(Y_{L0}^{(0)} + (ia_0)(Y_{L1}^{(0)} + b_L))(Y_L^{(1)}(a_0))^{-1} - (ia_0)^2(Y_L^{(1)}(a_0))^{-2} \right) = 0 \end{aligned} \quad (3.3.23)$$

As the low-frequency solution is being sought, Eq. (3.3.23) is satisfied by setting the coefficients of the power series to zero in ascending order. Setting the constant term to zero results in

$$\lambda^2 - (Y_{L0}^{(0)})^2 = 0 \quad (3.3.24)$$

Out of the two solutions, the one leading to the correct static stiffness  $S(a_0 = 0) = \lambda$  should be chosen. Inspecting Eq. (3.3.1) with  $Y^{(M_H+1)}(a_0 = 0) = Y_L(a_0 = 0) = Y_{L0}^{(0)}$  (Eqs. (3.3.18) and (3.3.22a)), the solution is

$$Y_{L0}^{(0)} = (-1)^{M_H+1} \lambda \quad (3.3.25)$$

Setting the coefficient of the  $(ia_0)$  term in Eq. (3.3.23) to zero leads to an equation for  $Y_{L1}^{(0)}$ . Using Eq. (3.3.20), its solution is expressed as

$$Y_{L1}^{(0)} = -b_L = (-1)^{M_H+1} \quad (3.3.26)$$

Setting the coefficient of the  $(ia_0)^2$  term in Eq. (3.3.23) to zero yields an equation of  $Y_L^{(1)}(a_0)$ . After substituting the solutions for  $Y_{L0}^{(0)}$  (Eq. (3.3.25)) and  $Y_{L1}^{(0)}$  (Eq. (3.3.26)), the equation is expressed as the  $i = 1$  case of the following equation:

$$(ia_0)^2 - 2b_L^{(i)} Y_L^{(i)}(a_0) - (Y_L^{(i)}(a_0))^2 = 0 \quad (3.3.27)$$

with the constant (Eq. (3.3.20))

$$b_L^{(1)} = -b_L \lambda = (-1)^{M_H+1} \lambda \quad (3.3.28)$$

A recursive procedure for determining the constants  $Y_{L0}^{(i)}$  in Eq. (3.3.22b) is established by substituting Eq. (3.3.22b) into Eq. (3.3.27). The resulting expression is arranged as

$$\begin{aligned} - \left( 2b_L^{(i)} Y_{L0}^{(i)} + (Y_{L0}^{(i)})^2 \right) + (ia_0)^2 \left( 1 + 2(b_L^{(i)} + Y_{L0}^{(i)}) (Y_L^{(i+1)}(a_0))^{-1} \right. \\ \left. - (ia_0)^2 (Y_L^{(i+1)}(a_0))^{-2} \right) = 0 \end{aligned} \quad (3.3.29)$$

Setting the term independent of  $(ia_0)$  to zero yields an equation for  $Y_{L0}^{(i)}$ . Its non-zero solution is

$$Y_{L0}^{(i)} = -2b_L^{(i)} \quad (3.3.30)$$

Setting the  $(ia_0)^2$  term to zero and using Eq. (3.3.30) result in the equation of  $Y_L^{(i+1)}(a_0)$

$$(ia_0)^2 + 2b_L^{(i)}Y_L^{(i+1)}(a_0) - (Y_L^{(i+1)}(a_0))^2 = 0 \quad (3.3.31)$$

It is simply the  $(i + 1)$  case of Eq. (3.3.27) with the constant

$$b_L^{(i+1)} = -b_L^{(i)} \quad (3.3.32)$$

Equations (3.3.28) and (3.3.32) lead to

$$b_L^{(i)} = (-1)^{M_H+i} \lambda \quad i = 1, 2, \dots M_L \quad (3.3.33)$$

The constants of the continued fraction are expressed explicitly as

$$Y_{L0}^{(i)} = (-1)^{M_H+i+1} 2\lambda \quad i = 1, 2, \dots M_L \quad (3.3.34)$$

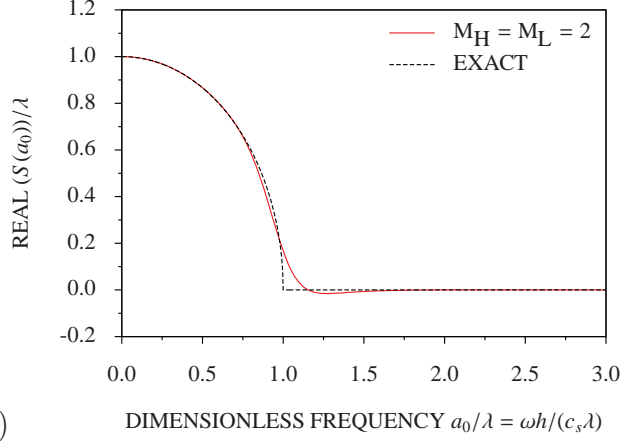
As an example, the order  $M_L = 2$  low-frequency continued fraction for the residual  $Y^{(3)}(a_0)$  of the order  $M_H = 2$  high-frequency continued fraction solution is expressed as

$$Y^{(3)}(a_0) = Y_L(a_0) = -\lambda - (ia_0) - \frac{(ia_0)^2}{2\lambda - \frac{(ia_0)^2}{-2\lambda}} \quad (3.3.35)$$

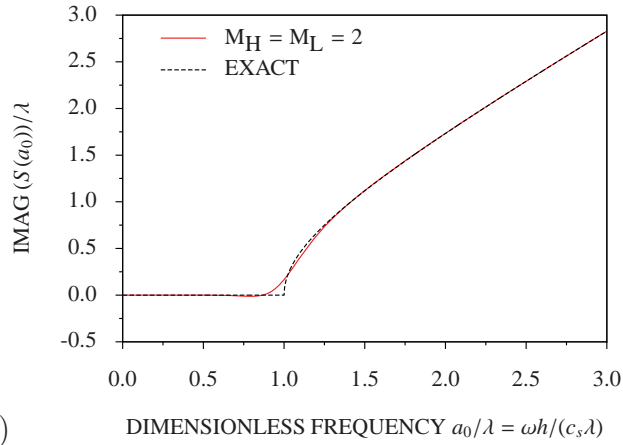
The doubly asymptotic continued fraction solution is constructed by combining the high-frequency continued fraction solution in Eq. (3.3.1) (or Eq. (3.3.2)) with the low-frequency solution in Eq. (3.3.21) (or Eq. (3.3.22)) using  $Y^{(M_H+1)}(a_0) = Y_L(a_0)$  (Eq. (3.3.18)). For example, the order  $M_H = M_L = 2$  doubly asymptotic continued fraction solution is obtained from Eqs. (3.3.13) and (3.3.35) as

$$S(a_0) = (ia_0) - \frac{\lambda^2}{-2(ia_0) - \frac{\lambda^2}{2(ia_0) - \frac{\lambda^2}{-\lambda - (ia_0) - \frac{(ia_0)^2}{2\lambda - \frac{(ia_0)^2}{-2\lambda}}}}} \quad (3.3.36)$$

The real and imaginary parts of the order  $M_H = M_L = 2$  doubly asymptotic solution are compared with the exact solution in Fig. 3.3.2. The present result is very accurate outside of a small range around the cut-off frequency.



(a)



(b)

Figure 3.3.2: Doubly asymptotic continued fraction solution for dynamic stiffness coefficient of semi-infinite layer with  $M_H = M_L = 2$ : (a) real part and (b) imaginary part

Further evaluation of the accuracy of the doubly asymptotic solution is reported in Section 3.5.1.

### 3.3.2 Circular cavity embedded in full-plane

#### 3.3.2.1 High-frequency continued fraction

Like the continued fraction solution in Eq. (3.3.2) for the semi-infinite layer, the high-frequency continued fraction is expressed as

$$S(a_0) = K_\infty + (ia_0)C_\infty - (Y^{(1)}(a_0))^{-1} \quad (3.3.37a)$$

$$Y^{(i)}(a_0) = Y_0^{(i)} + (ia_0)Y_1^{(i)} - (Y^{(i+1)}(a_0))^{-1} \quad (i = 1, 2, \dots, M_H) \quad (3.3.37b)$$

where  $C_\infty$  is the damping coefficient,  $K_\infty$  the spring coefficient and  $(Y^{(1)}(a_0))^{-1}$  the residual term. Substituting Eq. (3.3.37a) into Eq. (3.2.31) yields an equation in

terms of a power series of  $(ia_0)$ ,

$$(ia_0)^2(C_\infty^2 - 1) + (ia_0)(2C_\infty K_\infty - C_\infty) + (K_\infty^2 - \lambda^2 - 2((ia_0)C_\infty + K_\infty)(Y^{(1)}(a_0))^{-1} + (Y^{(1)}(a_0))^{-2} - a_0(Y^{(1)}(a_0))^{-2}Y^{(1)}(a_0)_{,a_0}) = 0 \quad (3.3.38)$$

This equation is satisfied by setting each term to zero in descending order of  $(ia_0)$ . The  $(ia_0)^2$  term leads to an equation of  $C_\infty$ . Its positive solution (satisfying the radiation condition) is equal to

$$C_\infty = 1 \quad (3.3.39)$$

The  $(ia_0)$  term leads to an equation of  $K_\infty$ . By using Eq. (3.3.39), its solution is expressed as

$$K_\infty = 0.5 \quad (3.3.40)$$

The remaining term is an equation of  $Y^{(1)}(a_0)$  representing the residual

$$K_\infty^2 - \lambda^2 - 2((ia_0)C_\infty + K_\infty)(Y^{(1)}(a_0))^{-1} + (Y^{(1)}(a_0))^{-2} - a_0(Y^{(1)}(a_0))^{-2}Y^{(1)}(a_0)_{,a_0} = 0 \quad (3.3.41)$$

Equation (3.3.41) is simplified by multiplying it with  $(Y^{(1)}(a_0))^2$  and using the solutions of  $C_\infty$  (Eq. (3.3.39)) and  $K_\infty$  (Eq. (3.3.40)). To construct a recursive procedure, the resulting equation is expressed as the  $i = 1$  case of

$$a^{(i)} - 2(b_0^{(i)} + (ia_0))Y^{(i)}(a_0) + c^{(i)}(Y^{(i)}(a_0))^2 - a_0(Y^{(i)}(a_0))_{,a_0} = 0 \quad (3.3.42)$$

with the coefficients defined as

$$a^{(1)} = 1 \quad (3.3.43a)$$

$$b_0^{(1)} = 0.5 \quad (3.3.43b)$$

$$c^{(1)} = 0.25 - \lambda^2 \quad (3.3.43c)$$

A recursive equation for determining the remaining constants in the continued fraction solution is obtained by substituting Eq. (3.3.37b) into Eq. (3.3.42)

$$\begin{aligned}
& (ia_0)^2 \left( -2Y_1^{(i)} + c^{(i)}(Y_1^{(i)})^2 \right) + (ia_0) \left( -2Y_0^{(i)} - 2b_0^{(i)}Y_1^{(i)} + 2c^{(i)}Y_0^{(i)}Y_1^{(i)} - Y_1^{(i)} \right) \\
& + \left( a^{(i)} - 2b_0^{(i)}Y_0^{(i)} + c^{(i)}(Y_0^{(i)})^2 + (-2c^{(i)}(Y_0^{(i)} + (ia_0)Y_1^{(i)}) \right. \\
& \quad \left. + 2((ia_0) + b_0^{(i)}))(Y^{(i+1)}(a_0))^{-1} + c^{(i)}(Y^{(i+1)}(a_0))^{-2} \right. \\
& \quad \left. - (Y^{(i+1)}(a_0))^{-2}a_0(Y^{(i+1)}(a_0))_{,a_0} \right) = 0 \quad (3.3.44)
\end{aligned}$$

This series equation in terms of  $(ia_0)$  is satisfied by setting the individual terms to zero in descending order of  $(ia_0)$ . The  $(ia_0)^2$  term leads to an equation of  $Y_1^{(i)}$ . Its non-zero solution is equal to

$$Y_1^{(i)} = 2/c^{(i)} \quad (3.3.45)$$

Setting the  $(ia_0)$  term in Eq. (3.3.44) to zero yields an equation of  $Y_0^{(i)}$ . By using Eq. (3.3.45), its solution is obtained as

$$Y_0^{(i)} = (2b_0^{(i)} + 1)/c^{(i)} \quad (3.3.46)$$

The remaining term is written as

$$\begin{aligned}
& a^{(i)} + Y_0^{(i)} - 2(c^{(i)}Y_0^{(i)} - b_0^{(i)} + (ia_0)(c^{(i)}Y_1^{(i)} - 1))(Y^{(i+1)}(a_0))^{-1} \\
& + c^{(i)}(Y^{(i+1)}(a_0))^{-2} - (Y^{(i+1)}(a_0))^{-2}a_0(Y^{(i+1)}(a_0))_{,a_0} = 0 \quad (3.3.47)
\end{aligned}$$

Using Eqs. (3.3.45) and (3.3.46), Eq. (3.3.47) is rewritten as an equation of  $Y^{(i+1)}(a_0)$ ,

$$\begin{aligned}
& c^{(i)} - 2(b_0^{(i)} + 1 + (ia_0))Y^{(i+1)}(a_0) + (a^{(i)} + Y_0^{(i)})(Y^{(i+1)}(a_0))^2 \\
& - a_0(Y^{(i+1)}(a_0))_{,a_0} = 0 \quad (3.3.48)
\end{aligned}$$

Introducing the recursive formula for the following coefficients:

$$a^{(i+1)} = c^{(i)} \quad (3.3.49a)$$

$$b_0^{(i+1)} = b_0^{(i)} + 1 \quad (3.3.49b)$$

$$c^{(i+1)} = a^{(i)} + Y_0^{(i)} \quad (3.3.49c)$$

Equation (3.3.48) is formulated as the  $i + 1$  case of Eq. (3.3.42). The constants  $Y_1^{(i)}$  and  $Y_0^{(i)}$  ( $i = 1, 2, \dots, M_H$ ) of the singly asymptotic continued fraction solution

are thus determined recursively. By combining Eqs. (3.3.43b) and (3.3.49b), the constant  $b_0^{(i)}$  can be expressed explicitly as

$$b_0^{(i)} = i - 0.5 \quad (3.3.50)$$

For later use, the following identity is derived from Eqs. (3.3.49), (3.3.46) and (3.3.43)

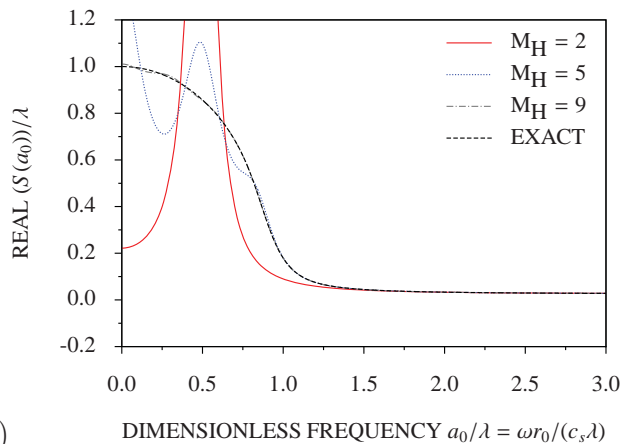
$$(b_0^{(i+1)})^2 - a^{(i+1)}c^{(i+1)} = (b_0^{(i)} + 1)^2 - c^{(i)}a^{(i)} - c^{(i)}Y_0^{(i)} = (b_0^{(i)})^2 - a^{(i)}c^{(i)} = \lambda^2 \quad (3.3.51)$$

As an example, the constants of the order  $M_H = 2$  continued fraction solution are evaluated

$$Y_0^{(1)} = \frac{8}{1 - 4\lambda^2}; \quad Y_1^{(1)} = \frac{8}{1 - 4\lambda^2} \quad (3.3.52a)$$

$$Y_0^{(2)} = \frac{4 - 16\lambda^2}{9 - 4\lambda^2}; \quad Y_1^{(2)} = \frac{2 - 8\lambda^2}{9 - 4\lambda^2} \quad (3.3.52b)$$

Together with the constants  $C_\infty$  and  $K_\infty$  given in Eqs. (3.3.39) and (3.3.40), the singly asymptotic solution is obtained after neglecting  $(Y^{(3)}(a_0))^{-1}$ . The normalized dynamic stiffness coefficient  $S(a_0)/\lambda$  of mode  $\lambda = 20$  is plotted as a function of the dimensionless frequency  $a_0/\lambda$  in Fig. 3.3.3. Although it is highly accurate at high frequencies ( $a_0/\lambda > 1.25$ ), the error increases as the frequency becomes lower. Below the frequency  $a_0/\lambda < 1$ , very large error exists. Unlike the case of the semi-infinite layer, the singly asymptotic solution converges to the exact solution over the whole range of frequency. As shown in Fig. 3.3.3, an accurate result is obtained at the order  $M_H = 9$ . The rate of convergence close to  $a_0 = 0$  is much slower than that at the high-frequency range. As it will be demonstrated in Section 3.5.2, the rate of convergence deteriorates as the modal eigenvalue increases.



(a)

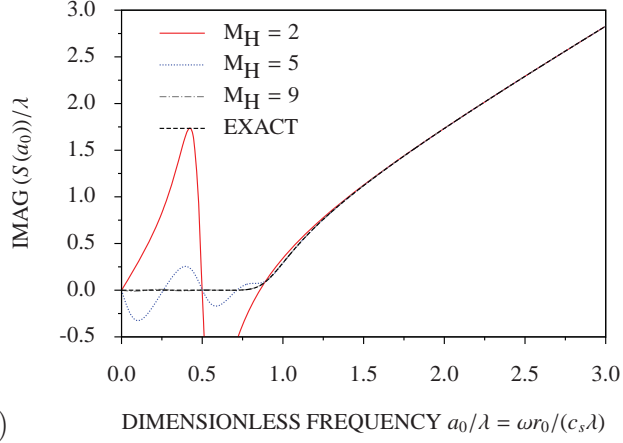


Figure 3.3.3: High-frequency continued fraction solution for dynamic stiffness coefficient of circular cavity ( $\lambda = 20$ ): (a) real part and (b) imaginary part

### 3.3.2.2 Doubly asymptotic continued fraction

$Y^{(M_H+1)}(a_0)$  represents the residual of the order  $M_H$  high-frequency continued fraction. It satisfies Eq. (3.3.48) with  $i = M_H$  and the coefficients in Eq (3.3.49). To facilitate the derivation of the low-frequency continued fraction solution, Eq. (3.3.48) is rewritten as

$$a_L - 2(b_{L0} + (ia_0))Y_L(a_0) + c_L(Y_L(a_0))^2 - a_0(Y_L(a_0))_{,a_0} = 0 \quad (3.3.53)$$

where the function is

$$Y_L(a_0) = Y^{(M_H+1)}(a_0) \quad (3.3.54)$$

and the constants are

$$a_L = a^{(M_H+1)} \quad (3.3.55a)$$

$$b_{L0} = b_0^{(M_H+1)} = M_H + 0.5 \quad (3.3.55b)$$

$$c_L = c^{(M_H+1)} \quad (3.3.55c)$$

The continued fraction solution at low frequencies is expressed as

$$Y_L(a_0) = Y_{L0}^{(0)} + (ia_0)Y_{L1}^{(0)} - (ia_0)^2(Y_L^{(1)}(a_0))^{-1} \quad (3.3.56a)$$

$$Y_L^{(i)}(a_0) = Y_{L0}^{(i)} + (ia_0)Y_{L1}^{(i)} - (ia_0)^2(Y_L^{(i+1)}(a_0))^{-1} \quad (i = 1, 2, \dots, M_L) \quad (3.3.56b)$$

Substituting Eq. (3.3.56a) into Eq. (3.3.53) yields an equation in terms of a power series of  $(ia_0)$

$$\begin{aligned} & \left( a_L - 2b_{L0}Y_{L0}^{(0)} + c_L(Y_{L0}^{(0)})^2 \right) + (ia_0) \left( -2Y_{L0}^{(0)} - 2b_{L0}Y_{L1}^{(0)} + 2c_L Y_{L0}^{(0)} Y_{L1}^{(0)} - Y_{L1}^{(0)} \right) \\ & + (ia_0)^2 \left( -2Y_{L1}^{(0)} + c_L(Y_{L1}^{(0)})^2 + (2(b_{L0} + ia_0)) - 2c_L(Y_{L0}^{(0)} + (ia_0)Y_{L1}^{(0)}) \right) \\ & \quad \times (Y_L^{(1)}(a_0))^{-1} + 2(Y_L^{(1)}(a_0))^{-1} + (ia_0)^2 c_L (Y_L^{(1)}(a_0))^{-2} \\ & \quad \quad \quad - (Y_L^{(1)}(a_0))^{-2} a_0 (Y_L^{(1)}(a_0))_{,a_0} \Big) = 0 \quad (3.3.57) \end{aligned}$$

It is satisfied by setting the terms to zero in ascending order of  $(ia_0)$ . The constant term yields

$$a_L - 2b_{L0}Y_{L0}^{(0)} + c_L(Y_{L0}^{(0)})^2 = 0 \quad (3.3.58)$$

By using Eqs. (3.3.51) and (3.3.55), the determinant of this quadratic algebraic equation is equal to

$$(2b_{L0})^2 - 4a_L c_L = 4\lambda^2 \quad (3.3.59)$$

The solution for  $Y_{L0}^{(0)}$  is expressed as

$$Y_{L0}^{(0)} = (b_{L0} + \lambda)/c_L = (M_H + 0.5 + \lambda)/c_L \quad (3.3.60)$$

Setting the  $(ia_0)$  term of Eq. (3.3.57) to zero leads to an equation of  $Y_{L1}^{(0)}$ . By using Eq. (3.3.60), its solution is equal to

$$Y_{L1}^{(0)} = 2Y_{L0}^{(0)}/(2\lambda - 1) \quad (3.3.61)$$

Setting the remaining term of Eq. (3.3.57) to zero results in an equation of  $Y_L^{(1)}(a_0)$ . It is denoted as the  $i = 1$  case of

$$(ia_0)^2 a_L^{(i)} - 2(b_{L0}^{(i)} + b_{L1}^{(i)}(ia_0))Y_L^{(i)}(a_0) + c_L^{(i)}(Y_L^{(i)}(a_0))^2 - a_0(Y_L^{(i)}(a_0))_{,a_0} = 0 \quad (3.3.62)$$

where the following constants are defined and simplified using Eqs. (3.3.60) and (3.3.61) as:

$$a_L^{(1)} = c_L \quad (3.3.63a)$$

$$b_{L0}^{(1)} = -1 - b_{L0} + c_L Y_{L0}^{(0)} = -1 + \lambda \quad (3.3.63b)$$

$$b_{L1}^{(1)} = -1 + c_L Y_{L1}^{(0)} = 2(M_H + 1)/(2\lambda - 1) \quad (3.3.63c)$$

$$c_L^{(1)} = -2Y_{L1}^{(0)} + c_L (Y_{L1}^{(0)})^2 \quad (3.3.63d)$$

Substituting Eq. (3.3.56b) into Eq. (3.3.62) results in an equation in terms of a power series of  $(ia_0)$

$$\begin{aligned} & \left( -2b_{L0}^{(i)} Y_{L0}^{(i)} + c_L^{(i)} (Y_{L0}^{(i)})^2 \right) + (ia_0) \left( -2(b_{L1}^{(i)} Y_{L0}^{(i)} + b_{L0}^{(i)} Y_{L1}^{(i)}) + 2c_L^{(i)} Y_{L0}^{(i)} Y_{L1}^{(i)} - Y_{L1}^{(i)} \right) \\ & + (ia_0)^2 \left( a_L^{(i)} - 2b_{L1}^{(i)} Y_{L1}^{(i)} + c_L^{(i)} (Y_{L1}^{(i)})^2 - 2(-1 - b_{L0}^{(i)} + c_L^{(i)} Y_{L0}^{(i)}) \right. \\ & + (ia_0)(-b_{L1}^{(i)} + c_L^{(i)} Y_{L1}^{(i)}) (Y_L^{(i+1)}(a_0))^{-1} + (ia_0)^2 c_L^{(i)} (Y_L^{(i+1)}(a_0))^{-2} \\ & \left. - (Y_L^{(i+1)}(a_0))^{-2} a_0 (Y_L^{(i+1)}(a_0))_{,a_0} \right) = 0 \quad (3.3.64) \end{aligned}$$

Setting the individual terms to zero in ascending order of  $(ia_0)$  leads to the equations of  $Y_{L0}^{(i)}$ ,  $Y_{L1}^{(i)}$  and  $Y_L^{(i+1)}(a_0)$ , respectively. The constant term independent of  $(ia_0)$  yields an equation of  $Y_{L0}^{(i)}$ . Its non-zero solution is equal to

$$Y_{L0}^{(i)} = 2b_{L0}^{(i)}/c_L^{(i)} \quad (3.3.65)$$

The  $(ia_0)$  term is an equation for  $Y_{L1}^{(i)}$ . By using Eq. (3.3.65), its solution is expressed as

$$Y_{L1}^{(i)} = 2b_{L1}^{(i)} Y_{L0}^{(i)} / (-1 + 2b_{L0}^{(i)}) \quad (3.3.66)$$

The last term of Eq. (3.3.64) results in an equation of  $Y_L^{(i+1)}(a_0)$

$$\begin{aligned} & (ia_0)^2 c_L^{(i)} - 2(-1 - b_{L0}^{(i)} + c_L^{(i)} Y_{L0}^{(i)}) + (ia_0)(-b_{L1}^{(i)} + c_L^{(i)} Y_{L1}^{(i)}) Y_L^{(i+1)}(a_0) \\ & + (a_L^{(i)} - 2b_{L1}^{(i)} Y_{L1}^{(i)} + c_L^{(i)} (Y_{L1}^{(i)})^2) (Y_L^{(i+1)}(a_0))^2 - a_0 (Y_L^{(i+1)}(a_0))_{,a_0} = 0 \quad (3.3.67) \end{aligned}$$

Introducing the recursive equations

$$a_L^{(i+1)} = c_L^{(i)} \quad (3.3.68a)$$

$$b_{L0}^{(i+1)} = -1 - b_{L0}^{(i)} + c_L^{(i)} Y_{L0}^{(i)} = -1 + b_{L0}^{(i)} \quad (3.3.68b)$$

$$b_{L1}^{(i+1)} = -b_{L1}^{(i)} + c_L^{(i)} Y_{L1}^{(i)} \quad (3.3.68c)$$

$$c_L^{(i+1)} = a_L^{(i)} - 2b_{L1}^{(i)} Y_{L1}^{(i)} + c_L^{(i)} (Y_{L1}^{(i)})^2 \quad (3.3.68d)$$

with the expression of  $b_{L0}^{(i+1)}$  simplified by using Eq. (3.3.65), Eq. (3.3.67) is expressed as the  $(i + 1)$  case of Eq. (3.3.62). With the combination of Eqs. (3.3.63b) and (3.3.68b), the constant  $b_{L0}^{(i)}$  is expressed as

$$b_{L0}^{(i)} = -i + \lambda \quad (3.3.69)$$

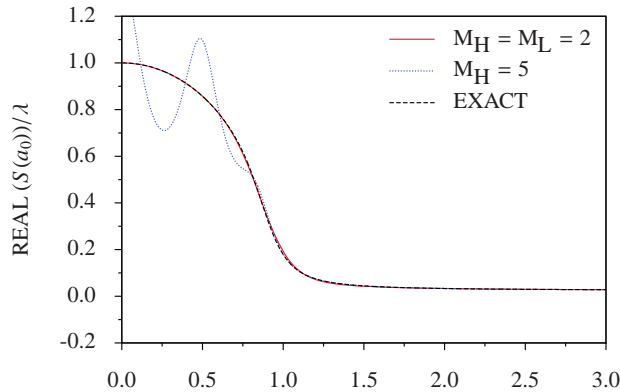
The doubly asymptotic solution can now be determined by combining the high-frequency continued fraction solution in Eq. (3.3.37) with the low-frequency continued fraction solution in Eq. (3.3.56) using  $Y^{(M_H+1)}(a_0) = Y_L(a_0)$  (Eq. (3.3.54)). As an example, the low-frequency continued fraction is determined for the residual term of the  $M_H = 2$  high-frequency continued fraction. The result of order  $M_L = 2$  is

$$Y_{L0}^{(0)} = \frac{18 - 8\lambda^2}{8\lambda^3 - 20\lambda^2 - 2\lambda + 5}; \quad Y_{L1}^{(0)} = \frac{-4(4\lambda^2 - 9)}{(2\lambda - 1)^2(4\lambda^2 - 8\lambda - 5)} \quad (3.3.70a)$$

$$Y_{L0}^{(1)} = \frac{(\lambda - 1)(2\lambda - 1)^3(4\lambda^2 - 8\lambda - 5)}{2(8\lambda^3 - 28\lambda^2 - 18\lambda + 63)}; \quad Y_{L1}^{(1)} = \frac{6(\lambda - 1)(2\lambda - 5)(2\lambda - 1)^2(2\lambda + 1)}{(2\lambda - 3)^2(4\lambda^2 - 8\lambda - 21)} \quad (3.3.70b)$$

$$Y_{L0}^{(2)} = \frac{-8(\lambda - 2)(2\lambda - 7)(2\lambda - 3)^3}{(2\lambda - 1)^3(8\lambda^3 - 52\lambda^2 + 62\lambda + 45)}; \quad Y_{L1}^{(2)} = \frac{-96(\lambda - 2)(2\lambda - 7)(2\lambda - 3)^2}{(2\lambda - 5)^2(2\lambda - 1)^3(4\lambda^2 - 16\lambda - 9)} \quad (3.3.70c)$$

The result of the order  $M_H = M_L = 2$  doubly asymptotic solution for the mode  $\lambda = 20$  is plotted in Fig. 3.3.4. Compared with the order  $M_H = 5$  singly asymptotic solution, which has the same number of terms, the doubly asymptotic solution is much more accurate.



(a) DIMENSIONLESS FREQUENCY  $a_0/\lambda = \omega r_0/(c_s \lambda)$

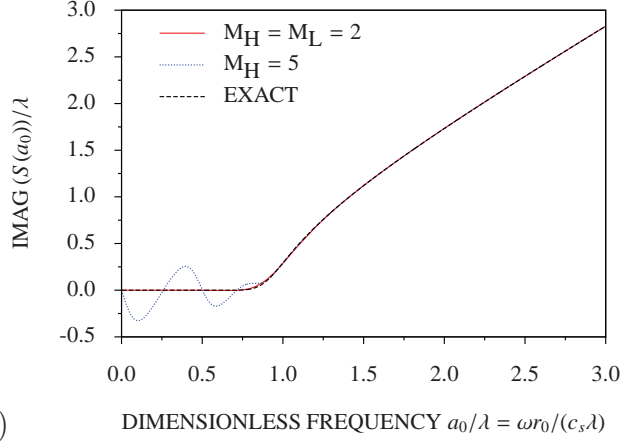


Figure 3.3.4: Dynamic stiffness coefficient of circular cavity ( $\lambda = 20$ ): (a) real part and (b) imaginary part

### 3.4 Doubly asymptotic open boundary condition

In the frequency domain, the open boundary condition is expressed as the force-displacement relationship (Eqs. (3.2.9) and (3.2.26))

$$\tilde{R} = S(a_0)\tilde{U} \quad (3.4.1)$$

When the dynamic stiffness coefficient  $S(a_0)$  is expressed as a continued fraction solution, the force-displacement relationship can be formulated in the time domain as a system of first-order ordinary differential equations with time-independent coefficient matrices, which represents a temporally local open boundary.

A doubly asymptotic continued fraction solution, which includes the expressions for the semi-infinite layer and circular cavity as special cases, is considered

$$S(a_0) = K_\infty + (ia_0)C_\infty - m^2(Y^{(1)}(a_0))^{-1} \quad (3.4.2a)$$

$$Y^{(i)}(a_0) = Y_0^{(i)} + (ia_0)Y_1^{(i)} - m^2(Y^{(i+1)}(a_0))^{-1} \quad (i = 1, 2, \dots, M_H) \quad (3.4.2b)$$

$$Y_L(a_0) = Y^{(M_H+1)}(a_0) \quad (3.4.2c)$$

$$Y_L(a_0) = Y_{L0} + (ia_0)Y_{L1} - (ia_0)^2(Y_L^{(1)}(a_0))^{-1} \quad (3.4.2d)$$

$$Y_L^{(i)}(a_0) = Y_{L0}^{(i)} + (ia_0)Y_{L1}^{(i)} - (ia_0)^2(Y_L^{(i+1)}(a_0))^{-1} \quad (i = 1, 2, \dots, M_L) \quad (3.4.2e)$$

with the dimensionless frequency

$$a_0 = \frac{\omega r_0}{c_s} \quad (3.4.3)$$

For the semi-infinite layer (Eqs. (3.3.2) and (3.3.22)),  $K_\infty = Y_0^{(i)} = Y_{L1}^{(i)} = 0$  and  $m = \lambda$  applies. The characteristic length  $r_0$  in Eq. (3.4.3) is replaced with the depth  $h$ . For the circular cavity (Eqs. (3.3.37) and (3.3.56)),  $m = 1$  applies. Substituting Eq. (3.4.2a) into the force-displacement relationship in Eq. (3.4.1) leads to

$$\tilde{R} = S(a_0)\tilde{U} = K_\infty\tilde{U} + (ia_0)C_\infty\tilde{U} - m\tilde{U}^{(1)} \quad (3.4.4)$$

where the auxiliary variable  $\tilde{U}^{(1)}$  is defined as

$$\tilde{U}^{(1)} = m(Y^{(1)}(a_0))^{-1}\tilde{U} \quad (3.4.5)$$

and then reformulated as

$$m\tilde{U} = Y^{(1)}(a_0)\tilde{U}^{(1)} \quad (3.4.6)$$

which is in the same form as the force-displacement relationship (Eq. (3.4.1)). Similarly, an auxiliary variable is introduced for each term of continued fraction in Eq. (3.4.2b)

$$m\tilde{U}^{(i)} = Y^{(i+1)}(a_0)\tilde{U}^{(i+1)} \quad (i = 0, 1, 2, \dots, M_H) \quad (3.4.7)$$

where Eq. (3.4.6) is included as the  $i = 0$  case with  $\tilde{U}^{(0)} = \tilde{U}$ . Multiplying Eq. (3.4.2b) by  $\tilde{U}^{(i)}$  and using the definition of auxiliary variables in Eq. (3.4.7) formulated with  $i$  and  $i - 1$  result in

$$m\tilde{U}^{(i-1)} = Y_0^{(i)}\tilde{U}^{(i)} + (ia_0)Y_1^{(i)}\tilde{U}^{(i)} - m\tilde{U}^{(i+1)} \quad (i = 1, 2, \dots, M_H) \quad (3.4.8)$$

The residual  $\tilde{U}^{(M_H+1)}$  of an order  $M_H$  high-frequency continued fraction solution is expressed in Eq. (3.4.7) at  $i = M_H$  as

$$m\tilde{U}^{(M_H)} = Y^{(M_H+1)}(a_0)\tilde{U}^{(M_H+1)} \quad (3.4.9)$$

$Y^{(M_H+1)}(a_0) = Y_L(a_0)$  (Eq. (3.4.2c)) is expressed in Eq. (3.4.2d) as a low-frequency continued fraction solution. Multiplying Eq. (3.4.2d) by  $\tilde{U}^{(M_H+1)}$  and using Eqs. (3.4.2c) and (3.4.9) lead to

$$m\tilde{U}^{(M_H)} = Y_{L0}\tilde{U}^{(M_H+1)} + (ia_0)Y_{L1}\tilde{U}^{(M_H+1)} - (ia_0)\tilde{U}_L^{(1)} \quad (3.4.10)$$

where the auxiliary variable  $\tilde{U}_L^{(1)}$  is defined in

$$(ia_0)\tilde{U}^{(M_H+1)} = Y_L^{(1)}(a_0)\tilde{U}_L^{(1)} \quad (3.4.11)$$

Again, an auxiliary variable is introduced for each term of the continued fraction in Eq. (3.4.2e) as

$$(ia_0)\tilde{U}_L^{(i)} = Y_L^{(i+1)}(a_0)\tilde{U}_L^{(i+1)} \quad (i = 0, 1, 2, \dots, M_L) \quad (3.4.12)$$

with  $\tilde{U}_L^{(0)} = \tilde{U}^{(M_H+1)}$ . Multiplying Eq. (3.4.2e) by  $\tilde{U}_L^{(i)}$  and using Eq. (3.4.12) with  $i - 1$  and  $i$  yield

$$(ia_0)\tilde{U}_L^{(i-1)} = Y_{L0}^{(i)}\tilde{U}_L^{(i)} + (ia_0)Y_{L1}^{(i)}\tilde{U}_L^{(i)} - (ia_0)\tilde{U}_L^{(i+1)} \quad (i = 1, 2, \dots, M_L) \quad (3.4.13)$$

For the order  $M_L$  low-frequency solution, the approximation  $\tilde{U}_L^{(M_L+1)} = 0$  is introduced.

Equations (3.4.4), (3.4.8), (3.4.10) and (3.4.13) are all combined to form a matrix equation

$$([K_h] + (i\omega)[C_h])\{Z\} = \{F\} \quad (3.4.14)$$

with

$$\{Z\} = [\tilde{U}, \tilde{U}^{(1)}, \dots, \tilde{U}^{(M_H)}, \tilde{U}^{(M_H+1)}, \tilde{U}_L^{(1)}, \dots, \tilde{U}_L^{(M_L)}]^T \quad (3.4.15a)$$

$$\{F\} = [\tilde{R}, 0, \dots, 0, 0, 0, \dots, 0]^T \quad (3.4.15b)$$



scheme) is employed for the time integration (see Section A.2 in Appendix A). The size of the time step is chosen as  $\Delta t = 0.01h/(\lambda c)$  for the semi-infinite layer and  $\Delta t = 0.01r_0/(\lambda c)$  for the circular cavity.

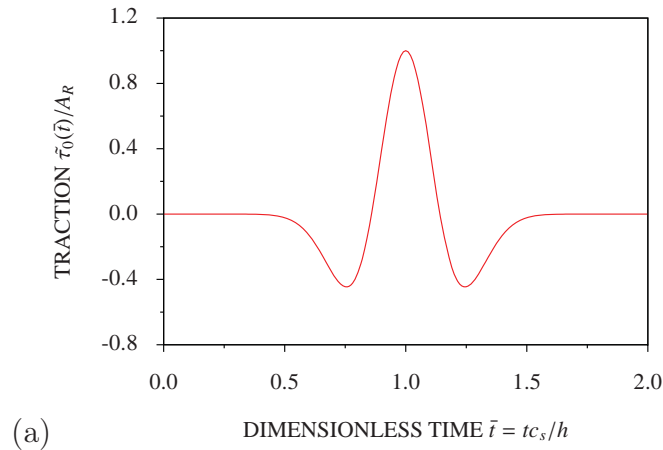
When the present doubly asymptotic open boundary is employed, the only two parameters for the users to select are the orders of high- and low-frequency continued fractions  $M_H$  and  $M_L$ . In this section, the same value is chosen for both parameters. With this simple, although not necessarily optimal, choice, the doubly asymptotic open boundaries perform much better than the singly asymptotic open boundaries with the same number of terms do.

The excitation by a unit impulse of traction  $\tilde{\tau}_{0I}(t) = \delta(t)$  is chosen to evaluate the accuracy of open boundaries as it covers the whole frequency range. When a unit impulse is applied, the initial condition is obtained by integrating Eq. (3.4.16) with the matrix  $[C_h]$  given in Eq. (3.4.15d) (Note that the first entry of  $\{f(t)\}$  and  $\{z(t)\}$  is  $\tilde{\tau}_{0I}(t)$  and  $\tilde{u}(t)$ , respectively.)

$$\tilde{u}(t = 0) = c/(r_0 C_\infty) \quad (3.5.1)$$

In the case of semi-infinite layer,  $r_0$  in Eq. (3.5.1) is replaced with the depth  $h$  of the layer.

To investigate the performance of the open boundary at a specified frequency range, the surface traction  $\tilde{\tau}_0(t)$  is prescribed as a Ricker wavelet with the parameters  $\bar{t}_s = ct_s/h = 1$ ,  $\bar{t}_0 = ct_0/h = 0.2$  and  $A_R = 10$ . The time history of the Ricker wavelet and its Fourier transform are given by Eqs. (A.1.1) and (A.1.2), respectively in Appendix A. The Ricker wavelet is plotted in Fig. 3.5.1(a). The amplitude of its Fourier transform is plotted in Fig. 3.5.1(b). The dominant dimensionless frequency of this wavelet is  $a_0 = 10$ .



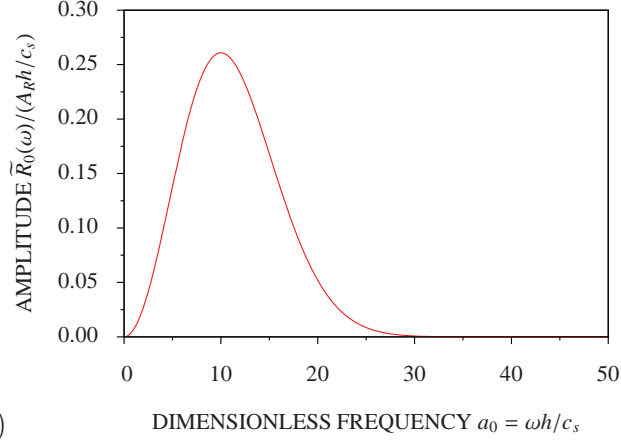


Figure 3.5.1: Prescribed traction as Ricker wavelet: (a) time history and (b) Fourier transform

### 3.5.1 Semi-infinite layer with constant depth

The case of a semi-infinite layer with a constant depth is a stringent test due to the existence of a cut-off frequency. Since the dynamic stiffness is not smooth at the cut-off frequency, this case is especially challenging for the doubly asymptotic continued fraction solution. At the cut-off frequency, the dynamic stiffness is equal to zero. As a result, waves around the cut-off frequency decay at a very slow rate (Eq. (3.2.14)). This requires that an absorbing boundary has to be accurate over a large time duration. The investigation of the semi-infinite layer is also significant because the construction of several higher-order absorbing boundaries is related to this case as shown in Section 3.3.1.2.

The performance of the singly asymptotic open boundary based solely on the high-frequency continued fraction solution is evaluated at first. The dynamic stiffness coefficient of the order  $M_H = 5$  continued fraction is plotted in Fig. 3.3.1. The cut-off frequency exists at  $a_0/\lambda = 1$ . The large error of the dynamic stiffness coefficient below the cut-off frequency ( $a_0/\lambda < 1$ ) indicates that the high-order singly asymptotic open boundary is unable to transmit evanescent waves. This is confirmed by the unit-impulse response of the  $M_H = 5$  open boundary plotted in Fig. 3.5.2. The early-time (high-frequency) response is very accurate. The response after the dimensionless time  $\lambda \bar{t} > 10$  suddenly exhibits a very large error and the amplitude of the error does not decay with time. Since this phenomenon is very similar to fictitious reflections caused by enforcing a simple (free or fixed) boundary condition at a certain distance, it is referred to as “fictitious reflections” in this thesis.

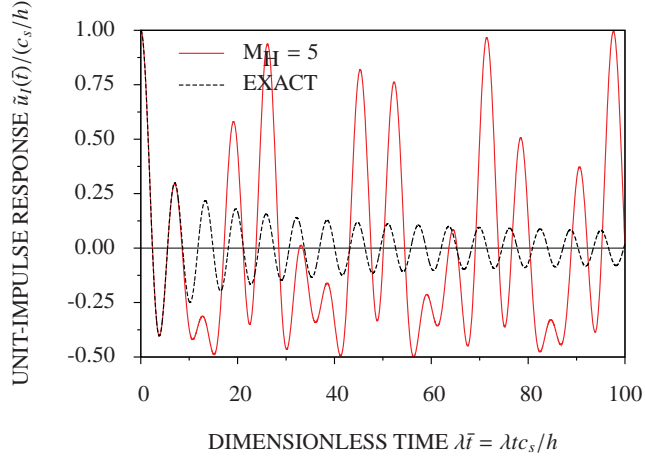
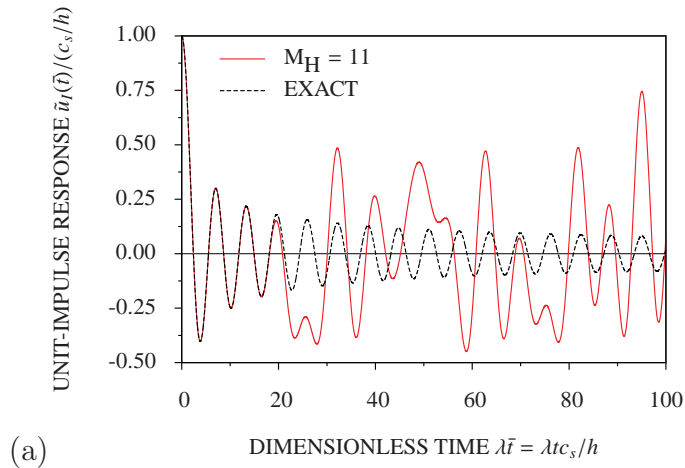


Figure 3.5.2: Unit-impulse response of semi-infinite layer by singly asymptotic open boundary  $M_H = 5$

The effect of the order of the singly asymptotic open boundary on its accuracy is also investigated by considering the orders  $M_H = 11$  and  $M_H = 99$ . The order  $M_H = 11$  continued fraction solution has 12 terms (double the number of terms of the  $M_H = 5$  solution). The order  $M_H = 99$  solution has 100 terms. The dynamic stiffness coefficients of both open boundaries are indistinguishable from the exact solution above the cut-off frequency as shown in Fig. 3.3.1 for the  $M_H = 11$  solution (The dynamic stiffness coefficient of the  $M_H = 99$  open boundary is not plotted). The unit-impulse responses of both open boundaries are shown in Fig. 3.5.3. As the order increases, the accuracy improves. However, significant “fictitious reflections” still occur, albeit at later time, even at order  $M_H = 99$ . As the amplitude of the “fictitious reflections” does not decay with time, the singly asymptotic open boundary is unsuitable for the analysis of long-time response.



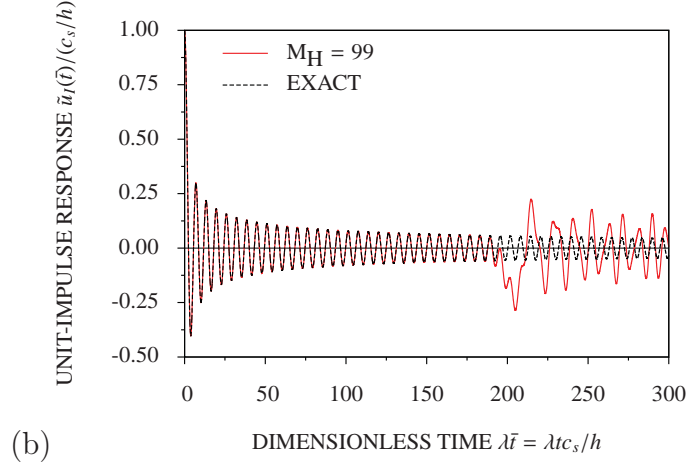


Figure 3.5.3: Unit-impulse response of semi-infinite layer by singly asymptotic open boundary: (a)  $M_H = 11$  and (b)  $M_H = 99$

The defect of the singly asymptotic open boundary in representing low-frequency responses can be mended by employing the doubly asymptotic continued fraction solution in Section 3.3.1.3. The corresponding higher-order doubly asymptotic open boundary is constructed in Section 3.4. For the  $M_H = M_L = 2$  doubly asymptotic open boundary, whose dynamic stiffness coefficient is shown in Fig. 3.3.2, the unit-impulse response is plotted in Fig. 3.5.4. It decays gradually and no “fictitious reflection” appears. It is observed by comparing Fig. 3.5.4 with Fig. 3.5.2 that the  $M_H = M_L = 2$  open boundary is much more accurate than the  $M_H = 5$  open boundary after  $\lambda \bar{t} > 10$ , although the number of equations of both formulations is equal to 5.

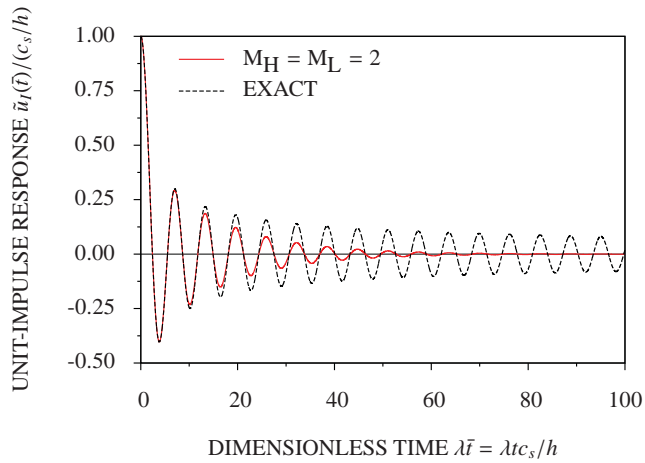


Figure 3.5.4: Unit-impulse response of semi-infinite layer by doubly asymptotic open boundary with  $M_H = M_L = 2$

The accuracy of the doubly asymptotic open boundary improves rapidly as its order increases. This is demonstrated by using the order  $M_H = M_L = 5$  open

boundary. Its dynamic stiffness coefficient is plotted in Fig. 3.5.5. It is indistinguishable from the exact solution except for the slight difference close to the cut-off frequency. The unit-impulse response is shown in Fig. 3.5.6. Good agreement with the exact solution is observed for about the first 10 periods. Compared with the unit-impulse response of the  $M_H = 11$  open boundary, which has the same number of variables, in Fig. 3.5.3(a), the doubly asymptotic open boundary is significantly more accurate at late time. No “fictitious reflection” occurs.

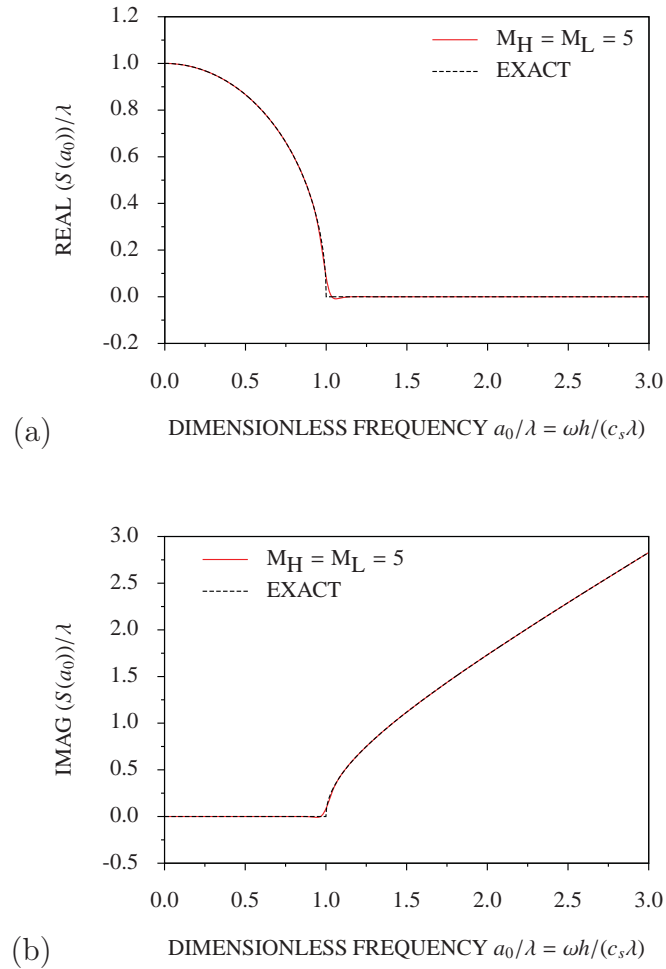


Figure 3.5.5: Doubly asymptotic continued fraction solution for dynamic stiffness coefficient of semi-infinite layer with  $M_H = M_L = 5$ : (a) real part and (b) imaginary part

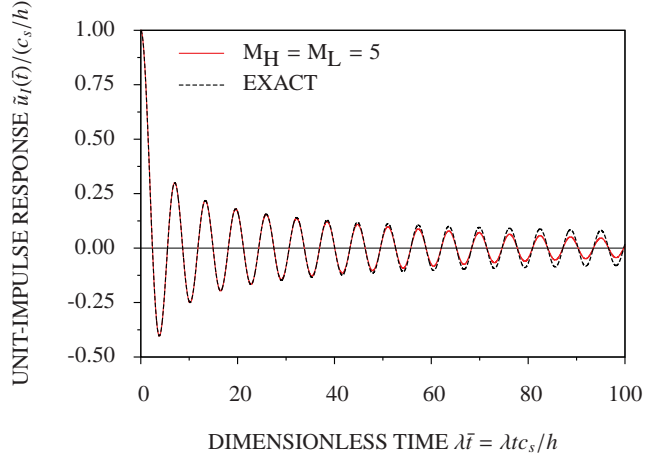
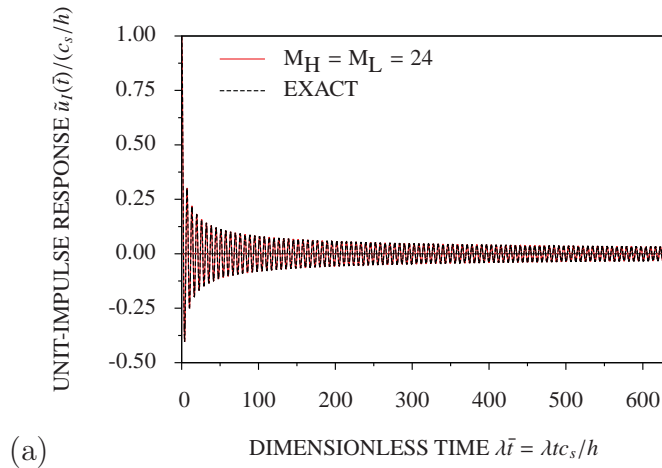


Figure 3.5.6: Unit-impulse response of semi-infinite layer by doubly asymptotic open boundary with  $M_H = M_L = 5$

To further investigate the convergence of the doubly asymptotic open boundary, a long-time analysis, with a duration of  $\lambda t c/h = 200\pi$ , of the unit-impulse response is performed. As the period of the asymptotic solution of the unit-impulse response is  $\lambda t c/h = 2\pi$ , this duration corresponds to 100 periods of vibration. The amplitude of the unit-impulse response decays from 1 at  $t = 0$  to about 0.032. The result of the  $M_H = M_L = 24$  open boundary is plotted in Fig. 3.5.7(a). The unit-impulse response decays gradually and no “fictitious reflections” occur. The numerical result is indistinguishable from the exact solution at the early stage (Fig. 3.5.7(b)) and in the middle of the duration (Fig. 3.5.7(c)). At the end of the duration, the error is merely about 0.0015. Thus, the  $M_H = M_L = 24$  open boundary is sufficiently accurate for most engineering applications.



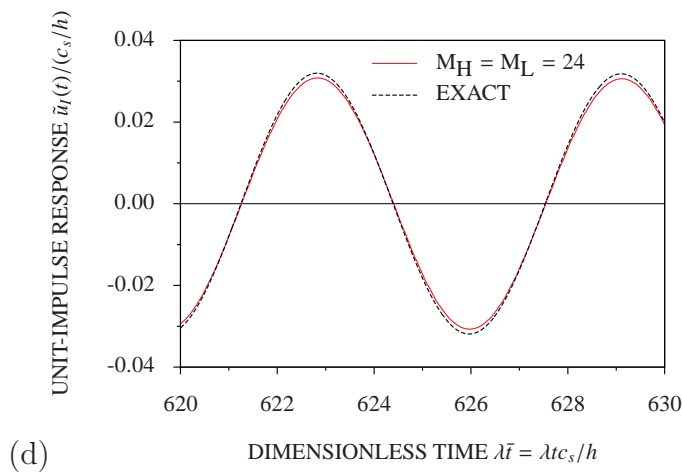
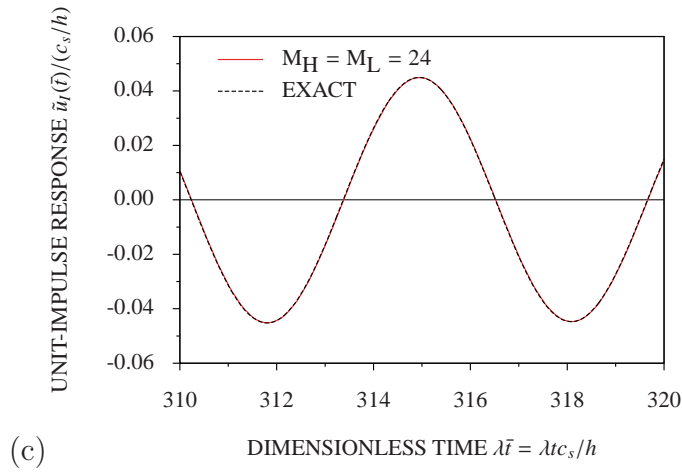
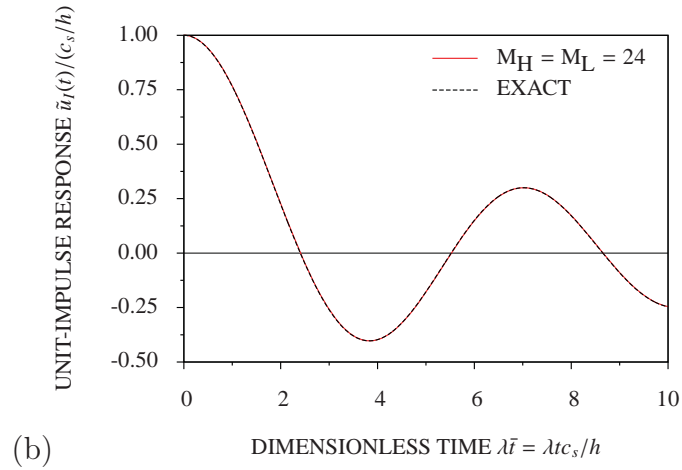
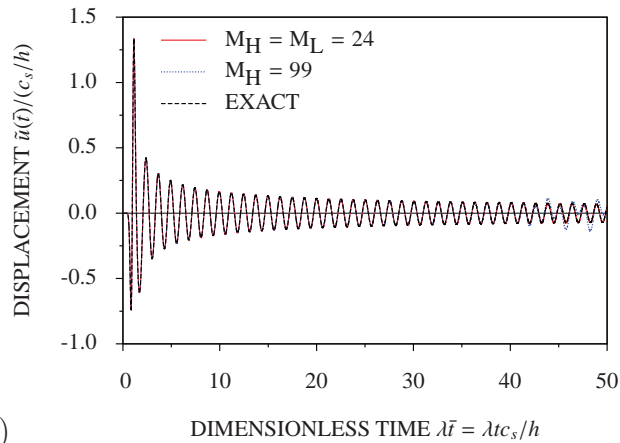


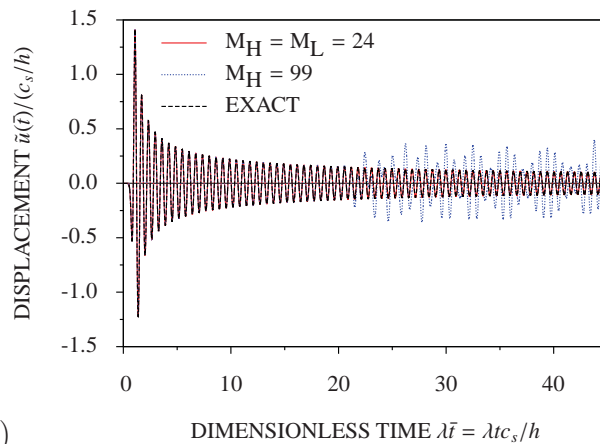
Figure 3.5.7: Unit-impulse response of semi-infinite layer by doubly asymptotic open boundary with  $M_H = M_L = 24$

The response to a surface traction prescribed as the Ricker wavelet shown in Fig. 3.5.1 ( $\bar{t}_s = ct_s/h = 1$ ,  $\bar{t}_0 = ct_0/h = 0.2$ ) is computed for three modes  $\lambda = 5$ ,

10 and 15. It is similar to the analysis of the semi-infinite layer by using modal superposition. The same amplitude of surface traction  $A_R = 10$  is assumed for all the three modes. The ratios between the dominate dimensionless frequencies to the modal eigenvalues are  $a_0/\lambda = 2, 1$  and  $2/3$ , respectively. The responses of the  $M_H = M_L = 24$  doubly asymptotic open boundary are plotted in Fig. 3.5.8. Very good agreement is observed for all the three modes. For comparison, the responses of the  $M_H = 99$  singly asymptotic open boundary are also shown. As its dynamic stiffness coefficient is very accurate above the cut-off frequency ( $a_0 > \lambda$ ), the response for the mode  $\lambda = 5$  (the ratio  $a_0/\lambda = 2$ ) is very accurate (Fig. 3.5.8(a)) with only a small error after  $\bar{t} > 45$ . As the mode increases, the “fictitious reflections” appear. For the mode  $\lambda = 15$  (the ratio  $a_0/\lambda = 0.5$ ), the amplitude of the “fictitious reflections” is very large. In addition, the “fictitious reflections” arrive earlier as the modal eigenvalue increases.



(a)



(b)

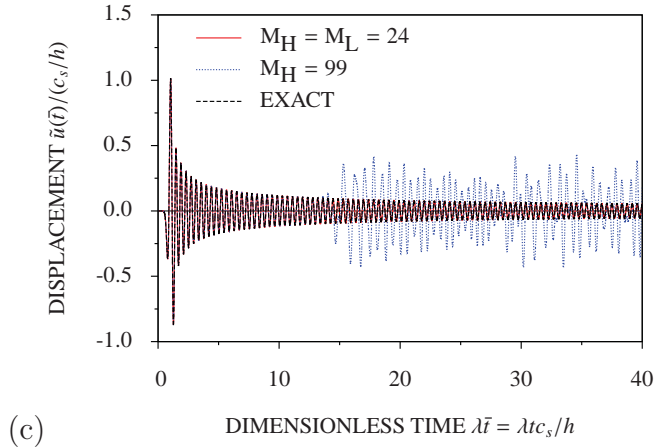


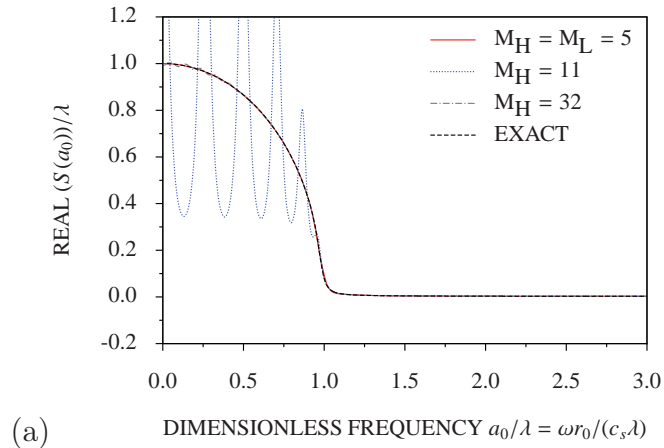
Figure 3.5.8: Response of semi-infinite layer to traction varying as Ricker wavelets by doubly asymptotic open boundary with  $M_H = M_L = 24$ : (a)  $\lambda = 5$ , (b)  $\lambda = 10$  and (c)  $\lambda = 15$

### 3.5.2 Circular cavity embedded in full-plane

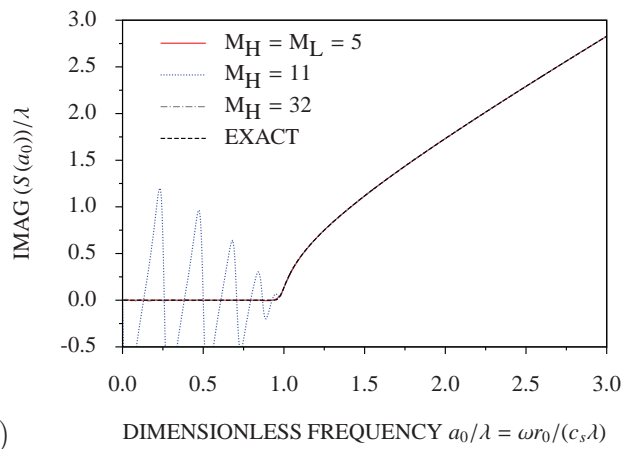
As shown in Bazyar and Song (2008), the high-frequency continued fraction solution for the dynamic stiffness coefficient converges to the exact solution for a circular cavity. As the modal eigenvalue increases, the rate of convergence decreases. This is consistent with the observation by Thompson *et al.* (2001), and Harari and Djellouli (2004) that the accuracy of high-order absorbing boundaries deteriorates as the modal eigenvalue increases.

It has been shown in Section 3.5.1 for the semi-infinite layer case that the high-order doubly asymptotic open boundary can effectively eliminate the “fictitious reflections” occurring in the singly asymptotic open boundary. As illustrated in Section 3.2.3, the dynamic stiffness coefficient of a mode of the circular cavity approaches that of the semi-infinite layer as the modal eigenvalue increases. It is thus expected the same advantage of the high-order doubly asymptotic open boundary exists when a mode of circular wave with a large eigenvalue is analyzed.

The mode  $\lambda = 200$  is, for example, addressed. The dynamic stiffness coefficient of the  $M_H = M_L = 5$  open boundary is shown in Fig. 3.5.9. Excellent agreement with the exact solution is obtained. The singly asymptotic continued fraction solution with the same number of terms ( $M_H = 11$ ) leads to a significant error below the cut-off frequency. Only when the order is higher than 32, the singly asymptotic solution is accurate over the whole frequency range. The same is also observed for the unit-impulse response plotted in Fig. 3.5.10.



(a)



(b)

Figure 3.5.9: Dynamic stiffness coefficient of circular cavity ( $\lambda = 200$ ): (a) real part and (b) imaginary part

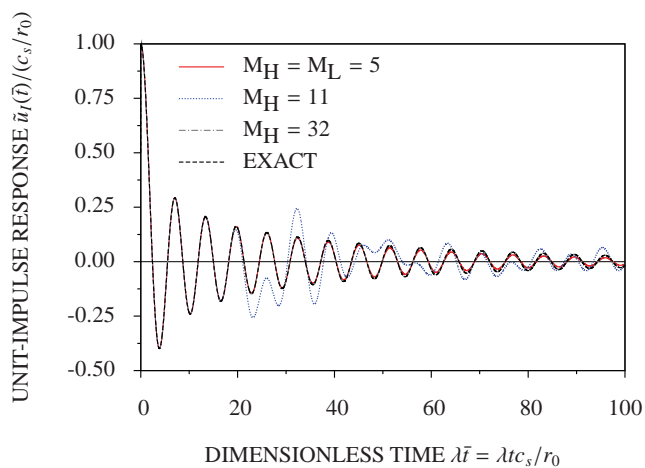


Figure 3.5.10: Unit-impulse response of circular cavity ( $\lambda = 200$ )

The dynamic stiffness coefficient of the mode  $\lambda = 2,000$  is plotted in Fig. 3.5.11. As expected, the accuracy of the singly asymptotic solution deteriorates when the

modal eigenvalue increases. The result of the order  $M_H = 32$  high-frequency continued fraction solution shows strong oscillation below the cut-off frequency. In contrast, the result of the order  $M_H = M_L = 5$  doubly asymptotic continued fraction solution is still very close to the exact solution. Only slight difference is observed close to the cut-off frequency. Higher accuracy of doubly asymptotic open boundary is also observed in the unit-impulse response as shown in Fig. 3.5.12. No “fictitious reflections” occur.

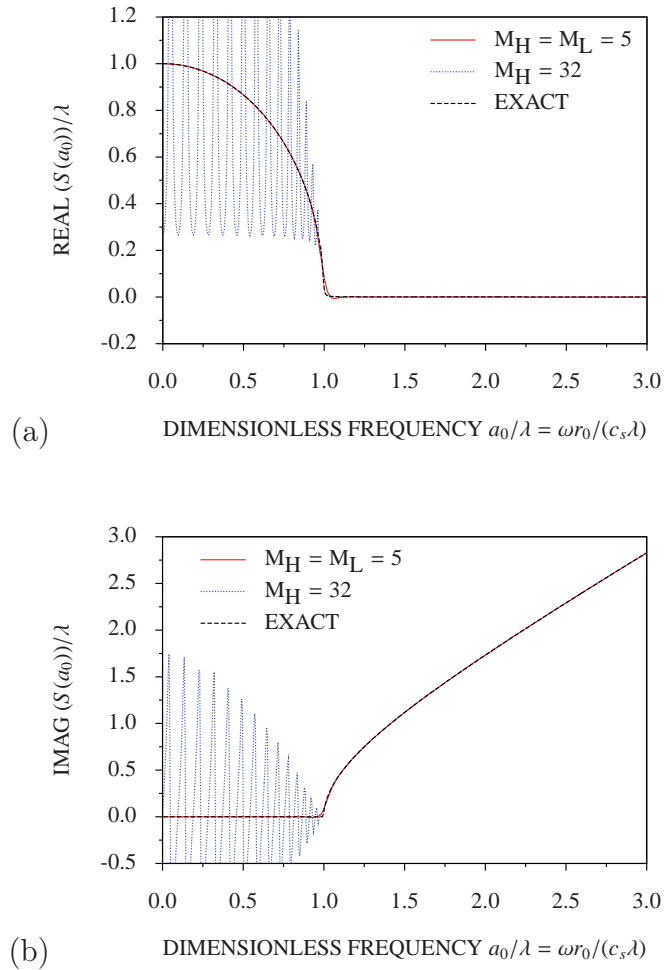


Figure 3.5.11: Dynamic stiffness coefficient of circular cavity ( $\lambda = 2,000$ ): (a) real part and (b) imaginary part

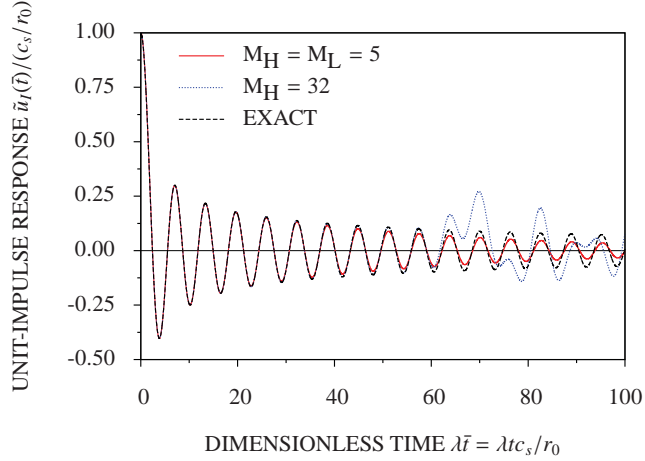
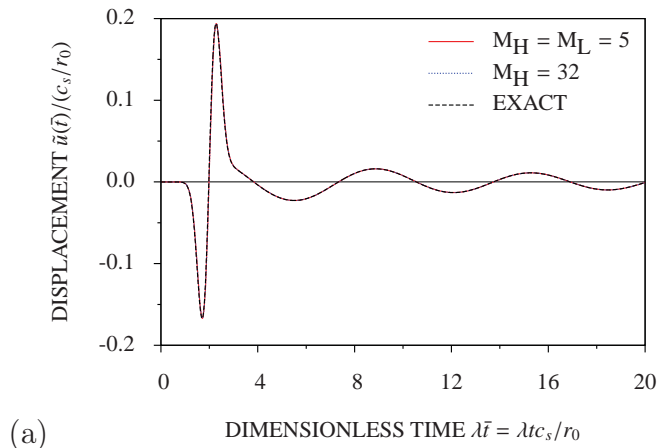


Figure 3.5.12: Unit-impulse response of circular cavity ( $\lambda = 2,000$ )

The response to a surface traction prescribed as the Ricker wavelet is evaluated. The parameters are chosen as  $\bar{t}_s = ct_s/h = 0.01$  and  $\bar{t}_0 = ct_0/h = 0.002$  and  $A_R = \lambda$ . The dominant dimensionless frequency is equal to  $a_0 = 1,000$ , which corresponds to the period of  $\bar{T} = 0.002\pi$ . The results of open boundaries for the modes  $\lambda = 200$  and  $2,000$  are compared with the exact solutions in Fig. 3.5.13. For the mode  $\lambda = 200$ , the ratio of dominant dimensionless frequency  $a_0$  to the eigenvalue  $\lambda = 200$  is equal to  $a_0/\lambda = 5$ . As shown in Fig. 3.5.11, both the  $M_H = 32$  singly asymptotic solution and the  $M_H = M_L = 5$  doubly asymptotic solution are highly accurate around this frequency. The responses of both open boundaries agree very well with the exact solution as shown in Fig. 3.5.13(a). For the mode  $\lambda = 2,000$ , the ratio of dominant dimensionless frequency  $a_0$  to the eigenvalue  $\lambda = 2,000$  becomes  $a_0/\lambda = 0.5$ . The  $M_H = 32$  singly asymptotic solution for the dynamic stiffness coefficient shows strong oscillation around the exact solution (Fig. 3.5.11). This leads to the “fictitious reflections” in the transient response in Fig. 3.5.13(b). Reasonably accurate response is obtained by using the  $M_H = M_L = 5$  doubly asymptotic open boundary.



(a)

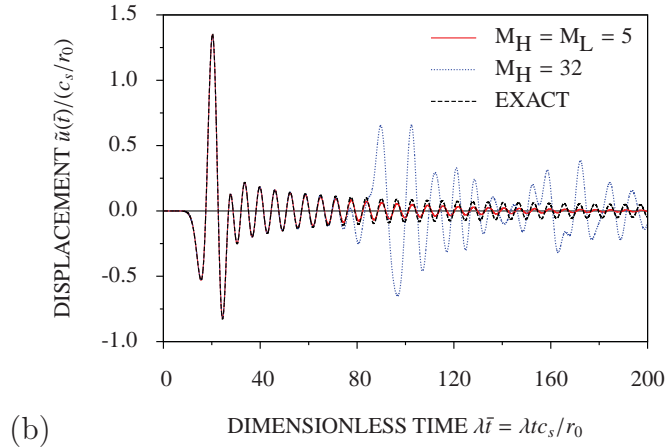


Figure 3.5.13: Response of circular cavity to traction varying as Ricker wavelets: (a)  $\lambda = 200$  and (b)  $\lambda = 2,000$

In a real finite-element analysis, the number of modes (eigenvalues) is often not easy to control. An open boundary should perform well for all modes, including those with very high eigenvalues, at the frequency range of interest. The above example demonstrates that a robust open boundary should ideally perform well for the case of semi-infinite layer with a constant depth.

### 3.6 Conclusions

A novel approach for constructing high-order doubly asymptotic open boundaries of arbitrary order has been proposed. The derivation and implementation are presented for the transient analysis of scalar waves in a semi-finite layer with a constant depth and a circular cavity in a full-plane. It is found from theoretical formulations and numerical experiments that

1. When a high-order open boundary for the semi-infinite layer with a constant depth is based solely on a high-frequency continued fraction expansion of the dynamic stiffness, i.e., singly asymptotic, it is equivalent to several well-established high-order absorbing boundaries. A singly asymptotic open boundary performs satisfactorily when the dimensionless frequency ( $ia_0$ ) content of the excitation is mostly higher than the highest modal eigenvalue ( $\lambda$ ), but it is unable to model evanescent waves caused by the part of excitation having dimensionless frequency lower than the highest modal eigenvalue. In a time-domain analysis, the error in modeling evanescent waves appears as numerical pollution similar to the “fictitious reflections” caused by simple boundary conditions.

2. As the modal eigenvalue  $\lambda$  of a circular cavity increases, the dynamic stiffness of the mode tends to that of a mode of a semi-infinite layer. Therefore, a robust open boundary for circular waves should also be able to model evanescent waves.
3. The dynamic stiffness of a doubly asymptotic open boundary converges rapidly to the exact solution in the frequency domain as its order increases. Evanescent waves and late-time (low-frequency) responses are simulated accurately. The doubly asymptotic open boundary shows significant improvement in accuracy in comparison with the singly asymptotic open boundary with the same number of terms.
4. The high-order doubly asymptotic open boundaries are expressed as first-order ordinary differential equations in time. The two time-independent coefficient matrices, the static stiffness and damping matrices, are banded and symmetric. Well-established time-stepping schemes in structural dynamics are directly applicable. The amount of computer time and storage are the same as those required by the singly asymptotic open boundary of the same order.

# Chapter 4

## Analysis of Gravity Dam-Reservoir Interaction Using Doubly Asymptotic Open Boundary

### Abstract

A procedure for the time-domain analysis of gravity dam-reservoir interaction is proposed. The dam and a part of the reservoir with irregular geometry are modeled with finite elements. A high-order doubly asymptotic open boundary condition is developed to model the remaining part of the reservoir simplified as a semi-infinite layer of a constant depth. This open boundary is temporally local, stable and converges rapidly as the order increases. It is directly coupled with the commercial finite element package, ABAQUS by using a sequential staggered implicit-implicit partition algorithm. Numerical examples demonstrate the high accuracy and long-time stability of the proposed technique.

### 4.1 Introduction

The computation of hydrodynamic pressure on dams is necessary and important in the analysis of dam-reservoir interaction during earthquakes. Research in this area was pioneered by Westergaard (1933). He derived the analytical solution for a rigid dam with a vertical upstream surface under a horizontal harmonic ground motion. The added-mass method originated from his paper has influenced the engineering design of dams since then. In 1967, Chopra developed an analytical formulation for the hydrodynamic pressure of compressive water on rigid dam with vertical upstream face under both horizontal and vertical earthquake excitation. When the

upstream face of a dam is inclined, water is often simplified as incompressible so that an analytical solution can be derived. For example, Chwang (1978) presented an exact solution for a rigid dam with an inclined upstream face of constant slope by using a two-dimensional potential theory. In the companion paper, Chwang and Housner (1978) employed the momentum-balance principle to solve the same problem approximately. As the dam is assumed to be rigid in the above studies, the effect of dam-reservoir interaction cannot be considered. Chopra and his coworkers (Chopra (1967); Chakrabarti and Chopra (1973)) and were the first to study the effects of flexible gravity dam-reservoir interaction by employing the first few modes of vibration of the dam obtained with an empty reservoir.

Analytical solutions are available only for reservoirs of regular geometries, such as semi-infinite layers or prisms. When the reservoir geometry is irregular, numerical methods such as finite element method are necessary to analyze the dam-reservoir interaction. Substructure method is often applied (see Fig. 4.2.1). The part of the reservoir with irregular geometry, called near field, is discretized with finite elements. To reduce the amount of computational cost, the finite element mesh is truncated at a distance from the dam. The remaining part of reservoir, called far field, is simplified as a semi-infinite layer with a constant depth. The near and far fields are coupled at the truncated boundary by satisfying the equations of motion and continuity. Various methods have been developed to model the far field. Saini *et al.* (1978) proposed the infinite element to analyze the two-dimensional response of reservoir-dam systems subjected to horizontal ground motions. Chopra and his coworkers (Chopra and Chakrabarti, 1981; Hall and Chopra, 1982) developed efficient procedures to analyze dam-reservoir interaction in the frequency domain. The finite element discretization on the truncated boundary was combined with a continuum representation in the infinite direction of the reservoir.

A direct time-domain analysis is required when the dam exhibits nonlinear material behavior, for example, under earthquakes. Zienkiewicz and Bettess (1978) studied fluid-structure interaction in the time domain by using Sommerfeld radiation condition to approximate the far field. Tsai *et al.* (1990) proposed an accurate implicit semi-analytical transmitting boundary in the time domain. Tsai and Lee (1991) established the corresponding time-domain models for the interaction analysis of dam-reservoir system by using the substructure method. This approach is temporally global, i.e. requires the evaluation of convolution integrals. It is expensive in computer time and memory for long-time analyses. To improve its computational efficiency, Yang *et al.* (1993) developed the explicit time-domain transmitting boundary which employed only a few eigenmodes in the evaluation of the convolution integrals. When the boundary element method (Touhei and Ohmachi, 1993;

Camara, 2000; Czygan and von Estorff, 2002) is applied to a direct time-domain analysis, the formulation is spatially and temporally global, which hinders its application to long-time computations of large-scale engineering problems.

Since mid-1990s, high-order transmitting boundaries have been proposed for the scalar wave equation. There is an extensive literature on this subject (see literature reviews (Tsynkov, 1998; Givoli, 2004)). They are constructed to absorb propagating waves radiating energy. The formulations are temporally local and more efficient by themselves than global procedures. They do not suffer from instability plagued earlier high-order transmitting boundaries. For problems of two- and three-dimensional cavities, they are shown to converge as the order increases. It was demonstrated in Chapter 3 that these transmitting boundaries are singly asymptotic at the high-frequency limit. They are efficient for radiative fields where all of the field energy is propagating out to infinity (Geers, 1998). However, a semi-infinite reservoir with a constant depth has a cut-off frequency. When the excitation frequency is close to or below the cut-off frequency, the wave field is not radiative. The high-order transmitting boundaries break down at low frequencies in a frequency domain analysis or at late times in a time domain analysis (Chapter 3).

One advance towards the modeling of an unbounded domain with possible presence of non-radiative wave fields is the introduction of doubly asymptotic boundaries (Geers, 1978; Underwood and Geers, 1981; Geers and Zhang, 1994; Geers and Lewis, 1997; Geers, 1998). The dynamic stiffness of the doubly asymptotic boundaries is selected as to fit the dynamic stiffness of the unbounded domain at the high-frequency limit and the low-frequency limit (i.e. statics). The resulting formulation is spatially global. The highest order reported in the literature is three (Geers and Toothaker, 2000). Another technique is the time-domain realization of the dynamic stiffness obtained in the frequency domain developed by Ruge *et al.* (2001) and Alpert *et al.* (2002). A rational approximation of the dynamic stiffness is constructed by curve-fitting. When it is transformed to the time domain, a recursive formula is obtained. Birk and Ruge (2007) applied such a technique to the dam-reservoir interaction analysis. Accurate results can be obtained for long-time computations, but a curve fitting by means of a least-squares process has to be performed for each order of the rational approximation.

Another type of popular techniques for modeling wave propagation is the perfectly matched layer (Berenger, 1994; Basu and Chopra, 2004). The performance of the perfectly matched layer is compared with that of a high-order transmitting boundary in Alpert *et al.* (2002). The high-order doubly asymptotic open boundary condition for modal equations of scalar waves has been presented in Chapter 3 by extending the work of Bazyar and Song (2008). It was constructed directly

from a differential equation of the dynamic stiffness matrix of an unbounded domain without evaluating its solution at discrete frequencies. This high-order doubly asymptotic boundary is capable of accurately mimicking the unbounded domain over the entire frequency range (i.e. from zero to infinity). For a one-dimensional problem corresponding to one mode of the horizontal layer, the coefficients of the open boundary condition are explicitly given. A boundary condition of any order can be constructed straightforwardly. Excellent accuracy and stability are observed for long-time transient analyses.

The purpose of this chapter is to extend the doubly asymptotic open boundary condition in Chapter 3 to the analysis of the hydrodynamic pressure of a semi-infinite layer with a constant depth. To facilitate the coupling with a commercial finite element package, the formulation of the open boundary condition is split into two parts. The first part is shown to be the simple Sommerfeld radiation boundary, also called viscous boundary in the dynamic soil-structure interaction analysis, which is spatially and temporally local. It can be included in the damping matrix of the system. The second part includes all the high order terms and is governed by a system of first-order ordinary differential equations. This part can be interpreted as external forces applied on the truncated boundary. Applying a sequential staggered implicit-implicit partition algorithm, the external forces are determined by the responses of the truncated boundary at the previous time station. This formulation does not modify the element connectivity and allows the direct coupling with a commercial finite element software package supporting two-way data exchange. This open boundary condition is implemented in the general-purpose finite element package ABAQUS to analyze gravity dam-reservoir interaction.

This chapter is organized as follows: in Section 4.2, the finite element formulation of dam-reservoir system is addressed. In Section 4.3, the scaled boundary finite element method is applied to derive a semi-discrete governing equation on the truncated boundary. In Section 4.4, a modal transformation is performed leading to a set of uncoupled equations for modal dynamic stiffness. In Section 4.5, the doubly asymptotic continued fraction solution of the dynamic stiffness is presented. In Section 4.6, a high-order doubly asymptotic open boundary condition is constructed by introducing auxiliary variables. In Section 4.7, the numerical implementation of the open boundary condition and the coupling with ABAQUS are addressed. In Section 4.8, numerical examples of a rigid dam and a flexible dam are presented. In the last section, conclusions are presented.

## 4.2 Finite element model of dam-reservoir system

A two-dimensional reservoir is addressed (Fig. 4.2.1). The water in the reservoir is assumed to be compressible, inviscid and irrotational with a small amplitude movement. The acceleration vector of water particles is denoted as  $\{\ddot{u}\} = [\ddot{u}_x(x, z, t) \quad \ddot{u}_z(x, z, t)]^T$  and the hydrodynamic pressure as  $p = p(x, z, t)$ . The reservoir is divided into a near field including the irregular geometry and a far field extending to infinity with a constant depth. The dam with possibly nonlinear material property and the near-field reservoir are modeled by finite elements. The hydrodynamic pressure  $p$  in the reservoir where the water is treated as acoustic fluid satisfies the scalar wave equation

$$\Delta p = \frac{1}{c^2} \frac{\partial^2 p}{\partial t^2} \quad (4.2.1)$$

with the Laplace operator  $\Delta$  and the compression wave velocity

$$c = \sqrt{\frac{K}{\rho}} \quad (4.2.2)$$

where  $K$  is the bulk modulus of water and  $\rho$  is the mass density.

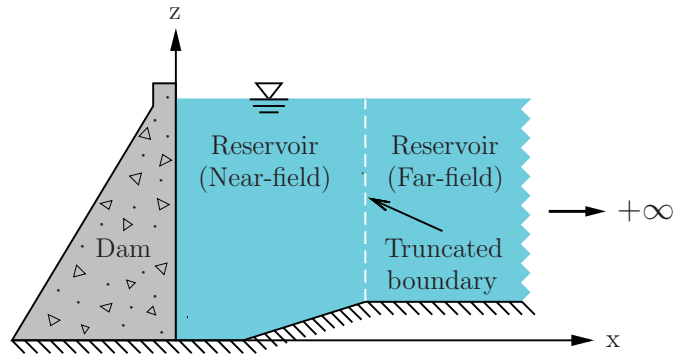


Figure 4.2.1: Typical gravity dam-reservoir system

On the dam-reservoir interface, the pressure should satisfy the boundary condition ( $n$  stands for the outward normal of the boundary)

$$\frac{\partial p}{\partial n} = -\rho \ddot{u}_n \quad (4.2.3)$$

The effect of surface waves on the hydrodynamic pressure on a dam is negligible. The boundary condition on the free surface is written as

$$p = 0 \quad (4.2.4)$$

At the reservoir bottom,

$$\frac{\partial p}{\partial n} = 0 \quad \text{or} \quad \ddot{u}_n = 0 \quad (4.2.5)$$

applies. The radiation condition should be satisfied at infinity

$$\frac{\partial p}{\partial n} = -\frac{\dot{p}}{c} \quad (4.2.6)$$

Without considering the material damping, the finite element formulation for the dam-reservoir system can be partitioned as

$$\begin{bmatrix} [M_s] & 0 & 0 \\ -[Q_{fs}] & [M_{ff}] & [M_{fb}] \\ 0 & [M_{bf}] & [M_{bb}] \end{bmatrix} \begin{Bmatrix} \{\ddot{u}_s\} \\ \{\ddot{p}_f\} \\ \{\ddot{p}_b\} \end{Bmatrix} + \begin{bmatrix} [K_s] & [Q_{fs}] & 0 \\ 0 & [K_{ff}] & [K_{fb}] \\ 0 & [K_{bf}] & [K_{bb}] \end{bmatrix} \begin{Bmatrix} \{u_s\} \\ \{p_f\} \\ \{p_b\} \end{Bmatrix} = \begin{Bmatrix} \{f_s\} \\ \{f_f\} \\ -\{r\} \end{Bmatrix} \quad (4.2.7)$$

where  $[M]$  stands for the mass matrix,  $[K]$  for the static stiffness matrix,  $[Q]$  for the coupling matrix between solid and fluid and  $\{f\}$  for the external force vector. Subscript  $s$  denotes degrees of freedom on the dam structure, subscript  $f$  denotes the degrees of freedom of the near-field water except for those on the truncated boundary that are denoted by the subscript  $b$ . Denoting the interaction load applied to the semi-infinite reservoir by the near-field water as  $\{r\}$ , the external load applied to the near-field water on the truncated boundary is equal to  $-\{r\}$ . The mass and stiffness matrices of water is expressed in ABAQUS as

$$[M_f] = \int_{v_f} \frac{1}{K} [N]^T [N] dV \quad (4.2.8)$$

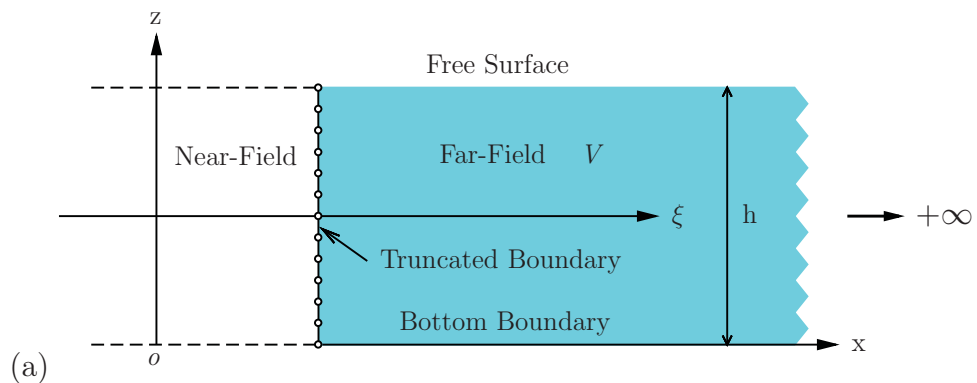
$$[K_f] = \int_{v_f} \frac{1}{\rho_f} \left( \frac{\partial [N]^T}{\partial x} \frac{\partial [N]}{\partial x} + \frac{\partial [N]^T}{\partial z} \frac{\partial [N]}{\partial z} \right) dV \quad (4.2.9)$$

$$\{f_f\} = \int_{s_f} \frac{1}{\rho_f} [N] \frac{\partial p}{\partial x} dS \quad (4.2.10)$$

where  $[N]$  are the shape functions of finite elements. In order to solve the dam-reservoir system expressed in Eq. (4.2.7), the relationship between the interaction load  $\{r\}$  and the hydrodynamic pressure  $\{p\}$  of the semi-infinite reservoir is determined in the following sections.

### 4.3 Scaled boundary finite element method for semi-infinite reservoir with constant depth

The scalar wave equation in a semi-infinite reservoir with a constant depth (far field) can be solved analytically in the frequency domain by the method of separation of variables. To facilitate the coupling with the finite elements of the near-field reservoir, a semi-analytical method is employed in this section. The reservoir is discretized along its depth by elements that have the same nodes and shape functions as the finite elements. Several derivations leading to similar semi-analytical approaches exist (see, e.g., Lysmer and Waas (1972); Song and Wolf (1997); Birk and Ruge (2007)). The scaled boundary finite element method, developed to model unbounded domains with arbitrary shape (Song and Wolf, 1997), is selected in this thesis considering the possibility of further extension of the present technique to problems with more complex geometry. The derivation of scaled boundary finite element method for elastodynamics is detailed in Song and Wolf (1997) and Wolf and Song (2000). In this thesis, the derivation is summarized for the two-dimensional semi-infinite reservoir with a vertical boundary (Fig. 4.3.1(a)). Streamlined expressions are presented for this special case.



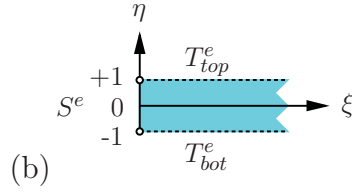


Figure 4.3.1: Semi-infinite reservoir with constant depth: (a) semi-discretization and (b) typical element

The equation of motion of water without body force is written as

$$\{L\}p + \rho\{\ddot{u}\} = 0 \quad (4.3.1)$$

where  $\{L\} = \left[ \frac{\partial}{\partial x} \quad \frac{\partial}{\partial z} \right]^T$  is the differential operator, and the equation of continuity considering the volumetric stress-strain relationship of compressible water is

$$\{L\}^T\{\ddot{u}\} = -\frac{1}{K} \frac{\partial^2 p}{\partial t^2} \quad (4.3.2)$$

The vertical boundary of the semi-infinite reservoir is specified by a constant coordinate  $x_b$ . It is discretized by one-dimensional elements (Fig. 4.3.1(a)). A typical element is shown in Fig. 4.3.1(b). The vertical coordinates of the nodes of an element in the Cartesian coordinate system are arranged in  $\{z_b\}$ . The geometry of an element is interpolated using the shape functions  $[N(\eta)]$  formulated in the local co-ordinate  $\eta$  as

$$z_b(\eta) = [N(\eta)]\{z_b\} \quad (4.3.3)$$

The Cartesian coordinates of a point  $(x, z)$  inside the semi-infinite reservoir are expressed as

$$x(\xi) = x_b + \xi \quad (4.3.4a)$$

$$z(\eta) = z_b(\eta) = [N(\eta)]\{z_b\} \quad (4.3.4b)$$

where the coordinate  $\xi$  is equal to 0 on the vertical boundary. The Jacobian matrix for the coordinate transformation from  $(x, z)$  to  $(\xi, \eta)$  equals

$$[J(\eta)] = \begin{bmatrix} x,\xi & z,\xi \\ x,\eta & z,\eta \end{bmatrix} = \begin{bmatrix} 1 & 0 \\ 0 & z_{b,\eta} \end{bmatrix} \quad (4.3.5)$$

For a two-dimensional problem with a unit length in the third dimension,

$$dV = |J(\eta)|d\xi d\eta \quad (4.3.6)$$

where  $|J(\eta)|$  is the determinant of the Jacobian matrix. The partial differential operator defined in Eq. (4.3.1) is expressed as

$$\{L\} = [J(\eta)]^{-1} \left[ \frac{\partial}{\partial \xi} \quad \frac{\partial}{\partial \eta} \right]^T = \{b^1\} \frac{\partial}{\partial \xi} + \{b^2(\eta)\} \frac{\partial}{\partial \eta} \quad (4.3.7)$$

with

$$\{b^1\} = [1 \quad 0]^T \quad (4.3.8a)$$

$$\{b^2(\eta)\} = \frac{1}{|J(\eta)|} [0 \quad 1]^T \quad (4.3.8b)$$

The governing differential equations in the local coordinates  $(\xi, \eta)$  are specified by Eq. (4.3.2) with the differential operator  $\{L\}$  in Eq. (4.3.7).

Along horizontal lines passing through a node on the boundary, the nodal hydrodynamic pressure functions  $\{p\} = \{p(\xi, t)\}$  are introduced. The nodal pressure on the boundary follows as  $\{p_b(t)\} = \{p(\xi = 0, t)\}$ . Isoparametric elements are used in the vertical direction. One element  $S^e$  on the boundary and the corresponding horizontal strip shown in Fig. 4.3.1(b) are addressed. The hydrodynamic pressure field  $p = p(\xi, \eta, t)$  is obtained by interpolating the nodal pressure functions

$$p = [N(\eta)]\{p\} \quad (4.3.9)$$

For acoustic fluid, the relationship between acceleration and pressure is equivalent to that between stress (or distributed load) and displacement in stress analysis. Substituting Eqs. (4.3.7) and (4.3.9) into Eq. (4.3.1), the acceleration  $\{\ddot{u}\} = \{\ddot{u}(\xi, \eta)\}$  is expressed as

$$\{\ddot{u}\} = -\frac{1}{\rho} ([B^1(\eta)]\{p\}_{,\xi} + [B^2(\eta)]\{p\}) \quad (4.3.10)$$

with

$$[B^1(\eta)] = \{b^1\}[N(\eta)] \quad (4.3.11a)$$

$$[B^2(\eta)] = \{b^2(\eta)\}[N(\eta)]_{,\eta} \quad (4.3.11b)$$

The Galerkin's weighted residual method is applied. Equation (4.3.2) is multiplied by a weight function  $w = w(\xi, \eta)$  and integrated over the semi-infinite strip corresponding to the element (Fig. 4.3.1(b))

$$\int_V w\{b^1\}^T\{\ddot{u}_{,\xi}\}dV + \int_V w\{b^2\}^T\{\ddot{u}_{,\eta}\}dV + \int_V w\frac{1}{K}\frac{\partial^2 p}{\partial t^2}dV = 0 \quad (4.3.12)$$

Using Eq. (4.3.6) and integrating the second term of Eq. (4.3.12) over  $\eta$  by parts yield

$$\int_0^\infty \left( \int_{-1}^{+1} \left( w\{b^1\}^T\{\ddot{u}_{,\xi}\} - w_{,\eta}\{b^2(\eta)\}^T\{\ddot{u}\} + w\frac{1}{K}\ddot{p} \right) |J(\eta)|d\eta \right. \\ \left. + w\{b^2(\eta)\}^T\{\ddot{u}\}|J(\eta)|\Big|_{-1}^{+1} \right) d\xi = 0 \quad (4.3.13)$$

Equation (4.3.13) is satisfied by setting the integrand of the integral over  $\xi$  equal to zero

$$\int_{-1}^{+1} \left( w\{b^1\}^T\{\ddot{u}_{,\xi}\} - w_{,\eta}\{b^2(\eta)\}^T\{\ddot{u}\} + w\frac{1}{K}\ddot{p} \right) |J(\eta)|d\eta \\ + w\{b^2(\eta)\}^T\{\ddot{u}\}|J(\eta)|\Big|_{-1}^{+1} = 0 \quad (4.3.14)$$

This corresponds to enforcing the scalar wave equation exactly in the horizontal direction. Note that no volume integrals are present in Eq. (4.3.14).

The weight function is constructed in the same way as the hydrodynamic pressure (Eq. (4.3.9))

$$w(\xi, \eta) = [N(\eta)]\{w(\xi)\} \quad (4.3.15)$$

Substituting Eq. (4.3.15) into Eq. (4.3.14) yields, for arbitrary  $\{w(\xi)\}$ ,

$$\int_{-1}^{+1} [B^1(\eta)]^T\{\ddot{u}_{,\xi}\}|J(\eta)|d\eta - \int_{-1}^{+1} [B^2(\eta)]^T\{\ddot{u}\}|J(\eta)|d\eta \\ + \int_{-1}^{+1} [N(\eta)]^T\frac{1}{K}\ddot{p}|J(\eta)|d\eta + \{T\} = 0 \quad (4.3.16)$$

where  $\{T\}$  is the equivalent nodal acceleration vector resulting from the acceleration distribution along the top and bottom of the strip

$$\{T\} = [N(\eta)]\{b^2(\eta)\}^T\{\ddot{u}\}|J(\eta)|\Big|_{-1}^{+1} \quad (4.3.17)$$

Substituting Eq. (4.3.10) into Eq. (4.3.16) leads to the scaled boundary finite element equation in hydrodynamic pressure

$$[E^0]\{p\}_{,\xi\xi} - [E^2]\{p\} - [M^0]\{\ddot{p}\} - \{T\} = 0 \quad (4.3.18)$$

where  $[E^0]$ ,  $[E^2]$  and  $[M^0]$  are coefficient matrices

$$[E^0] = \int_{-1}^{+1} [B^1(\eta)]^T \frac{1}{\rho} [B^1(\eta)] |J(\eta)| d\eta = \int_{-1}^{+1} [N(\eta)]^T \frac{1}{\rho} [N(\eta)] |J(\eta)| d\eta \quad (4.3.19a)$$

$$[E^2] = \int_{-1}^{+1} [B^2(\eta)]^T \frac{1}{\rho} [B^2(\eta)] |J(\eta)| d\eta = \int_{-1}^{+1} [N(\eta)]_{,\eta}^T \frac{1}{\rho} [N(\eta)]_{,\eta} \frac{1}{|J(\eta)|} d\eta \quad (4.3.19b)$$

$$[M^0] = \int_{-1}^{+1} [N(\eta)]^T \frac{1}{K} [N(\eta)] |J(\eta)| d\eta = \frac{1}{c^2} [E^0] \quad (4.3.19c)$$

The horizontal strips corresponding to the individual elements on boundary are assembled. The nodal acceleration vectors  $\{T\}$  cancel at the common boundaries. On the bottom of the reservoir, the nodal acceleration vanishes (Eq. (4.2.5)). After enforcing the boundary condition  $p(\xi, t) = 0$  on the free surface, the scaled boundary finite element equation for the two-dimensional semi-infinite reservoir with constant depth is expressed as

$$[E^0]\{p\}_{,\xi\xi} - [E^2]\{p\} - \frac{1}{c^2} [E^0]\{\ddot{p}\} = 0 \quad (4.3.20)$$

The standard numerical integration techniques in the finite element method are directly applicable to evaluate these coefficient matrices. Like the static stiffness and mass matrices in the finite element method, the coefficient matrices  $[E^0]$  and  $[E^2]$  are sparse and positive definite.

For acoustic fluid, the acoustic nodal load vector  $\{r\} = \{r(\xi, t)\}$  on a vertical surface with a constant  $\xi$  is expressed as

$$\{r\} = -[E^0]\{p\}_{,\xi} \quad (4.3.21)$$

It is the equivalent nodal vector of acceleration distribution based on virtual work principle. Assuming the time-harmonic response  $\{p(\xi, t)\} = \{P(\xi, \omega)\} e^{+i\omega t}$  ( $\omega$  is the excitation frequency) with the amplitudes of the hydrodynamic pressure  $\{P\} = \{P(\xi, \omega)\}$ , Eq. (4.3.20) is transformed into the frequency domain as

$$[E^0]\{P\}_{,\xi\xi} - [E^2]\{P\} + \frac{\omega^2}{c^2} [E^0]\{P\} = 0 \quad (4.3.22)$$

The amplitudes of the acoustic nodal load  $\{R\} = \{R(\xi, \omega)\}$  ( $\{r(\xi, t)\} = \{R(\xi, \omega)\}e^{+i\omega t}$ ) are expressed as (Eq. (4.3.21))

$$\{R\} = -[E^0]\{P\}_{,\xi} \quad (4.3.23)$$

## 4.4 Modal decomposition of scaled boundary finite element equation

The system of ordinary differential equations in Eq. (4.3.22) can be decoupled by a modal transformation. The modes are obtained from the following generalized eigenvalue problem ( $[\bullet]$  stands for a diagonal matrix)

$$[E^2][\Phi] = [E^0][\Phi][\lambda^2]/h^2 \quad (4.4.1)$$

where  $[\lambda^2]$  is the diagonal matrix of positive eigenvalues,  $[\Phi]$  are the eigenvectors representing the modes, and  $h$  is a characteristic length, for example the depth of the layer, to non-dimensionlize the eigenvalues. The eigenvectors  $[\Phi]$  are normalized as

$$[\Phi]^T[E^0][\Phi] = [I] \quad (4.4.2)$$

Pre-multiplying Eq. (4.4.1) by  $[\Phi]^T$  results in

$$[\Phi]^T[E^2][\Phi] = [\lambda^2]/h^2 \quad (4.4.3)$$

It is noted from Eq. (4.4.2) that the inverse of the eigenvector matrix can be obtained by using the matrix multiplication

$$[\Phi]^{-1} = [\Phi]^T[E^0] \quad (4.4.4)$$

The amplitude of the hydrodynamic pressures are expressed as a linear combination of the eigenvectors

$$\{P\} = [\Phi]\{\tilde{P}\} \quad (4.4.5)$$

where  $\{\tilde{P}\} = \{\tilde{P}(\xi, \omega)\}$  are the amplitudes of the modal hydrodynamic pressures. Substituting Eq. (4.4.5) into Eq. (4.3.22) pre-multiplied by  $[\Phi]^T$  and using Eqs.

(4.4.2) and (4.4.3) lead to a system of decoupled equations

$$\tilde{P}_{j,\xi\xi} + \frac{1}{h^2}(a_0^2 - \lambda_j^2)\tilde{P}_j = 0 \quad (4.4.6)$$

with the dimensionless frequency

$$a_0 = \frac{\omega h}{c} \quad (4.4.7)$$

where the index  $j$  indicates the modal number. Substituting Eq. (4.4.5) into Eq. (4.3.23), the acoustic nodal force vector is expressed as

$$\{R\} = -[E^0][\Phi]^T \{\tilde{P}\}_{,\xi} \quad (4.4.8)$$

The amplitude of the modal nodal force vector  $\{\tilde{R}\} = \{\tilde{R}(\xi, \omega)\}$  is defined as

$$\{\tilde{R}\} = -h\{\tilde{P}\}_{,\xi} \quad \text{or} \quad \tilde{R}_j = -h\tilde{P}_{j,\xi} \quad (4.4.9)$$

Pre-multiplying Eq. (4.4.8) by  $[\Phi]^T$  and using Eqs. (4.4.2) and (4.4.9) yield

$$\{\tilde{R}\} = h[\Phi]^T \{R\} \quad (4.4.10)$$

This equation transforms the amplitude of the acoustic nodal force vector to the amplitude of the modal force vector. It can be used together with Eq. (4.4.9) to specify the boundary condition for the modal equation (Eq. (4.4.6)) from the prescribed amplitude of acoustic nodal force vector  $\{R\}$ .

Equation (4.4.6) can be solved analytically. The key equations given in Chapter 3 are summarized in the following. The modal dynamic stiffness coefficient  $\tilde{S}_j(a_0)$  is defined as

$$\tilde{R}_j = \tilde{S}_j(a_0)\tilde{P}_j \quad (4.4.11)$$

Its solution is equal to

$$\tilde{S}_j(a_0) = \sqrt{\lambda_j^2 - a_0^2} \quad (4.4.12)$$

Note that the modal dynamic stiffness is independent of the horizontal coordinate  $\xi$ . Performing the inverse Fourier transformation of  $\tilde{P}_j$  determined from Eqs. (4.4.11)

and (4.4.12) leads to

$$\tilde{p}_j(\xi, t) = \frac{c}{h} \int_0^t J_0 \left( \lambda_j \frac{c(t-\tau)}{h} \right) \tilde{r}_j(\xi, \tau) d\tau \quad (4.4.13)$$

where  $J_0$  is the zero order first kind Bessel function. Substituting Eq. (4.4.13) into Eq. (4.4.5) and using Eq. (4.4.10) yield

$$\{p(\xi, t)\} = c[\Phi] \int_0^t \left[ J_0 \left( \lambda_j \frac{c(t-\tau)}{h} \right) \right] [\Phi]^T \{r(\xi, \tau)\} d\tau \quad (4.4.14)$$

When the time history of the nodal forces  $\{r(\xi, t)\}$  is prescribed at a vertical boundary specified with a constant  $\xi$ , the nodal hydrodynamic pressure  $\{p(\xi, t)\}$  can be computed by using Eq. (4.4.14). However, this equation is temporally global, and the Bessel function decays very slowly at a rate of  $1/\sqrt{t}$ . The computational effort increases rapidly with the number of time steps.

## 4.5 Doubly asymptotic continued fraction solution for modal dynamic stiffness

A temporally local open boundary condition is constructed in Chapter 3 for a single mode of wave propagation. It is based on a doubly asymptotic solution of the modal dynamic stiffness coefficient  $\tilde{S}_j(a_0)$ . By eliminating  $\tilde{R}_j$  and  $\tilde{P}_j$  from Eqs. (4.4.6), (4.4.9) and (4.4.11), an equation for the dynamic stiffness coefficient is derived

$$(\tilde{S}_j(a_0))^2 + a_0^2 - \lambda_j^2 = 0 \quad (4.5.1)$$

The solution of Eq. (4.5.1) is expressed as a doubly asymptotic continued fraction. An order  $M_H$  high-frequency continued fraction is constructed first

$$\tilde{S}_j(a_0) = (ia_0)\tilde{C}_{\infty,j} - \frac{\lambda_j^2}{(ia_0)\tilde{Y}_{1,j}^{(1)} - \frac{\lambda_j^2}{(ia_0)\tilde{Y}_{1,j}^{(2)} - \frac{\lambda_j^2}{\dots - \frac{\lambda_j^2}{(ia_0)\tilde{Y}_{1,j}^{(M_H)}(a_0) - \frac{\lambda_j^2}{\tilde{Y}_{1,j}^{(M_H+1)}(a_0)}}}} \quad (4.5.2)$$

which is equivalent to

$$\tilde{S}_j(a_0) = (ia_0)\tilde{C}_{\infty,j} - \lambda_j^2(\tilde{Y}_j^{(1)}(a_0))^{-1} \quad (4.5.3a)$$

$$\tilde{Y}_j^{(i)}(a_0) = (ia_0)\tilde{Y}_{1,j}^{(i)} - \lambda_j^2(\tilde{Y}_j^{(i+1)}(a_0))^{-1} \quad (i = 1, 2, \dots, M_H) \quad (4.5.3b)$$

where the constants  $\tilde{C}_{\infty,j}$  and  $\tilde{Y}_{1,j}^{(i)}$  ( $i = 1, 2, \dots, M_H$ ) are determined by satisfying Eq. (4.5.1) at the high-frequency limit ( $a_0 \rightarrow +\infty$ ). Substituting Eq. (4.5.3a) into Eq. (4.5.1) results in an equation in terms of a power series of ( $ia_0$ )

$$(ia_0)^2(\tilde{C}_{\infty,j} - 1) + \lambda_j^2(-1 - 2(ia_0)\tilde{C}_{\infty,j}(\tilde{Y}_j^{(1)}(a_0))^{-1} + \lambda_j^2(\tilde{Y}_j^{(1)}(a_0))^{-2}) = 0 \quad (4.5.4)$$

This equation is satisfied by setting, in descending order, the two terms to zero. The damping coefficient  $\tilde{C}_{\infty,j}$  is obtained from the first term. To satisfy the radiation condition, the positive solution is chosen

$$\tilde{C}_{\infty,j} = 1 \quad (4.5.5)$$

The second term of Eq. (4.5.4) is an equation for the residual term  $\tilde{Y}_j^{(1)}(a_0)$  as  $\tilde{C}_{\infty,j}$  is known. To derive a recursive formula for determining the constants of the continued fraction, it is rewritten as the  $i = 1$  case of

$$\lambda_j^2 - 2b_{1,j}^{(i)}(ia_0)\tilde{Y}_j^{(i)}(a_0) - (\tilde{Y}_j^{(i)}(a_0))^2 = 0 \quad (i = 1, 2, \dots, M_H) \quad (4.5.6)$$

with the constant

$$b_{1,j}^{(1)} = 1 \quad (4.5.7)$$

Substituting Eq. (4.5.3b) into Eq. (4.5.6) leads to an equation in terms of a power series of ( $ia_0$ )

$$- (ia_0)^2((\tilde{Y}_{1,j}^{(i)})^2 + 2b_{1,j}^{(i)}\tilde{Y}_{1,j}^{(i)}) + \lambda_j^2(1 + 2(ia_0)(\tilde{Y}_{1,j}^{(i)} + b_{1,j}^{(1)})(\tilde{Y}_j^{(1)}(a_0))^{-1} - \lambda_j^2(\tilde{Y}_j^{(1)}(a_0))^{-2}) = 0 \quad (4.5.8)$$

Being similar to the process from Eq. (4.5.4) to Eq. (4.5.8), the coefficients in the continued fraction in Eq. (4.5.3b) are determined by solving Eq. (4.5.8) recursively

$$\tilde{b}_{1,j}^{(i)} = (-1)^{i+1} \quad (i = 1, 2, \dots, M_H) \quad (4.5.9)$$

$$\tilde{Y}_{1,j}^{(i)} = (-1)^i 2 \quad (i = 1, 2, \dots, M_H) \quad (4.5.10)$$

Using Eq. (4.5.5) and Eq. (4.5.10), the high-frequency continued fraction in Eq. (4.5.3a) is expressed as

$$\tilde{S}_j(a_0) = (ia_0) - \lambda_j^2(\tilde{Y}_j^{(1)}(a_0))^{-1} \quad (4.5.11a)$$

$$\tilde{Y}_j^{(i)}(a_0) = (-1)^i 2(ia_0) - \lambda_j^2(\tilde{Y}_j^{(i+1)}(a_0))^{-1} \quad (i = 1, 2, \dots, M_H) \quad (4.5.11b)$$

It is shown in Chapter 3 that the high-frequency continued fraction does not converge below the cut-off frequency. To determine a solution that is valid over the whole frequency range, a low-frequency continued fraction solution is sought for the residual term  $\tilde{Y}_j^{(M_H+1)}(a_0)$ . Denoting the residual term for mode  $j$  as

$$\tilde{Y}_{L,j}^{(i)}(a_0) = \tilde{Y}_j^{(M_H+1)}(a_0) \quad (4.5.12)$$

The  $i = M_H + 1$  case of Eq. (4.5.6) is rewritten as

$$\lambda_j^2 - 2b_{L,j}(ia_0)\tilde{Y}_{L,j}^{(i)}(a_0) - (\tilde{Y}_{L,j}^{(i)}(a_0))^2 = 0 \quad (4.5.13)$$

with the constant

$$b_{L,j} = b_{1,j}^{(M_H+1)} = (-1)^{M_H} \quad (4.5.14)$$

The continued fraction solution for  $\tilde{Y}_{L,j}^{(i)}(a_0)$  at the low-frequency limit is written as

$$\tilde{Y}_{L,j}(a_0) = \tilde{Y}_{L0,j}^{(0)} + (ia_0)\tilde{Y}_{L1,j}^{(0)} - \frac{(ia_0)^2}{\tilde{Y}_{L0,j}^{(1)} - \frac{(ia_0)^2}{\tilde{Y}_{L0,j}^{(2)} - \frac{(ia_0)^2}{\dots - \frac{(ia_0)^2}{\tilde{Y}_{L0,j}^{(M_L)}}}}} \quad (4.5.15)$$

It is equivalent to

$$\tilde{Y}_{L,j}(a_0) = \tilde{Y}_{L0,j}^{(0)} + (ia_0)\tilde{Y}_{L1,j}^{(0)} - (ia_0)^2(\tilde{Y}_{L,j}^{(1)}(a_0))^{-1} \quad (4.5.16a)$$

$$\tilde{Y}_{L,j}^{(i)}(a_0) = \tilde{Y}_{L0,j}^{(i)} - (ia_0)^2(\tilde{Y}_{L,j}^{(i+1)}(a_0))^{-1} \quad (i = 1, 2, \dots, M_L) \quad (4.5.16b)$$

The coefficients  $\tilde{Y}_{L0,j}^{(0)}$  and  $\tilde{Y}_{L1,j}^{(0)}$  in Eq. (4.5.16a) and  $\tilde{Y}_{L0,j}^{(i)}$  ( $i = 1, 2, \dots, M_L$ ) in Eq. (4.5.16b) are determined by satisfying Eq. (4.5.13) at the low frequency limit ( $a_0 \rightarrow 0$ ). Substituting Eq. (4.5.16a) into Eq. (4.5.13) leads to an equation in terms

of a power series of  $(ia_0)$

$$\begin{aligned} & \left( \lambda_j^2 - (\tilde{Y}_{L0,j}^{(0)})^2 \right) - (ia_0)(2\tilde{b}_{L,j}\tilde{Y}_{L0,j}^{(0)} + 2\tilde{Y}_{L0,j}^{(0)}\tilde{Y}_{L1,j}^{(0)}) + (ia_0)^2 \left( -2\tilde{b}_{L,j}\tilde{Y}_{L1,j}^{(0)} - (\tilde{Y}_{L1,j}^{(0)})^2 \right. \\ & \left. + 2(\tilde{Y}_{L0,j}^{(0)} + (ia_0)(\tilde{Y}_{L1,j}^{(0)} + \tilde{b}_{L,j}))(\tilde{Y}_{L,j}^{(1)}(a_0))^{-1} - (ia_0)^2(\tilde{Y}_{L,j}^{(1)}(a_0))^{-2} \right) = 0 \quad (4.5.17) \end{aligned}$$

As the low-frequency solution is being sought, Eq. (4.5.17) is satisfied by setting the coefficients of the power series to zero in ascending order. The constant term leads to two solutions for  $\tilde{Y}_{L0,j}^{(0)}$ , the one leads to the correct modal static dynamic stiffness  $S_j(a_0 = 0) = \lambda_j$  should be chosen. Inspecting Eq. (4.5.2) with  $\tilde{Y}_j^{(M_H+1)}(0) = \tilde{Y}_{L,j}(0) = \tilde{Y}_{L0,j}^{(0)}$ , the solution is

$$\tilde{Y}_{L0,j}^{(0)} = (-1)^{M_H+1}\lambda_j \quad (4.5.18)$$

For the coefficient of  $(ia_0)$  term in Eq. (4.5.17), using Eq. (4.5.14), the solution of  $\tilde{Y}_{L0,j}^{(0)}$  is

$$\tilde{Y}_{L1,j}^{(0)} = (-1)^{M_H+1} \quad (4.5.19)$$

The equation for the residual  $\tilde{Y}_{L,j}^{(1)}(a_0)$  is expressed as the  $i = 1$  case of

$$(ia_0)^2 - 2\tilde{b}_{L,j}^{(i)}\tilde{Y}_{L,j}^{(i)}(a_0) - (\tilde{Y}_{L,j}^{(i)}(a_0))^2 = 0 \quad (i = 1, 2, \dots, M_L) \quad (4.5.20)$$

with the constant

$$\tilde{b}_{L,j}^{(1)} = -\tilde{b}_{L,j}\lambda_j = (-1)^{M_H+1}\lambda_j \quad (4.5.21)$$

After substituting Eq. (4.5.16b) into Eq. (4.5.20), following the procedure for constructing the continued fraction solution at high frequency, the solutions of  $\tilde{Y}_{L0,j}^{(i)}$  ( $i = 1, 2, \dots, M_L$ ) are recursively obtained as

$$\tilde{Y}_{L0,j}^{(i)} = (-1)^{M_H+i+1}2\lambda_j \quad (i = 1, 2, \dots, M_L) \quad (4.5.22)$$

For an order  $M_L$  low-frequency solution, the residual  $(ia_0)^2(\tilde{Y}_{L,j}^{(M_H+1)}(a_0))^{-1}$  is neglected. Using Eqs. (4.5.18), (4.5.19) and Eq. (4.5.22), the low-frequency continued fraction solution in Eq. (4.5.16) is equal to

$$\tilde{Y}_{L,j}(a_0) = (-1)^{M_H+1}\lambda_j + (-1)^{M_H+1}(ia_0) - (ia_0)^2(\tilde{Y}_{L,j}^{(1)}(a_0))^{-1} \quad (4.5.23a)$$

$$\tilde{Y}_{L,j}^{(i)}(a_0) = (-1)^{M_H+i+1}2\lambda_j - (ia_0)^2(\tilde{Y}_{L,j}^{(i+1)}(a_0))^{-1} \quad (i = 1, 2, \dots, M_L) \quad (4.5.23b)$$

Combining the high-frequency solution (Eq. (4.5.2)) and the low-frequency solution (Eq. (4.5.15)) by using Eq. (4.5.12), yields the doubly asymptotic continued fraction solution. For example, the order  $M_H = M_L = 2$  doubly asymptotic continued fraction solution for mode  $j$  is expressed as

$$\tilde{S}_j(a_0) = (ia_0) - \frac{\lambda_j^2}{-2(ia_0) - \frac{\lambda_j^2}{2(ia_0) - \frac{\lambda_j^2}{-\lambda_j - (ia_0) - \frac{(ia_0)^2}{2\lambda_j - \frac{(ia_0)^2}{-2\lambda_j}}}}} \quad (4.5.24)$$

## 4.6 Doubly asymptotic open boundary condition

Following the procedure developed for modal space in Chapter 3, the acoustic force-pressure relationship in the time domain is formulated by using the continued fraction solution of the dynamic stiffness and introducing auxiliary variables. A system of first-order ordinary differential equations with symmetric coefficient matrices is obtained, which represents a temporally local open boundary condition. Substituting the first term of the continued fraction solution (Eq. (4.5.11a)) into Eq. (4.4.11), the amplitude of modal force is written as

$$\tilde{R}_j = (ia_0)\tilde{P}_j - \lambda_j\tilde{P}_j^{(1)} \quad (4.6.1)$$

where the auxiliary variable  $\tilde{P}_j^{(1)}$  is defined in

$$\lambda_j\tilde{P}_j = \tilde{Y}_j^{(1)}(a_0)\tilde{P}_j^{(1)} \quad (4.6.2)$$

Using Eqs. (4.4.10) and (4.6.1), the amplitude of nodal force vector is expressed as

$$h\{R\} = (ia_0)[\Phi]^{-T}\{\tilde{P}\} - [\Phi]^{-T}[\lambda]\{\tilde{P}^{(1)}\} \quad (4.6.3)$$

Substituting  $\{\tilde{P}\} = [\Phi]^{-1}\{P\}$  (Eq. (4.4.5)) and  $[E^0] = [\Phi]^{-T}[\Phi]^{-1}$  (Eq. (4.4.2)) into Eq. (4.6.3) leads to

$$h\{R\} = (ia_0)[E^0]\{P\} - [\Phi]^{-T}[\lambda]\{\tilde{P}^{(1)}\} \quad (4.6.4)$$

Substituting Eq. (4.5.11b) into Eq. (4.6.2) leads to

$$\lambda_j\tilde{P}_j = -2(ia_0)\tilde{P}_j^{(1)} - \lambda_j\tilde{P}_j^{(2)} \quad (4.6.5)$$

where  $\tilde{P}_j^{(2)}$  is defined as the  $i = 1$  case in

$$\lambda_j \tilde{P}_j^{(i)} = \tilde{Y}_j^{(i+1)}(a_0) \tilde{P}_j^{(i+1)} \quad (4.6.6)$$

Substituting  $\{\tilde{P}\} = [\Phi]^{-1}\{P\}$  (Eq. (4.4.5)) into Eq. (4.6.5) formulated for all the modes yields

$$[\lambda][\Phi]^{-1}\{P\} = -2(ia_0)\{\tilde{P}^{(1)}\} - [\lambda]\{\tilde{P}^{(2)}\} \quad (4.6.7)$$

Substituting the remaining terms of the continued fraction solution in Eq. (4.5.11b) into Eq. (4.6.6) results in

$$\lambda_j \tilde{P}_j^{(i-1)} = (-1)^i 2(ia_0) \tilde{P}_j^{(i)} - \lambda_j \tilde{P}_j^{(i+1)} \quad (i = 2, 3, \dots, M_H) \quad (4.6.8)$$

The residual term of an order  $M_H$  high-frequency continued fraction solution given by Eq. (4.6.6) at  $i = M_H$  is the initial term of the low-frequency continued fraction (Eq. (4.5.23a)). It is expressed as

$$\lambda_j \tilde{P}_j^{(M_H)} = \tilde{Y}_j^{(M_H+1)}(a_0) \tilde{P}_j^{(M_H+1)} = \tilde{Y}_{L,j}(a_0) \tilde{P}_{L,j}^{(0)} \quad (4.6.9)$$

with the auxiliary variable  $\tilde{P}_{L,j}^{(0)} = \tilde{P}_j^{(M_H+1)}$ . Substituting Eq. (4.5.23a) into Eq. (4.6.9) leads to

$$\lambda_j \tilde{P}_j^{(M_H)} = (-1)^{M_H+1} \lambda_j \tilde{P}_{L,j}^{(0)} + (-1)^{M_H+1} (ia_0) \tilde{P}_{L,j}^{(0)} - (ia_0) \tilde{P}_{L,j}^{(1)} \quad (4.6.10)$$

where the auxiliary variable  $\tilde{P}_{L,j}^{(1)}$  is defined in the  $i = 1$  case of

$$(ia_0) \tilde{P}_{L,j}^{(i-1)} = \tilde{Y}_{L,j}^{(i)}(a_0) \tilde{P}_{L,j}^{(i)} \quad (4.6.11)$$

Substituting Eq. (4.5.23b) into Eq. (4.6.11) leads to

$$(ia_0) \tilde{P}_{L,j}^{(i-1)} = (-1)^{M_H+i+1} 2\lambda_j \tilde{P}_{L,j}^{(i)} - (ia_0) \tilde{P}_{L,j}^{(i+1)} \quad (i = 1, 2, \dots, M_L) \quad (4.6.12)$$

For an order  $M_L$  low-frequency continued fraction solution,  $\tilde{P}_{L,j}^{(M_L+1)} = 0$  applies. Equations (4.6.4), (4.6.7), (4.6.8), (4.6.10) and (4.6.12) constitute a system of linear equations for the amplitude of nodal force vector  $\{R\}$ , the amplitude of nodal pressure vector  $\{P\}$ , and auxiliary variables  $\{\tilde{P}^{(i)}\}$  ( $i = 1, 2, \dots, M_H$ ) and  $\{\tilde{P}_L^{(i)}\}$  ( $i = 0, 1, \dots, M_L$ ). This system of equations describes an acoustic nodal force-pressure relationship equivalent to the doubly asymptotic continued fraction solution of the modal dynamic stiffness. This formulation is linear in  $(ia_0)$  and can

be directly transformed to the time domain. The inverse Fourier transforms of Eqs. (4.6.4), (4.6.7), (4.6.8), (4.6.10) and (4.6.12) divided by  $h$  are written as

$$\{r\} = \frac{1}{c}[E^0]\{\dot{p}\} - \frac{1}{h}[\Phi]^{-T}[\lambda]\{\tilde{p}^{(1)}\} \quad (4.6.13)$$

$$\frac{1}{h}[\lambda][\Phi]^{-1}\{p\} = -\frac{2}{c}\{\dot{p}^{(1)}\} - \frac{1}{h}[\lambda]\{\tilde{p}^{(2)}\} \quad (4.6.14)$$

$$\frac{1}{h}\lambda_j\tilde{p}_j^{(i-1)} = (-1)^i\frac{2}{c}\dot{p}_j^{(i)} - \frac{1}{h}\lambda_j\tilde{p}_j^{(i+1)} \quad (i = 2, 3, \dots, M_H) \quad (4.6.15)$$

$$\frac{1}{h}\lambda_j\tilde{p}_j^{(M_H)} = (-1)^{M_H+1}\frac{1}{h}\lambda_j\tilde{p}_{L,j}^{(0)} + (-1)^{M_H+1}\frac{1}{c}\dot{p}_{L,j}^{(0)} - \frac{1}{c}\dot{p}_{L,j}^{(1)} \quad (4.6.16)$$

$$\frac{1}{c}\dot{p}_{L,j}^{(i-1)} = (-1)^{M_H+i+1}\frac{2}{h}\lambda_j\tilde{p}_{L,j}^{(i)} - \frac{1}{c}\dot{p}_{L,j}^{(i+1)} \quad (i = 1, 2, \dots, M_L) \quad (4.6.17)$$

Assembling Eq. (4.6.13) to Eq. (4.6.17) leads to a system of first order ordinary differential equations with banded and symmetric coefficient matrices. This system of ordinary differential equations relating the interaction load  $\{r\}$  and hydrodynamic pressure  $\{p\}$  in the time domain is a temporally local high-order open boundary condition for the semi-infinite reservoir with a constant depth. It is directly established on the nodes of a vertical boundary. This boundary condition can be coupled seamlessly with finite elements. However, it introduces auxiliary variables as additional degrees of freedom. The coupling with commercial software packages is not feasible for a user without access to the source codes. To overcome this difficulty, the following sequential staggered implicit-implicit partition algorithm is adopted.

## 4.7 Numerical implementation in time domain

Substituting Eq. (4.6.13) into Eq. (4.2.7), the equation of motion of the dam-reservoir system considering the interaction between the near-field water and the semi-infinite reservoir is expressed as

$$\begin{aligned} & \begin{bmatrix} [M_s] & 0 & 0 \\ -[Q_{fs}] & [M_{ff}] & [M_{fb}] \\ 0 & [M_{bf}] & [M_{bb}] \end{bmatrix} \begin{Bmatrix} \{\ddot{u}_s\} \\ \{\ddot{p}_f\} \\ \{\ddot{p}_b\} \end{Bmatrix} + \frac{1}{c} \begin{bmatrix} 0 & 0 & 0 \\ 0 & 0 & 0 \\ 0 & 0 & [E^0] \end{bmatrix} \begin{Bmatrix} \{\dot{u}_s\} \\ \{\dot{p}_f\} \\ \{\dot{p}_b\} \end{Bmatrix} \\ & + \begin{bmatrix} [K_s] & [Q_{fs}] & 0 \\ 0 & [K_{ff}] & [K_{fb}] \\ 0 & [K_{bf}] & [K_{bb}] \end{bmatrix} \begin{Bmatrix} \{u_s\} \\ \{p_f\} \\ \{p_b\} \end{Bmatrix} = \begin{Bmatrix} \{f_s\} \\ \{f_f\} \\ [\Phi]^{-T}[\lambda]\{\tilde{p}^{(1)}\}/h \end{Bmatrix} \quad (4.7.1) \end{aligned}$$

Note that an additional damping term appears in Eq. (4.7.1). Comparing the expression of  $[E^0]$  in Eq. (4.3.19a) with the Sommerfeld radiation condition (see also

Eq. (4.2.6))

$$\frac{\partial p}{\partial x} = -\frac{\dot{p}}{c} \quad \text{i.e.} \quad \ddot{u}_x = -\frac{1}{\rho} \frac{\partial p}{\partial x} = \frac{\dot{p}}{\rho c} \quad (4.7.2)$$

it is found that the damping term is equivalent to the Sommerfeld radiation boundary, which is provided in ABAQUS. This term is, therefore, evaluated and assembled by the internal code of ABAQUS. The coupling term  $[\Phi]^{-T}[\lambda]\{\tilde{p}^{(1)}\}/h$  on the right-hand side of Eq. (4.7.1) represents the contribution of the high-order terms of the doubly asymptotic boundary. It can be regarded as an external load applied on the truncated boundary. When this term is set to zero, the high-order boundary condition degenerates to the Sommerfeld radiation boundary. As shown in Eq. (4.6.14), its value depends on the response history of the hydrodynamic pressure  $\{p\}$ . For efficiency consideration in the numerical implementation, the hydrodynamic pressure  $\{p\}$  is transformed to the modal hydrodynamic pressure (Eq. (4.4.5))

$$\{\tilde{p}\} = [\Phi]^{-1}\{p\} \quad (4.7.3)$$

Using Eq. (4.7.3) and multiplying Eq. (4.6.14) by  $h/\lambda_j$  leads to

$$\tilde{p}_j = -\frac{2h}{c\lambda_j}\dot{\tilde{p}}_j^{(1)} - \tilde{p}_j^{(2)} \quad (4.7.4)$$

Equations (4.7.4), (4.6.15), (4.6.16) and (4.6.17) are decoupled for individual modes. For each mode, they are assembled as a system of ordinary differential equations for the auxiliary variables

$$[K_A]\{z_{A,j}(t)\} + \frac{h}{c\lambda_j}[C_A]\{\dot{z}(t)\} = \{f_{A,j}(t)\} \quad (4.7.5)$$

where the vector  $\{z_{A,j}(t)\}$  consists of the auxiliary variables of mode  $j$  (The semi-colon “;” stands for the vertical concatenation of vectors)

$$\{z_{A,j}(t)\} = \{\tilde{p}_j^{(i)}; \dots; \tilde{p}_j^{(M_H)}, \tilde{p}_{.L,j}^{(0)}, \tilde{p}_{.L,j}^{(1)}, \dots, \tilde{p}_{.L,j}^{(M_L)}\} \quad (4.7.6)$$

The only nonzero entry on the right-hand side is the modal hydrodynamic pressure  $\tilde{p}_j$  determined from Eq. (4.7.3)

$$\{f_{A,j}(t)\} = \{-\tilde{p}_j^{(i)}; \dots; 0, 0, 0, \dots, 0\} \quad (4.7.7)$$



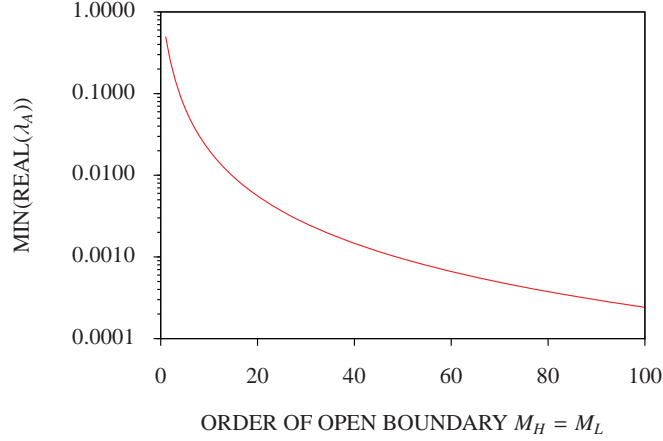


Figure 4.7.1: Minimum real part of eigenvalues of coefficient matrices (Eq. (4.7.9)) vs. order of open boundary  $M_H = M_L$

Equation (4.7.1) for the near field and Eq. (4.7.5) for the far field are coupled by the auxiliary variables  $\{\tilde{p}^{(1)}\}$ . These two sets of equations are solved by a sequential staggered implicit-implicit partitioned procedure proposed by Park (1980) and Park and Felippa (1980). Equation (4.7.1) is integrated implicitly by using the trapezoidal rule to evaluate the hydrodynamic pressure. The value of the auxiliary variables  $\{\tilde{p}^{(1)}\}$  at time station  $t_{n+1}$  is obtained from the last-solution extrapolation predictor (Park, 1980; Park and Felippa, 1980)

$$\{\tilde{p}^{(1)}\}_{n+1}^p = \{\tilde{p}^{(1)}\}_n \quad (4.7.10)$$

The auxiliary variables  $\{\tilde{p}^{(1)}\}$  are obtained by integrating Eq. (4.7.5) for prescribed hydrodynamic pressure  $\{p\}$  (Eqs. (4.7.3) and (4.7.7)).

Based on the restart function of ABAQUS, a two-way data-exchange sequential coupling scheme is proposed to solve Eqs. (4.7.1) and (4.7.5) alternately. The algorithm proceeds as follows:

1. Initialize variables  $\{u\}_0$  and  $\{p\}_0$  in Eq. (4.7.1) and  $\{z_{A,j}\} = 0$  for each mode in Eq. (4.7.5);
2. Extracting  $\{\tilde{p}^{(1)}\}_n$  from  $\{z_{A,j}\}_n$  of each mode (4.7.6) and assign to  $\{\tilde{p}^{(1)}\}_{n+1}^p$  (the last-solution extrapolation predictor (4.7.10));
3. Form the right-hand term of Eq. (4.7.1), compute  $\{u\}_{n+1}$  and  $\{p\}_{n+1}$  in ABAQUS by using an implicit method;
4. Calculate the modal hydrodynamic pressure  $\{\tilde{p}\}_{n+1}$  by using Eq. (4.7.3) and form the right-hand term of Eq. (4.7.5);
5. Compute  $\{z_{A,j}\}_{n+1}$  in home code for each mode by using implicit method;
6. Increment  $n$  to  $n + 1$  and go to Step 2.

From the point of view of wave propagation, this high-order doubly asymptotic open boundary is spatially global as all the degrees of freedom are coupled via the eigenvectors  $[\Phi]$  as shown in Eq. (4.4.5). In its numerical implementation shown in Eq. (4.7.1), the Sommerfeld boundary term expressed as the damping matrix is spatially local. The term  $[\Phi]^{-T}[\lambda]\{\tilde{p}^{(1)}\}/h$  is obtained by solving a system of decoupled equations (Eq. (4.7.5)) whose number of equations equal to the number of degrees of freedom on boundary. Therefore, from the point of view of computational cost, this open boundary condition is spatially local.

## 4.8 Numerical examples

Two numerical examples are analyzed to evaluate the accuracy and efficiency of the present doubly asymptotic open boundary condition. The first one is a rigid dam with a vertical upstream face and a semi-infinite reservoir with a constant depth. The doubly asymptotic open boundary is applied directly on the upstream face of the dam. The computational efficiency of the present technique is evaluated by measuring the computer time. The accuracy of the results is assessed by comparing with the analytical solution obtained by Chopra (1967). The second one is a flexible dam with an irregular near-field of the reservoir. The open boundary is employed to represent the regular far field of the reservoir. The results are compared with extended mesh solutions. The time integration of Eqs. (4.7.1) and (4.7.5) are both performed by using the implicit Newmark's method with  $\gamma = 0.5$  and  $\beta = 0.25$  i.e. trapezoidal integration (see Section A.2 in Appendix A).

### 4.8.1 Rigid dam

A rigid dam with a vertical upstream face is shown in Fig. 4.8.1. The constant depth of the reservoir extending to infinity is  $h = 180$  m. The pressure wave velocity is  $c = 1,437.8$  m/s and the density is  $\rho = 1,000$  kg/m<sup>3</sup>. The high-order doubly asymptotic open boundary is directly applied on the interface between rigid dam and reservoir. Twelve 3-node quadratic line elements are used to discretize the interface and the nodal interval is 7.5 m. The coupling with ABAQUS is not required. Equation (4.6.13) replaces Eq. (4.7.3) in the sequential staggered implicit-implicit partitioned procedure with the last-solution extrapolation predictor (Eq. (4.7.10)).

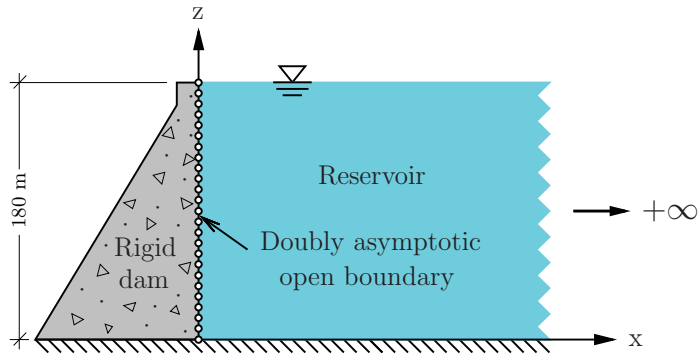
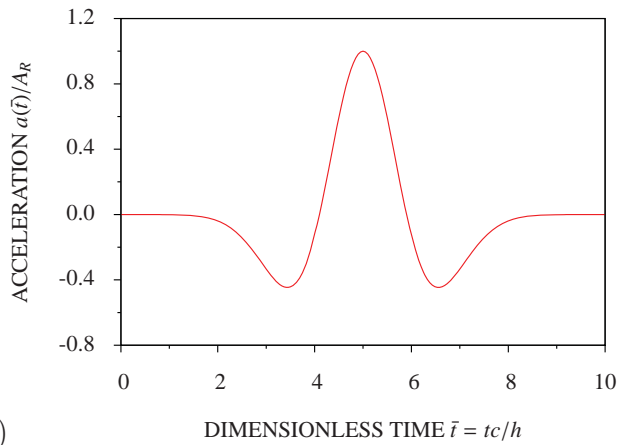


Figure 4.8.1: Rigid dam with semi-infinite reservoir of constant depth

The horizontal acceleration  $a(t)$  of the rigid dam is prescribed as a Ricker wavelet (see Eqs. (A.1.1) and (A.1.2) in Appendix A). The first cut-off frequency of the reservoir is  $\omega = \pi c/(2h)$  which corresponds to a dimensionless frequency  $a_0 = \omega h/c = \pi/2$ . The parameters of the Ricker wavelet are chosen as  $\bar{t}_s = t_s c/h$ ,  $\bar{t}_0 = t_0 c/h$  and  $A_R = 1$ . Its dominant frequency is equal to the first cut-off frequency of the reservoir. The time history and Fourier transform of the Ricker wavelet are shown in Fig. 4.8.2(a) and Fig. 4.8.2(b), respectively. The time step  $\Delta t = 0.001h/c$  is chosen.



(a)

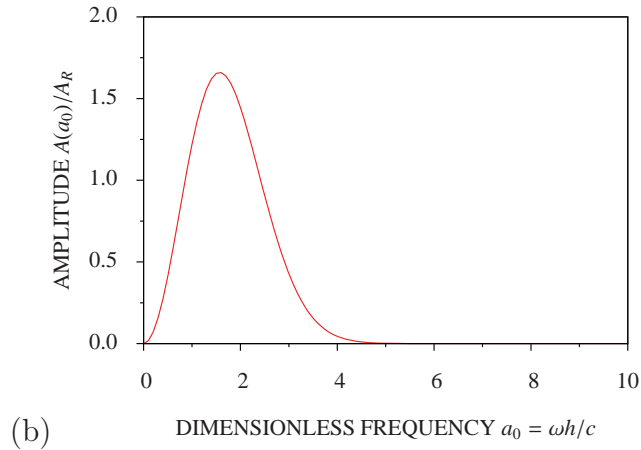
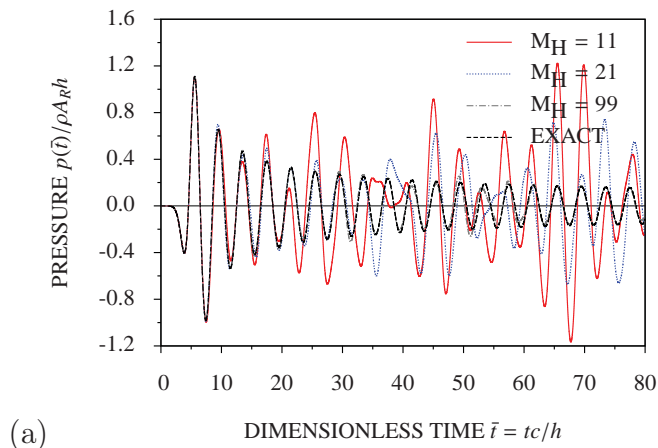
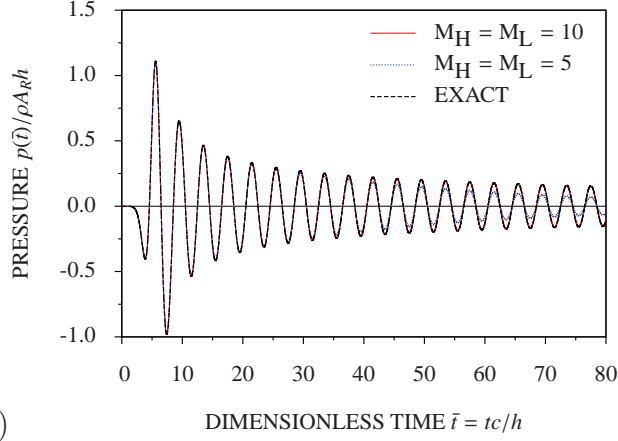


Figure 4.8.2: Prescribed acceleration as Ricker wavelet: (a) time history and (b) Fourier transform

The singly asymptotic boundary condition constructed by including only the high-frequency expansion is investigated. It is demonstrated in Chapter 3 that this boundary condition is closely related to several high-order transmitting boundaries. When the excitation frequency is lower than the cut-off frequency of a mode, “fictitious reflections” are observed in a long-time analysis of the modal response. For the case of the rigid dam, the hydrodynamic pressure responses at the dam heel are computed with the singly asymptotic boundary condition of orders  $M_H = 11$ ,  $M_H = 21$  and  $M_H = 99$ . The results are plotted in Fig. 4.8.3(a). The analytical solution Chopra (1967) is shown for comparison. The responses are accurate at early time, but “fictitious reflections” occur at late time. Although the arrival time of the “fictitious reflections” increases with the order of boundary condition, the rate of increase is slow. It is until the order is increased to  $M_H = 99$  that a reasonably accurate result is obtained for a duration of  $\bar{t} = tc/h = 80$ . Therefore, singly asymptotic boundaries are not suitable for long-time computation of dam-reservoir interaction.





(b)

Figure 4.8.3: Hydrodynamic pressure at dam heel under Ricker-wavelet acceleration: (a) singly asymptotic open boundary and (b) doubly asymptotic open boundary

The doubly asymptotic boundary condition leads to a significant improvement in accuracy at the same computational cost. The singly asymptotic boundary conditions of orders  $M_H = 11$  and  $M_H = 21$  have 12 terms and 22 terms, respectively, in the continued fraction solution of dynamic stiffness. The orders of the doubly asymptotic boundary conditions having the same number of terms are  $M_H = M_L = 5$  and  $M_H = M_L = 10$ , respectively. The results obtained with them are plotted in Fig. 4.8.3(b). It is observed that “fictitious reflections” do not occur as expected from the investigation on a single mode (Chapter 3). By comparing Fig. 4.8.3(b) with Fig. 4.8.3(a), it can be found that the doubly asymptotic boundary is much more accurate than the singly asymptotic boundary with the same number of terms. The  $M_H = M_L = 10$  doubly asymptotic boundary condition is even more accurate than  $M_H = 99$  the singly asymptotic boundary condition.

The computer time taken by the present high-order doubly asymptotic boundary is recorded on a laptop with a 2.53 GHz dual-core CPU. For an analysis of 80,000 time steps, the computer time are listed in Table 4.8.1 for open boundaries of orders  $M_H = M_L = 5$ ,  $M_H = M_L = 10$ , and  $M_H = M_L = 20$ . It is observed that the computer time increases linearly with the order of the open boundary. The increase in computer time with the number of time steps is also investigated. Using the order  $M_H = M_L = 10$  boundary condition, the analyses are performed for durations of dimensionless time  $\bar{t} = tc/h = 20, 40, 60$  and  $80$ . The computer time is shown in Table 4.8.2. As expected for this temporally local open boundary, the computer time increases linearly with the number of time steps.

Table 4.8.1: Computer time for doubly asymptotic open boundaries of various orders

Order ( $M_H = M_L$ )	5	10	15	20
CPU time (sec.)	18.99	27.80	36.17	44.75

Table 4.8.2: Computer time for doubly asymptotic open boundaries with various time durations of analysis

Time durations ( $\bar{t} = tc/h$ )	20	40	60	80
CPU time (sec.)	6.92	13.78	20.75	27.80

A triangular impulse of acceleration that has different frequency characteristics from the Ricker wavelet is addressed. The triangular impulse  $a(t)$  with a duration  $3h/c$  and a peak value  $A_T$  is plotted in Fig. 4.8.4(a). Its Fourier transform  $A(\omega)$  is illustrated in Fig. 4.8.4(b). The time step is chosen as  $\Delta t = 0.001h/c$ .

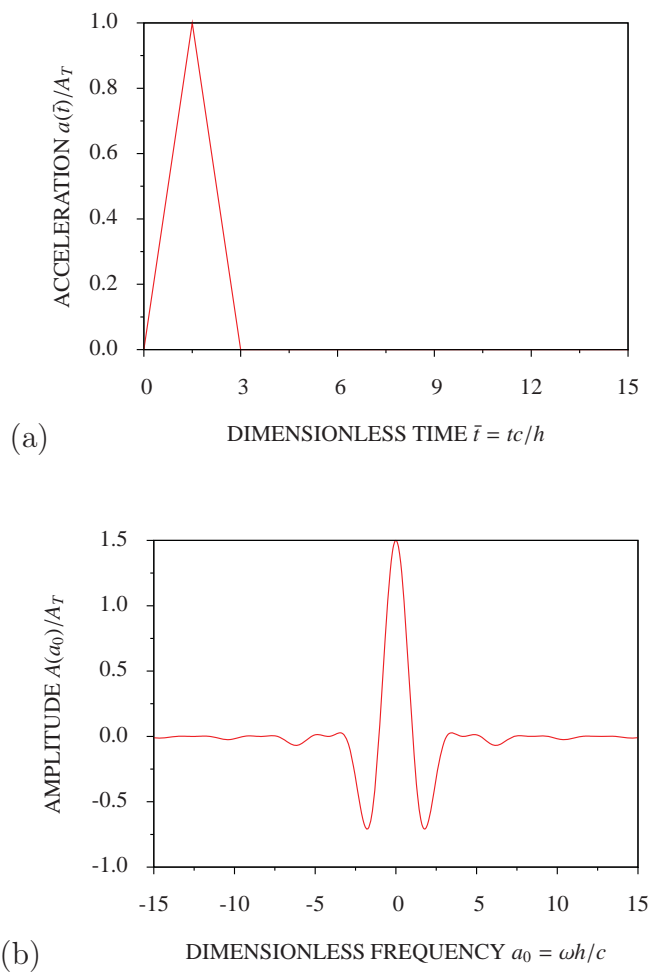


Figure 4.8.4: Triangular impulse of acceleration: (a) time history and (b) Fourier transform

The hydrodynamic pressure at the heel of dam is plotted in Fig. 4.8.5. The result obtained from the order  $M_H = M_L = 10$  doubly asymptotic boundary is in excellent agreement with the analytical solution.

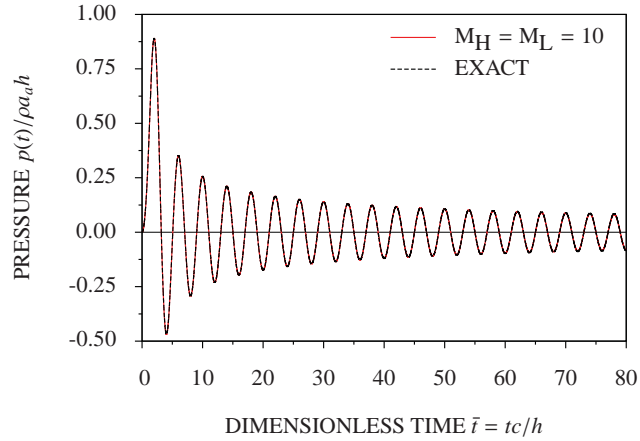


Figure 4.8.5: Hydrodynamic pressure at dam heel under triangular-impulse acceleration

To investigate the performance of the presented doubly asymptotic transmitting boundary under earthquake load, the El-Centro earthquake ground motions in the direction of North-South is applied (see Fig. 4.8.6). The size of time step is selected as  $\Delta t = 0.0001$  s. The order of the doubly asymptotic boundary of order is  $M_H = M_L = 10$ .

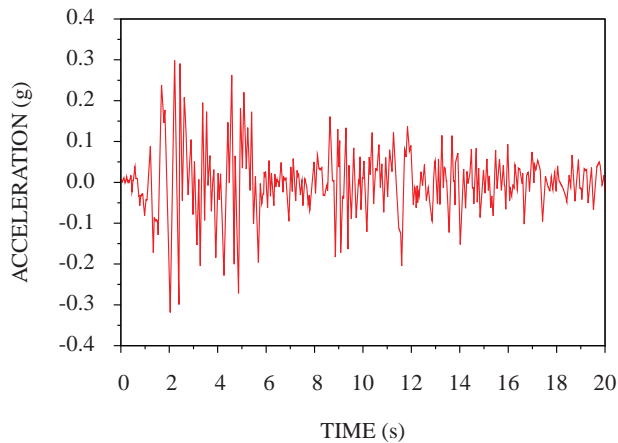


Figure 4.8.6: Time history of El-Centro earthquake

The hydrodynamic pressure response at the heel of dam is shown in Fig. 4.8.7. Again, no fictitious reflections occur. Excellent agreement with the analytical solution is achieved.

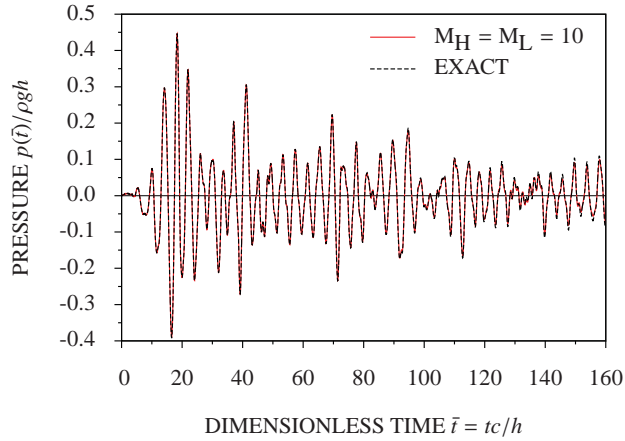
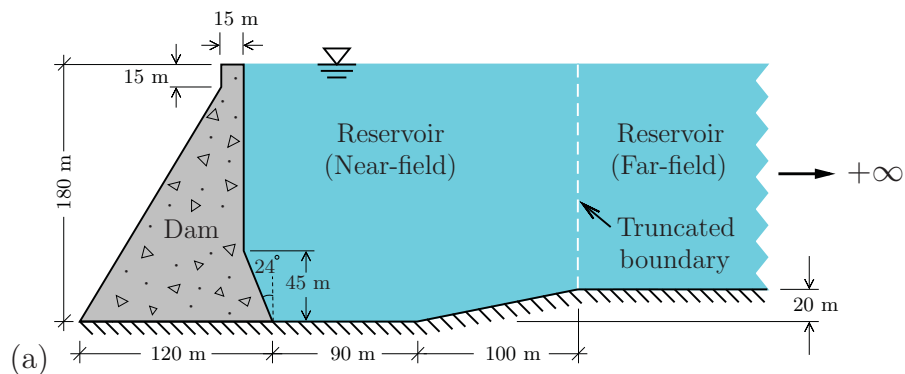


Figure 4.8.7: Hydrodynamic pressure at dam heel under acceleration of El-Centro earthquake

## 4.8.2 Flexible dam

A typical flexible gravity dam-reservoir system with an irregular near-field is shown in Fig. 4.8.8(a). The dam body has a modulus of elasticity  $E = 35$  GPa, Poisson's ratio  $\nu = 0.2$  and mass density  $\rho = 2,400$  kg/m<sup>3</sup>. The physical property of water is the same as that in the example of the rigid dam. The finite element mesh is shown in Fig. 4.8.8(b). The system is divided into three parts: the dam body, the near-field reservoir and the far-field reservoir with a constant depth. The dam body is discretized with 52 eight-node solid elements, and the near-field reservoir with 156 eight-node fluid elements. The solid elements and fluid elements are coupled on the upstream dam face by 13 three-node interface elements. The far-field reservoir is modeled by 13 three-node quadratic line elements. The elements share the same nodes and are compatible on the truncated boundary with those of the near-field fluid elements. The total number of nodes in the whole model is 653.



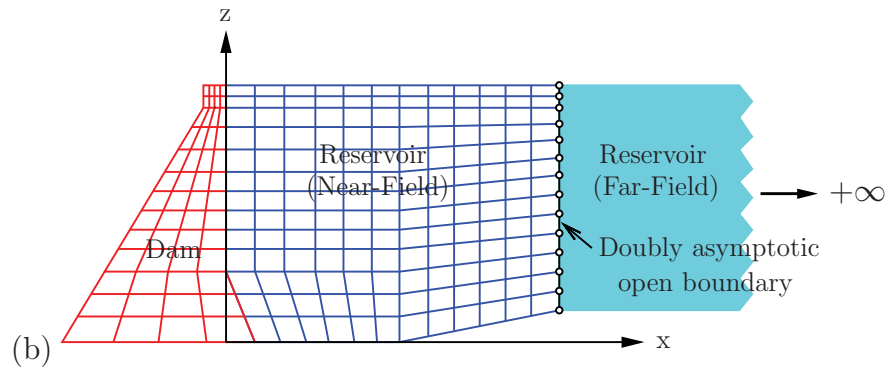


Figure 4.8.8: Gravity dam-reservoir system with irregular near field: (a) geometry and (b) mesh

The triangular impulse (Fig. 4.8.4) is imposed as the horizontal acceleration at the base of the dam. The time step is  $\Delta t = 0.01h/c$ . During one time step, the pressure waves travel about one quarter of the distance between two adjacent nodes. 8,000 time steps are computed. The responses of the hydrodynamic pressure at the heel of dam and the horizontal displacement at the crest of dam are shown in Fig. 4.8.9 and Fig. 4.8.10, respectively. To verify the results, an extended mesh covering a far-field reservoir region of 7,200 m is analyzed. This region is discretized with 5,733 eight-node elements of uniform size (not shown). The total number of nodes is 18,067. The size of extended mesh is sufficiently large to avoid the pollution of the dam response by the waves reflected on the truncated boundary for a time duration of  $t = 80h/c \approx 10$  s. Excellent agreement between the present solutions and the extended mesh solutions is observed.

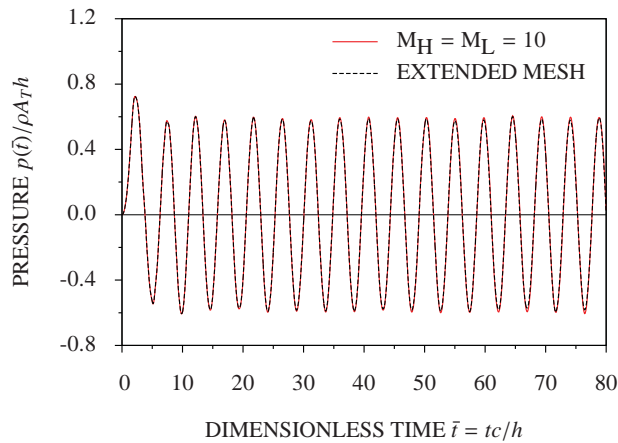


Figure 4.8.9: Hydrodynamic pressure at dam heel under triangular-impulse acceleration

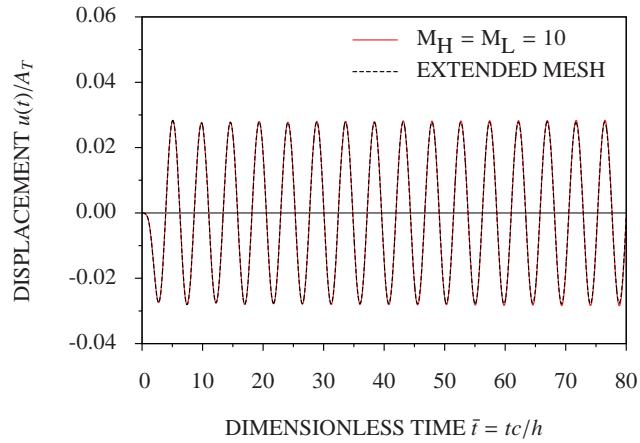


Figure 4.8.10: Horizontal displacement at dam crest under triangular-impulse acceleration

The response of the dam-reservoir system subjected to the El-Centro earthquake ground motion (Fig. 4.8.6) is analyzed. The time step is chosen as 0.002 s during which pressure wave travels about one third of the distance between two adjacent nodes. The responses of the first 20 s are plotted in Fig. 4.8.11 for the hydrodynamic pressure at the heel of dam and in Fig. 4.8.12 for the horizontal displacement at the crest of dam. The results agree very well with the extended mesh solutions during the first 10 s (before the waves reflected on the truncated boundary arrive at the dam).

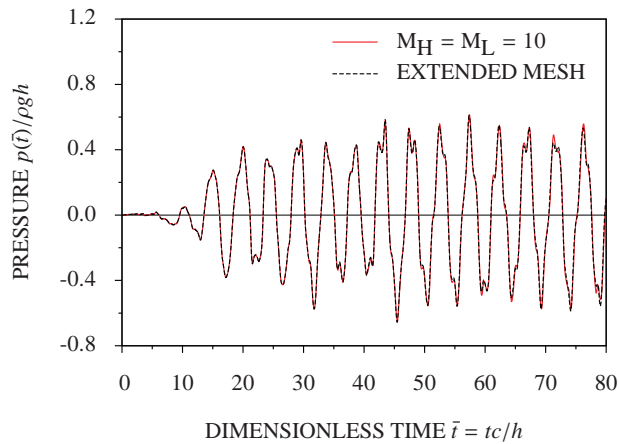


Figure 4.8.11: Hydrodynamic pressure at dam heel under El-Centro ground motion

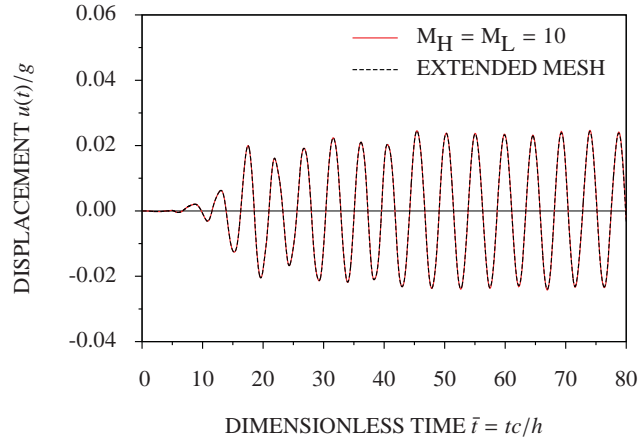


Figure 4.8.12: Horizontal displacement at dam crest under El-Centro ground motion

## 4.9 Conclusions

A high-order doubly asymptotic open boundary condition is developed for evaluating the hydrodynamic pressure in a semi-infinite reservoir with a constant depth. It is established on a vertical truncated boundary by using the scaled boundary finite element method. The same isoparametric finite elements are used in modeling the near field and the far field of semi-infinite reservoir. The open boundary condition is split into a Sommerfeld radiation boundary and external nodal load. Making use of the restart function in the general-purpose finite element package ABAQUS, the response of the gravity dam-reservoir system is solved by a sequential staggered implicit-implicit partitioned procedure. From the point of view of computational cost, this boundary condition is local in both space and time. Numerical examples demonstrate the excellent performance of this present technique for not only early-time but also long-time computations. The open boundary condition is stable and converges rapidly as the order increases.

## Chapter 5

# Improved Doubly Asymptotic Open Boundary for Scalar Wave Propagation in Full-Plane with Circular Cavity

### Abstract

A high-order doubly asymptotic open boundary is improved specifically for scalar wave propagation in a homogeneous full-plane with a circular cavity by extending the scaled boundary finite element method. With the technique of continued fraction, the doubly asymptotic continued fraction solution for modal dynamic stiffness coefficients is derived in the frequency domain. The additional factor coefficients are introduced to the continued fraction solution. The numerical stability of the solution is improved and the singularity problem is avoided. The coefficients of the solution are determined recursively by satisfying the dynamic stiffness equation at both high- and low-frequency limits. By introducing auxiliary variables and the doubly asymptotic continued fraction solution to the force-displacement relationship in the frequency domain, the high-order doubly asymptotic open boundary condition is obtained. It is equivalent to a system of first-order ordinary differential equations in the time domain which is similar to the equation of motion in structural dynamics to which the standard time-step schemes are directly applicable. No parameters other than the orders of continued fraction are selected by the user.

## 5.1 Introduction

Numerical modeling of an unbounded domain is a difficult task since the boundary condition at infinity must be satisfied. Due to the fact that the condition of vanishing displacement amplitude at infinity is insufficient, a radiation condition has to be applied to guarantee the uniqueness of the solution (Wolf and Song, 1996). The radiation condition of scalar wave propagation in an unbounded domain was first introduced to the frequency domain by Sommerfeld in 1949 (Sommerfeld, 1949) as expressed in Eq. (5.1.1),

$$\lim_{r \rightarrow \infty} r^{\frac{(s-1)}{2}} (u(\omega),_r + iku(\omega)) = 0 \quad (5.1.1)$$

where  $u(\omega)$  is the displacement amplitude,  $k$  wave number,  $r$  the radial coordinate,  $s$  the spatial dimension, and  $\omega$  the excitation frequency.

The finite element method (FEM) is the most popular numerical method in analysis of engineering structures. When it is applied to the simulation of wave propagation in an unbounded domain, only a finite part of the unbounded domain (computational domain) can be discretized with finite elements due to the limitation of computer resources. To prevent waves from being reflected at the exterior boundary of the finite element mesh back to the computational domain, it is usually necessary to apply a transmitting or open boundary condition at the exterior boundary. Various methods aiming to construct accurate and efficient open boundaries have been proposed (Wolf and Song, 1996; Givoli, 1992a, 1991; Tsynkov, 1998; Givoli, 2004). Most of the methods can be classified as either rigorous methods or approximate methods.

Rigorous methods attempt to enforce a boundary condition representing the dynamic property of the unbounded domain to ensure that no energy is radiated from infinity towards the excitation source. The well known rigorous methods are, for example, the boundary element method (BEM) and the scaled boundary finite element method (SBFEM). The BEM arises from the potential problems, having a long history of development as documented in papers (Beskos, 1987, 1997) and books (Dominguez, 1993; Hall and Oliveto, 2003). This approach is suited to the modeling of unbounded domains since it can automatically satisfy the radiation condition by using a fundamental solution (Green's function). Moreover, only the boundary representing the unbounded domain is discretized, leading to a reduction of the spatial dimension by one. However, the computational cost of a transient boundary element analysis increases rapidly with the number of time steps due to

the existence of convolution integrals. When the unbounded domain is anisotropic, the evaluation of the fundamental solution become much more complicated.

The SBFEM, a novel semi-analytical approach based on the finite element formulation, is well suited for modeling of unbounded domains (Wolf and Song, 1996; Song and Wolf, 1997; Wolf and Song, 2000; Wolf, 2003). It combines some of the advantages of the FEM and the BEM. Only the boundary is discretized. No fundamental solution is required. The radiation condition is satisfied rigorously.

Rigorous methods are non-local in space and time, in other words, spatially and temporally global. The responses at a specified node and time is evaluated by considering the responses of all nodes on the boundary at all previous time stations. This results in a large computational effort that is inappropriate for modeling large-scale problems.

Approximate methods aim to significantly reduce the computational cost of rigorous methods and provide sufficiently accurate results at the same time. These methods are generally (spatially and temporally) local. In a local procedure, the response at a specified node and time depends on only the responses of a few adjacent nodes at a few previous time stations.

Approximate methods are often formulated as artificial boundary conditions representing unbounded domains. Such boundary conditions are normally enforced on the truncated boundary of the computational domain to absorb energy carried by propagating waves. These artificial boundary conditions are known by different names e.g. transmitting boundary condition, absorbing boundary condition, open boundary condition etc. Usually, an artificial boundary must be placed far enough from the excitation source to prevent spurious reflection. The first artificial boundary is the viscous boundary, also known as the Lysmer-Kuhlemeyer boundary introduced in 1969 (Lysmer and Kuhlemeyer, 1969). This artificial boundary is a low-order absorbing boundary since the order of derivatives in the formulation is one.

Several years later, various high-order absorbing boundary conditions (high-order ABCs) were developed in order to improve the accuracy. The well-known high-order ABCs include the Engquist-Majda ABC (Engquist and Majda, 1979), the Bayliss-Gunzburger-Turkel ABC (Bayliss *et al.*, 1982) and the Higdon ABC (Higdon, 1986). In theory, their orders can increase up to any desired values and their accuracy can be improved by increasing the order. In fact, when the orders are typically higher than two, the algorithms become unstable. The implementation in the time-domain analysis is cumbersome due to the high-order derivatives.

In 1993, Collino first developed a high-order ABC by replacing the high-order derivatives with auxiliary variables. This facilitates the implementation of the absorbing boundary in numerical methods. Several local high-order ABCs e.g. the Hagstrom-Warburton ABC (Hagstrom and Warburton, 2004), the Hagstrom-Mar-Or-Givoli ABC (Hagstrom *et al.*, 2008) and the Bécache-Givoli-Hagstrom ABC (Bécache *et al.*, 2010) follow the method of Collino. Recently, a new approach to constructing a temporally local transmitting boundary of arbitrarily high order has been proposed by Bazyar and Song (2008). The transmitting boundary is applicable to unbounded domains with arbitrary geometry. In addition, anisotropic unbounded media can be analyzed without additional computation cost. The boundary condition enforced on the transmitting boundary is expressed as a system of first-order ordinary differential equations in time. This allows well-established time-stepping schemes in structural dynamics to be applicable to the time domain analysis.

Most of the high-order absorbing boundaries are only singly asymptotic at the high-frequency limit. Thus they are appropriate for radiative fields i.e. all of the field energy virtually propagates out to infinity. In the case of a circular cavity embedded in a full-plane, the rate of convergence of the high-order singly asymptotic open boundary is slow as demonstrated in Chapter 3. From an application point of view, it is highly desirable to develop a temporally local open boundary that is capable of accurately mimicking an unbounded domain over the entire frequency range (i.e. from zero to infinity). A well-known approach is the doubly-asymptotic approximation (DAA) which can be regarded as an ABC. The DAA has a long time history of development as reported by Geers (1978), Underwood and Geers (1981), Geers and Zhang (1994), Geers and Lewis (1997) and Geers and Toothaker (2000). The formulation of the DAA is temporally local but spatially global. The dynamic stiffness obtained from the DAA is accurate not only at the high-frequency limit but also at statics. The highest order of the DAA as reported in the literature is three (Geers and Toothaker, 2000).

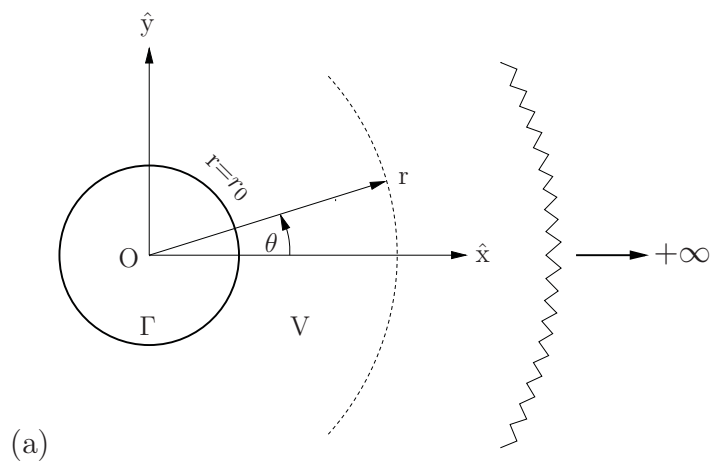
The high-order doubly asymptotic open boundary constructed in Chapter 3 was developed specifically for the modal equations of scalar waves. It is doubly asymptotic at both high- and low-frequency limits. The formulation is expressed as a system of first-order ordinary differential equations in the time domain. Well-established time-stepping schemes in structural dynamics are directly applicable. The high-order open boundary is temporally local. The amount of computer time and storage are the same as those required by the high-order singly asymptotic open boundary.

The objective of this chapter is to improve the high-order doubly asymptotic open boundary for a circular cavity embedded in a full-plane in Chapter 3. Factor

coefficients are introduced in the derivation of the doubly asymptotic continued fraction solution to improve the numerical stability of the solution procedure. As a result, the denominators of the continued fraction coefficients turn into only sign functions which can avoid the singularity and ill-conditioned problems. This chapter is organized as follows: in Section 5.2, the governing differential equation of a two-dimensional scalar wave for a full-plane with a circular cavity is presented. In Section 5.3, the scaled boundary finite element equation in displacement is derived in the frequency domain. In Section 5.4, the equations of modal dynamic stiffness coefficients are formulated. In Section 5.5, the derivation of the doubly asymptotic continued fraction solution for modal dynamic stiffness coefficients is presented. In Section 5.6, the high-order doubly asymptotic boundary condition of the full-plane with a circular cavity is constructed in both frequency and time domains. In Section 5.7, the numerical examples are demonstrated in the frequency and time domains. In Section 5.8, conclusions are presented.

## 5.2 Governing differential equation of scalar waves

A circular cavity of radius  $r_0$  embedded in a full-plane is shown in Fig. 5.2.1(a). The full-plane is homogeneous and the material constants are the shear modulus  $G$  and the mass density  $\rho$ . The out-of-plane or anti-plane motion  $u = u(\hat{x}, \hat{y}, t)$  of the full-plane in the Cartesian coordinates  $(\hat{x}, \hat{y})$  is considered. For the boundary condition, it is assumed that the circular boundary  $\Gamma$  located at  $r = r_0$  is subjected to time-dependent out-of-plane shear stresses.



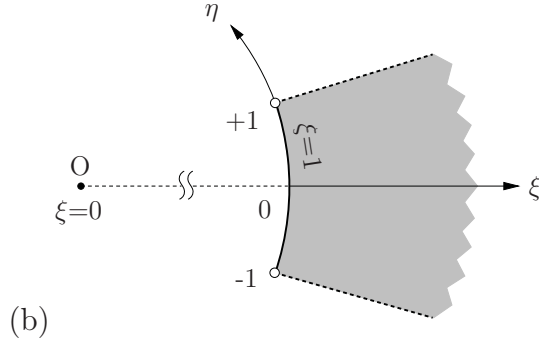


Figure 5.2.1: Full-plane with circular cavity: (a) Cartesian and polar coordinates and (b) typical element and scaled boundary coordinates

Introducing the differential operator denoting the vector of spatial derivatives in the Cartesian coordinates,

$$\{L\} = \left[ \frac{\partial}{\partial \hat{x}} \quad \frac{\partial}{\partial \hat{y}} \right]^T \quad (5.2.1)$$

The out-of-plane strains  $\{\gamma\} = [\gamma_{\hat{z}\hat{x}} \quad \gamma_{\hat{z}\hat{y}}]^T$  are expressed as

$$\{\gamma\} = \{L\}u \quad (5.2.2)$$

The out-of-plane shear stresses  $\{\tau\} = [\tau_{\hat{z}\hat{x}} \quad \tau_{\hat{z}\hat{y}}]^T$  are equal to

$$\{\tau\} = G\{\gamma\} \quad (5.2.3)$$

where  $\tau_{\hat{z}\hat{x}}$  and  $\tau_{\hat{z}\hat{y}}$  are out-of-plane shear stresses, and  $\gamma_{\hat{z}\hat{x}}$  and  $\gamma_{\hat{z}\hat{y}}$  are the corresponding shear strains. They are expressed as

$$\gamma_{\hat{z}\hat{x}} = u_{,\hat{x}} \quad (5.2.4a)$$

$$\gamma_{\hat{z}\hat{y}} = u_{,\hat{y}} \quad (5.2.4b)$$

The governing differential equation of motion is expressed as

$$\{L\}^T\{\tau\} - \rho\ddot{u} = 0 \quad (5.2.5)$$

where  $\ddot{u}$  is the acceleration in the out-of-plane direction. Substituting Eq. (5.2.3) into Eq. (5.2.5) and using Eqs. (5.2.1) and (5.2.2) lead to the scalar wave equation formulated in two-dimensional Cartesian coordinates,

$$\nabla^2 u = \frac{1}{c_s^2} \ddot{u} \quad (5.2.6)$$

where  $\nabla^2$  is the Laplace operator,

$$\nabla^2 = \frac{\partial^2}{\partial \hat{x}^2} + \frac{\partial^2}{\partial \hat{y}^2} \quad (5.2.7)$$

and  $c_s$  the speed of shear wave,

$$c_s = \sqrt{\frac{G}{\rho}} \quad (5.2.8)$$

### 5.3 Scaled boundary finite element method for full-plane with circular cavity

The scaled boundary finite element method (SBFEM) is a novel semi-analytical approach. It was first developed for modeling unbounded domains with arbitrary geometry as the consistent infinitesimal finite-element cell method (Wolf and Song, 1996). The original derivation of the SBFEM for scalar wave propagation was proposed by Song and Wolf (1995). In modeling of a circular cavity embedded in a full-plane with radius  $r_0$  (see Fig. 5.2.1(a)), the scaling center  $O$  is located at the center of the circular cavity so that the circular boundary  $\Gamma$  can be visible from it.

The circular boundary  $\Gamma$  shown in Fig. 5.2.1(a) is discretized by one-dimensional line elements. The total number of nodes is denoted as  $n$ . A typical element is shown in Fig. 5.2.1(b). Its geometry can be expressed in the scaled boundary coordinates  $(\xi, \eta)$  as

$$\hat{x} = \xi x(\eta) \quad (5.3.1a)$$

$$\hat{y} = \xi y(\eta) \quad (5.3.1b)$$

where  $\xi$  is the radial coordinate that  $\xi \geq 1$ , and  $\eta$  the circumferential coordinate that  $-1 \leq \eta \leq 1$ . The functions  $x(\eta)$  and  $y(\eta)$  in Eq. (5.3.1) are defined as functions of the circumferential coordinate  $\eta$ ,

$$x(\eta) = r \cos(\theta(\eta)) \quad (5.3.2a)$$

$$y(\eta) = r \sin(\theta(\eta)) \quad (5.3.2b)$$

Only the coordinate  $\theta(\eta)$  is interpolated by using the shape functions  $[N(\eta)]$  as

$$\theta(\eta) = [N(\eta)]\{\theta\} \quad (5.3.3)$$

where  $\{\theta\}$  denotes the circumferential coordinate vector of the nodes on the circular boundary  $\Gamma$ . As referred in Wolf and Song (1996) and Wolf (2003), the vector of spatial derivatives in the Cartesian coordinates  $\{L\}$  related to those in the scaled boundary coordinates  $[\frac{\partial}{\partial\xi} \quad \frac{\partial}{\partial\eta}]^T$  is expressed as

$$\{L\} = [\hat{J}(\xi, \eta)]^{-1} [\frac{\partial}{\partial\xi} \quad \frac{\partial}{\partial\eta}]^T \quad (5.3.4)$$

where  $[\hat{J}(\xi, \eta)]$  is the Jacobian matrix, which is expressed as

$$[\hat{J}(\xi, \eta)] = \begin{bmatrix} \hat{x}_{,\xi} & \hat{y}_{,\xi} \\ \hat{x}_{,\eta} & \hat{y}_{,\eta} \end{bmatrix} = \begin{bmatrix} 1 & \\ & \xi \end{bmatrix} [J(\eta)] \quad (5.3.5)$$

and its inverse is

$$[\hat{J}(\xi, \eta)]^{-1} = [J(\eta)]^{-1} \begin{bmatrix} 1 & \\ & 1/\xi \end{bmatrix} \quad (5.3.6)$$

$[J(\eta)]$  in Eq. (5.3.5) is expressed as (using Eq. (5.3.2)),

$$[J(\eta)] = \begin{bmatrix} x & y \\ x_{,\eta} & y_{,\eta} \end{bmatrix} = r \begin{bmatrix} \cos(\theta(\eta)) & \sin(\theta(\eta)) \\ -\sin(\theta(\eta))\theta(\eta)_{,\eta} & \cos(\theta(\eta))\theta(\eta)_{,\eta} \end{bmatrix} \quad (5.3.7)$$

Its inverse and determinant are

$$[J(\eta)]^{-1} = \frac{r}{|J(\eta)|} \begin{bmatrix} \cos(\theta(\eta))\theta(\eta)_{,\eta} & -\sin(\theta(\eta)) \\ \sin(\theta(\eta))\theta(\eta)_{,\eta} & \cos(\theta(\eta)) \end{bmatrix} \quad (5.3.8)$$

$$|J(\eta)| = r^2\theta(\eta)_{,\eta} = r^2[N(\eta)]_{,\eta} \{\theta\} \quad (5.3.9)$$

respectively. Substituting Eq. (5.3.6) into Eq. (5.3.4) and using Eq. (5.3.8) yield

$$\{L\} = \{b^1(\eta)\} \frac{\partial}{\partial\xi} + \frac{1}{\xi} \{b^2(\eta)\} \frac{\partial}{\partial\eta} \quad (5.3.10)$$

where  $\{b^1(\eta)\}$  and  $\{b^2(\eta)\}$  are defined as

$$\{b^1(\eta)\} = \frac{1}{r} [\cos(\theta(\eta)) \quad \sin(\theta(\eta))]^T \quad (5.3.11a)$$

$$\{b^2(\eta)\} = \frac{r}{|J(\eta)|} [-\sin(\theta(\eta)) \quad \cos(\theta(\eta))]^T \quad (5.3.11b)$$

Note that  $\{b^1(\eta)\}$  and  $\{b^2(\eta)\}$  are orthogonal.

The displacements along radial lines passing through the scaling center  $O$  and a node on the boundary are represented by nodal displacement functions  $\{u(\xi)\}$ .

The displacement field  $u$  in Eq. (5.2.2) is approximated by interpolating the nodal displacement function  $\{u(\xi)\}$  piecewisely,

$$u = u(\xi, \eta) = [N(\eta)]\{u(\xi)\} \quad (5.3.12)$$

Substituting Eqs. (5.3.10) and (5.3.12) into Eq. (5.2.2) yields

$$\{\gamma\} = [B^1(\eta)]\{u(\xi)\}_{,\xi} + \frac{1}{\xi}[B^2(\eta)]\{u(\xi)\} \quad (5.3.13)$$

where  $[B^1(\eta)]$  and  $[B^2(\eta)]$  are defined as

$$[B^1(\eta)] = \{b^1(\eta)\}[N(\eta)] \quad (5.3.14a)$$

$$[B^2(\eta)] = \{b^2(\eta)\}[N(\eta)]_{,\eta} \quad (5.3.14b)$$

Substituting Eq. (5.3.13) into Eq. (5.2.3) leads to

$$\{\tau\} = G([B^1(\eta)]\{u(\xi)\}_{,\xi} + \frac{1}{\xi}[B^2(\eta)]\{u(\xi)\}) \quad (5.3.15)$$

Applying the virtual work principle or the Galerkin's weighted residual method (Wolf, 2003), the scaled boundary finite element equation in displacement is obtained as

$$[E^0]\xi^2\{U(\xi)\}_{,\xi\xi} + [E^0]\xi\{U(\xi)\}_{,\xi} - [E^2]\{U(\xi)\} + \omega^2[M^0]\xi^2\{U(\xi)\} = 0 \quad (5.3.16)$$

where  $\omega$  is the excitation frequency,  $\{U(\xi)\}$  denotes the nodal displacement amplitudes in the frequency domain, and the coefficient matrices  $[E^0]$ ,  $[E^2]$  and  $[M^0]$  are defined as

$$[E^0] = \int_{-1}^{+1} [B^1(\eta)]^T G [B^1(\eta)] |J(\eta)| d\eta \quad (5.3.17a)$$

$$[E^2] = \int_{-1}^{+1} [B^2(\eta)]^T G [B^2(\eta)] |J(\eta)| d\eta \quad (5.3.17b)$$

$$[M^0] = \int_{-1}^{+1} [N(\eta)]^T \rho [N(\eta)] |J(\eta)| d\eta \quad (5.3.17c)$$

$[E^0]$  and  $[M^0]$  are symmetric and positive definite.  $[E^2]$  is also symmetric but semi-positive definite. Because  $\{b^1(\eta)\}$  and  $\{b^2(\eta)\}$  are orthogonal for the circular boundary  $\Gamma$ , the coefficient  $[E^1]$  occurring in an arbitrary boundary vanishes (Fan and Li, 2008).

The internal nodal force vector  $\{Q\}$  is expressed as

$$\{Q\} = [E^0]\xi\{U(\xi)\}_{,\xi} \quad (5.3.18)$$

By substituting Eq. (5.3.14a) into Eq. (5.3.17a) and using Eq. (5.3.11a), Eq. (5.3.17a) can be rewritten as

$$[E^0] = \frac{1}{r^2} \int_{-1}^{+1} [N(\eta)]^T G [N(\eta)] |J(\eta)| d\eta \quad (5.3.19)$$

Equations (5.3.17c) and (5.3.19) are proportional to each other and can be written in terms of

$$[M^0] = (r/c_s)^2 [E^0] \quad (5.3.20)$$

using Eq. (5.2.8). After substituting Eq. (5.3.20) into Eq. (5.3.16), Eq. (5.3.16) can be expressed as

$$[E^0]\xi^2\{U(\xi)\}_{,\xi\xi} + [E^0]\xi\{U(\xi)\}_{,\xi} - [E^2]\{U(\xi)\} + a^2[E^0]\{U(\xi)\} = 0 \quad (5.3.21)$$

where the dimensionless frequency  $a$  is defined as

$$a = \frac{\omega r \xi}{c_s} \quad (5.3.22)$$

Note that the coefficient matrices of the full-plane at the circular boundary  $\Gamma$  are obtained from the assembly of the coefficient matrices  $[E^0]$ ,  $[E^2]$  and  $[M^0]$  of individual elements. To simplify the nomenclature, the same symbols are used for the assembled coefficient matrices.

## 5.4 Modal dynamic stiffness coefficients of full-plane with circular cavity

The scaled boundary finite element equation (Eq. (5.3.21)) can be decoupled by using the following eigenvalue problem,

$$[E^2][\Phi] = [E^0][\Phi][\lambda^2] \quad (5.4.1)$$

where  $[\lambda^2]$  and  $[\Phi]$  denote the eigenvalues and eigenvectors, respectively. Since  $[E^0]$  is positive definite and  $[E^2]$  is semi-positive definite, the eigenvectors are orthogonal.

They are normalized as

$$[\Phi]^T [E^0] [\Phi] = [I] \quad (5.4.2a)$$

$$[\Phi]^T [E^2] [\Phi] = [\lambda^2] \quad (5.4.2b)$$

Pre- and post-multiplying Eq. (5.3.21) by  $[\Phi]^T$  and  $[\Phi]$ , respectively and using Eq. (5.4.2) result in

$$\xi^2 \{\tilde{U}\}_{,\xi\xi} + \xi \{\tilde{U}\}_{,\xi} - [\lambda^2] \{\tilde{U}\} + a^2 \{\tilde{U}\} = 0 \quad (5.4.3)$$

with

$$\{\tilde{U}\} = [\Phi]^{-1} \{U(\xi)\} \quad (5.4.4)$$

Equation (5.4.3) is decomposed into a series of independent modal equations,

$$\xi^2 \tilde{U}_{j,\xi\xi} + \xi \tilde{U}_{j,\xi} + (a^2 - \lambda_j^2) \tilde{U}_j = 0 \quad (j = 1, 2, \dots, n) \quad (5.4.5)$$

where  $j$  denotes the modal index. The interaction force vector  $\{R\}$  relates to the internal nodal force vector  $\{Q\}$  as the following equations:

$$\{R\} = -\{Q\} \quad (5.4.6)$$

Substituting Eq. (5.3.18) into Eq. (5.4.6), pre-multiplying the equation by  $[\Phi]^T$ , and using Eqs. (5.4.2a) and (5.4.4) leads to the modal forces

$$\{\tilde{R}\} = -\xi \{\tilde{U}\}_{,\xi} \quad (5.4.7)$$

with

$$\{\tilde{R}\} = [\Phi]^T \{R\} \quad (5.4.8)$$

Equation (5.4.8) is equivalent to a series of modal equations,

$$\tilde{R}_j = -\xi \tilde{U}_{j,\xi} \quad (j = 1, 2, \dots, n) \quad (5.4.9)$$

The modal dynamic stiffness coefficient  $S_j = S_j(a, \xi)$  is defined by the force-displacement relationship of each mode

$$\tilde{R}_j = S_j \tilde{U}_j \quad (j = 1, 2, \dots, n) \quad (5.4.10)$$

Proceeding as in Chapter 3 by eliminating  $\tilde{R}_j$  and  $\tilde{U}_j$  from Eqs. (5.4.5), (5.4.9), and (5.4.10), the equations of modal dynamic stiffness coefficients on the circular boundary  $\Gamma$  ( $r = r_0$  and  $\xi = 1$ ) can be obtained as

$$(S_j(a_0))^2 - a_0(S_j(a_0))_{,a_0} + a_0^2 - \lambda_j^2 = 0 \quad (j = 1, 2, \dots, n) \quad (5.4.11)$$

where the dimensionless frequency is

$$a_0 = \frac{\omega r_0}{c_s} \quad (5.4.12)$$

The exact solution of the modal stiffness was obtained in Chapter 3 and given in Eq. (3.2.27) as

$$S_{\text{ex},j}(a_0) = -\frac{a_0}{H_{\lambda_j}^{(2)}(a_0)}(H_{\lambda_j}^{(2)}(a_0))_{,a_0} = \lambda_j - \frac{H_{\lambda_j-1}^{(2)}(a_0)}{H_{\lambda_j}^{(2)}(a_0)} \quad (j = 1, 2, \dots, n) \quad (5.4.13)$$

where  $H_{\lambda_j}^{(2)}(a_0)$  and  $H_{\lambda_j-1}^{(2)}(a_0)$  are the second-kind Hankel functions of order  $\lambda_j$  and order  $\lambda_j - 1$ , respectively.

## 5.5 Doubly asymptotic continued fraction solution for modal dynamic stiffness coefficients

This section describes the solution of the scaled boundary finite element equation for modal dynamic stiffness coefficient (Eq. (5.4.11)). The solution is sought as a doubly asymptotic continued fraction solution. Two steps are involved in the solution procedure. In the first step detailed in Section 5.5.1, a continued fraction solution is determined at the high-frequency limit recursively. In each recursion, the coefficients of one term of the continued fractions is obtained, and an equation is established for the residual. In the second step detailed in Section 5.5.2, a continued fraction solution of the residual equation of the high-frequency solution is determined at the low-frequency limit recursively. The doubly asymptotic solution is obtained by joining the low-frequency solution to the last term of the high-frequency solution. For simplicity in the derivation, the modal index  $j$  is omitted in this section.

### 5.5.1 Continued fraction solution at high frequency

The continued fraction solution at high frequency is written as

$$S(a_0) = K_\infty + (ia_0)C_\infty - (\psi^{(1)})^2(Y^{(1)}(a_0))^{-1} \quad (5.5.1a)$$

$$Y^{(i)}(a_0) = Y_0^{(i)} + (ia_0)Y_1^{(i)} - (\psi^{(i+1)})^2(Y^{(i+1)}(a_0))^{-1} \quad (i = 1, 2, \dots, M_H) \quad (5.5.1b)$$

where  $K_\infty$ ,  $C_\infty$ ,  $Y_0^{(i)}$  and  $Y_1^{(i)}$  are coefficients to be determined recursively in the solution procedure. In comparison with the solution in Eq. (3.3.2) in Chapter 3 for the modal stiffness of the homogeneous, the additional factor coefficients  $\psi^{(1)}$  and  $\psi^{(i+1)}$  are introduced in order to improve the numerical stability of the solution procedure. To maintain the symmetry of the coefficient matrices of the open boundary (Eq. (5.6.16) in Section 5.6), the square of the factor coefficients are used in the residual terms  $(\psi^{(1)})^2(Y^{(1)}(a_0))^{-1}$  and  $(\psi^{(i+1)})^2(Y^{(i+1)}(a_0))^{-1}$ .  $M_H$  is the order of the continued fraction solution at high frequency.

The coefficients  $K_\infty$  and  $C_\infty$  are determined by substituting Eq. (5.5.1a) into Eq. (5.4.11). This leads to an equation of a power series of  $(ia_0)$ , including the following three terms:

$$\begin{aligned} (ia_0)^2(C_\infty^2 - 1) + ia_0(2C_\infty K_\infty - C_\infty) + (K_\infty^2 - \lambda^2 - 2((ia_0)C_\infty + K_\infty)(\psi^{(1)})^2(Y^{(1)}(a_0))^{-1} \\ + (\psi^{(1)})^4(Y^{(1)}(a_0))^{-2} - a_0(\psi^{(1)})^2(Y^{(1)}(a_0))^{-2}(Y^{(1)}(a_0))_{,a_0}) = 0 \end{aligned} \quad (5.5.2)$$

This equation is satisfied by setting all the three terms equal to zero. Thus the solution for  $C_\infty$  that satisfies the radiation condition is obtained from the first term ( $(ia_0)^2$  term) by selecting the positive root

$$C_\infty = 1 \quad (5.5.3)$$

By substituting Eq. (5.5.3) into the second term of Eq. (5.5.2) ( $(ia_0)$  term), the solution for  $K_\infty$  is determined as

$$K_\infty = 0.5 \quad (5.5.4)$$

The last term of Eq. (5.5.2) is an equation of  $(Y^{(1)}(a_0))^{-1}$ . After being multiplied by  $(Y^{(1)}(a_0))^2(\psi^{(1)})^{-2}$ , it is expressed as the  $i = 1$  case of

$$a^{(i)} - 2(b_0^{(i)} + (ia_0))Y^{(i)}(a_0) + c^{(i)}(Y^{(i)}(a_0))^2 - a_0(Y^{(i)}(a_0))_{,a_0} = 0 \quad (5.5.5)$$

with the following constants:

$$a^{(1)} = (\psi^{(1)})^2 \quad (5.5.6a)$$

$$b_0^{(1)} = 0.5 \quad (5.5.6b)$$

$$c^{(1)} = (0.25 - \lambda^2)/(\psi^{(1)})^2 = \text{sgn}^{(1)} \quad (5.5.6c)$$

The factor coefficient  $\psi^{(1)}$  is selected to avoid the occurrence of  $c^{(1)} = 0$ . A simple and convenient choice is

$$\psi^{(1)} = |0.25 - \lambda^2|^{1/2} \quad (5.5.7)$$

Equation (5.5.6) is rewritten as

$$a^{(1)} = |0.25 - \lambda^2| \quad (5.5.8a)$$

$$b_0^{(1)} = 0.5 \quad (5.5.8b)$$

$$c^{(1)} = \text{sgn}^{(1)} = \begin{cases} +1, & \text{when } 0.25 - \lambda^2 \geq 0 \\ -1, & \text{when } 0.25 - \lambda^2 < 0 \end{cases} \quad (5.5.8c)$$

with the sign function  $\text{sgn}^{(1)}$ .

To begin the recursive procedure, Eq. (5.5.1b) is substituted into Eq. (5.5.5). This also results in an equation of a power series of  $(ia_0)$  grouped into the following three terms:

$$\begin{aligned} & (ia_0)^2(c^{(i)}(Y_1^{(i)})^2 - 2Y_1^{(i)}) + (ia_0)(2c^{(i)}Y_0^{(i)}Y_1^{(i)} - 2b_0^{(i)}Y_1^{(i)} - 2Y_0^{(i)} - Y_1^{(i)}) \\ & + (a^{(i)} - 2b_0^{(i)}Y_0^{(i)} + c^{(i)}(Y_0^{(i)})^2 + (2((ia_0) + b_0^{(i)}) - 2c^{(i)}(Y_0^{(i)} + (ia_0)Y_1^{(i)})) \\ & \quad \times (\psi^{(i+1)})^2(Y^{(i+1)}(a_0))^{-1} + c^{(i)}(\psi^{(i+1)})^4(Y^{(i+1)}(a_0))^{-2} \\ & \quad - (\psi^{(i+1)})^2(Y^{(i+1)}(a_0))^{-2}a_0(Y^{(i+1)}(a_0))_{,a_0} = 0 \quad (5.5.9) \end{aligned}$$

Equation (5.5.9) is also satisfied by setting all the three terms equal to zero. The first term ( $(ia_0)^2$  term) leads to an equation of  $Y_1^{(i)}$ . Its non-zero solution is equal to

$$Y_1^{(i)} = 2/c^{(i)} = 2/\text{sgn}^{(i)} \quad (5.5.10)$$

Setting the second term (( $ia_0$ ) term) to zero yields an equation of  $Y_0^{(i)}$ . By using Eq. (5.5.10), its solution is obtained as

$$Y_0^{(i)} = (2b_0^{(i)} + 1)/c^{(i)} = (2b_0^{(i)} + 1)/sgn^{(i)} \quad (5.5.11)$$

Note that the solution of  $Y_1^{(i)}$  in Eq. (5.5.10) and of  $Y_0^{(i)}$  in Eq. (5.5.11) will be singular when the constant  $c^{(i)}$  appearing in the denominators is equal to zero. In the original doubly asymptotic continued fraction solution, this situation occurs when the modal number  $\lambda = i/2$  ( $i = 1, 2, \dots$ ). When a modal number is close to these values,  $Y_1^{(i)}$  and  $Y_0^{(i)}$  become very large and the continued fraction solution becomes ill-conditioned. The above choice of the factor coefficient  $\psi^{(1)}$  in Eq. (5.5.7) ensures that the solutions of  $Y_1^{(i)}$  and  $Y_0^{(i)}$  remain finite as  $c^{(i)}$  is equal to either +1 or -1. This improves the numerical accuracy and stability of the continued fraction solution.

The last term in Eq. (5.5.9) is an equation of  $Y^{(i+1)}(a_0)$ . It is simplified by substituting  $-2b_0^{(i)}Y_0^{(i)} + c^{(i)}(Y_0^{(i)})^2 = Y_0^{(i)}$  reformulated from Eq. (5.5.11). Multiplying the resulting equation by  $(Y^{(i+1)}(a_0))^2(\psi^{(i+1)})^{-2}$  leads to an equation in the same form as Eq. (5.5.5),

$$a^{(i+1)} - 2(b_0^{(i+1)} + (ia_0))(Y^{(i+1)}(a_0)) + c^{(i+1)}(Y^{(i+1)}(a_0))^2 - a_0(Y^{(i+1)}(a_0))_{,a_0} = 0 \quad (5.5.12)$$

with the constant

$$a^{(i+1)} = c^{(i)}(\psi^{(i+1)})^2 \quad (5.5.13a)$$

$$b_0^{(i+1)} = b_0^{(i)} + 1 \quad (5.5.13b)$$

$$c^{(i+1)} = (a^{(i)} + Y_0^{(i)})/(\psi^{(i+1)})^2 = sgn^{(i+1)} \quad (5.5.13c)$$

The factor coefficient  $\psi^{(i+1)}$  is set equal to

$$\psi^{(i+1)} = \begin{cases} |a^{(i)} + Y_0^{(i)}|^{1/2}, & \text{when } i < M_H \\ |(2\lambda - 1)(a^{(M_H)} + Y_0^{(M_H)})|^{1/2}, & \text{when } i = M_H \end{cases} \quad (5.5.14)$$

Equation (5.5.13) is rewritten as

$$a^{(i+1)} = c^{(i)}(\psi^{(i+1)})^2 \quad (5.5.15a)$$

$$b_0^{(i+1)} = i + 0.5 \quad (5.5.15b)$$

$$c^{(i+1)} = \text{sgn}^{(i+1)} = \begin{cases} +1, & \text{when } a^{(i)} + Y_0^{(i)} \geq 0 \\ -1, & \text{when } a^{(i)} + Y_0^{(i)} < 0 \end{cases} \quad (5.5.15c)$$

where  $b_0^{(i+1)}$  in Eq. (5.5.15b) is obtained from Eqs. (5.5.8b) and (5.5.13b).

The continued fraction solution is determined recursively using Eqs. (5.5.10) and (5.5.11) where the constants  $a^{(i)}$ ,  $b_0^{(i)}$  and  $c^{(i)}$  are initialized by Eq. (5.5.8) and updated during the recursion with Eq. (5.5.15). As an example, the order  $M_H = 2$  continued fraction solution is evaluated explicitly as

$$Y_0^{(1)} = 2/\text{sgn}^{(1)}; \quad Y_1^{(1)} = 2/\text{sgn}^{(1)}; \quad \psi^{(1)} = |0.25 - \lambda^2|^{1/2} \quad (5.5.16a)$$

$$Y_0^{(2)} = 4/\text{sgn}^{(2)}; \quad Y_1^{(2)} = 2/\text{sgn}^{(2)}; \quad \psi^{(2)} = |2.25 - \lambda^2|^{1/2} \quad (5.5.16b)$$

After an  $M_H$  order continued fraction solution is obtained at the high-frequency limit, the residual satisfies Eq. (5.5.12) with  $i = M_H$ . For later use in the low-frequency limit, the following identity is derived from Eqs. (5.5.13), (5.5.11) and (5.5.6):

$$(b_0^{(i+1)})^2 - a^{(i+1)}c^{(i+1)} = (b_0^{(i)} + 1)^2 - c^{(i)}a^{(i)} - c^{(i)}Y_0^{(i)} = (b_0^{(i)})^2 - c^{(i)}a^{(i)} = \lambda^2 \quad (5.5.17)$$

## 5.5.2 Continued fraction solution at low frequency

The residual equation (Eq. (5.5.12)) of the high-frequency continued fraction solution is solved again by a continued fraction but at low frequency limit  $\omega \rightarrow 0$ . For simplicity in notation, the residual is expressed as

$$Y_L(a_0) = Y^{(M_H+1)}(a_0) \quad (5.5.18)$$

and Eq. (5.5.12) is rewritten as

$$a_L - 2(b_{L0} + ia_0)(Y_L(a_0)) + c_L(Y_L(a_0))^2 - a_0(Y_L(a_0))_{,a_0} = 0 \quad (5.5.19)$$

with the following constants used at the low-frequency limit:

$$a_L = a^{(M_H+1)} = c^{(M_H)}(\psi_L^{(0)})^2 \quad (5.5.20a)$$

$$b_{L0} = b_0^{(M_H+1)} = M_H + 0.5 \quad (5.5.20b)$$

$$c_L = c^{(M_H+1)} = (a^{(M_H)} + Y_0^{(M_H)})/(\psi_L^{(0)})^2 = \text{sgn}_L^{(0)}/|2\lambda - 1| \quad (5.5.20c)$$

where

$$\psi_L^{(0)} = \psi^{(M_H+1)} \quad (5.5.21a)$$

$$\text{sgn}_L^{(0)} = \text{sgn}^{(M_H+1)} \quad (5.5.21b)$$

The continued fraction solution at the low-frequency limit is expressed as

$$Y_L(a_0) = Y_{L0}^{(0)} + (ia_0)Y_{L1}^{(0)} - (ia_0)^2(\psi_L^{(1)})^2(Y_L^{(1)}(a_0))^{-1} \quad (5.5.22a)$$

$$Y_L^{(i)}(a_0) = Y_{L0}^{(i)} + (ia_0)Y_{L1}^{(i)} - (ia_0)^2(\psi_L^{(i+1)})^2(Y_L^{(i+1)}(a_0))^{-1} \quad (i = 1, 2, \dots, M_L) \quad (5.5.22b)$$

where  $Y_{L0}^{(0)}$ ,  $Y_{L1}^{(0)}$ ,  $Y_{L0}^{(i)}$  and  $Y_{L1}^{(i)}$  are coefficients to be determined recursively. The factor coefficients  $\psi_L^{(1)}$  and  $\psi_L^{(i+1)}$  are introduced to improve the numerical stability of the solution.  $(ia_0)^2(\psi_L^{(1)})^2(Y_L^{(1)}(a_0))^{-1}$  and  $(ia_0)^2(\psi_L^{(i+1)})^2(Y_L^{(i+1)}(a_0))^{-1}$  are residual terms.  $M_L$  is the order of the continued fraction solution at low frequency.

Substituting Eq. (5.5.22a) into Eq. (5.5.19) leads to an equation of a power series of  $(ia_0)$ ,

$$\begin{aligned} & (a_L - 2b_{L0}Y_{L0}^{(0)} + c_L(Y_{L0}^{(0)})^2) + (ia_0)(-2Y_{L0}^{(0)} - 2b_{L0}Y_{L1}^{(0)} + 2c_L Y_{L0}^{(0)} Y_{L1}^{(0)} - Y_{L1}^{(0)}) \\ & + (ia_0)^2 \left( -2Y_{L1}^{(0)} + c_L(Y_{L1}^{(0)})^2 + (2(b_{L0} + (ia_0)) - 2c_L(Y_{L0}^{(0)} + (ia_0)Y_{L1}^{(0)})) \right. \\ & \times (\psi_L^{(1)})^2(Y_L^{(1)}(a_0))^{-1} + 2(\psi_L^{(1)})^2(Y_L^{(1)}(a_0))^{-1} + (ia_0)^2 c_L (\psi_L^{(1)})^4 (Y_L^{(1)}(a_0))^{-2} \\ & \left. - (\psi_L^{(1)})^2 (Y_L^{(1)}(a_0))^{-2} a_0 (Y_L^{(1)}(a_0))_{,a_0} \right) = 0 \quad (5.5.23) \end{aligned}$$

Similarly, this equation is satisfied by setting each of the three terms equal to zero. The first term (constant term independent of  $(ia_0)$ ) yields

$$a_L - 2b_{L0}Y_{L0}^{(0)} + c_L(Y_{L0}^{(0)})^2 = 0 \quad (5.5.24)$$

By using Eqs. (5.5.17) and (5.5.20), the determinant of this quadratic algebraic equation is equal to

$$(2b_{L0})^2 - 4a_L c_L = 4\lambda^2 \quad (5.5.25)$$

Thus the solution for  $Y_{L0}^{(0)}$  in Eq. (5.5.24) can be determined as

$$Y_{L0}^{(0)} = (b_{L0} + \lambda)/c_L = (b_{L0} + \lambda)|2\lambda - 1|/sgn_L^{(0)} \quad (5.5.26)$$

by using Eq. (5.5.25). Setting the second term ( $(ia_0)$  term) in Eq. (5.5.23) to zero and using Eq. (5.5.26) lead to the solution for  $Y_{L1}^{(0)}$ ,

$$Y_{L1}^{(0)} = 2Y_{L0}^{(0)}/(2\lambda - 1) = 2(b_{L0} + \lambda)/(sgn_L^{(0)} sgn_{L0}^{(0)}) \quad (5.5.27)$$

with the sign function

$$sgn_{L0}^{(0)} = \begin{cases} +1, & \text{when } 2\lambda - 1 \geq 0 \\ -1, & \text{when } 2\lambda - 1 < 0 \end{cases} \quad (5.5.28)$$

Multiplying the last term ( $(ia_0)^2$  term) of Eq. (5.5.23) by  $(Y_L^{(1)}(a_0))^2(\psi_L^{(1)})^{-2}$  results in an equation of  $Y_L^{(1)}(a_0)$ . It is expressed as the  $i = 1$  case of

$$(ia_0)^2 a_L^{(i)} - 2(b_{L0}^{(i)} + (ia_0)b_{L1}^{(i)})Y_L^{(i)}(a_0) + c_L^{(i)}(Y_L^{(i)}(a_0))^2 - a_0(Y_L^{(i)}(a_0))_{,a_0} = 0 \quad (5.5.29)$$

with the following constants:

$$a_L^{(1)} = c_L(\psi_L^{(1)})^2 \quad (5.5.30a)$$

$$b_{L0}^{(1)} = -1 - b_{L0} + c_L Y_{L0}^{(0)} = -1 + \lambda \quad (5.5.30b)$$

$$b_{L1}^{(1)} = -1 + c_L Y_{L1}^{(0)} = 2(M_H + 1)/(2\lambda - 1) \quad (5.5.30c)$$

$$c_L^{(1)} = (-2Y_{L1}^{(0)} + c_L(Y_{L1}^{(0)})^2)/(\psi_L^{(1)})^2 = sgn_L^{(1)}/|(2b_{L0}^{(1)} - 1)(2\lambda - 1)| \quad (5.5.30d)$$

where the factor coefficient  $\psi_L^{(1)}$  is chosen as

$$\psi_L^{(1)} = |(2b_{L0}^{(1)} - 1)(2\lambda - 1)(-2Y_{L1}^{(0)} + c_L(Y_{L1}^{(0)})^2)|^{1/2} \quad (5.5.31)$$

and the sign function  $sgn_L^{(1)}$  is equal to

$$sgn_L^{(1)} = \begin{cases} +1, & \text{when } -2Y_{L1}^{(0)} + c_L(Y_{L1}^{(0)})^2 \geq 0 \\ -1, & \text{when } -2Y_{L1}^{(0)} + c_L(Y_{L1}^{(0)})^2 < 0 \end{cases} \quad (5.5.32)$$

Substituting the recursive equation of the low-frequency limit (Eq. (5.5.22b)) into Eq. (5.5.29), and rearranging the equation lead an equation of a power series of  $(ia_0)$ ,

$$\begin{aligned}
& (-2b_{L0}^{(i)}Y_{L0}^{(i)} + c_L^{(i)}(Y_{L0}^{(i)})^2) + (ia_0) \left( -2(b_{L1}^{(i)}Y_{L0}^{(i)} + b_{L0}^{(i)}Y_{L1}^{(i)}) + 2c_L^{(i)}Y_{L0}^{(i)}Y_{L1}^{(i)} - Y_{L1}^{(i)} \right) \\
& + (ia_0)^2 \left( a_L^{(i)} - 2b_{L1}^{(i)}Y_{L1}^{(i)} + c_L^{(i)}(Y_{L1}^{(i)})^2 - 2(-1 - b_{L0}^{(i)} + c_L^{(i)}Y_{L0}^{(i)} + (ia_0)(-b_{L1}^{(i)} + c_L^{(i)}Y_{L1}^{(i)})) \right. \\
& \quad \times (\psi_L^{(i+1)})^2(Y_L^{(i+1)}(a_0))^{-1} + (ia_0)^2 c_L^{(i)}(\psi_L^{(i+1)})^4(Y_L^{(i+1)}(a_0))^{-2} \\
& \quad \left. - (\psi_L^{(i+1)})^2(Y_L^{(i+1)}(a_0))^{-2} a_0(Y_L^{(i+1)}(a_0))_{,a_0} \right) = 0 \quad (5.5.33)
\end{aligned}$$

This equation is satisfied by setting each term equal to zero. The first term (constant term independent of  $(ia_0)$ ) yields

$$Y_{L0}^{(i)} = 2b_{L0}^{(i)}/c_L^{(i)} = 2b_{L0}^{(i)} \left( \prod_{k=1}^i (2b_{L0}^{(k)} - 1) \right) (2\lambda - 1) / \text{sgn}_L^{(i)} \quad (5.5.34)$$

Setting the second term of Eq. (5.5.33) ( $(ia_0)$  term) to zero and using Eq. (5.5.34) result in the solution for  $Y_{L1}^{(i)}$ ,

$$\begin{aligned}
Y_{L1}^{(i)} &= 2b_{L1}^{(i)}Y_{L0}^{(i)} / (2b_{L0}^{(i)} - 1) \\
&= 4(M_H + 1) \left( \prod_{k=1}^{i-1} (2b_{L0}^{(k)} + 1) \right) (2b_{L0}^{(i)}) / (\text{sgn}_L^{(i)} \left( \prod_{k=0}^i \text{sgn}_{L0}^{(k)} \right)) \quad (5.5.35)
\end{aligned}$$

where the sign function

$$\text{sgn}_{L0}^{(i)} = \begin{cases} +1, & \text{when } 2b_{L0}^{(i)} - 1 \geq 0 \\ -1, & \text{when } 2b_{L0}^{(i)} - 1 < 0 \end{cases} \quad (5.5.36)$$

Note that the term  $\prod_{k=1}^{i-1} (2b_{L0}^{(k)} + 1)$  in Eq. (5.5.35) is equal to one for  $i = 1$ . Multiplying the last term of Eq. (5.5.33) by  $(Y_L^{(i+1)}(a_0))^2 (\psi_L^{(i+1)})^{-2}$  yields the residual equation

$$\begin{aligned}
& (ia_0)^2 a_L^{(i+1)} - 2(b_{L0}^{(i+1)} + (ia_0)b_{L1}^{(i+1)})Y_L^{(i+1)}(a_0) + c_L^{(i+1)}(Y_L^{(i+1)}(a_0))^2 \\
& \quad - a_0(Y_L^{(i+1)}(a_0))_{,a_0} = 0 \quad (5.5.37)
\end{aligned}$$

with the constants updated recursively by

$$a_L^{(i+1)} = c_L^{(i)} (\psi_L^{(i+1)})^2 \quad (5.5.38a)$$

$$b_{L0}^{(i+1)} = c_L^{(i)} Y_{L0}^{(i)} - b_{L0}^{(i)} - 1 = b_{L0}^{(i)} - 1 \quad (5.5.38b)$$

$$b_{L1}^{(i+1)} = c_L^{(i)} Y_{L1}^{(i)} - b_{L1}^{(i)} \quad (5.5.38c)$$

$$\begin{aligned} c_L^{(i+1)} &= (a_L^{(i)} - 2b_{L1}^{(i)} Y_{L1}^{(i)} + c_L^{(i)} (Y_{L1}^{(i)})^2) / (\psi_L^{(i+1)})^2 \\ &= \text{sgn}_L^{(i+1)} / |(\prod_{k=1}^{i+1} (2b_{L0}^{(k)} - 1))(2\lambda - 1)| \end{aligned} \quad (5.5.38d)$$

where the factor coefficient  $\psi_L^{(i+1)}$  is chosen as

$$\psi_L^{(i+1)} = |(\prod_{k=1}^{i+1} (2b_{L0}^{(k)} - 1))(2\lambda - 1)(a_L^{(i)} - 2b_{L1}^{(i)} Y_{L1}^{(i)} + c_L^{(i)} (Y_{L1}^{(i)})^2)|^{1/2} \quad (5.5.39)$$

and the sign function  $\text{sgn}_L^{(i+1)}$  is equal to

$$\text{sgn}_L^{(i+1)} = \begin{cases} +1, & \text{when } a_L^{(i)} - 2b_{L1}^{(i)} Y_{L1}^{(i)} + c_L^{(i)} (Y_{L1}^{(i)})^2 \geq 0 \\ -1, & \text{when } a_L^{(i)} - 2b_{L1}^{(i)} Y_{L1}^{(i)} + c_L^{(i)} (Y_{L1}^{(i)})^2 < 0 \end{cases}$$

The continued fraction solution at low frequency is evaluated by using Eqs. (5.5.34) and (5.5.35) whereby the recursive constants are initialized by Eq. (5.5.30) and updated by Eq. (5.5.38). The doubly asymptotic continued fraction solution is determined by combining the high-frequency continued fraction solution in Eq. (5.5.1) with the low-frequency continued fraction solution in Eq. (5.5.22) using  $Y^{(M_H+1)}(a_0) = Y_L(a_0)$  (Eq. (5.5.18)). It is expressed as

$$\begin{aligned} S(a_0) &= K_\infty + (ia_0)C_\infty \\ &= \frac{(\psi_L^{(1)})^2}{Y_0^{(1)} + (ia_0)Y_1^{(1)} - \frac{(\psi_L^{(2)})^2}{(\psi_L^{(M_H)})^2} \dots} \\ &= \frac{(\psi_L^{(1)})^2}{Y_0^{(M_H)} + (ia_0)Y_1^{(M_H)} - \frac{(\psi_L^{(0)})^2}{Y_{L0}^{(0)} + (ia_0)Y_{L1}^{(0)} - \frac{(ia_0)^2 (\psi_L^{(1)})^2}{Y_{L0}^{(1)} + (ia_0)Y_{L1}^{(1)} - \frac{(ia_0)^2 (\psi_L^{(2)})^2}{\dots - \frac{(ia_0)^2 (\psi_L^{(M_L)})^2}{Y_{L0}^{(M_L)} + (ia_0)Y_{L1}^{(M_L)}}}}}} \end{aligned} \quad (5.5.40)$$

Note that the residual term  $(ia_0)^2 (\psi_L^{(M_L+1)})^2 / Y_L^{(M_L+1)}(a_0)$  at the low-frequency limit is neglected.

As an example, the low-frequency part of the order  $M_H = M_L = 2$  doubly asymptotic continued fraction solution is evaluated explicitly as

$$Y_{L0}^{(0)} = \frac{(\lambda + 2.5)|2\lambda - 1|}{\text{sgn}_L^{(0)}}; \quad Y_{L1}^{(0)} = \frac{2(\lambda + 2.5)}{\text{sgn}_L^{(0)} \text{sgn}_{L0}^{(0)}}; \quad \psi_L^{(0)} = |(\lambda + 2.5)(2.5 - \lambda)(2\lambda - 1)|^{1/2} \quad (5.5.41a)$$

$$Y_{L0}^{(1)} = \frac{2(\lambda-1)|(2\lambda-1)(2\lambda-3)|}{sgn_L^{(1)}}; \quad Y_{L1}^{(1)} = \frac{24(\lambda-1)}{sgn_L^{(1)} \prod_{k=0}^1 (sgn_{L0}^{(k)})};$$

$$\psi_L^{(1)} = |4(\lambda+2.5)(3.5-\lambda)(2\lambda-3)|^{1/2} \quad (5.5.41b)$$

$$Y_{L0}^{(2)} = \frac{2(\lambda-2)|(2\lambda-1)(2\lambda-3)(2\lambda-5)|}{sgn_L^{(2)}}; \quad Y_{L1}^{(2)} = \frac{24(2\lambda-1)(\lambda-2)}{sgn_L^{(2)} \prod_{k=0}^2 (sgn_{L0}^{(k)})};$$

$$\psi_L^{(2)} = |4(\lambda+2.5)(3.5-\lambda)(2\lambda-3)^2 + 288(\lambda-1)(2\lambda-5)|^{1/2} \quad (5.5.41c)$$

The complete doubly asymptotic solution is obtained by combining Eqs. (5.5.16) and (5.5.41).

## 5.6 Doubly asymptotic open boundary condition

The procedure of constructing the high-order doubly asymptotic open boundary condition described in this section is based on the one described in Chapter 3. The procedure begins with the modal force-displacement relationship in the frequency domain as expressed in Eq. (5.4.10). The circular boundary  $\Gamma$  ( $a = a_0$  and  $\xi = 1$ ) is considered. By substituting the first equation of the continued fraction solution at the high-frequency limit (Eq. (5.5.1a)) into Eq. (5.4.10), the following equation is obtained:

$$\tilde{R}_j = S_j(a_0)\tilde{U}_j = K_{\infty,j}\tilde{U} + (ia_0)C_{\infty,j}\tilde{U}_j - (\psi_j^{(1)})^2(Y_j^{(1)}(a_0))^{-1}\tilde{U}_j \quad (5.6.1)$$

Substituting Eqs. (5.5.4) and (5.5.3) into Eq. (5.6.1), and also introducing an auxiliary variable  $\tilde{U}^{(1)}$  to the equation lead to

$$\tilde{R}_j = 0.5\tilde{U}_j + (ia_0)\tilde{U}_j - \psi_j^{(1)}\tilde{U}_j^{(1)} \quad (5.6.2)$$

where the auxiliary variable  $\tilde{U}_j^{(1)}$  is defined in

$$\psi_j^{(1)}\tilde{U}_j^{(1)} = Y_j^{(1)}(a_0)\tilde{U}_j^{(1)} \quad (5.6.3)$$

By using Eqs. (5.4.8) and (5.6.2), the amplitude of the nodal force vector is expressed as

$$\{R\} = 0.5[\Phi]^{-T}\{\tilde{U}\} + (ia_0)[\Phi]^{-T}\{\tilde{U}\} - [\Phi]^{-T}[\psi^{(1)}]\{\tilde{U}^{(1)}\} \quad (5.6.4)$$

Substituting  $\{\tilde{U}\} = [\Phi]^{-1}\{U\}$  (Eq. (5.4.4)) and  $[E^0] = [\Phi]^{-T}[\Phi]^{-1}$  (Eq. (5.4.2a)) into Eq. (5.6.4) leads to

$$\{R\} = 0.5[E^0]\{U\} + (ia_0)[E^0]\{U\} - [\Phi]^{-T}[\psi^{(1)}]\{\tilde{U}^{(1)}\} \quad (5.6.5)$$

where  $\{U\}$  denotes  $\{U(\xi = 1)\}$ . Substituting Eq. (5.5.1b) into Eq. (5.6.3) yields

$$\psi_j^{(1)}\tilde{U}_j = Y_{0,j}^{(1)}\tilde{U}_j^{(1)} + (ia_0)Y_{1,j}^{(1)}\tilde{U}_j^{(1)} - \psi_j^{(2)}\tilde{U}_j^{(2)} \quad (5.6.6)$$

where the auxiliary variable  $\tilde{U}_j^{(2)}$  is defined as the  $i = 1$  case in

$$\psi_j^{(i+1)}\tilde{U}_j^{(i)} = Y_j^{(i+1)}(a_0)\tilde{U}_j^{(i+1)} \quad (5.6.7)$$

Substituting  $\{\tilde{U}\} = [\Phi]^{-1}\{U\}$  (Eq. (5.4.4)) into Eq. (5.6.6) formulated for all the modes yields

$$[\psi^{(1)}][\Phi]^{-1}\{U\} = [Y_0^{(1)}]\{\tilde{U}^{(1)}\} + (ia_0)[Y_1^{(1)}]\{\tilde{U}^{(1)}\} - [\psi^{(2)}]\{\tilde{U}^{(2)}\} \quad (5.6.8)$$

Substituting the remaining terms of the continued fraction solution in Eq. (5.5.1b) into Eq. (5.6.7) results in

$$\psi_j^{(i)}\tilde{U}_j^{(i-1)} = Y_{0,j}^{(i)}\tilde{U}_j^{(i)} + (ia_0)Y_{1,j}^{(i)}\tilde{U}_j^{(i)} - \psi_j^{(i+1)}\tilde{U}_j^{(i+1)} \quad (i = 2, 3, \dots, M_H) \quad (5.6.9)$$

The residual term of an order  $M_H$  high-frequency continued fraction solution given in Eq. (5.6.7) with  $i = M_H$  is the initial term of the low-frequency continued fraction (Eq. (5.5.22a)). It is expressed as

$$\psi_j^{(M_H+1)}\tilde{U}_j^{(M_H)} = Y_j^{(M_H+1)}(a_0)\tilde{U}_j^{(M_H+1)} = Y_{L,j}(a_0)\tilde{U}_{L,j}^{(0)} \quad (5.6.10)$$

with the auxiliary variable  $\tilde{U}_{L,j}^{(0)} = \tilde{U}_j^{(M_H+1)}$ . Substituting Eq. (5.5.22a) into Eq. (5.6.10) leads to

$$\psi_{L,j}^{(0)}\tilde{U}_j^{(M_H)} = Y_{L0,j}^{(0)}\tilde{U}_{L,j}^{(0)} + (ia_0)Y_{L1,j}^{(0)}\tilde{U}_{L,j}^{(0)} - (ia_0)\psi_{L,j}^{(1)}\tilde{U}_{L,j}^{(1)} \quad (5.6.11)$$

where the auxiliary variable  $\tilde{U}_{L,j}^{(1)}$  is defined in the  $i = 1$  case of

$$(ia_0)\psi_{L,j}^{(i)}\tilde{U}_{L,j}^{(i-1)} = Y_{L,j}^{(i)}(a_0)\tilde{U}_{L,j}^{(i)} \quad (5.6.12)$$



Equation (5.6.14) represents the high-order doubly asymptotic open boundary condition in the frequency domain. It is expressed in the time domain as a system of first-order ordinary differential equations

$$[K_h]\{z(t)\} + [C_h]\{\dot{z}(t)\} = \{f(t)\} \quad (5.6.17)$$

with

$$\{z(t)\} = [\{u(t)\}, \{\tilde{u}^{(1)}(t)\}, \dots, \{\tilde{u}^{(M_H)}(t)\}, \{\tilde{u}_L^{(0)}\}, \{\tilde{u}_L^{(1)}(t)\}, \dots, \{\tilde{u}_L^{(M_L)}(t)\}]^T \quad (5.6.18a)$$

$$\{f(t)\} = [\{r(t)\}, 0, \dots, 0, 0, 0, \dots, 0]^T \quad (5.6.18b)$$

Equation (5.6.17) represents the high-order doubly asymptotic open boundary condition. It is temporally local. When the low-frequency terms are neglected, it becomes a high-order singly asymptotic boundary condition.

## 5.7 Numerical examples

In this section, the accuracy of the improved high-order doubly asymptotic open boundary is evaluated in the frequency and time domain. The ratio of the material constants used in the analysis is  $G/\rho = 1$ .

In Section 5.7.1, a modal equation with the modal eigenvalue  $\lambda = 1.5$ , for which the original doubly-asymptotic continued fraction solution in Chapter 3 breaks down, is addressed to illustrate the robustness of the improved procedure. Afterwards, the accuracy of the improved procedure for the analysis of a circular cavity embedded in a full-plane is examined. The boundary of the circular cavity is discretized into line elements. Applying the scaled boundary finite element method leads to a system of modal equations. The mode with the highest modal eigenvalue and another mode of an intermediate modal eigenvalues are taken as examples to illustrate the accuracy of the improved procedure for the whole range of modes.

In Sections 5.7.2, 5.7.3 and 5.7.4, the responses of the circular cavity to surface tractions applied on its wall are computed. Several cases of surface tractions and time history are considered. To verify the responses of the proposed open boundary, analyses of extended finite element mesh are performed using ABAQUS, a commercial finite element package, with 8-node isoparametric quadrilateral elements. In all the analyses, the highest frequency of interest  $\omega_h$  is determined from the Fourier transform of the time histories of the surface tractions. The corresponding shortest wave period is equal to  $2\pi/\omega_h$ , and the shortest wavelength is equal to  $c_s T$ . The

mesh and size of time step  $\Delta t$  are chosen in such a way that 1 wavelength/period is represented by at least 9 nodes/time steps.

The Newmark's method with  $\gamma = 0.5$  and  $\beta = 0.25$  or the average acceleration scheme (see Section A.2 in Appendix A) is adopted for Eq. (5.6.17). All the results of displacement responses are normalized and plotted with respect to either the dimensionless frequency  $a_0 = \omega r_0/c_s$  (Eq. (5.4.12)) or the corresponding dimensionless time  $\bar{t} = tc_s/r_0$ .

### 5.7.1 Illustration of robustness of improved doubly asymptotic open boundary for modal dynamic stiffness

As mentioned in Section 5.5, the factor coefficients are introduced to the doubly asymptotic continued fraction solution to avoid the breakdown of the original continued fraction solution in Chapter 3. The breakdown occurs when the modal eigenvalue is equal to  $i + 0.5$  ( $i$  is an integer). The mode with modal eigenvalue  $\lambda = 1.5$  is chosen as an example. Since  $\lambda = 1.5$ , the singularity problem occurs when  $Y_{L0}^{(0)}$  is calculated in case of using the order  $M_H = M_L = 1$ , and  $Y_1^{(2)}$  in case of using the order  $M_H = M_L = 2$  with the formulation in Chapter 3.  $c_L$  which is the denominator of Eq. (3.3.60) is zero, and thus  $Y_{L0}^{(0)}$  calculated from Eq. (3.3.60) becomes infinity. Similarly,  $c^{(2)}$  which is the denominator of Eq. (3.3.45) is zero, and thus  $Y_1^{(2)}$  calculated from Eq. (3.3.45) becomes infinity. This singularity problem always breaks down the procedures of determining the coefficients, and consequently, the results cannot be plotted.

In contrast, by using the present formulation herein with the factor coefficients,  $Y_{L0}^{(0)}$  can be determined from Eq. (5.5.26) since the denominator is  $sgn_L^{(0)} = 1$ . Similarly,  $Y_1^{(2)}$  can be determined from Eq. (5.5.10) since the denominator is  $sgn^{(2)} = 1$ . Thus, the singularity problem can be avoided and the results can be plotted. The results of the solution are normalized by  $\lambda$  and plotted as a function of the dimensionless frequency  $a_0/\lambda$  as shown in Fig. 5.7.1.

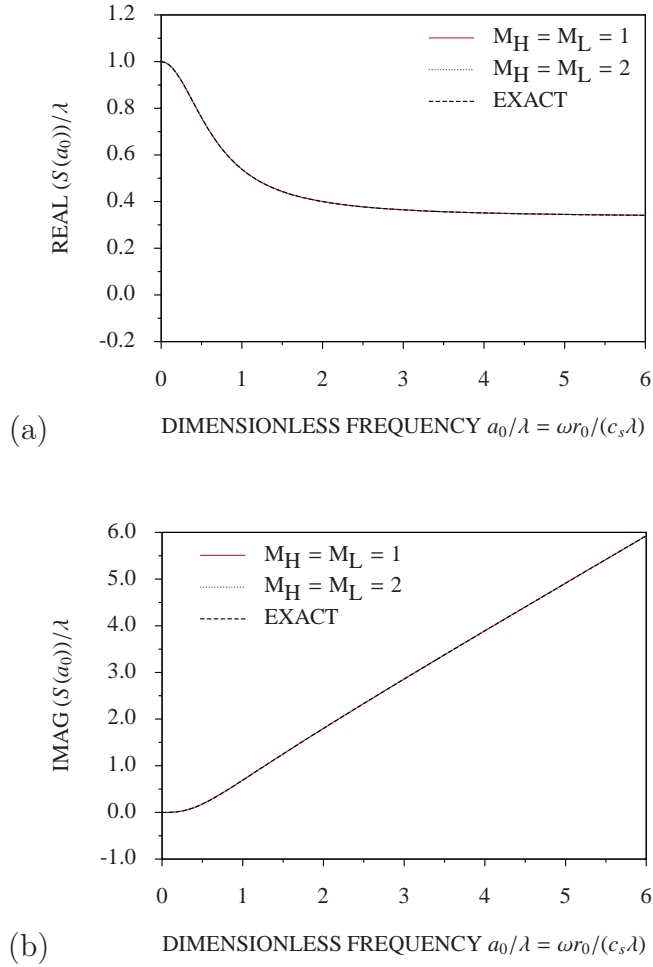


Figure 5.7.1: Doubly asymptotic continued fraction solution for dynamic stiffness coefficient ( $\lambda = 1.5$ ): (a) real part and (b) imaginary part

When coupling the present open boundaries with the FEM, the SBFEM or other numerical methods, a common mesh on the boundary is employed. The number of modes and the modal eigenvalues depend on the mesh on the boundary. In the following sections, the open boundary is discretized by 400 three-node elements leading to 800 nodes in total. The nodes are spaced equally in the circumferential direction (The mesh is not shown). The modal eigenvalues from Eq. (5.4.2b). The eigenvalue of the first (lowest) mode  $\lambda_1$  is found to be 0 and that of the last (highest) mode  $\lambda_{800}$  is equal to 493.124. It was shown by Bazyar and Song (2008) that when the modal eigenvalue  $\lambda$  is lower than 6, accurate results can be obtained from the singly asymptotic open boundary with the order  $M_H = 4$ . In this case, doubly asymptotic solution is not required.

The 40th mode is addressed. Its eigenvalue is  $\lambda_{40} \approx 20$ . The orders of the doubly asymptotic continued fraction solution are chosen as  $M_H = M_L = 1$  and  $M_H = M_L = 2$ . The solutions are plotted in Fig. 5.7.2 together with the exact

solution in Eq. (5.4.13). The result of the order  $M_H = M_L = 1$  open boundary agrees very well with the exact solution except for the frequency range close to  $a_0/\lambda = 1$ . When the order increases to  $M_H = M_L = 2$ , both the real and imaginary parts converge to the those of the exact solution. The difference is almost inappreciable.

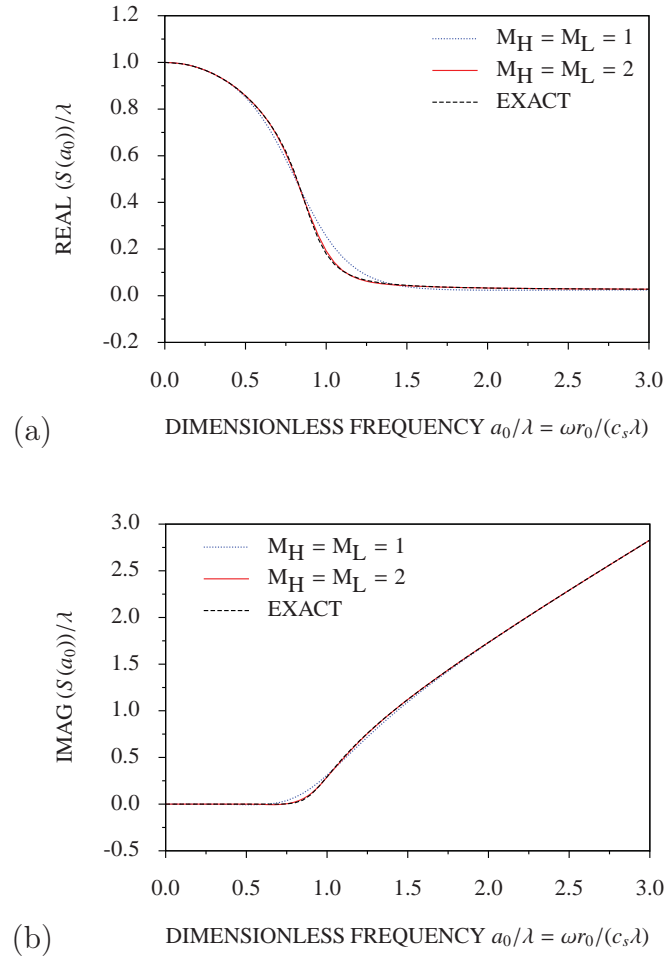


Figure 5.7.2: Doubly asymptotic continued fraction solution for dynamic stiffness coefficient ( $\lambda = 20$ ): (a) real part and (b) imaginary part

The singly asymptotic continued fraction solution at high frequency is then investigated. The solution obtained from the order  $M_H = 5$ , which has the same number of terms as the  $M_H = M_L = 2$  doubly asymptotic continued fraction solution, is plotted in Fig. 5.7.3. The result is accurate only at high frequencies ( $a_0/\lambda > 1$ ). At low frequencies ( $a_0/\lambda < 1$ ), the result does not agree with the exact solution. The error increases when the frequency approaches zero. The accuracy of the solution below  $a_0/\lambda < 1$  is significantly improved when the order is increased to  $M_H = 15$ , which is about 2.6 times the number of terms of the order  $M_H = M_L = 2$  doubly asymptotic continued fraction solution. This shows that the rate of convergence of the singly asymptotic continued fraction solution is much slower.

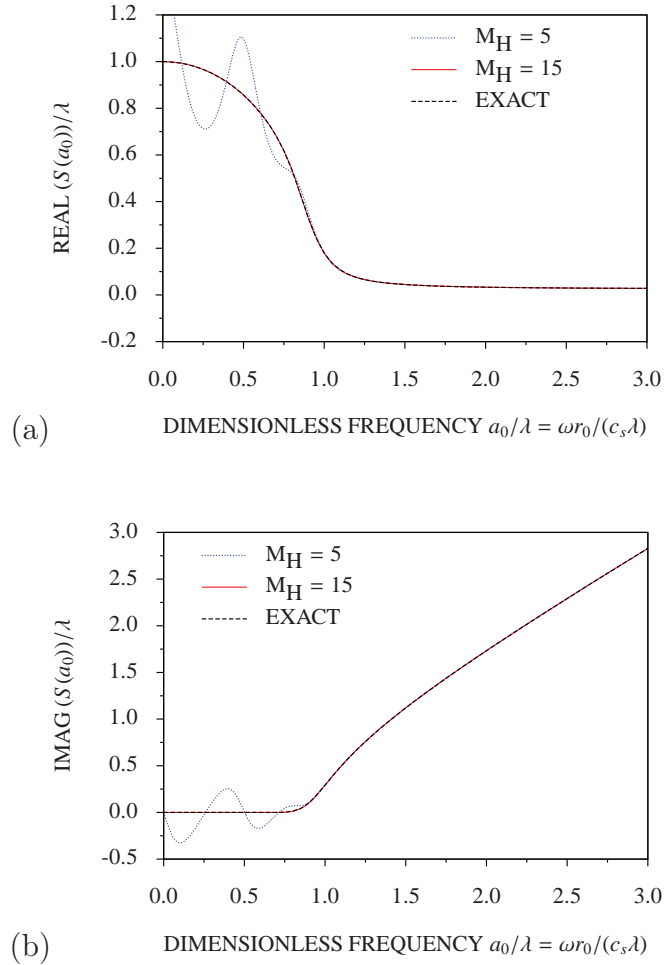


Figure 5.7.3: Singly asymptotic continued fraction solution for dynamic stiffness coefficient ( $\lambda = 20$ ): (a) real part and (b) imaginary part

As illustrated in Chapter 3 and Bazyar and Song (2008), when the modal eigenvalue  $\lambda$  increases, the order of singly asymptotic continued fraction has to be increased to maintain the same accuracy of results. Hence, mode 642 with modal eigenvalue  $\lambda_{642} \approx 400$  is chosen to further evaluate the accuracy of the doubly asymptotic continued fraction solution. The results obtained from the orders  $M_H = M_L = 1$  and  $M_H = M_L = 2$  are plotted in Fig. 5.7.4. It can be seen that the order  $M_H = M_L = 1$  doubly asymptotic continued fraction solution is reasonably accurate. At the order  $M_H = M_L = 2$ , the accuracy of the solution improves significantly, especially in the range of  $0.5 < a_0/\lambda < 1.5$ . The doubly asymptotic solution agrees well with the exact solution.

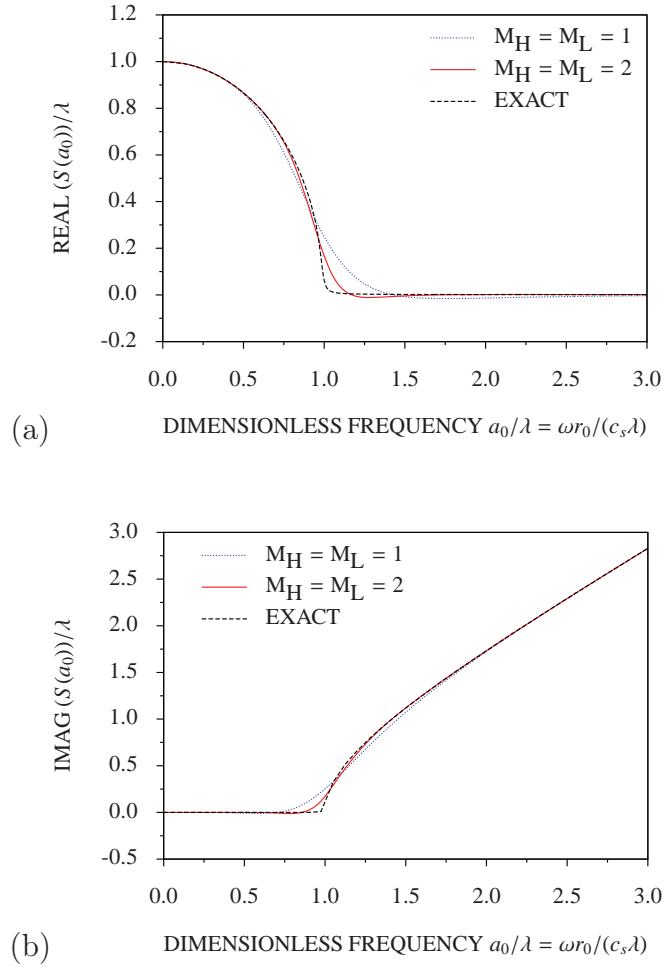


Figure 5.7.4: Doubly asymptotic continued fraction solution for dynamic stiffness coefficient ( $\lambda = 400$ ): (a) real part and (b) imaginary part

Comparison with the singly asymptotic continued fraction solution is performed. The results obtained from the order  $M_H = 5$ ,  $M_H = 17$  and  $M_H = 57$  singly asymptotic solution are plotted in Fig. 5.7.5. It can be seen that the singly asymptotic solution converges very slowly at low frequencies ( $a_0/\lambda < 1$ ). An accurate result is obtained only when the order is increased up to  $M_H = 57$ . This indicates that the accuracy of the singly asymptotic continued fraction solution deteriorates as the modal eigenvalue increases. In contrast, the accuracy of the doubly asymptotic continued fraction solution is much less sensitive to the modal eigenvalue. Accurate results can be achieved by using much fewer terms.

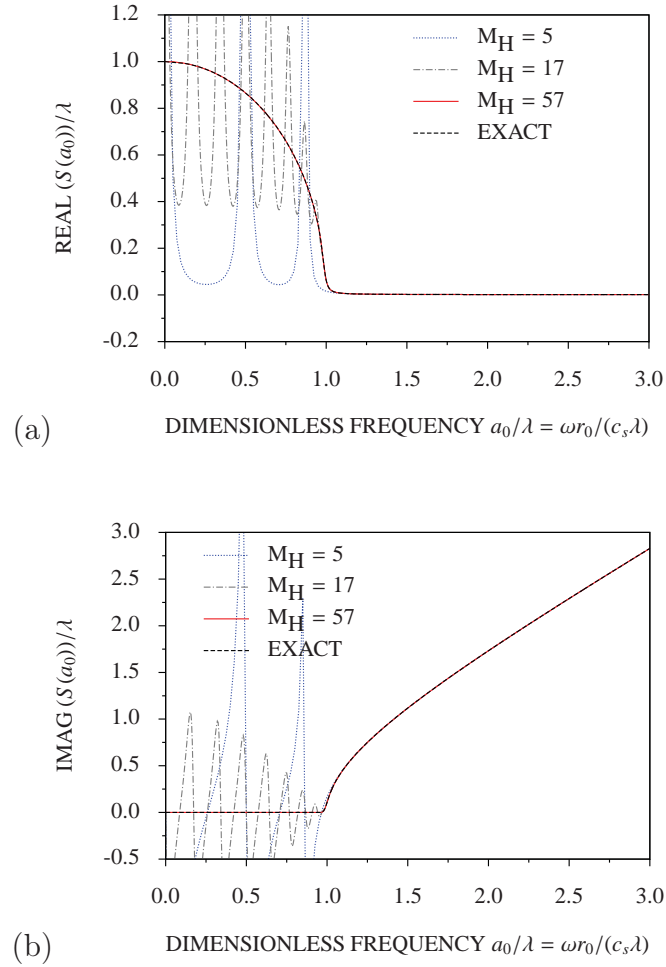


Figure 5.7.5: Singly asymptotic continued fraction solution for dynamic stiffness coefficient ( $\lambda = 400$ ): (a) real part and (b) imaginary part

### 5.7.2 Circular cavity subjected to transient surface traction on entire boundary

The circular cavity is subjected to a surface traction  $p_1(\theta, t)$  on the entire circular boundary  $\Gamma$ . The surface traction  $p_1(\theta, t)$  is given as

$$p_1(\theta, t) = h(\theta)f(t) \quad (5.7.1)$$

where  $h(\theta)$  is a function of coordinate  $\theta$  describing the spatial variation, and  $f(t)$  describes the time history. The spatial function  $h(\theta)$  is expressed as a cosine function,

$$h(\theta) = \cos(m \times \theta) \quad (5.7.2)$$

where the integer  $m$  is selected as 60 so that the 60 wavelengths on the circular boundary  $\Gamma$  can be represented by the 800 nodes. The time history  $f(t)$  is plotted

in Fig. 5.7.6(a) with respect to the dimensionless time  $\bar{t} = tc_s/r_0$ . The peak value is denoted as  $F_T$ . The Fourier transform of the function  $f(t)$  is also plotted in Fig. 5.7.6(b) with respect to the dimensionless frequency  $a_0$ . The highest dimensionless frequency of interest  $a_h$  is observed as 20.

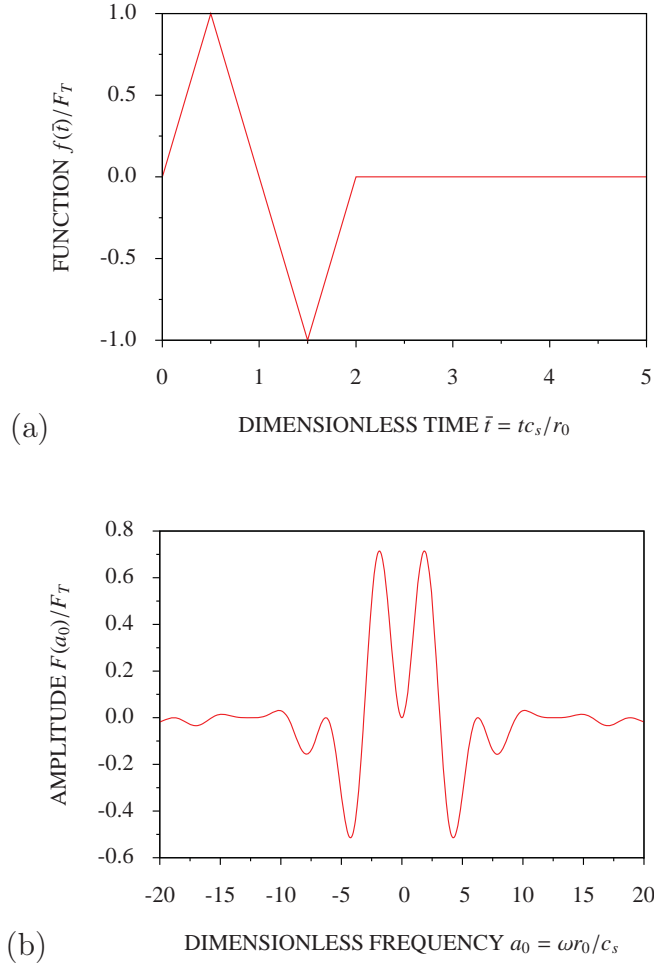


Figure 5.7.6: Function of antisymmetric triangle  $f(t)$ : (a) time history and (b) Fourier transform

The open boundary conditions are applied directly on the cavity wall  $\Gamma$ . The present open boundary is discretized by 400 three-node elements.

An extended finite element mesh, as shown in Fig. 5.7.7, is analyzed in order to obtain a reference solution to evaluate the accuracy of the present open boundary. The radius of the outer circular boundary of the extended mesh is  $r = 3r_0$ . The mesh density on the circular boundary  $\Gamma$  is similar to that of the open boundary. The circumferential direction is discretized by 400 elements spaced evenly and the radial direction by 42 elements spaced evenly. The total number of nodes in the mesh is 51,200 which is 64 times the total number of nodes generated by the SBFEM.

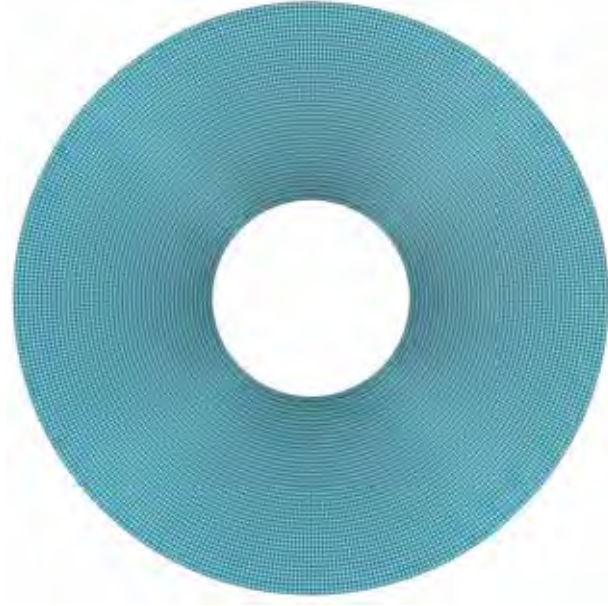


Figure 5.7.7: Mesh generated by FEM

The accuracy of the displacement responses at 5 specified points on the boundary  $\Gamma$  are investigated. The points are spaced evenly with Point  $A$  located at  $\theta = 0^\circ$ , Point  $B$  at  $\theta = 45^\circ$ , Point  $C$  at  $\theta = 90^\circ$ , Point  $D$  at  $\theta = 135^\circ$  and Point  $E$  at  $\theta = 180^\circ$ .

The displacement responses obtained by using the order  $M_H = M_L = 1$  doubly asymptotic open boundary and the order  $M_H = 3$  and  $M_H = 9$  singly asymptotic open boundary are normalized by  $F_T/G$  and plotted in Figs. 5.7.8 and 5.7.9 with respect to the dimensionless time  $\bar{t}$ . It can be observed that the results obtained from the doubly asymptotic open boundary are very accurate at all the 5 points throughout the entire duration even at the order  $M_H = M_L = 1$ .

In comparison, the accuracy of the singly asymptotic open boundary is much lower. At the order  $M_H = 3$ , which has the same number of terms as the order  $M_H = M_L = 1$  doubly asymptotic open boundary, very poor results are observed, especially within the range of  $0 < \bar{t} < 2$ . Although the accuracy of the results is improved when the order is increased to  $M_H = 9$ , the results still differ significantly from those of the extended mesh. Accurate results are obtained only when the order is increased up to  $M_H = 17$  (the results are not plotted here since they are the same as those of the extended mesh method). This clearly demonstrates that the rate of convergence of the doubly asymptotic open boundary is much more higher than that of the singly asymptotic open boundary.

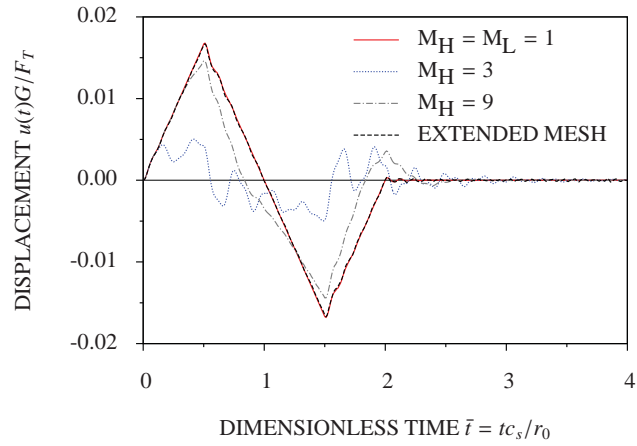


Figure 5.7.8: Displacement responses at Points  $A$ ,  $C$ , and  $E$  to surface traction  $p_1(\theta, t)$  obtained by doubly and singly asymptotic open boundaries

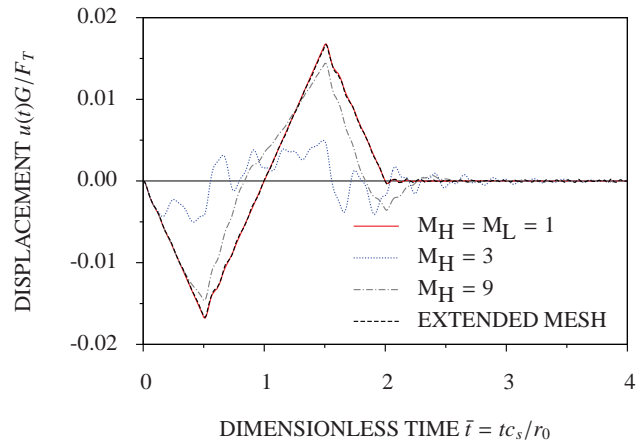


Figure 5.7.9: Displacement responses at Points  $B$  and  $D$  to surface traction  $p_1(\theta, t)$  obtained by doubly and singly asymptotic open boundaries

### 5.7.3 Circular cavity partially subjected to transient surface traction

In this example, a part of the boundary of the circular cavity is subjected to a surface traction  $p_2(\theta, t)$  given by

$$p_2(\theta, t) = g(\theta)j(t) \tag{5.7.3}$$

where  $g(\theta)$  is a multi-linear function depending on the coordinate  $\theta$ ,

$$g(\theta) = \begin{cases} -4 - \theta/|\theta_1 - \theta_2| & \text{when } \theta_1 \leq \theta < \theta_2 \\ 2 + 2\theta/|\theta_2 - \theta_3| & \text{when } \theta_2 \leq \theta < \theta_3 \\ -\theta/|\theta_3 - \theta_4| & \text{when } \theta_3 \leq \theta \leq \theta_4 \\ -\theta/|\theta_4 - \theta_5| & \text{when } \theta_4 \leq \theta < \theta_5 \\ -2 + 2\theta/|\theta_5 - \theta_6| & \text{when } \theta_5 \leq \theta < \theta_6 \\ 4 - \theta/|\theta_6 - \theta_7| & \text{when } \theta_6 \leq \theta \leq \theta_7 \\ 0 & \text{otherwise} \end{cases} \quad (5.7.4)$$

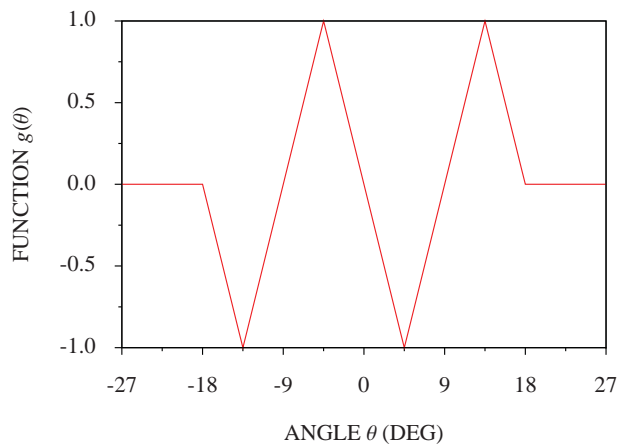
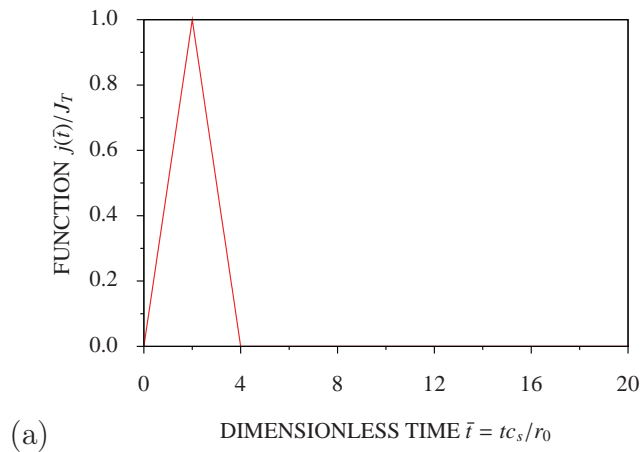


Figure 5.7.10: Multi-linear function  $g(\theta)$

Here  $\theta_1 = -18^\circ$ ,  $\theta_2 = -13.5^\circ$ ,  $\theta_3 = -4.5^\circ$ ,  $\theta_4 = 0^\circ$ ,  $\theta_5 = 4.5^\circ$ ,  $\theta_6 = 13.5^\circ$  and  $\theta_7 = 18^\circ$ , and  $j(t)$  is the time history plotted in Fig. 5.7.11(a). The peak value is denoted as  $J_T$ . The Fourier transform of the function  $j(t)$  is also plotted in Fig. 5.7.11(b). The highest dimensionless frequency of interest  $a_h$  is observed as 6.



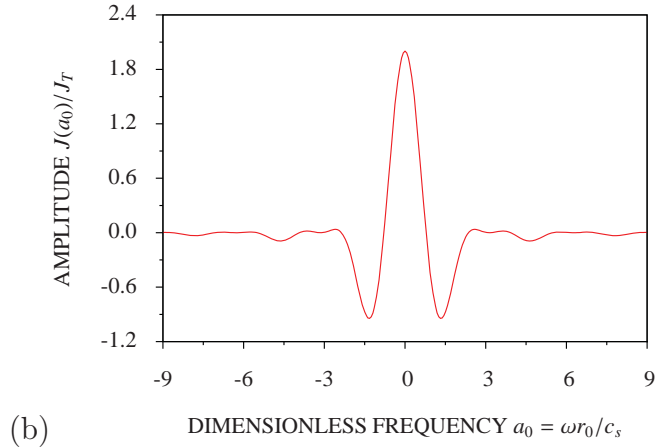
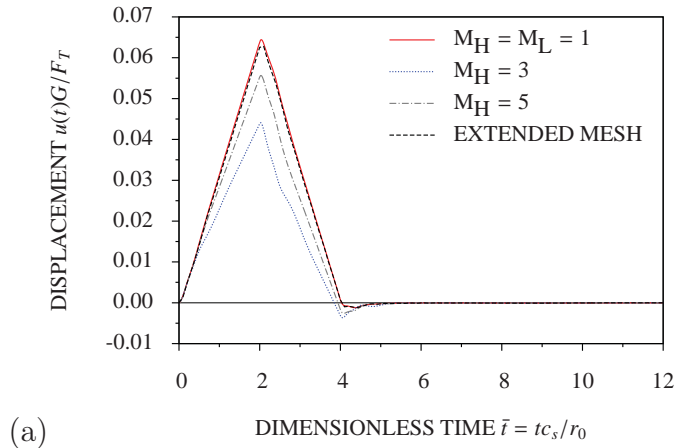


Figure 5.7.11: Function of antisymmetric triangle  $j(t)$ : (a) time history, and (b) Fourier transform

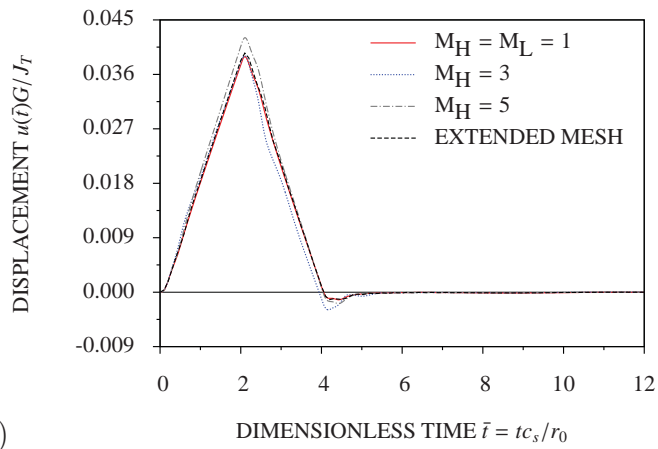
This problem is challenging since the waves radiated from the vicinity of  $\theta = 0^\circ$  are attenuated by a geometric spreading loss as they propagate along longitudes down to the south pole  $\theta = 180^\circ$ .

An extended finite element mesh is analyzed. The outer circular boundary of the mesh is located at the radius  $r = 8r_0$ . 400 elements of equal length are introduced along the circumferential direction, and 56 elements along the radial direction. The total number of nodes in the mesh is 68,000. It is obvious that the number of nodes required by the SBFEM is considerably less than those of the FEM. The mesh generated by the FEM is not shown since the mesh is very dense. The displacement responses at 5 specified points (Points  $F$ ,  $G$ ,  $H$ ,  $I$  and  $J$ ) on the circular boundary  $\Gamma$  are investigated. Point  $F$  is located at  $\theta = 13.5^\circ$  where the maximum traction occurs, Point  $G$  at  $\theta = 18^\circ$  (an extremity of the loaded area), Point  $H$  at  $\theta = 45^\circ$ , Point  $I$  at  $\theta = 108^\circ$ , and Point  $J$  at  $\theta = 166.5^\circ$ .

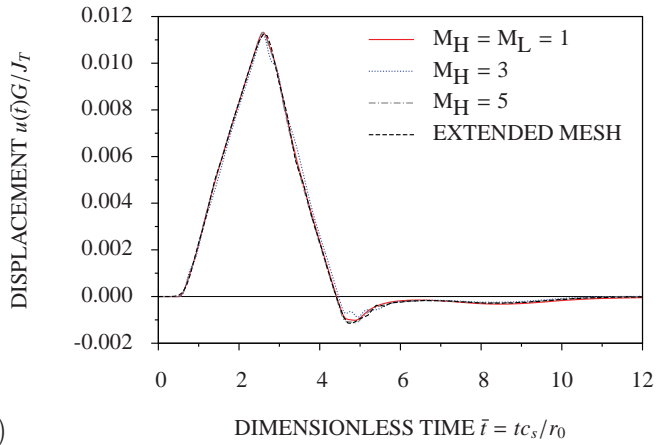
The displacement responses obtained by using the order  $M_H = M_L = 1$  and  $M_H = M_L = 2$  doubly asymptotic open boundary, and the order  $M_H = 3$  and  $M_H = 5$  singly asymptotic open boundary are plotted in Figs. 5.7.12 and 5.7.13. The order  $M_H = M_L = 1$  doubly asymptotic open boundary yields the accurate results at Points  $F$ ,  $G$  (in the loaded area) and  $H$  (the vicinity of the loaded area) throughout the entire duration as plotted in Fig. 5.7.12. At Points  $I$  and  $J$ , where are far from the source of excitation, the order  $M_H = M_L = 1$  open boundary still yields the accurate results as shown in Fig. 5.7.13. Note that the relative differences between the results obtained from the order  $M_H = M_L = 1$  doubly asymptotic open boundary and the results obtained from the extended mesh are very small.



(a)



(b)



(c)

Figure 5.7.12: Displacement responses to surface traction  $p_2(\theta, t)$  by doubly and singly asymptotic open boundaries: (a) at Point  $F$ , (b) at Point  $G$  and (c) at Point  $H$

In case of the order  $M_H = 3$  singly asymptotic open boundary with the same number of terms as the order  $M_H = M_L = 1$  doubly asymptotic open boundary, the results at Points  $F$ ,  $G$  and  $H$  are inaccurate within the range of  $0 < \bar{t} < 5$  as plotted

in Fig. 5.7.12. By increasing the order to  $M_H = 5$ , the results at Points  $F$  and  $G$  are fairly improved but still having some differences from those of the extended mesh. At Point  $H$ , the result becomes almost the same as that of the extended mesh. To obtain sufficiently accurate results at Points  $F$  and  $G$ , the order must be increased to  $M_H = 9$  (the results are not plotted here since they are the same as those of the extended mesh method). At Points  $I$  and  $J$ , the order  $M_H = 3$  singly asymptotic open boundary yields accurate results as plotted in Fig. 5.7.13. This example shows that the accuracy of the doubly asymptotic open boundary is much higher within the loaded area, and at the locations away from the loaded area, the accuracy of both open boundaries are similar.

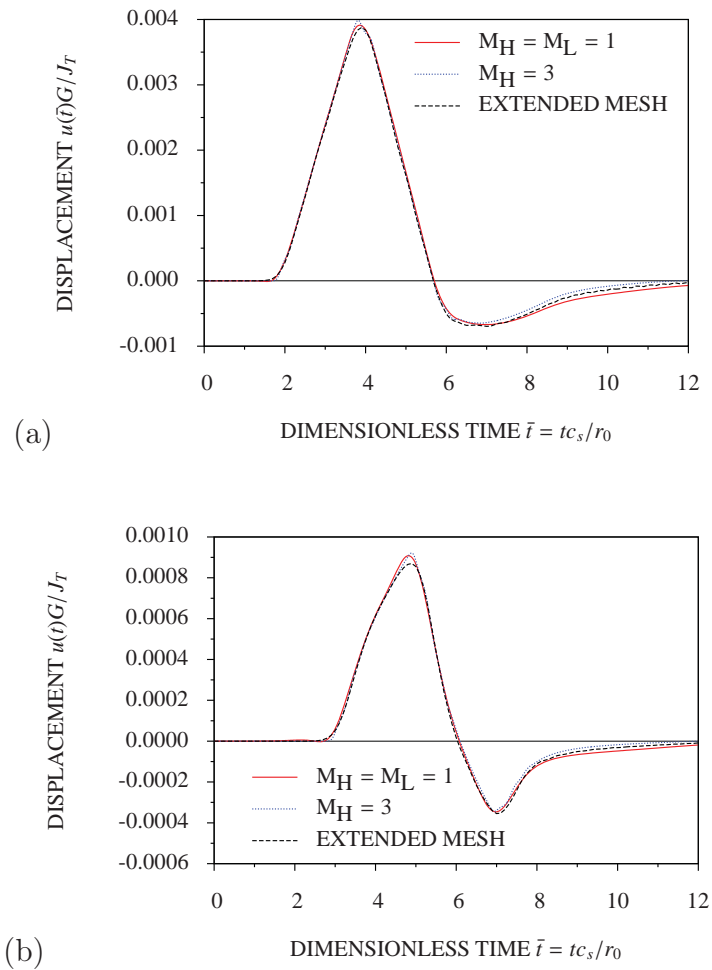


Figure 5.7.13: Displacement responses to surface traction  $p_2(\theta, t)$  by doubly and singly asymptotic open boundaries: (a) at Point  $I$  and (b) at Point  $J$

### 5.7.4 Circular cavity subjected to concentrated surface traction

In the last example, the circular cavity is subjected to a surface traction  $p_3(\theta, t)$  concentrated on a small area of the circular boundary  $\Gamma$ . The surface traction  $p_3(\theta, t)$  is given as

$$p_3(\theta, t) = k(\theta)\tau_0(t) \quad (5.7.5)$$

where  $k(\theta)$  is a multi-linear function of the coordinate  $\theta$ , and  $\tau_0(t)$  is the time history prescribed as a Ricker wavelet function with  $\bar{t}_s = 4$  and  $\bar{t}_0 = 1$  (see Eqs. (A.1.1) and (A.1.2) in Appendix A). The multi-linear function  $k(\theta)$  is given as

$$k(\theta) = \begin{cases} -2 - \theta/|\theta_1 - \theta_2| & \text{when } \theta_1 \leq \theta < \theta_2 \\ 2\theta/|\theta_2 - \theta_3| & \text{when } \theta_2 \leq \theta < \theta_3 \\ 2 - \theta/|\theta_4 - \theta_5| & \text{when } \theta_3 \leq \theta \leq \theta_4 \\ 0 & \text{otherwise} \end{cases} \quad (5.7.6)$$

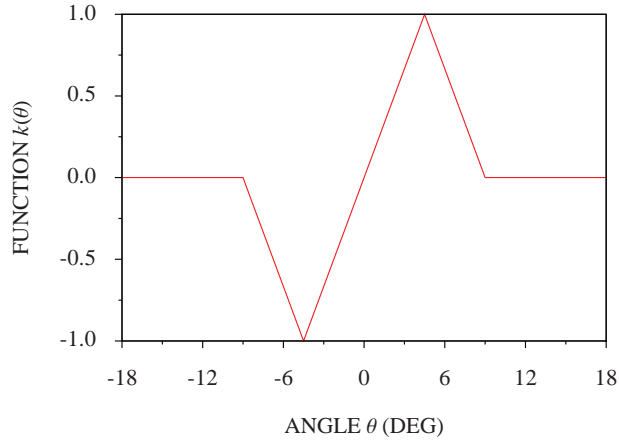


Figure 5.7.14: Multi-linear function  $k(\theta)$

where  $\theta_1 = -9^\circ$ ,  $\theta_2 = -4.5^\circ$ ,  $\theta_3 = 4.5^\circ$  and  $\theta_4 = 9^\circ$ . The Ricker wavelet function is plotted in Fig. 5.7.15(a) and its Fourier transform plotted in Fig. 5.7.15(b). The dominant dimensionless frequency  $a_d$  is 2 while the highest dimensionless frequency of interest  $a_h$  is observed as 6.

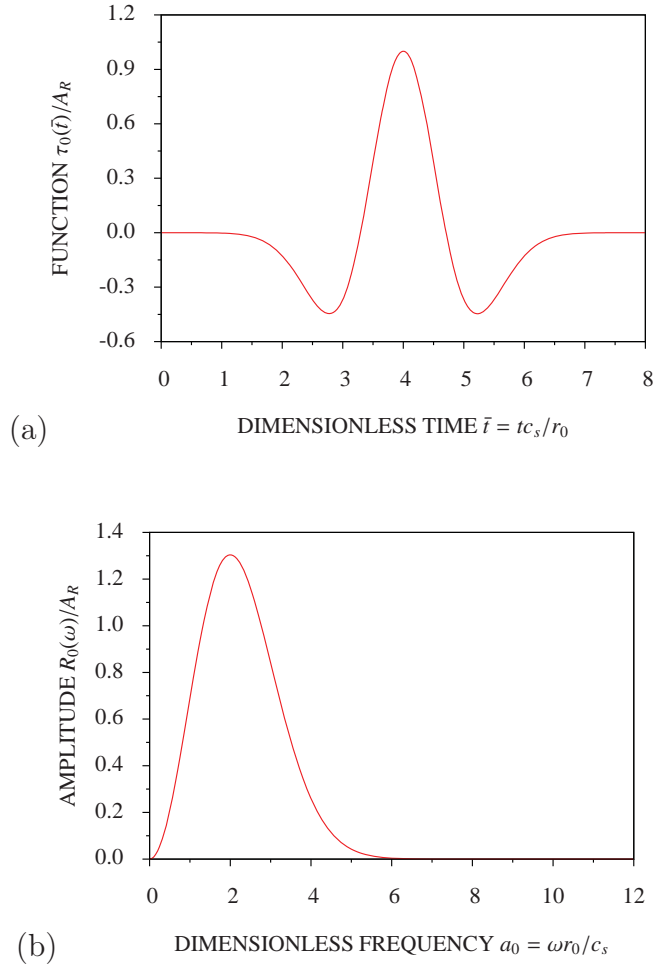


Figure 5.7.15: Ricker wavelet function: (a) time history and (b) Fourier transform

In the extended mesh analysis, the region between the circular boundary  $\Gamma$  and the outer circular boundary at  $r = 11r_0$  is discretized by finite elements. The region is divided into 400 elements in the circumferential direction and 58 elements in the radial direction. The total number of nodes in the mesh is 70,400. The displacements responses at 5 specified points (Points  $K$ ,  $L$ ,  $M$ ,  $N$  and  $O$ ) on the circular boundary  $\Gamma$  are investigated to evaluate the accuracy of the doubly and singly asymptotic open boundaries. Point  $K$  is located at  $\theta = 4.5^\circ$  where the maximum surface traction occurs, Point  $L$  at  $\theta = 9^\circ$  (an extremity of the loaded area), Point  $M$  at  $\theta = 45^\circ$ , Point  $N$  at  $\theta = 108^\circ$ , and Point  $O$  at  $\theta = 175.5^\circ$ .

The analyses are performed by using the order  $M_H = M_L = 1$  doubly asymptotic open boundary, and the order  $M_H = 3$  and  $M_H = 5$  singly asymptotic open boundary. The displacement responses are plotted in Figs. 5.7.16 and 5.7.17. The results at Points  $K$ ,  $L$  (in the loaded area) and Point  $M$  (in the vicinity of the loaded area) obtained from the order  $M_H = M_L = 1$  doubly asymptotic open boundary are accurate throughout the entire duration as shown in Fig. 5.7.16. At Points  $N$  and

$O$ , which are opposite to the loaded area, the order  $M_H = M_L = 1$  open boundary also leads to the accurate results as shown in Fig. 5.7.17.

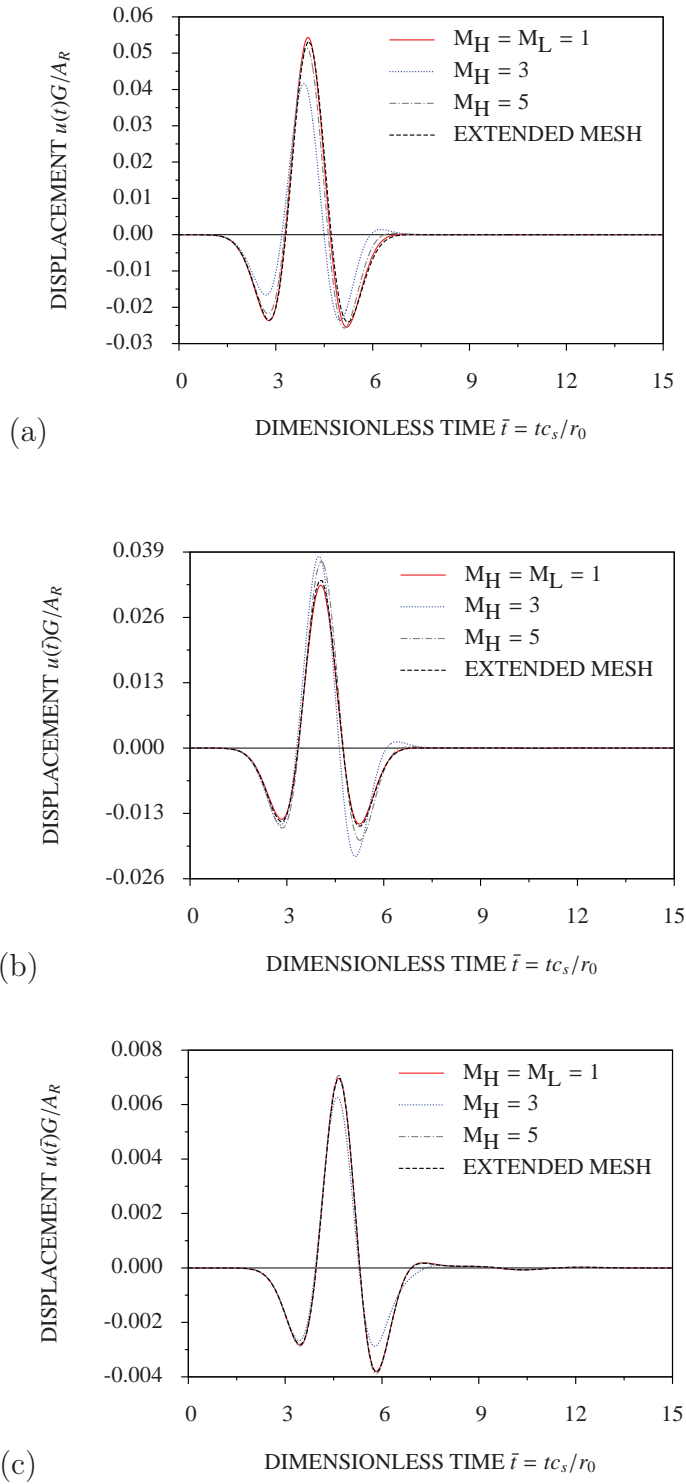


Figure 5.7.16: Displacement responses to surface traction  $p_3(\theta, t)$  by doubly and singly asymptotic open boundaries: (a) at Point  $K$ , (b) at Point  $L$  and (c) at Point  $M$

The singly asymptotic open boundary at the order  $M_H = 3$  exhibits fairly low accuracy at Points  $K$ ,  $L$  and  $M$  within the range of  $0 < \bar{t} < 4$  as shown in Fig. 5.7.16. Its accuracy improves as the order becomes higher. To achieve similar accuracy to the order  $M_H = M_L = 1$  doubly asymptotic open boundary, the order must be increased to  $M_H = 9$  (the results are not plotted here since they are the same as those of the extended method). Nevertheless, at Points  $N$  and  $O$ , the results obtained from the order  $M_H = 3$  singly asymptotic open boundary are as accurate as those of the order  $M_H = M_L = 1$  doubly asymptotic open boundary. This example confirms that the accuracy of the doubly asymptotic open boundary is superior within or close to the loaded area.

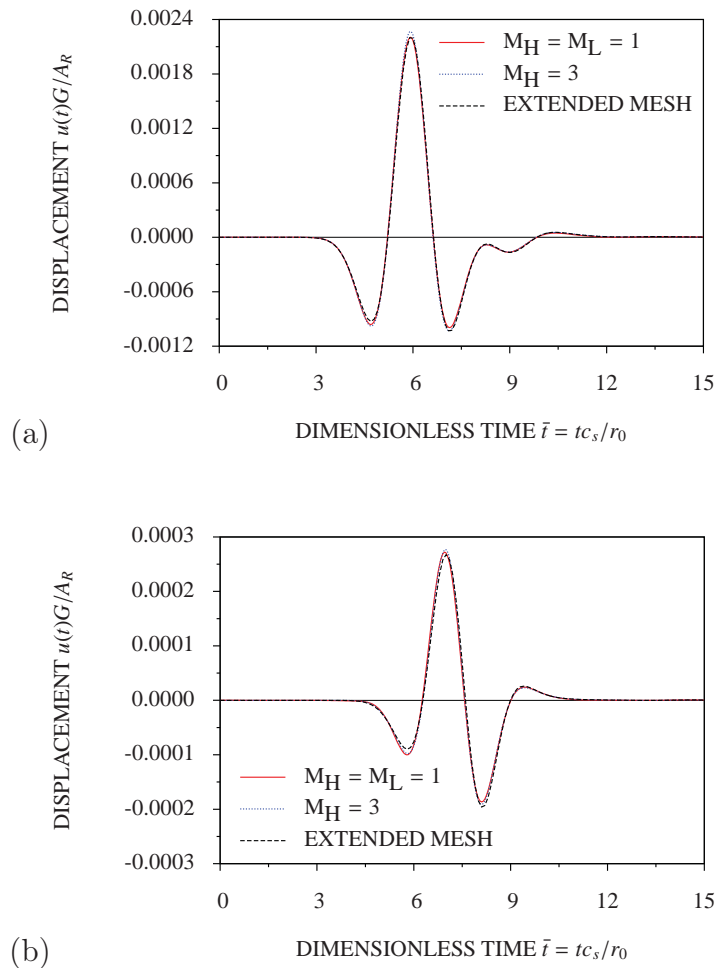


Figure 5.7.17: Displacement responses to surface traction  $p_3(\theta, t)$  by doubly and singly asymptotic open boundaries: (a) at Point  $N$  and (b) at Point  $O$

## 5.8 Conclusions

The high-order doubly asymptotic open boundary has been constructed herein for scalar wave propagation in a full-plane with a circular cavity. From the numerical results obtained in the frequency and time domain, it can be concluded that

1. The present procedure introducing the factor coefficients improves the numerical robustness of the doubly asymptotic continued fraction solution. In comparison with the singly asymptotic solution at high frequency, the doubly asymptotic continued fraction solution with the same number of terms is more accurate. In addition, the rate of convergence of the doubly asymptotic solution is much higher than that of the singly asymptotic solution when the modal eigenvalue is high.
2. The improved doubly asymptotic continued fraction solution are formulated in the time domain as an open boundary condition. The open boundary is temporally local. It is expressed as first-order ordinary differential equation in time. The two time-independent coefficient matrices, the stiffness matrix  $[K_h]$  and the damping matrix  $[C_h]$  are banded and symmetric. Thus well-established time-stepping schemes in structural dynamics are directly applicable.
3. In a time domain analysis, the improved doubly asymptotic open boundary exhibits significantly higher accuracy than the singly asymptotic open boundary, especially within and close to the loaded areas. The high-order doubly asymptotic open boundary is advantageous for transient analyses where high-order modes are excited.

## Chapter 6

# Doubly Asymptotic Open Boundary for Scalar Wave Propagation in Semi-Infinite Layered Systems

### Abstract

The propagation of scalar waves in semi-infinite layered systems with a constant depth is addressed. The challenge is that the scaled boundary finite element equations cannot be decoupled by frequency-independent modes and has to be solved in matrix form. The doubly asymptotic continued fraction solution for a dynamic stiffness matrix is obtained by solving the scaled boundary finite element equations in matrix form. The factor matrices are introduced to the continued fraction solution to improve the numerical stability of the solution. The coefficients of the solution are determined recursively by satisfying the scaled boundary finite element equation in dynamic stiffness at both high- and low-frequency limits. By introducing auxiliary variables and using the doubly asymptotic continued fraction solution, the force-displacement relationship on the boundary is formulated as a high-order doubly asymptotic open boundary condition in the frequency domain. The open boundary is expressed as a system of first-order ordinary differential equations in the time domain. Standard time-step schemes can be directly applied to perform the time integration. No parameters other than the orders of continued fraction are selected by the user.

## 6.1 Introduction

In modeling of unbounded domains for wave propagation problems, the boundary condition at infinity must be satisfied. Imposing the condition of vanishing displacement amplitude at infinity is insufficient to seek a unique solution for a wave propagation problem. A radiation condition has to be enforced. In 1949, Sommerfeld proposed the radiation condition in order to guarantee the uniqueness of solution for scalar waves in the frequency domain (Sommerfeld, 1949). Only outgoing waves can satisfy the radiation condition while incoming waves cannot.

When the boundary element method (BEM) (Dominguez, 1993; Hall and Oliveto, 2003), which is a rigorous method, is employed in the modeling of an unbounded domain, the radiation condition is automatically satisfied as part of the fundamental solution. Only the boundary of the unbounded domain is discretized, thereby reducing the spatial dimension by one. Nevertheless, the fundamental solution may be very complex, for example, in the case of anisotropic materials (Wolf and Song, 1996). The scaled boundary finite element method (SBFEM) is a rigorous method which is suited for modeling unbounded domains (Wolf and Song, 1996; Song and Wolf, 1997; Wolf and Song, 2000; Wolf, 2003). This approach combines some of the appealing features of the finite element method (FEM) and the BEM. It can satisfy the radiation condition automatically without any use of fundamental solutions. In recent years, the SBFEM has been extended to non-homogeneous unbounded domains for static and dynamic analyses as reported by Doherty and Deeks (2003c,b,a) and Bazyar and Song (2006a,b). For the modeling of unbounded domains as layered media, the thin-layer method (TLM), which is also a rigorous method, has been widely used for long time. This approach has been developed continuously so that it can be employed in both frequency- and time-domain analyses (Lysmer, 1970; Lysmer and Waas, 1972; Waas, 1972; Kausel, 1994). It is also applicable to inhomogeneous layered media as presented by Waas and Hartmann (1988). In recent years, the TLM has been formulated in the wavenumber-time domain for a homogeneous layer underlain by an elastic half-space in two dimensions (Park and Kausel, 2006; Kausel and Park, 2006).

However, when these rigorous methods are employed for the modeling of unbounded domains, the procedure for calculation is spatially and temporally global due to convolution integrals (Feltrin, 1997). This results in a large computational effort which is inappropriate for evaluating large practical problems because of their large demand on storage capacity and computing time (Bennett, 1976). In addition to these rigorous methods, unbounded domains can be modeled by employing the FEM with either the extended mesh method or an artificial boundary. The extended

mesh method is simple but cannot satisfy the radiation condition due to the wave reflections at the truncated boundary. Therefore, the truncated boundary must be sufficiently far from the source of excitation to prevent such wave reflections. In case of using an artificial boundary, propagating waves are able to be transmitted through the boundary without any reflections (Givoli, 1991).

The boundary conditions enforced on artificial boundaries are chosen to be spatially and temporally local and, therefore, approximate. No convolution integrals are required. Hence they are numerically much more efficient than the rigorous methods (Feltrin, 1997). The first artificial boundary is the viscous boundary, a low-order absorbing boundary (Lysmer and Kuhlemeyer, 1969), which was further developed by White *et al.* (1977) and Akiyoshi (1978). In order to improve the accuracy of low-order absorbing boundaries, several high-order absorbing boundary conditions (high-order ABCs) have been developed such as the Engquist-Majda ABC (Engquist and Majda, 1979), the Bayliss-Gunzburger-Turkel ABC (Bayliss *et al.*, 1982) and the Higdon ABC (Higdon, 1986). However, the increase of the derivative orders of these ABCs renders them impractical for implementation when the orders are typically higher than two (Givoli, 2004). This led to the development of local high-order ABCs (Collino, 1993; Hagstrom and Warburton, 2004; Bécache *et al.*, 2010). These local high-order ABCs are convenient for implementation since no high derivatives involve in the derivation due to use of auxiliary variables (Givoli, 2004).

Most of artificial boundaries are only singly asymptotic at the high-frequency limit, in other words, they take into account only propagating modes. They are thus appropriate for simulating propagating waves, but not evanescent waves. Hagstrom *et al.* (2008) showed that the inclusion of evanescent modes was able to improve the accuracy of the long-time behavior of the absorbing boundary. This has also been proved in Chapter 3 that the singly asymptotic open boundary is unable to transmit evanescent waves below the cut-off frequencies in the semi-infinite layer with a constant depth, thereby causing “fictitious reflections” in late-time responses. Only the doubly asymptotic open boundary is suitable for simulating wave propagation in long-time analyses.

The objective of this chapter is to develop a doubly asymptotic open boundary for scalar wave propagation in semi-infinite layered systems by extending the SBFEM. This is a challenging task as the scaled boundary finite element equation can no longer be decoupled into a series of one-dimensional problems and has to be solved in matrix form. This chapter is organized as follows: in Section 6.2, the governing differential equation (the equation of the out-of-plane motion) of a semi-infinite layered system is derived for scalar waves. In Section 6.3, the SBFEM equation in displacement of the semi-infinite layered system is derived in the time domain. In

Section 6.4, the SBFEM equation in dynamic stiffness of the semi-infinite layered system is derived in the frequency domain. In Section 6.5, the derivation of the doubly asymptotic continued fraction solution for dynamic stiffness is presented. In Section 6.6, the high-order doubly asymptotic open boundary condition of the semi-infinite layered system is constructed in both frequency and time domains. In Section 6.7, numerical examples are demonstrated in the frequency and time domains. In Section 6.8, conclusions are presented.

## 6.2 Governing differential equation of scalar waves

A semi-infinite layered system with constant depth  $h$  is shown in Fig. 6.2.1(a). The semi-infinite layered system composes of sublayers. A sublayer is shown in Fig. 6.2.1(b). The material constants are the shear modulus  $G$  and the density  $\rho$  which are assumed to be constant throughout each sublayer and may change from sublayer to sublayer. The out-of-plane motion  $u = u(x, y, t)$  of a sublayer in the Cartesian coordinates  $(x, y)$  is considered. For the boundary conditions, it is assumed that the vertical boundary  $\Gamma_V$  located at  $x = x_b$  is subjected to time-dependent out-of-plane shear stresses. The Neumann boundary condition is imposed on the upper boundary  $\Gamma_U$  i.e. it is allowed to be free ( $u_{,y}(y = h) = 0$ ), and the Dirichlet boundary condition is imposed on the lower boundary, which is fixed ( $u(y = 0) = 0$ ).

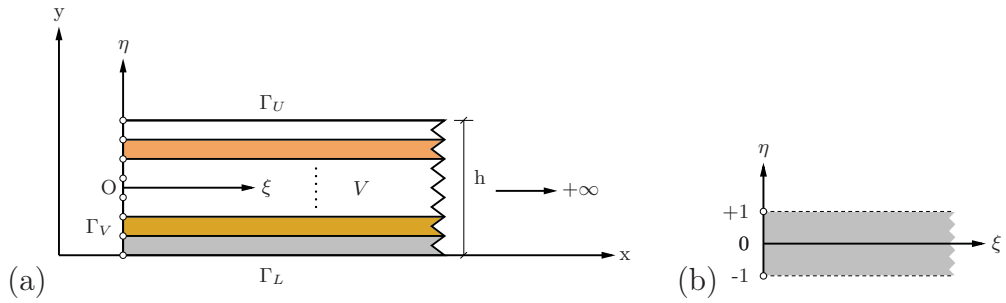


Figure 6.2.1: Semi-infinite layered system with constant depth: (a) geometry and semi-discretization, and (b) sublayer and typical element

Introducing the differential operator denoting the vector of spatial derivatives in the Cartesian coordinates,

$$\{L\} = \left[ \frac{\partial}{\partial x} \quad \frac{\partial}{\partial y} \right]^T \quad (6.2.1)$$

The out-of-plane shear strains  $\{\gamma\} = \left[ \gamma_{zx} \quad \gamma_{zy} \right]^T$  are expressed as

$$\{\gamma\} = \{L\}u \quad (6.2.2)$$

The out-of-plane shear stresses  $\{\tau\} = [ \tau_{zx} \quad \tau_{zy} ]^T$  are equal to

$$\{\tau\} = G\{\gamma\} \quad (6.2.3)$$

The governing differential equation of motion is expressed as

$$\{L\}^T\{\tau\} - \rho\ddot{u} = 0 \quad (6.2.4)$$

where  $\ddot{u}$  is acceleration in the out-of-plane direction. Substituting Eq. (6.2.3) into Eq. (6.2.4) and using Eqs. (6.2.2) and (6.2.1) lead to the scalar wave equation formulated in two-dimensional Cartesian coordinates,

$$\nabla^2 u = \frac{1}{c_s^2} \ddot{u} \quad (6.2.5)$$

where  $\nabla^2$  is the Laplace operator,

$$\nabla^2 = \frac{\partial^2}{\partial x^2} + \frac{\partial^2}{\partial y^2} \quad (6.2.6)$$

and  $c_s$  the speed of shear wave,

$$c_s = \sqrt{\frac{G}{\rho}} \quad (6.2.7)$$

### 6.3 Scaled boundary finite element method for semi-infinite layered system

The scaled boundary finite element method (SBFEM) is a novel semi-analytical approach. It was first developed for modeling unbounded domains with arbitrary geometry as the consistent infinitesimal finite-element cell method (Wolf and Song, 1996). The original derivation of the SBFEM for scalar wave propagation was proposed by Song and Wolf (1995). In modeling of the semi-infinite layered system with constant depth  $h$ , which is a special case (see Fig. 6.2.1(a)), the scaling center  $O$  is located at infinity, and thus the scaling corresponds to translating the vertical boundary  $\Gamma_V$  (Li *et al.*, 2005).

The vertical boundary  $\Gamma_V$  shown in Fig. 6.2.1(a) is discretized by one-dimensional line elements. A typical element is shown in Fig. 6.2.1(b). Its geometry can be

expressed in the scaled boundary coordinates  $(\xi, \eta)$  as

$$x(\xi) = x_b + \xi \quad (6.3.1a)$$

$$y(\eta) = [N(\eta)]\{y_b\} \quad (6.3.1b)$$

where  $\xi$  is the horizontal coordinate that  $\xi \geq 0$ ,  $\eta$  the vertical coordinate that  $-1 \leq \eta \leq 1$ ,  $[N(\eta)]$  the shape function formulated in the coordinate  $\eta$ , and  $\{y_b\}$  the vertical coordinate vector of the nodes on the vertical boundary  $\Gamma_V$ . As referred in Wolf and Song (1996) and Wolf (2003), the vector of spatial derivatives in the Cartesian coordinates  $\{L\}$  is related to those in the scaled boundary coordinates  $[\frac{\partial}{\partial \xi} \quad \frac{\partial}{\partial \eta}]^T$  by

$$\{L\} = [J(\eta)]^{-1} [\frac{\partial}{\partial \xi} \quad \frac{\partial}{\partial \eta}]^T \quad (6.3.2)$$

where  $[J(\eta)]$  is the Jacobian matrix, which is expressed as

$$[J(\eta)] = \begin{bmatrix} x(\xi)_{,\xi} & y(\eta)_{,\xi} \\ x(\xi)_{,\eta} & y(\eta)_{,\eta} \end{bmatrix} = \begin{bmatrix} 1 & 0 \\ 0 & y(\eta)_{,\eta} \end{bmatrix} \quad (6.3.3)$$

Its inverse and determinant are

$$[J(\eta)]^{-1} = \frac{1}{|J(\eta)|} \begin{bmatrix} y(\eta)_{,\eta} & 0 \\ 0 & 1 \end{bmatrix} \quad (6.3.4)$$

$$|J(\eta)| = y(\eta)_{,\eta} = [N(\eta)]_{,\eta} \{y_b\} \quad (6.3.5)$$

respectively. Substituting Eq. (6.3.4) into Eq. (6.3.2) and using Eq. (6.3.5) yield

$$\{L\} = \{b^1\} \frac{\partial}{\partial \xi} + \{b^2(\eta)\} \frac{\partial}{\partial \eta} \quad (6.3.6)$$

where  $\{b^1\}$  and  $\{b^2(\eta)\}$  are defined as

$$\{b^1\} = [1 \quad 0]^T \quad (6.3.7a)$$

$$\{b^2(\eta)\} = \frac{1}{|J(\eta)|} [0 \quad 1]^T \quad (6.3.7b)$$

Note that  $\{b^1\}$  and  $\{b^2(\eta)\}$  are orthogonal.

The displacements along the horizontal direction and a node on the boundary are represented by nodal displacement functions  $\{u(\xi)\}$ . The displacement field  $u$  in

Eq. (6.2.2) is approximated by interpolating the nodal displacement function  $\{u(\xi)\}$  piecewisely,

$$u = u(\xi, \eta) = [N(\eta)]\{u(\xi)\} \quad (6.3.8)$$

Substituting Eqs. (6.3.6) and (6.3.8) into Eq. (6.2.2) yields

$$\{\gamma\} = [B^1(\eta)]\{u(\xi)\}_{,\xi} + [B^2(\eta)]\{u(\xi)\} \quad (6.3.9)$$

where  $[B^1(\eta)]$  and  $[B^2(\eta)]$  are defined as

$$[B^1(\eta)] = \{b^1\}[N(\eta)] \quad (6.3.10a)$$

$$[B^2(\eta)] = \{b^2(\eta)\}[N(\eta)]_{,\eta} \quad (6.3.10b)$$

Substituting Eq. (6.3.9) into Eq. (6.2.3) leads to

$$\{\tau\} = G([B^1(\eta)]\{u(\xi)\}_{,\xi} + [B^2(\eta)]\{u(\xi)\}) \quad (6.3.11)$$

In the derivation of the scale boundary finite element equation in displacement, the virtual work principle

$$\int_V \{\gamma^*\}^T \{\tau\} dV = \int_V u^*(\xi, \eta) \rho \ddot{u} dV + \int_{\Gamma_V} u^*(\xi, \eta) \tau_s d\Gamma_V \quad (6.3.12)$$

is employed (Wolf, 2003). The left-hand side of the equation represents the internal virtual work where the virtual shear strain vector  $\{\gamma^*\}$  is formulated as the same as the shear strain vector in Eq. (6.3.9). The right-hand side is the external work of the inertial force and the surface traction  $\tau_s$  where the virtual displacements  $u^*(\xi, \eta)$  is approximated by

$$u^*(\xi, \eta) = [N(\eta)]\{u^*(\xi)\} = \{u^*(\xi)\}^T [N(\eta)]^T \quad (6.3.13)$$

using the same shape function as that in Eq. (6.3.8). For a two-dimensional problem, the third dimension is assumed to be a unit length. An infinitesimal area  $dV$  and an infinitesimal boundary  $d\Gamma_V$  are expressed as

$$dV = |J(\eta)| d\xi d\eta \quad (6.3.14a)$$

$$d\Gamma_V = |J(\eta)| d\eta \quad (6.3.14b)$$

respectively. For convenience, each term in Eq. (6.3.12) is considered individually. Using Eq. (6.3.9) for  $\{\gamma^*\}$  (but replace  $\{u(\xi)\}$  with  $\{u^*(\xi)\}$ ) and substituting Eqs. (6.3.11) and (6.3.14a) into the single term on the left-hand side of Eq. (6.3.12) yield

$$\int_V \{\gamma^*\}^T \{\tau\} dV = \int_0^\infty \{u^*(\xi)\}_{,\xi}^T [E^0] \{u(\xi)\}_{,\xi} d\xi + \int_0^\infty \{u^*(\xi)\}^T [E^2] \{u(\xi)\} d\xi \quad (6.3.15)$$

where the coefficient matrices  $[E^0]$  and  $[E^2]$  are defined as

$$[E^0] = \int_{-1}^{+1} [B^1(\eta)]^T G [B^1(\eta)] |J(\eta)| d\eta \quad (6.3.16a)$$

$$[E^2] = \int_{-1}^{+1} [B^2(\eta)]^T G [B^2(\eta)] |J(\eta)| d\eta \quad (6.3.16b)$$

$[E^0]$  is symmetric and positive definite.  $[E^2]$  is also symmetric but semi-positive definite. Since  $\{b^1(\eta)\}$  and  $\{b^2(\eta)\}$  are orthogonal for the vertical boundary  $\Gamma_V$ , the coefficient  $[E^1]$  occurring in an arbitrary boundary vanishes (Fan and Li, 2008).

To eliminate the derivatives  $\{u^*(\xi)\}_{,\xi}^T$  in the first term on the right-hand side of Eq. (6.3.15), integration by parts is applied. This results in

$$\begin{aligned} \int_0^\infty \{u^*(\xi)\}_{,\xi}^T [E^0] \{u(\xi)\}_{,\xi} d\xi &= \{u^*(\xi)\}^T [E^0] \{u(\xi)\}_{,\xi} \\ &\quad - \int_0^\infty \{u^*(\xi)\}^T [E^0] \{u(\xi)\}_{,\xi\xi} d\xi \end{aligned} \quad (6.3.17)$$

Substituting Eq. (6.3.17) back into Eq. (6.3.15) results in

$$\begin{aligned} \int_V \{\gamma^*\}^T \{\tau\} dV &= \{u^*(\xi)\}^T [E^0] \{u(\xi)\}_{,\xi} - \int_0^\infty \{u^*(\xi)\}^T [E^0] \{u(\xi)\}_{,\xi\xi} d\xi \\ &\quad + \int_0^\infty \{u^*(\xi)\}^T [E^2] \{u(\xi)\} d\xi \end{aligned} \quad (6.3.18)$$

Substituting Eqs. (6.3.8), (6.3.13) and (6.3.14a) into the first term on the right-hand side of Eq. (6.3.12) results in

$$\int_V u^*(\xi, \eta) \rho \ddot{u} dV = \int_0^\infty \{u^*(\xi)\}^T [M^0] \{\ddot{u}\} d\xi \quad (6.3.19)$$

where the coefficient matrix  $[M^0]$  is defined as

$$[M^0] = \int_{-1}^{+1} [N(\eta)]^T \rho [N(\eta)] |J(\eta)| d\eta \quad (6.3.20)$$

$[M^0]$  is also symmetric and positive definite. Substituting Eqs. (6.3.13) and (6.3.14b) into the last term on the right-hand side of Eq. (6.3.12) results in

$$\int_{\Gamma_V} u^*(\xi, \eta) \tau_s d\Gamma_V = \{u^*(\xi)\}^T \{Q\} \quad (6.3.21)$$

where the internal nodal force vector  $\{Q\}$  is defined as

$$\{Q\} = \int_{-1}^{+1} [N(\eta)]^T \tau_s |J(\eta)| d\eta \quad (6.3.22)$$

Substituting Eqs. (6.3.18), (6.3.19), and (6.3.21) into Eq. (6.3.12) leads to

$$\begin{aligned} & \{u^*(\xi)\}^T [E^0] \{u(\xi)\}_{,\xi} - \{u^*(\xi)\}^T \{Q\} - \int_0^\infty (\{u^*(\xi)\}^T [E^0] \{u(\xi)\}_{,\xi\xi} \\ & - \{u^*(\xi)\}^T [E^2] \{u(\xi)\} - \{u^*(\xi)\}^T [M^0] \{\ddot{u}\}) d\xi = 0 \end{aligned} \quad (6.3.23)$$

Equation (6.3.23) is satisfied when

$$\{u^*(\xi)\}^T [E^0] \{u(\xi)\}_{,\xi} - \{u^*(\xi)\}^T \{Q\} = 0 \quad (6.3.24)$$

and the integrand of the integral over  $\xi$  becomes zero,

$$\{u^*(\xi)\}^T ([E^0] \{u(\xi)\}_{,\xi\xi} - [E^2] \{u(\xi)\} - [M^0] \{\ddot{u}\}) = 0 \quad (6.3.25)$$

Rearranging Eq. (6.3.24) and eliminating all the terms  $\{u^*(\xi)\}^T$  lead to

$$\{Q\} = [E^0] \{u(\xi)\}_{,\xi} \quad (6.3.26)$$

in the time domain, which is equivalent to

$$\{Q\} = [E^0] \{U(\xi)\}_{,\xi} \quad (6.3.27)$$

in the frequency domain, where  $\{U(\xi)\}$  denotes the nodal displacement amplitudes. Similarly, eliminating all the terms  $\{u^*(\xi)\}^T$  in Eq. (6.3.25) leads to the scaled boundary finite element equation in displacement formulated in the time domain,

$$[E^0] \{u(\xi)\}_{,\xi\xi} - [E^2] \{u(\xi)\} - [M^0] \{\ddot{u}\} = 0 \quad (6.3.28)$$

The scaled boundary finite element equation in displacement formulated in the frequency domain is obtained from the Fourier transform of Eq. (6.3.28) as

$$[E^0]\{U(\xi)\}_{,\xi\xi} - [E^2]\{U(\xi)\} + \omega^2[M^0]\{U(\xi)\} = 0 \quad (6.3.29)$$

where  $\omega$  is the excitation frequency. Note that the coefficient matrices of the semi-infinite layered system at the vertical boundary  $\Gamma_V$  are obtained from the assembly of the coefficient matrices  $[E^0]$ ,  $[E^2]$  and  $[M^0]$  of individual elements. To simplify the nomenclature, the same symbols are used for the assembled coefficient matrices.

## 6.4 Dynamic stiffness matrix of semi-infinite layered systems

In the frequency domain, the excitation force-displacement relationship with the corresponding displacements is expressed as

$$\{R\} = [S^\infty(\omega)]\{U(\xi)\} \quad (6.4.1)$$

where  $[S^\infty(\omega)]$  is the dynamic stiffness matrix of the semi-infinite layered system, and  $\{R\}$  the interaction forces that relates to the internal nodal force vector  $\{Q\}$  by the following equation:

$$\{R\} = -\{Q\} \quad (6.4.2)$$

Substituting Eq. (6.4.2) into Eq. (6.4.1) and using Eq. (6.3.27) yield

$$-[E^0]\{U(\xi)\}_{,\xi} = [S^\infty(\omega)]\{U(\xi)\} \quad (6.4.3)$$

Taking the derivative of Eq. (6.4.3) with respect to  $\xi$  and rearranging the equation result in

$$-[E^0]\{U(\xi)\}_{,\xi\xi} - [S^\infty(\omega)]\{U(\xi)\}_{,\xi} = 0 \quad (6.4.4)$$

Combining Eq. (6.3.29) and Eq. (6.4.4) leads to

$$-[S^\infty(\omega)]\{U(\xi)\}_{,\xi} - [E^2]\{U(\xi)\} + \omega^2[M^0]\{U(\xi)\} = 0 \quad (6.4.5)$$

Equation (6.4.3) is rearranged as

$$\{U(\xi)\}_{,\xi} = -[E^0]^{-1}[S^\infty(\omega)]\{U(\xi)\} \quad (6.4.6)$$

Substituting Eq. (6.4.6) back into Eq. (6.4.5) and eliminating all the terms  $\{U(\xi)\}$  lead to the scaled boundary finite element equation in dynamic stiffness formulated in the frequency domain,

$$[S^\infty(\omega)][E^0]^{-1}[S^\infty(\omega)] - [E^2] + \omega^2[M^0] = 0 \quad (6.4.7)$$

Note that the matrix  $[M^0]$  is not proportional to the matrix  $[E^0]$  as the layers may have different wave velocities.

A concise formulation results when the transformation based on the following eigenvalue problem is introduced

$$[M^0][\Phi] = [E^0][\Phi][\Lambda^2] \quad (6.4.8)$$

where  $[\Lambda^2]$  and  $[\Phi]$  denote the eigenvalues and eigenvectors, respectively. Since  $[E^0]$  and  $[M^0]$  are positive definite, the eigenvectors are orthogonal. They are normalized as

$$[\Phi]^T[E^0][\Phi] = [I] \quad (6.4.9a)$$

$$[\Phi]^T[M^0][\Phi] = [\Lambda^2] \quad (6.4.9b)$$

Pre- and post-multiplying Eq. (6.4.7) by  $[\Phi]^T$  and  $[\Phi]$ , respectively and using Eq. (6.4.9) result in

$$[s^\infty(\omega)]^2 - [e^2] + \omega^2[\Lambda^2] = 0 \quad (6.4.10)$$

where

$$[s^\infty(\omega)] = [\Phi]^T[S^\infty(\omega)][\Phi] \quad (6.4.11)$$

$$[e^2] = [\Phi]^T[E^2][\Phi] \quad (6.4.12)$$

The solution for  $[s^\infty(\omega)]$  can be determined directly from Eq. (6.4.10) by rearranging the equation as

$$[s^\infty(\omega)]^2 = [e^2] - \omega^2[\Lambda^2] \quad (6.4.13)$$

Using the eigen-decomposition for the right-hand side of Eq. (6.4.13) results in

$$[e^2] - \omega^2[\Lambda^2] = [\Psi][\Omega][\Psi]^{-1} \quad (6.4.14)$$

where  $[\Omega]$  is the eigenvalues which are real numbers, and  $[\Psi]$  the eigenvectors which are orthogonal i.e.  $[\Psi]^{-1} = [\Psi]^T$  as  $[e^2]$  is real. Substituting Eq. (6.4.14) back into Eq. (6.4.13) yields the solution for  $[s^\infty(\omega)]$ ,

$$[s^\infty(\omega)] = [\Psi][\Omega]^{-\frac{1}{2}}[\Psi]^{-1} \quad (6.4.15)$$

which is equivalent to the solution obtained from the scaled boundary finite element equation in dynamic stiffness. Only the positive roots (positive real or imaginary numbers) of the diagonal entries of  $[\Omega]$  are chosen to satisfy the radiation condition.

Although the scaled boundary finite element equation can be solved analytically, the analytical solution leads to convolution integrals when being applied as open boundary conditions in the time domain.

## 6.5 Doubly asymptotic continued fraction solution for dynamic stiffness matrix

This section describes the solution of the scaled boundary finite element equation for dynamic stiffness matrix (Eq. (6.4.10)). The solution is sought as a doubly asymptotic continued fraction solution. Two steps are involved in the solution procedure. In the first step detailed in Section 6.5.1, a continued fraction solution is determined at the high-frequency limit recursively. In each recursion, the coefficient matrices of one term of the continued fractions is obtained, and an equation is established for the residual. In the second step detailed in Section 6.5.2, a continued fraction solution of the residual equation of the high-frequency solution is determined at the low-frequency limit recursively. The doubly asymptotic solution is obtained by joining the low-frequency solution to the last term of the high-frequency solution.

### 6.5.1 Continued fraction solution at high frequency

The continued fraction solution at the high-frequency limit ( $\omega \rightarrow \infty$ ) is written as

$$[s^\infty(\omega)] = (i\omega)[c_\infty] - [\psi^{(1)}][y^{(1)}(\omega)]^{-1}[\psi^{(1)}]^T \quad (6.5.1a)$$

$$[y^{(i)}(\omega)] = (i\omega)[y_1^{(i)}] - [\psi^{(i+1)}][y^{(i+1)}(\omega)]^{-1}[\psi^{(i+1)}]^T \quad (i = 1, 2, \dots, M_H) \quad (6.5.1b)$$

where  $[c_\infty]$  and  $[y_1^{(i)}]$  are coefficient matrices to be determined recursively in the solution procedure. The additional factor matrices  $[\psi^{(1)}]$  and  $[\psi^{(i+1)}]$  are introduced in order to improve numerical stability of the solution. To maintain the symmetry of the coefficient matrices of the open boundary (Eq. (6.6.16) in Section 6.6), the factor matrices and the transposed factor matrices are used in the residual terms  $[\psi^{(1)}][y^{(1)}(\omega)]^{-1}[\psi^{(1)}]^T$  and  $[\psi^{(i+1)}][y^{(i+1)}(\omega)]^{-1}[\psi^{(i+1)}]^T$ .  $M_H$  is the order of the continued fraction solution at high frequency.

The coefficient matrix  $[c_\infty]$  is determined by substituting Eq. (6.5.1a) into Eq. (6.4.10). This leads to an equation of a power series of  $(i\omega)$ , including the following two terms:

$$\begin{aligned} (i\omega)^2([c_\infty]^2 - [\Lambda^2]) + (-[e^2] - (i\omega)([c_\infty][\psi^{(1)}][y^{(1)}(\omega)]^{-1}[\psi^{(1)}]^T \\ + [\psi^{(1)}][y^{(1)}(\omega)]^{-1}[\psi^{(1)}]^T [c_\infty]) + [\psi^{(1)}][y^{(1)}(\omega)]^{-1}[\psi^{(1)}]^T \\ \times [\psi^{(1)}][y^{(1)}(\omega)]^{-1}[\psi^{(1)}]^T = 0 \end{aligned} \quad (6.5.2)$$

This equation is satisfied by setting all the two terms equal to zero. Thus the solution for  $[c_\infty]$  that satisfies the radiation condition is obtained from the first term ( $(i\omega)^2$  term) by selecting the positive root of each element on the diagonal of  $[\Lambda^2]$ ,

$$[c_\infty] = [\Lambda] \quad (6.5.3)$$

The last term of Eq. (6.5.2) is an equation of  $[y^{(1)}(\omega)]^{-1}$ . After being pre- and post-multiplied by  $[\psi^{(1)}]^{-1}[y^{(1)}(\omega)]$  and  $[y^{(1)}(\omega)][\psi^{(1)}]^{-T}$ , respectively, it is expressed as the  $i = 1$  case of

$$[a^{(i)}] - (i\omega)([b_1^{(i)}][y^{(i)}(\omega)] + [y^{(i)}(\omega)][b_1^{(i)}]^T) + [y^{(i)}(\omega)][c^{(i)}][y^{(i)}(\omega)] = 0 \quad (6.5.4)$$

with the following coefficient matrices:

$$[a^{(1)}] = [\psi^{(1)}]^T [\psi^{(1)}] \quad (6.5.5a)$$

$$[b_1^{(1)}] = [\psi^{(1)}]^T [c_\infty] [\psi^{(1)}]^{-T} \quad (6.5.5b)$$

$$[c^{(1)}] = [\psi^{(1)}]^{-1} (-[e^2]) [\psi^{(1)}]^{-T} \quad (6.5.5c)$$

The factor matrix  $[\psi^{(1)}]$  is selected to improve the stability condition of  $[c^{(1)}]$ . A good choice is

$$[\psi^{(1)}] = [L^{(1)}] \quad (6.5.6)$$

where the lower triangular matrix  $[L^{(1)}]$  is obtained from the following  $LDT^T$  decomposition:

$$-[e^2] = [L^{(1)}][D^{(1)}][L^{(1)}]^T \quad (6.5.7)$$

$[L^{(1)}]$  is normalized such that the entries of the diagonal matrix  $[D^{(1)}]$  are  $\pm 1$ . By using Eqs. (6.5.6) and (6.5.7), Eq. (6.5.5) is rewritten as

$$[a^{(1)}] = [L^{(1)}]^T [L^{(1)}] \quad (6.5.8a)$$

$$[b_1^{(1)}] = [L^{(1)}]^T [c_\infty] [L^{(1)}]^{-T} \quad (6.5.8b)$$

$$[c^{(1)}] = [D^{(1)}] \quad (6.5.8c)$$

To begin the recursive procedure, Eq. (6.5.1b) is substituted into Eq. (6.5.4). This also results in an equation of a power series of  $(i\omega)$  grouped into the following two terms:

$$\begin{aligned} & (i\omega)^2 ([y_1^{(i)}][c^{(i)}][y_1^{(i)}] - [y_1^{(i)}][b_1^{(i)}]^T - [b_1^{(i)}][y_1^{(i)}]) + ([a^{(i)}] - (i\omega)(-[b_1^{(i)}] + [y_1^{(i)}][c^{(i)}]) \\ & \quad \times [\psi^{(i+1)}][y^{(i+1)}(\omega)]^{-1}[\psi^{(i+1)}]^T - (i\omega)[\psi^{(i+1)}][y^{(i+1)}(\omega)]^{-1}[\psi^{(i+1)}]^T \\ & \quad \times (-[b_1^{(i)}]^T + [c^{(i)}][y_1^{(i)}]) + [\psi^{(i+1)}][y^{(i+1)}(\omega)]^{-1}[\psi^{(i+1)}]^T [c^{(i)}] \\ & \quad \times [\psi^{(i+1)}][y^{(i+1)}(\omega)]^{-1}[\psi^{(i+1)}]^T = 0 \quad (6.5.9) \end{aligned}$$

Equation (6.5.9) is also satisfied by setting all the two terms equal to zero. Pre- and post-multiplying the first term ( $(i\omega)^2$  term) by  $[y_1^{(i)}]^{-1}$  yield the Lyapunov equation of  $[y_1^{(i)}]^{-1}$ ,

$$[b_1^{(i)}]^T [y_1^{(i)}]^{-1} + [y_1^{(i)}]^{-1} [b_1^{(i)}] = [c^{(i)}] \quad (6.5.10)$$

which can be solved by the function “lyap” in MATLAB.  $[y_1^{(i)}]$  is obtained from the inverse of the solution of Eq. (6.5.10).  $[y_1^{(i)}]$  is symmetric as well as  $[b_1^{(i)}]$  and  $[c^{(i)}]$ .

The last term in Eq. (6.5.9) is an equation of  $[y^{(i+1)}(\omega)]^{-1}$ . Pre- and post-multiplying the last term by  $[y^{(i+1)}(\omega)][\psi^{(i+1)}]^{-1}$  and  $[\psi^{(i+1)}]^{-T}[y^{(i+1)}(\omega)]$ , respectively yield the residual equation,

$$\begin{aligned} & [a^{(i+1)}] - (i\omega)([b_1^{(i+1)}][y^{(i+1)}(\omega)] + [y^{(i+1)}(\omega)][b_1^{(i+1)}]^T) \\ & \quad + [y^{(i+1)}(\omega)][c^{(i+1)}][y^{(i+1)}(\omega)] = 0 \quad (6.5.11) \end{aligned}$$

with the coefficient matrices

$$[a^{(i+1)}] = [\psi^{(i+1)}]^T [c^{(i)}] [\psi^{(i+1)}] \quad (6.5.12a)$$

$$[b_1^{(i+1)}] = [\psi^{(i+1)}]^T (-[b_1^{(i)}]^T + [c^{(i)}][y_1^{(i)}]) [\psi^{(i+1)}]^{-T} \quad (6.5.12b)$$

$$[c^{(i+1)}] = [\psi^{(i+1)}]^{-1} [a^{(i)}] [\psi^{(i+1)}]^{-T} = [D^{(i+1)}] \quad (6.5.12c)$$

The factor matrix  $[\psi^{(i+1)}]$  is set equal to

$$[\psi^{(i+1)}] = [L^{(i+1)}] \quad (6.5.13)$$

where the diagonal matrix  $[D^{(i+1)}]$  and the lower triangular matrix  $[L^{(i+1)}]$  are obtained from the following  $LDT^T$  decomposition:

$$[a^{(i)}] = [L^{(i+1)}][D^{(i+1)}][L^{(i+1)}]^T \quad (6.5.14)$$

$[L^{(i+1)}]$  is normalized such that the entries of the diagonal matrix  $[D^{(i+1)}]$  are  $\pm 1$ . The continued fraction solution is determined recursively using Eq. (6.5.10) where the coefficient matrices  $[a^{(1)}]$ ,  $[b_1^{(1)}]$  and  $[c^{(1)}]$  are initialized by Eq. (6.5.8) and updated during the recursion with Eq. (6.5.12).

After an order  $M_H$  continued fraction solution is obtained at the high-frequency limit, the residual satisfies Eq. (6.5.11) with  $i = M_H$ .

## 6.5.2 Continued fraction solution at low frequency

The residual equation (Eq. (6.5.11)) of the high-frequency continued fraction solution is solved again by a continued fraction but at the low frequency limit ( $\omega \rightarrow 0$ ). For simplicity in notation, the residual is expressed as

$$[y_L(\omega)] = [y^{(M_H+1)}(\omega)] \quad (6.5.15)$$

and Eq. (6.5.11) is rewritten as

$$[a_L] - (i\omega)([b_{L1}][y_L(\omega)] + [y_L(\omega)][b_{L1}]^T) + [y_L(\omega)][c_L][y_L(\omega)] = 0 \quad (6.5.16)$$

with the following coefficient matrices used at the low-frequency limit:

$$[a_L] = [a^{(M_H+1)}] = [\psi_L^{(0)}]^T [c^{(M_H)}] [\psi_L^{(0)}] \quad (6.5.17a)$$

$$[b_{L1}] = [b_1^{(M_H+1)}] = [\psi_L^{(0)}]^T (-[b_1^{(M_H)}]^T + [c^{(M_H)}][y_1^{(M_H)}]) [\psi_L^{(0)}]^{-T} \quad (6.5.17b)$$

$$[c_L] = [c^{(M_H+1)}] = [\psi_L^{(0)}]^{-1} [a^{(M_H)}] [\psi_L^{(0)}]^{-T} = [D_L^{(0)}] \quad (6.5.17c)$$

where

$$[\psi_L^{(0)}] = [\psi^{(M_H+1)}] \quad (6.5.18a)$$

$$[D_L^{(0)}] = [D^{(M_H+1)}] \quad (6.5.18b)$$

The continued fraction solution at the low-frequency limit is expressed as

$$[y_L(\omega)] = [y_{L0}^{(0)}] + (i\omega)[y_{L1}^{(0)}] - (i\omega)^2[\psi_L^{(1)}][y_L^{(1)}(\omega)]^{-1}[\psi_L^{(1)}]^T \quad (6.5.19a)$$

$$[y_L^{(i)}(\omega)] = [y_{L0}^{(i)}] + (i\omega)[y_{L1}^{(i)}] - (i\omega)^2[\psi_L^{(i+1)}][y_L^{(i+1)}(\omega)]^{-1}[\psi_L^{(i+1)}]^T \quad (i = 1, 2, \dots, M_L) \quad (6.5.19b)$$

where  $[y_{L0}^{(0)}]$ ,  $[y_{L1}^{(0)}]$ ,  $[y_{L0}^{(i)}]$  and  $[y_{L1}^{(i)}]$  are coefficient matrices to be determined recursively. The factor matrices  $[\psi_L^{(1)}]$  and  $[\psi_L^{(i+1)}]$  are introduced to improve numerical stability of the solution.  $(i\omega)^2[\psi_L^{(1)}][y_L^{(1)}(\omega)]^{-1}[\psi_L^{(1)}]^T$  and  $(i\omega)^2[\psi_L^{(i+1)}][y_L^{(i+1)}(\omega)]^{-1}[\psi_L^{(i+1)}]^T$  are residual terms.  $M_L$  is the order of the continued fraction solution at low frequency.

Substituting Eq. (6.5.19a) into Eq. (6.5.16) leads to an equation of a power series of  $(i\omega)$ ,

$$\begin{aligned} & ([a_L] + [y_{L0}^{(0)}][c_L][y_{L0}^{(0)}]) + (i\omega)(-[b_{L1}][y_{L0}^{(0)}] - [y_{L0}^{(0)}][b_{L1}]^T + [y_{L0}^{(0)}][c_L][y_{L1}^{(0)}] \\ & + [y_{L1}^{(0)}][c_L][y_{L0}^{(0)}]) + (i\omega)^2 \left( (-[b_{L1}][y_{L1}^{(0)}] - [y_{L1}^{(0)}][b_{L1}]^T + [y_{L1}^{(0)}][c_L][y_{L1}^{(0)}]) \right. \\ & - \left( [y_{L0}^{(0)}][c_L] + (i\omega)(-[b_{L1}] + [y_{L1}^{(0)}][c_L]) \right) [\psi_L^{(1)}][y_L^{(1)}(\omega)]^{-1}[\psi_L^{(1)}]^T \\ & - [\psi_L^{(1)}][y_L^{(1)}(\omega)]^{-1}[\psi_L^{(1)}]^T \left( [c_L][y_{L0}^{(0)}] + (i\omega)(-[b_{L1}]^T + [c_L][y_{L1}^{(0)}]) \right) \\ & \left. + (i\omega)^2[\psi_L^{(1)}][y_L^{(1)}(\omega)]^{-1}[\psi_L^{(1)}]^T [c_L][\psi_L^{(1)}][y_L^{(1)}(\omega)]^{-1}[\psi_L^{(1)}]^T \right) = 0 \quad (6.5.20) \end{aligned}$$

Similarly, this equation is satisfied by setting each of the three terms equal to zero.  $[y_{L0}^{(0)}]$  can also be determined from the static stiffness matrix  $[s^\infty(\omega = 0)]$ . Substituting Eqs. (6.5.15), (6.5.18a) and (6.5.19a) into Eq. (6.5.1) results in

$$\begin{aligned} [s^\infty(\omega)] = & (i\omega)[c_\infty] - [\psi^{(1)}]((i\omega)[y_1^{(1)}] - [\psi^{(2)}]((i\omega)[y_1^{(2)}] - \dots \\ & - [\psi^{(M_H)}]((i\omega)[y_1^{(M_H)}] - [\psi_L^{(0)}]([y_{L0}^{(0)}] + (i\omega)[y_{L1}^{(0)}] \\ & - (i\omega)^2[\psi_L^{(1)}][y_L^{(1)}(\omega)]^{-1}[\psi_L^{(1)}]^T)^{-1}[\psi_L^{(0)}]^T)^{-1}[\psi^{(M_H)}]^T \\ & \dots)^{-1}[\psi^{(2)}]^T)^{-1}[\psi^{(1)}]^T \quad (6.5.21) \end{aligned}$$

Setting  $\omega$  equal to zero and rearranging Eq. (6.5.21) reversely yield the solution for  $[y_{L0}^{(0)}]$ ,

$$[y_{L0}^{(0)}] = \begin{cases} [s^\infty(\omega = 0)] & \text{when } M_H \text{ is odd number} \\ -[s^\infty(\omega = 0)]^{-1} & \text{when } M_H \text{ is even number} \end{cases} \quad (6.5.22)$$

$[s^\infty(\omega = 0)]$  can be determined from Eq. (6.4.13) by setting  $\omega$  equal to zero

$$[s^\infty(\omega = 0)] = [e^2]^{\frac{1}{2}} \quad (6.5.23)$$

Only the positive roots are chosen to obtain the positive-definite matrix for  $[s^\infty(\omega = 0)]$ .  $[y_{L0}^{(0)}]$  is symmetric as well as  $[s^\infty(\omega = 0)]$ . Setting the second term ( $(i\omega)$  term) in Eq. (6.5.20) leads to the Lyapunov equation of  $[y_{L1}^{(0)}]$ ,

$$([y_{L0}^{(0)}][c_L])[y_{L1}^{(0)}] + [y_{L1}^{(0)}]([c_L][y_{L0}^{(0)}]) = [b_{L1}][y_{L0}^{(0)}] + [y_{L0}^{(0)}][b_{L1}]^T \quad (6.5.24)$$

which can be solved by the function ‘‘lyap’’ in MATLAB.  $[y_{L1}^{(0)}]$  is symmetric as well as  $[c_L]$  and  $[y_{L0}^{(0)}]$ .

The last term ( $(i\omega)^2$  term) in Eq. (6.5.20) is an equation of  $[y_L^{(1)}(\omega)]^{-1}$ . Pre- and post-multiplying the last term by  $[y_L^{(1)}(\omega)][\psi_L^{(1)}]^{-1}$  and  $[\psi_L^{(1)}]^{-T}[y_L^{(1)}(\omega)]$ , respectively result in an equation of  $[y_L^{(i)}(\omega)]$ . It is expressed as the  $i = 1$  case of

$$(i\omega)^2[a_L^{(i)}] - ([b_{L0}^{(i)}] + (i\omega)[b_{L1}^{(i)}])[y_L^{(i)}(\omega)] - [y_L^{(i)}(\omega)]([b_{L0}^{(i)}]^T + (i\omega)[b_{L1}^{(i)}]^T) + [y_L^{(i)}(\omega)][c_L^{(i)}][y_L^{(i)}(\omega)] = 0 \quad (6.5.25)$$

with the following coefficient matrices:

$$[a_L^{(1)}] = [\psi_L^{(1)}]^T [c_L] [\psi_L^{(1)}] \quad (6.5.26a)$$

$$[b_{L0}^{(1)}] = [\psi_L^{(1)}]^T [c_L] [y_{L0}^{(0)}] [\psi_L^{(1)}]^{-T} \quad (6.5.26b)$$

$$[b_{L1}^{(1)}] = [\psi_L^{(1)}]^T (-[b_{L1}]^T + [c_L][y_{L1}^{(0)}]) [\psi_L^{(1)}]^{-T} \quad (6.5.26c)$$

$$[c_L^{(1)}] = [\psi_L^{(1)}]^{-1} (-[b_{L1}][y_{L1}^{(0)}] - [y_{L1}^{(0)}][b_{L1}]^T + [y_{L1}^{(0)}][c_L][y_{L1}^{(0)}]) [\psi_L^{(1)}]^{-T} = [D_L^{(1)}] \quad (6.5.26d)$$

The factor matrix  $[\psi_L^{(1)}]$  is set equal to

$$[\psi_L^{(1)}] = [L_L^{(1)}] \quad (6.5.27)$$

where the diagonal matrix  $[D_L^{(1)}]$  and the lower triangular matrix  $[L_L^{(1)}]$  are obtained from the following  $LDT^T$  decomposition:

$$-[b_{L1}][y_{L1}^{(0)}] - [y_{L1}^{(0)}][b_{L1}]^T + [y_{L1}^{(0)}][c_L][y_{L1}^{(0)}] = [L_L^{(1)}][D_L^{(1)}][L_L^{(1)}]^T \quad (6.5.28)$$

$[L_L^{(1)}]$  is normalized such that the entries of the diagonal matrix  $[D_L^{(1)}]$  are  $\pm 1$ . Substituting the recursive equation of the low-frequency limit (Eq. (6.5.19b)) into Eq. (6.5.25) and rearranging the equation lead to an equation of a power series of  $(i\omega)$ ,

$$\begin{aligned} & (-[b_{L0}^{(i)}][y_{L0}^{(i)}] - [y_{L0}^{(i)}][b_{L0}^{(i)}]^T + [y_{L0}^{(i)}][c_L^{(i)}][y_{L0}^{(i)}]) + (i\omega) \left( (-[b_{L0}^{(i)}] + [y_{L0}^{(i)}][c_L^{(i)}])[y_{L1}^{(i)}] \right. \\ & \quad \left. + [y_{L1}^{(i)}](-[b_{L0}^{(i)}]^T + [c_L^{(i)}][y_{L0}^{(i)}]) - [b_{L1}^{(i)}][y_{L0}^{(i)}] - [y_{L0}^{(i)}][b_{L1}^{(i)}]^T \right) + (i\omega)^2 \left( ([a_L^{(i)}] \right. \\ & \quad \left. - [b_{L1}^{(i)}][y_{L1}^{(i)}] - [y_{L1}^{(i)}][b_{L1}^{(i)}]^T + [y_{L1}^{(i)}][c_L^{(i)}][y_{L1}^{(i)}]) - \left( (-[b_{L0}^{(i)}] + [y_{L0}^{(i)}][c_L^{(i)}]) \right. \right. \\ & \quad \left. \left. + (i\omega)(-[b_{L1}^{(i)}] + [y_{L1}^{(i)}][c_L^{(i)}]) \right) [\psi_L^{(i+1)}][y_L^{(i+1)}(\omega)]^{-1}[\psi_L^{(i+1)}]^T \right. \\ & \quad \left. - [\psi_L^{(i+1)}][y_L^{(i+1)}(\omega)]^{-1}[\psi_L^{(i+1)}]^T \left( (-[b_{L0}^{(i)}]^T + [c_L^{(i)}][y_{L0}^{(i)}]) \right. \right. \\ & \quad \left. \left. + (i\omega)(-[b_{L1}^{(i)}]^T + [c_L^{(i)}][y_{L1}^{(i)}]) \right) \right) + (i\omega)^2 [\psi_L^{(i+1)}][y_L^{(i+1)}(\omega)]^{-1} \\ & \quad \times [\psi_L^{(i+1)}]^T [c_L^{(i)}][\psi_L^{(i+1)}][y_L^{(i+1)}(\omega)]^{-1}[\psi_L^{(i+1)}]^T = 0 \quad (6.5.29) \end{aligned}$$

This equation is satisfied by setting each term equal to zero. Pre- and post-multiplying the first term (the constant term independent of  $(i\omega)$ ) by  $[y_{L0}^{(i)}]^{-1}$  lead to the Lyapunov equation of  $[y_{L0}^{(i)}]^{-1}$ ,

$$[b_{L0}^{(i)}]^T [y_{L0}^{(i)}]^{-1} + [y_{L0}^{(i)}]^{-1} [b_{L0}^{(i)}] - [c_L^{(i)}] = 0 \quad (6.5.30)$$

which can be solved by the function “lyap” in MATLAB.  $[y_{L0}^{(i)}]$  is obtained from the inverse of the solution of Eq. (6.5.30). It is symmetric as well as  $[c_L^{(i)}]$ . The second term ( $(i\omega)$  term) in Eq. (6.5.29) is the Lyapunov equation of  $[y_{L1}^{(i)}]$ ,

$$(-[b_{L0}^{(i)}] + [y_{L0}^{(i)}][c_L^{(i)}])[y_{L1}^{(i)}] + [y_{L1}^{(i)}](-[b_{L0}^{(i)}]^T + [c_L^{(i)}][y_{L0}^{(i)}]) = [b_{L1}^{(i)}][y_{L0}^{(i)}] + [y_{L0}^{(i)}][b_{L1}^{(i)}]^T \quad (6.5.31)$$

which can be solved by the function “lyap” in MATLAB.  $[y_{L1}^{(i)}]$  is symmetric as well as  $[y_{L0}^{(i)}]$ .

The last term in Eq. (6.5.29) is an equation of  $[y_L^{(i+1)}(\omega)]^{-1}$ . Pre- and post-multiplying the last term by  $[y_L^{(i+1)}(\omega)][\psi_L^{(i+1)}]^{-1}$  and  $[\psi_L^{(i+1)}]^{-T}[y_L^{(i+1)}(\omega)]$ , respec-

tively lead to an equation in the same form as Eq. (6.5.25)

$$\begin{aligned}
(i\omega)^2[a_L^{(i+1)}] - ([b_{L0}^{(i+1)}] + (i\omega)[b_{L1}^{(i+1)}])[y_L^{(i+1)}(\omega)] - [y_L^{(i+1)}(\omega)][b_{L0}^{(i+1)}]^T \\
+ (i\omega)[b_{L1}^{(i+1)}]^T + [y_L^{(i+1)}(\omega)][c_L^{(i+1)}][y_L^{(i+1)}(\omega)] = 0 \quad (6.5.32)
\end{aligned}$$

with the coefficient matrices updated recursively by

$$[a_L^{(i+1)}] = [\psi_L^{(i+1)}]^T [c_L^{(i)}] [\psi_L^{(i+1)}] \quad (6.5.33a)$$

$$[b_{L0}^{(i+1)}] = [\psi_L^{(i+1)}]^T (-[b_{L0}^{(i)}]^T + [c_L^{(i)}][y_{L0}^{(i)}]) [\psi_L^{(i+1)}]^{-T} \quad (6.5.33b)$$

$$[b_{L1}^{(i+1)}] = [\psi_L^{(i+1)}]^T (-[b_{L1}^{(i)}]^T + [c_L^{(i)}][y_{L1}^{(i)}]) [\psi_L^{(i+1)}]^{-T} \quad (6.5.33c)$$

$$\begin{aligned}
[c_L^{(i+1)}] &= [\psi_L^{(i+1)}]^{-1} ([a_L^{(i)}] - [b_{L1}^{(i)}][y_{L1}^{(i)}] - [y_{L1}^{(i)}][b_{L1}^{(i)}]^T + [y_{L1}^{(i)}][c_L^{(i)}][y_{L1}^{(i)}]) [\psi_L^{(i+1)}]^{-T} \\
&= [D_L^{(i+1)}] \quad (6.5.33d)
\end{aligned}$$

The factor matrix  $[\psi_L^{(i+1)}]$  is set equal to

$$[\psi_L^{(i+1)}] = [L_L^{(i+1)}] \quad (6.5.34)$$

where the diagonal matrix  $[D_L^{(i+1)}]$  and the lower triangular matrix  $[L_L^{(i+1)}]$  are obtained from the following  $LDT^T$  decomposition:

$$[a_L^{(i)}] - [b_{L1}^{(i)}][y_{L1}^{(i)}] - [y_{L1}^{(i)}][b_{L1}^{(i)}]^T + [y_{L1}^{(i)}][c_L^{(i)}][y_{L1}^{(i)}] = [L_L^{(i+1)}][D_L^{(i+1)}][L_L^{(i+1)}]^T \quad (6.5.35)$$

$[L_L^{(i+1)}]$  is normalized such that the entries of the diagonal matrix  $[D_L^{(i+1)}]$  are  $\pm 1$ .

The continued fraction solution at low frequency is evaluated by using Eqs. (6.5.30) and (6.5.31) whereby the recursive coefficient matrices are initialized by Eq. (6.5.26) and updated by Eq. (6.5.33). The doubly asymptotic continued fraction solution is determined by combining the high-frequency continued fraction solution in Eq. (6.5.1) with the low-frequency continued fraction solution in Eq. (6.5.19) using  $[y^{(MH+1)}(\omega)] = [y_L(\omega)]$  (Eq. (6.5.15)). It is expressed as

$$\begin{aligned}
[s^\infty(\omega)] &= (i\omega)[c_\infty] - [\psi^{(1)}]((i\omega)[y_1^{(1)}] - [\psi^{(2)}]((i\omega)[y_1^{(2)}] - \dots \\
&\quad - [\psi^{(MH)}]^{-T}((i\omega)[y_1^{(MH)}] - [\psi_L^{(0)}]([y_{L0}^{(0)}] + (i\omega)[y_{L1}^{(0)}] \\
&\quad - (i\omega)^2[\psi_L^{(1)}]([y_{L0}^{(1)}] + (i\omega)[y_{L1}^{(1)}] - \dots - (i\omega)^2[\psi_L^{(ML)}]([y_{L0}^{(ML)}] \\
&\quad + (i\omega)[y_{L1}^{(ML)}])^{-1}[\psi_L^{(ML)}]^T \dots)^{-1}[\psi_L^{(1)}]^T)^{-1}[\psi_L^{(0)}]^T)^{-1}[\psi^{(MH)}]^T \\
&\quad \dots)^{-1}[\psi^{(2)}]^T)^{-1}[\psi^{(1)}]^T \quad (6.5.36)
\end{aligned}$$

Note that the residual term  $(i\omega)^2[\psi_L^{(ML+1)}][y_L^{(ML+1)}(\omega)]^{-1}[\psi_L^{(ML+1)}]^T$  at the low-frequency limit is neglected.

## 6.6 Doubly asymptotic open boundary condition

The procedure of constructing the high-order doubly asymptotic open boundary condition described in this section is based on the one described in Chapter 3. The vertical boundary ( $\xi = 0$ ) is considered. With use of Eq. (6.4.11), Eq. (6.4.1) mentioned previously in Section 6.4 can be transformed into Eq. (6.6.1),

$$\{\tilde{R}\} = [s^\infty(\omega)]\{\tilde{U}\} \quad (6.6.1)$$

which depends on the excitation frequency  $\omega$ , where

$$\{\tilde{R}\} = [\Phi]^T \{R\} \quad (6.6.2a)$$

$$\{\tilde{U}\} = [\Phi]^{-1} \{U\} \quad (6.6.2b)$$

where  $\{U\}$  denotes  $\{U(\xi = 0)\}$ . Substituting Eq. (6.5.1a) into Eq. (6.6.1) leads to

$$\{\tilde{R}\} = (i\omega)[c_\infty]\{\tilde{U}\} - [\psi^{(1)}]\{\tilde{U}^{(1)}\} \quad (6.6.3)$$

where the auxiliary variable  $\{\tilde{U}^{(1)}\}$  is defined as

$$\{\tilde{U}^{(1)}\} = [y^{(1)}(\omega)]^{-1}[\psi^{(1)}]^T \{\tilde{U}\} \quad (6.6.4)$$

and then reformulated as

$$[\psi^{(1)}]^T \{\tilde{U}\} = [y^{(1)}(\omega)]\{\tilde{U}^{(1)}\} \quad (6.6.5)$$

which is the same form as Eq. (6.6.1). Similarly, an auxiliary variable is introduced for each term of the continued fraction in Eq. (6.5.1b). This yields

$$[\psi^{(i+1)}]^T \{\tilde{U}^{(i)}\} = [y^{(i+1)}(\omega)]\{\tilde{U}^{(i+1)}\} \quad (i = 0, 1, 2, \dots, M_H) \quad (6.6.6)$$

where Eq. (6.6.5) is included as the  $i = 0$  case with  $\{\tilde{U}^{(0)}\} = \{\tilde{U}\}$ . Multiplying Eq. (6.5.1b) by  $\{\tilde{U}^{(i)}\}$  and using the definition of auxiliary variables in Eq. (6.6.6) with  $i - 1$  and  $i$  result in

$$[\psi^{(i)}]^T \{\tilde{U}^{(i-1)}\} = (i\omega)[y_1^{(i)}]\{\tilde{U}^{(i)}\} - [\psi^{(i+1)}]\{\tilde{U}^{(i+1)}\} \quad (i = 1, 2, \dots, M_H) \quad (6.6.7)$$

The residual  $\{\tilde{U}^{(M_H+1)}\}$  of an order  $M_H$  high-frequency continued fraction solution is expressed in Eq. (6.6.6) with  $i = M_H$  as

$$[\psi^{(M_H)}]^T \{\tilde{U}^{(M_H)}\} = [y^{(M_H+1)}(\omega)] \{\tilde{U}^{(M_H+1)}\} \quad (6.6.8)$$

$[y^{(M_H+1)}(\omega)] = [y_L(\omega)]$  (Eq. (6.5.15)) is expressed in Eq. (6.5.19a) as a low-frequency continued fraction solution. Multiplying Eq. (6.5.19a) by  $\{\tilde{U}^{(M_H+1)}\}$  and using Eqs. (6.5.15) and (6.6.8) lead to

$$[\psi_L^{(0)}]^T \{\tilde{U}^{(M_H)}\} = [y_{L0}^{(0)}] \{\tilde{U}^{(M_H+1)}\} + (i\omega)[y_{L1}^{(0)}] \{\tilde{U}^{(M_H+1)}\} - (i\omega)[\psi_L^{(1)}] \{\tilde{U}_L^{(1)}\} \quad (6.6.9)$$

where the auxiliary variable  $\{\tilde{U}_L^{(1)}\}$  is defined in

$$(i\omega)[\psi_L^{(1)}]^T \{\tilde{U}^{(M_H+1)}\} = [y_L^{(1)}(\omega)] \{\tilde{U}_L^{(1)}\} \quad (6.6.10)$$

Again, an auxiliary variable is introduced for each term of the continued fraction in Eq. (6.5.19b). This results in

$$(i\omega)[\psi_L^{(i+1)}]^T \{\tilde{U}_L^{(i)}\} = [y_L^{(i+1)}(\omega)] \{\tilde{U}_L^{(i+1)}\} \quad (i = 0, 1, 2, \dots, M_L) \quad (6.6.11)$$

with  $\{\tilde{U}_L^{(0)}\} = \{\tilde{U}^{(M_H+1)}\}$ . Multiplying Eq. (6.5.19b) by  $\{\tilde{U}_L^{(i)}\}$  and using the definition of auxiliary variables in Eq. (6.6.11) with  $i - 1$  and  $i$  result in

$$(i\omega)[\psi_L^{(i)}]^T \{\tilde{U}_L^{(i-1)}\} = [y_{L0}^{(i)}] \{\tilde{U}_L^{(i)}\} + (i\omega)[y_{L1}^{(i)}] \{\tilde{U}_L^{(i)}\} - (i\omega)[\psi_L^{(i+1)}] \{\tilde{U}_L^{(i+1)}\} \quad (i = 1, 2, \dots, M_L) \quad (6.6.12)$$

For the low-frequency solution with  $i = M_L$ , the approximation  $\{\tilde{U}_L^{(M_L+1)}\} = 0$  is introduced. Substituting Eqs. (6.6.2a) and (6.6.2b) back into Eq. (6.6.1) results in

$$\{R\} = (i\omega)[\Phi]^{-T} [c_\infty] [\Phi]^{-1} \{U\} - [\Phi]^{-T} [\psi^{(1)}] \{\tilde{U}^{(1)}\} \quad (6.6.13)$$

Assembling Eqs. (6.6.13), (6.6.7), (6.6.9) and (6.6.12) leads to a system of linear equations,

$$([K_h] + (i\omega)[C_h]) \{Z\} = \{F\} \quad (6.6.14)$$

where  $\{Z\}$  contains the displacement amplitudes on the vertical boundary  $\Gamma_V$  and the auxiliary variables,  $\{F\}$  is the amplitudes of the excitation forces applied on the



Equation (6.6.17) represents the high-order doubly asymptotic open boundary condition. It is temporally local. When the low-frequency terms are neglected, it becomes a high-order singly asymptotic boundary condition.

## 6.7 Numerical examples

In this section, three layered systems with different material constants are analyzed in the frequency and time domains. The first one that is a single layer is analyzed in Section 6.7.1. The second one that is a semi-infinite two-layered system is analyzed in Section 6.7.2. The third one that is a semi-infinite three-layered system is analyzed in Section 6.7.3.

When evaluating the accuracy of the continued fraction solutions, the equivalent dynamic stiffness coefficient expressed in Eq. (A.3.1) in Appendix A is computed. The equivalent dynamic stiffness coefficients are normalized by the shear modulus  $G$  and plotted with respect to the dimensionless frequency  $a_0$ , which is defined as

$$a_0 = \frac{\omega h}{c_s} \quad (6.7.1)$$

The solution in Eq. (6.4.15) serves as the reference solution.

In the time-domain analysis, the Newmark's method with  $\gamma = 0.5$  and  $\beta = 0.25$  (average acceleration scheme) is adopted to integrate Eq. (6.6.17) (see Section A.2 in Appendix A). An extended finite element mesh is analyzed by using ABAQUS, a commercial finite element package, to provide a reference solution to verify the high-order singly and doubly asymptotic open boundaries. Eight-node isoparametric quadrilateral element (Q8) is selected for the extended mesh method.

Based on the highest frequency of interest  $\omega_h$ , the wave period  $T = 2\pi/\omega_h$  and the minimum wavelength  $\lambda_w = c_s T$  of each sublayer are calculated. The SBFEM and FEM meshes are divided in such a way that 1 wavelength is represented by at least 13 nodes. The size of the time step  $\Delta t$  is chosen as 1/12 of the shortest period.

### 6.7.1 Semi-infinite layer

The first layered system is of one layer with depth  $h$  as illustrated in Fig. 6.7.1(a). The ratio of the material constants used in the analysis is  $G/\rho = 1$ .

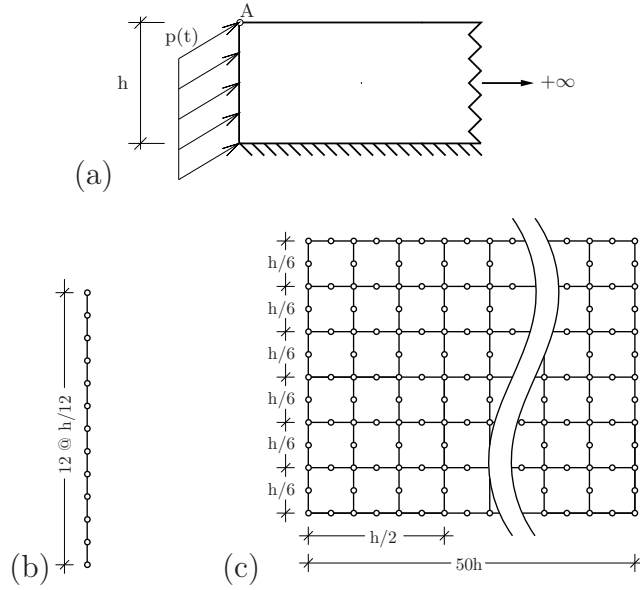
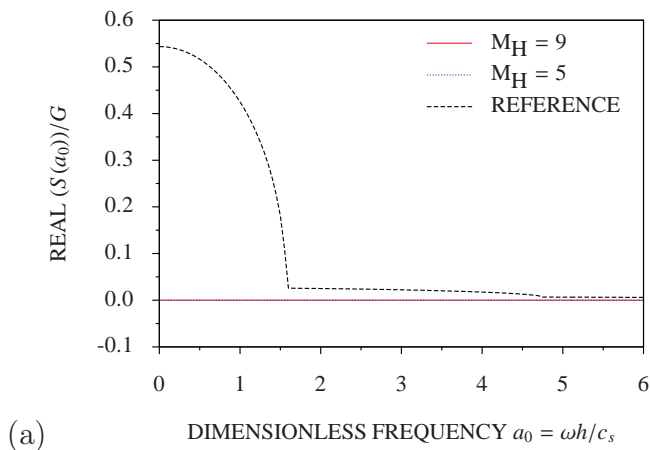


Figure 6.7.1: Semi-infinite layer: (a) geometry, (b) SBFEM mesh and (c) FE mesh

The present open boundary based on the SBFEM is formulated directly on the the vertical boundary  $\Gamma_V$  of the layer. The boundary is discretized with 12 two-node elements in the SBFEM as shown in Fig. 6.7.1(b).

The singly asymptotic continued fraction solution at high frequency is investigated at first. The results of equivalent dynamic stiffness coefficients obtained from the orders  $M_H = 5$  and  $M_H = 9$  are plotted as the real parts in Fig. 6.7.2(a) and the imaginary parts in Fig. 6.7.2(b). They differ considerably from those of the reference solution. The real parts of the singly asymptotic solution are always equal to zero. The imaginary parts oscillate strongly, especially below the first cut-off frequency  $a_0 < \pi/2$ . This example indicates that the singly asymptotic continued fraction solution cannot model evanescent waves below cut-off frequencies.



(a)

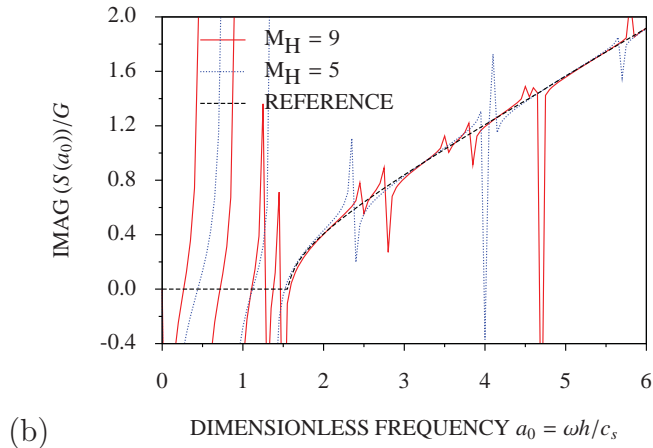
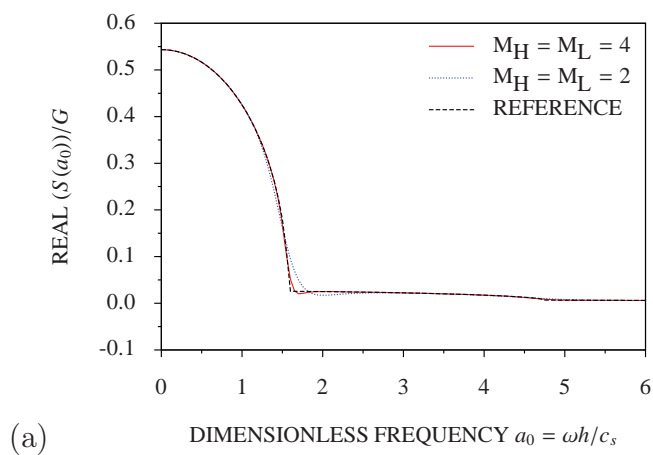


Figure 6.7.2: Equivalent dynamic stiffness coefficient of semi-infinite layer by singly asymptotic continued fraction solution: (a) real part and (b) imaginary part

The doubly asymptotic continued fraction solution are then investigated. The equivalent dynamic stiffness coefficients obtained from the orders  $M_H = M_L = 2$  and  $M_H = M_L = 4$  are plotted in Fig. 6.7.3. Both the real part and the imaginary part of the result obtained at the order  $M_H = M_L = 2$  agree well with those of the reference solution. This indicates that the doubly asymptotic continued fraction solution can model the evanescent waves below the cut-off frequencies. When the order increases to  $M_H = M_L = 4$ , the accuracy of the result also increases. This shows that the doubly asymptotic continued fraction solution converges to the reference solution with increasing orders.



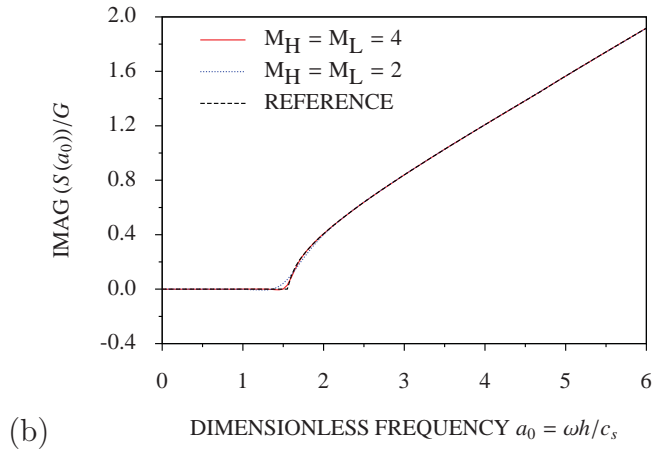
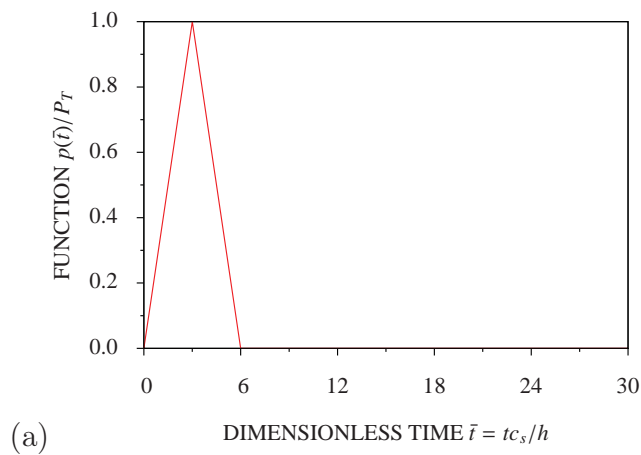


Figure 6.7.3: Equivalent dynamic stiffness coefficient of semi-infinite layer by doubly asymptotic continued fraction solution: (a) real part and (b) imaginary part

The transient response of the semi-infinite layer to a uniformly distributed surface traction  $p(t)$  on the vertical boundary  $\Gamma_V$  as shown in Fig. 6.7.1 is evaluated. The time-dependence of the surface traction  $p(t)$  is prescribed as a triangular function as plotted in Fig. 6.7.4(a) with respect to the dimensionless time  $\bar{t} = tc_s/h$ . The maximum surface traction is denoted as  $P_T$ . The Fourier transform of the triangular function is also plotted in Fig. 6.7.4(b) with respect to the dimensionless frequency  $a_0$ . The highest dimensionless frequency of interest  $a_h$  is observed as 6.



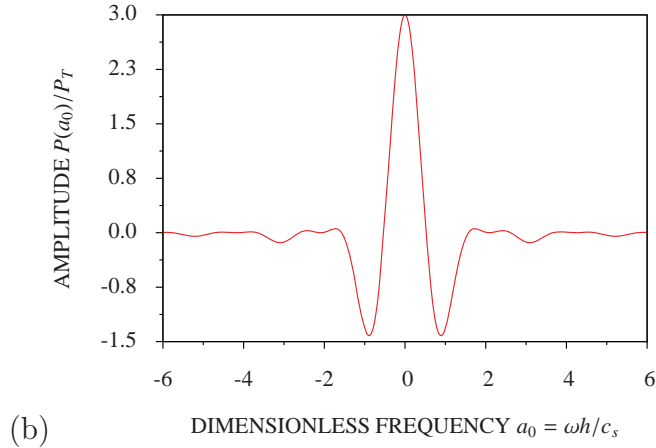


Figure 6.7.4: Triangular function: (a) time history and (b) Fourier transform

To obtain a reference solution, an extended finite element mesh as shown in Fig. 6.7.1(c) is analyzed. The number of nodes on the vertical boundary  $\Gamma_V$  is the same as that of the SBFEM. The length of the extended mesh is chosen as  $50h$  so that responses are not affected by the waves reflected at the truncated boundary. The total number of nodes in the extended finite element mesh is 6,013 while the scaled boundary finite element mesh has only 13 nodes. The dimensionless time step  $\Delta \bar{t}$  of 0.05 is chosen for both the extended mesh and the open boundaries.

The displacement responses at Point *A* located at the top of the vertical boundary  $\Gamma_V$  (Fig. 6.7.1(a)) is chosen to evaluate the accuracy of the open boundaries. The results obtained from the order  $M_H = 5$  and  $M_H = 9$  singly asymptotic open boundary are non-dimensionalized and plotted with respect to the dimensionless time  $\bar{t}$  as shown in Fig. 6.7.5(a). At the order  $M_H = 5$ , the result is accurate at the early time ( $0 < \bar{t} < 3$ ), but exhibits “fictitious reflection” at the late time ( $\bar{t} > 3$ ). At the order  $M_H = 9$ , the result becomes more accurate but only at the early time. Moreover, “fictitious reflection” still occurs at the late time. These “fictitious reflections” are similar to those in Chapter 3. This example shows that the singly asymptotic open boundary, which is closely related to several high-order absorbing boundaries, cannot transmit evanescent waves below cut-off frequencies. Therefore, this open boundary is unsuitable for a long-time analysis.

Compared to the singly asymptotic open boundary, the doubly asymptotic open boundary at the orders  $M_H = M_L = 2$  and  $M_H = M_L = 4$  yield more accurate results as shown in Fig. 6.7.5(b). With merely  $M_H = M_L = 2$ , the displacement response agrees very well with that of the extended mesh method. No “fictitious reflection” is observed. In addition, the accuracy of the result at the late time increases as the order increases to  $M_H = M_L = 4$ . By comparing Figs. 6.7.5(a)

and 6.7.5(b), the doubly asymptotic open boundary is much more accurate than the singly asymptotic open boundary with the same number of terms.

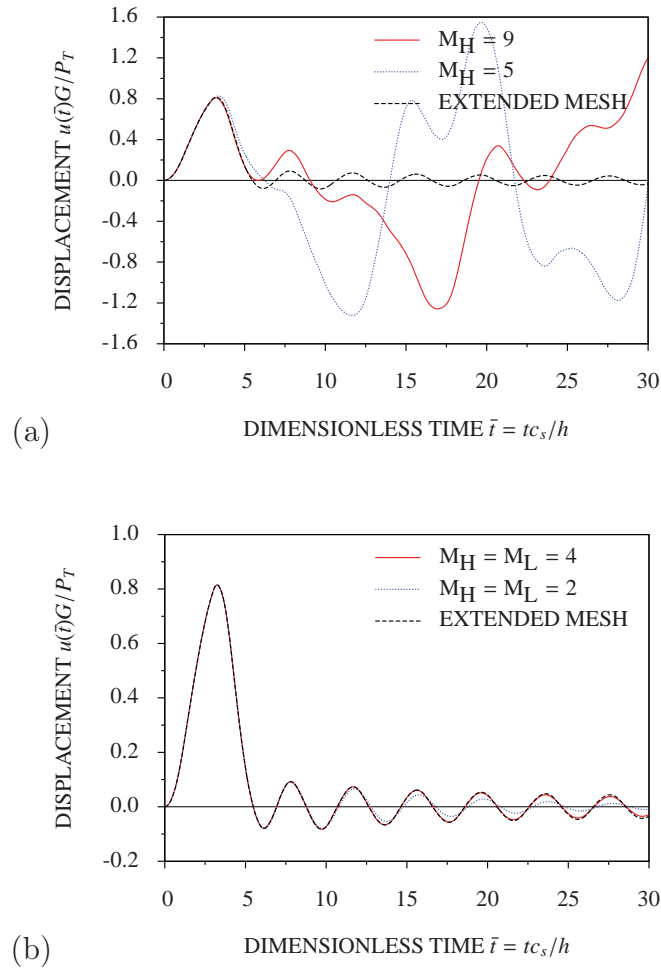


Figure 6.7.5: Displacement responses of semi-infinite layer at Point  $A$  to surface traction  $p(t)$ : (a) by singly asymptotic open boundary and (b) by doubly asymptotic open boundary

## 6.7.2 Semi-infinite two-layered system

A two-layered system is illustrated in Fig. 6.7.6(a). The depth of each sublayer is  $h/2$ . The ratios of the material constants are  $G_2/G_1 = 5$ ,  $G_1/\rho_1 = 1$  and  $\rho_2/\rho_1 = 1$ .

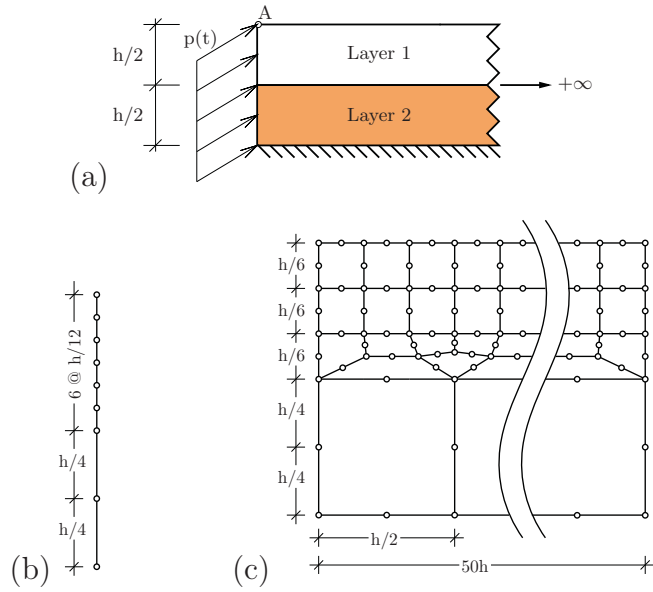
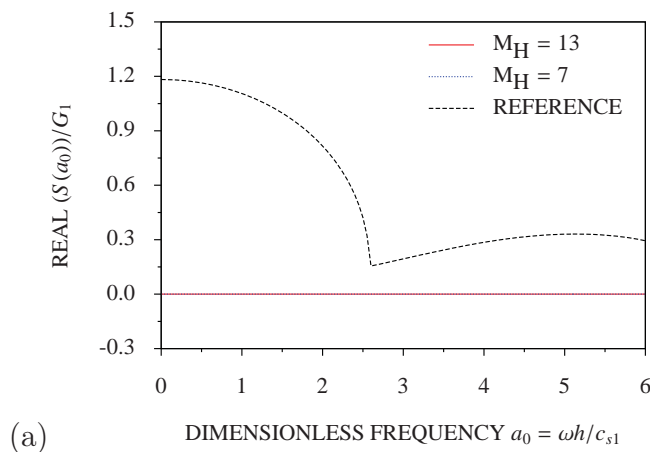


Figure 6.7.6: Semi-infinite two-layered system: (a) geometry, (b) SBFEM mesh and (c) FE mesh

In mesh modeling, the meshes of the singly and doubly asymptotic open boundaries are identical and modeled by the SBFEM with 8 two-node elements. Only the vertical boundary  $\Gamma_V$  of the layered system is discretized as shown in Fig. 6.7.6(b).

The equivalent dynamic stiffness coefficients obtained from the order  $M_H = 7$  and  $M_H = 13$  singly asymptotic continued fraction solution at high frequency are plotted in Fig. 6.7.7. Neither the real parts nor the imaginary parts agree with those of the reference solution. Again, the real parts are always zero, and the imaginary parts exhibit strong oscillations. The accuracy is even worse than the case of the singly layered system (Section 6.7.1). Thus the singly asymptotic continued fraction solution cannot model evanescent waves below cut-off frequencies.



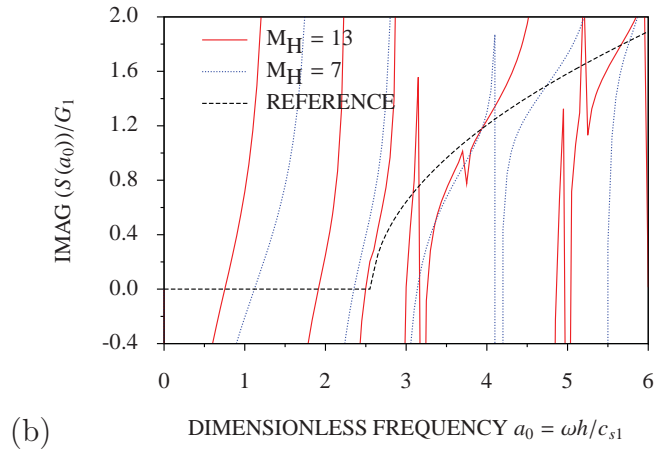
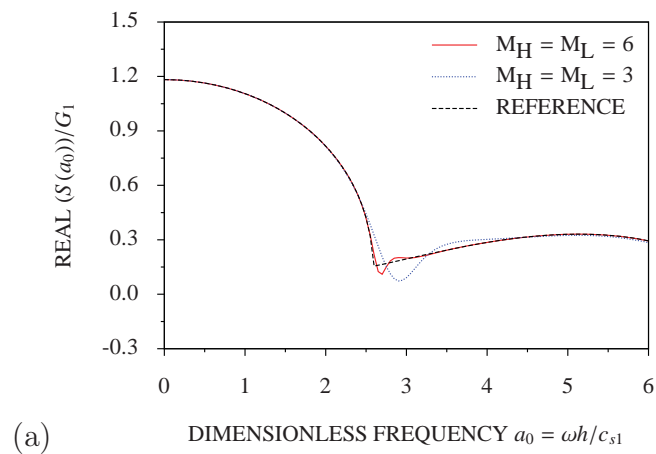


Figure 6.7.7: Equivalent dynamic stiffness coefficient of semi-infinite two-layered system by singly asymptotic continued fraction solution: (a) real part and (b) imaginary part

In contrast, the doubly asymptotic continued fraction solution with the same numbers of terms i.e. using  $M_H = M_L = 3$  and  $M_H = M_L = 6$  performs better. The real and imaginary parts of the results as plotted in Fig. 6.7.8 together with those of the reference solution. With the order  $M_H = M_L = 6$ , the accuracy of the result increases, and the real and imaginary parts around  $a_0 = 2.5$  converge to those of the reference solution. Therefore, the doubly asymptotic continued fraction solution can model evanescent waves below the cut-off frequencies. It is noticed that a higher order of continued fraction is required by the two-layered system than by the singly layered system.



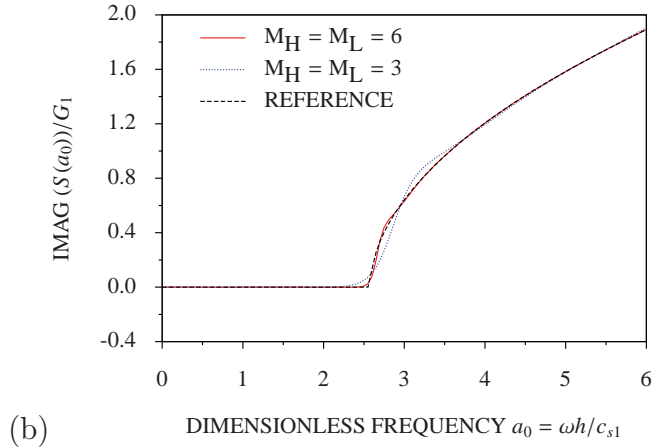
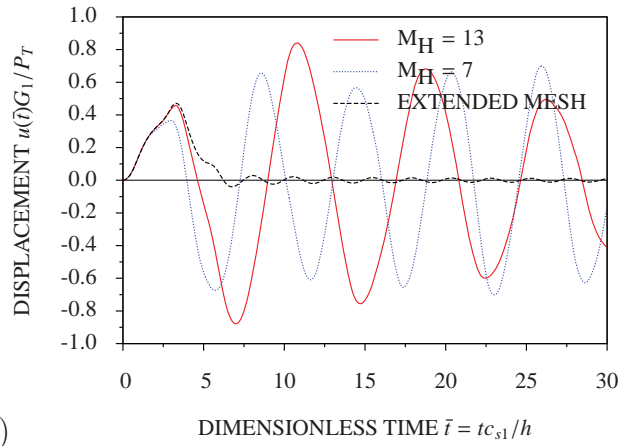


Figure 6.7.8: Equivalent dynamic stiffness coefficient of semi-infinite two-layered system by doubly asymptotic continued fraction solution: (a) real part and (b) imaginary part

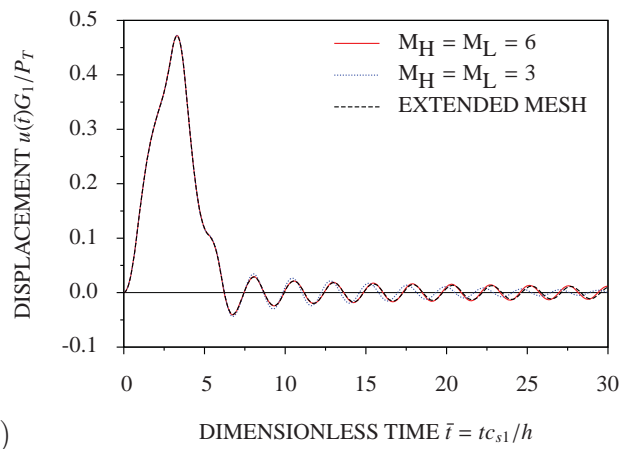
The transient response of the layered system is investigated. The same uniform surface traction  $p(t)$  as in Section 6.7.1 is applied to the vertical boundary  $\Gamma_V$ . The time history of  $p(t)$  is shown in Fig. 6.7.4(a). A reference solution is obtained from an extended mesh (Fig. 6.7.6(c)). The number of nodes on the vertical boundary  $\Gamma_V$  is the same as that of the SBFEM. The length of the extended mesh is chosen as  $50h$ . The total number of nodes in the mesh is 4,006 which is about 445 times the total number of nodes of the SBFEM. The size of the dimensionless time step is chosen as  $\Delta\bar{t} = 0.05$ .

The displacement responses at Point  $A$  obtained by using the order  $M_H = 7$  and  $M_H = 13$  singly asymptotic boundary are plotted in Fig. 6.7.9(a). At the very early time ( $0 < \bar{t} < 1.5$  for  $M_H = 7$  and  $0 < \bar{t} < 3$  for  $M_H = 13$ ), the results agree well with those of the extended mesh method. However, at the late time significant “fictitious reflections” occur. The improvement by increasing the order of the boundary condition is marginal.

In contrast, the doubly asymptotic open boundary with the same numbers of terms performs excellently. The results obtained from the orders  $M_H = M_L = 3$  and  $M_H = M_L = 6$  are plotted in Fig. 6.7.9(b). All the results correspond to those of the extended mesh method, and no “fictitious reflection” is observed throughout the whole duration. The accuracy of the result at the late time increases when the order increases to  $M_H = M_L = 6$ . Thus the doubly asymptotic open boundary is more suitable for a long-time analysis of this layered system.



(a)



(b)

Figure 6.7.9: Displacement responses of semi-infinite two-layered system at Point  $A$  to surface traction  $p(t)$ : (a) by singly asymptotic open boundary and (b) by doubly asymptotic open boundary

### 6.7.3 Semi-infinite three-layered system

A three layered system with the depth of each sublayer equal to  $h/3$ , is illustrated in Fig. 6.7.10(a). The ratios of the material constants used in the analysis are  $G_3/G_1 = 3/5$ ,  $G_2/G_1 = 1/5$ ,  $G_1/\rho_1 = 5$  and  $\rho_3/\rho_1 = \rho_2/\rho_1 = 1$ .

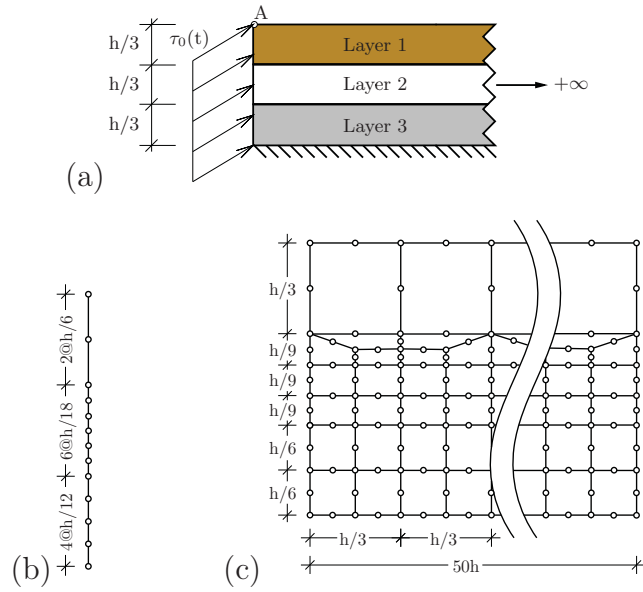
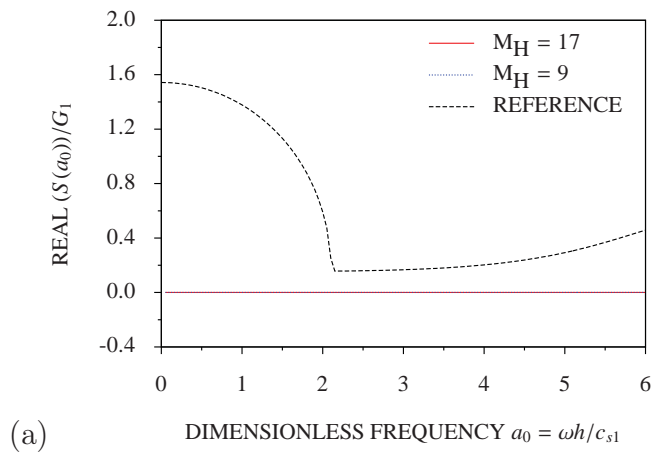


Figure 6.7.10: Semi-infinite three-layered system: (a) geometry, (b) SBFEM mesh and (c) FE mesh

The doubly and singly asymptotic open boundaries are applied directly on the vertical boundary  $\Gamma_V$  of the layered system. Only the vertical boundary  $\Gamma_V$  is discretized in the SBFEM with 12 two-node elements as shown in Fig. 6.7.10(b).

The equivalent dynamic stiffness coefficients are evaluated. The results obtained with the singly asymptotic continued fraction solution at the orders  $M_H = 9$  and  $M_H = 17$  are plotted in Fig. 6.7.11. Significant difference with the reference solution is observed.



(a)

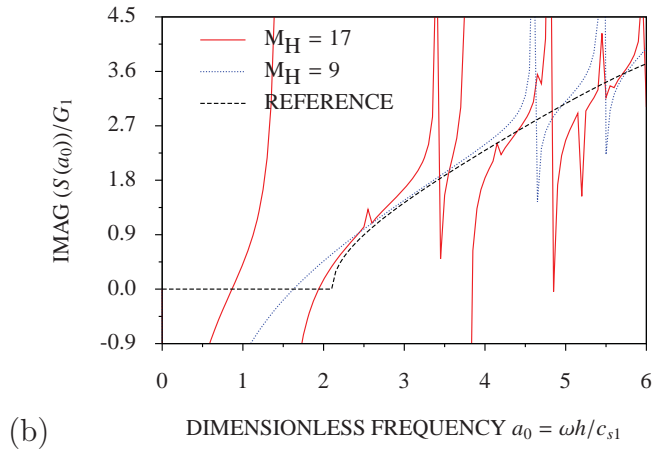
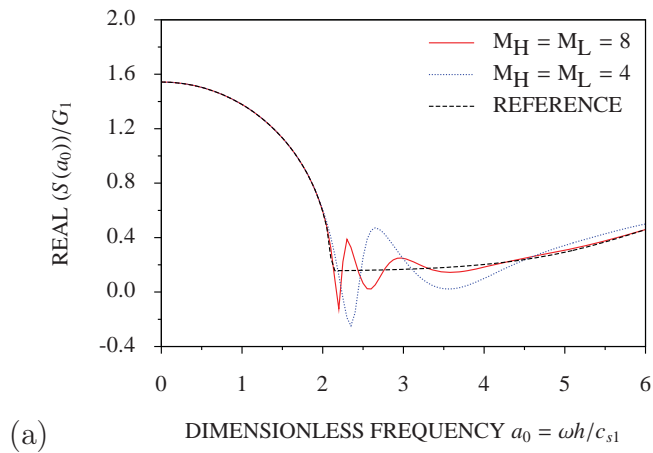


Figure 6.7.11: Equivalent dynamic stiffness coefficient of semi-infinite three-layered system by singly asymptotic continued fraction solution: (a) real part and (b) imaginary part

The equivalent dynamic stiffness coefficient obtained from the doubly asymptotic continued fraction at the order  $M_H = M_L = 4$  is shown in Fig. 6.7.12. Both the real and imaginary parts agree well with those of the reference solution at low frequencies ( $0 < a_0 < 1$ ) and high frequencies ( $a_0 > 2$ ). The accuracy in the intermediate frequency range improves when the order is increased to  $M_H = M_L = 8$ .



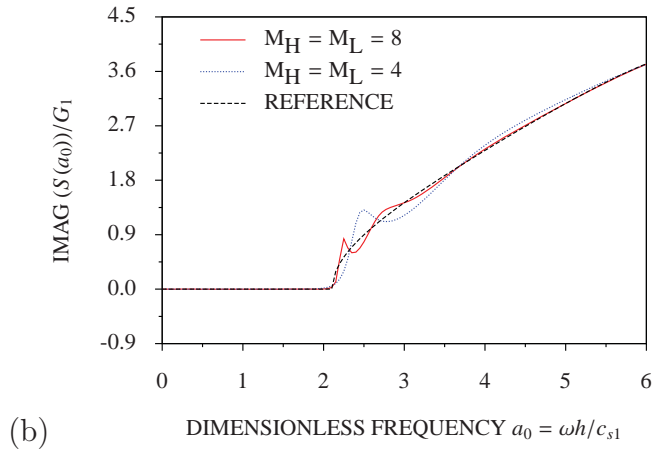
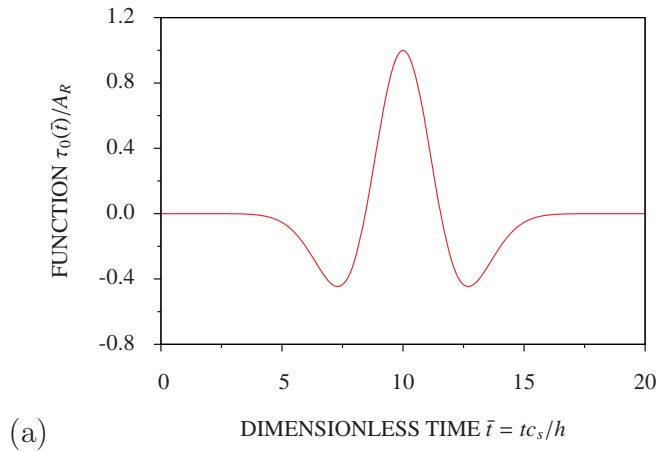


Figure 6.7.12: Equivalent dynamic stiffness coefficient of semi-infinite three-layered system by doubly asymptotic continued fraction solution: (a) real part and (b) imaginary part

The response of the layered system to a uniformly distributed surface traction  $\tau_0(t)$  applied on the vertical boundary  $\Gamma_V$  is computed. The time history of  $\tau_0(t)$  is prescribed as a function of Ricker wavelet with  $\bar{t}_s = 10$  and  $\bar{t}_0 = 2.2$  (see Eqs. (A.1.1) and (A.1.2) in Appendix A). The time history is plotted in Fig. 6.7.13(a) of which Fourier transform is shown in Fig. 6.7.13(b). The highest dimensionless frequency of interest  $a_h$  is observed as 3.



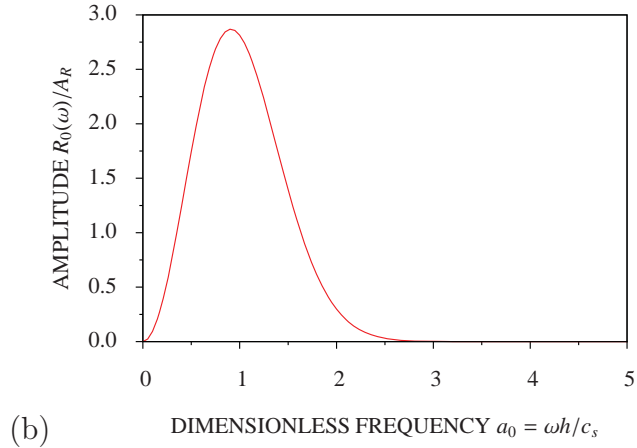


Figure 6.7.13: Ricker wavelet function: (a) time history and (b) Fourier transform

Again, an extended finite element mesh (Fig. 6.7.10(c)) is analyzed. The number of nodes on the vertical boundary  $\Gamma_V$  is the same as that in the mesh of the SBFEM. The total number of nodes in the mesh is 5,863 which is about 451 times the total number of nodes generated by the SBFEM. The dimensionless time step  $\Delta \bar{t} = 0.05$  is chosen.

The singly asymptotic open boundary is investigated first. The displacement responses at Point  $A$  obtained at the orders  $M_H = 9$  and  $M_H = 17$  are plotted in Fig. 6.7.14(a). Again, the results are only accurate at the early time. Significant “fictitious reflections” are observed at the late time.

The doubly asymptotic open boundary with the same numbers of terms is applied. The results are much more accurate as plotted in Fig. 6.7.14(b). The result obtained from using the order  $M_H = M_L = 4$  does not exhibit any “fictitious reflection” throughout the entire duration. The accuracy of the result at the late time increases when the order is increased to  $M_H = M_L = 8$ . The result is almost the same as that of the extended mesh method, and no “fictitious reflection” occurs. Thus the doubly asymptotic open boundary is more suitable for a long-time analysis of this layered system.

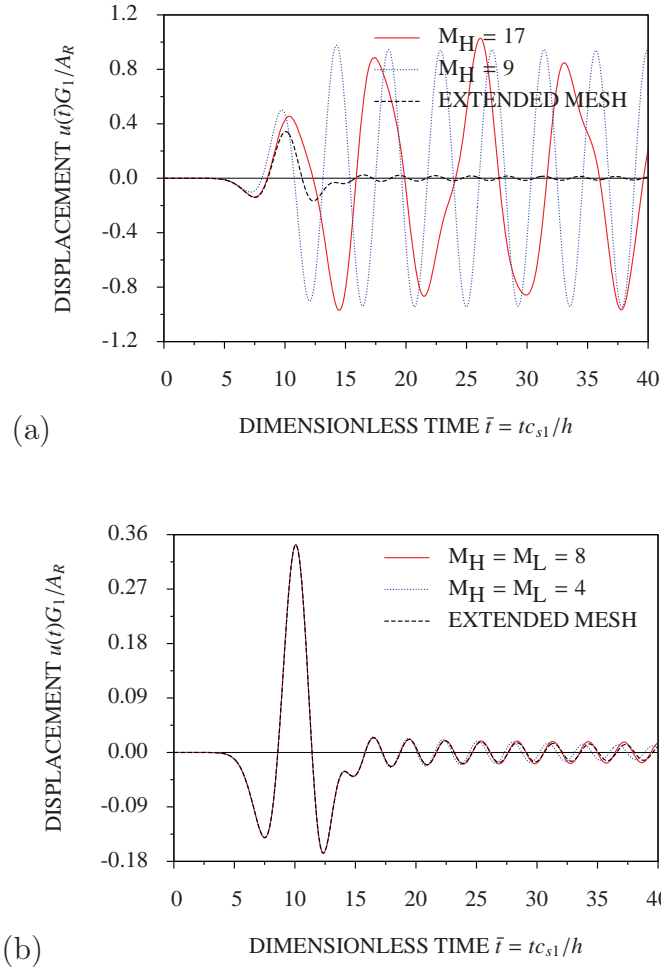


Figure 6.7.14: Displacement responses of semi-infinite three-layered system at Point  $A$  to surface traction  $\tau_0(t)$ : (a) by singly asymptotic open boundary and (b) by doubly asymptotic open boundary

## 6.8 Conclusions

A matrix solution for the scaled boundary finite element equation in dynamic stiffness is obtained for the modeling of scalar wave propagation in semi-infinite layered systems. The solution is expressed as high-order doubly asymptotic continued fraction in the frequency domain. It is formulated in the time domain as a high-order open boundary condition. From the analysis results obtained in the frequency and time domains, it can be concluded as follows:

1. In the frequency domain, the singly asymptotic continued fraction solution can only model the propagating waves at high frequencies (i.e. above cut-off frequencies), but cannot model the evanescent waves at low frequencies (i.e. below cut-off frequencies). In contrast, the doubly asymptotic continued

fraction solution can model not only the propagating waves at high frequencies, but also the evanescent waves at low frequencies. The solution rapidly converges to the reference solution as the orders increase.

2. In the time domain, the accuracy of the results obtained from the singly asymptotic open boundary improves very slowly with increasing order. In addition, “fictitious reflection” always occurs at the late time. In case of the doubly asymptotic open boundary with the same number of terms, “fictitious reflection” does not exist. In addition, the accuracy of the results is more higher at both early time and late time.
3. The high-order doubly asymptotic open boundary for scalar wave propagation in semi-infinite layered systems is indispensable to long-time analyses. The open boundary is temporally local. It is expressed as a system of first-order ordinary differential equation in time. The two time-independent coefficient matrices, the stiffness matrix  $[K_h]$  and the damping matrix  $[C_h]$  are banded and symmetric. Thus well-established time-stepping schemes in structural dynamics are directly applicable.

# Chapter 7

## Doubly Asymptotic Open Boundary for Vector Wave Propagation in Semi-Infinite Layer

### Abstract

The propagation of vector waves in a semi-infinite layer with a constant depth is addressed by using the scaled boundary finite element method. In comparison with scalar wave problems in previous chapter, an extra coefficient matrix  $[E^1]$  appears in the scaled boundary finite element equation. The doubly asymptotic continued fraction solution is rederived to include the contribution of  $[E^1]$ . The factor matrices are introduced to the continued fraction solution to improve the numerical stability of the solution. The coefficients of the solution are determined recursively by satisfying the scaled boundary finite element equation in dynamic stiffness at both high- and low-frequency limits. By introducing auxiliary variables and using the doubly asymptotic continued fraction solution, the force-displacement relationship on the boundary is formulated as a high-order doubly asymptotic open boundary condition in the frequency domain. The open boundary is expressed as a system of first-order ordinary differential equations in the time domain. Standard time-step schemes can be directly applied to perform the time integration. No parameters other than the orders of continued fraction are selected by the user.

### 7.1 Introduction

As mentioned in the previous chapters, it is necessary to introduce an artificial boundary to the boundary of the computational domain or the interior region when-

ever an unbounded domain or an exterior region is modeled for a wave propagation problem. The boundary condition enforced on the artificial boundary is aimed at absorbing propagating waves to prevent fictitious reflection at the boundary which often pollutes the solution. Today there are several absorbing boundary conditions (ABCs) which can be classified into two groups. The ABCs in the first group are global ABCs obtained from employing rigorous methods. The ABCs in the second group are local ABCs obtained from employing approximate methods. The global ABCs provide high accuracy and robustness, but are computationally expensive due to convolution integrals, while the local ABCs are geometrically universal, computationally efficient, but less accurate (Tsynkov, 1998).

For a long-time analysis of large-scale problems, the global ABCs are more impractical due to their large demand on storage capacity and computing time (Bennett, 1976). This led to the search for high quality approximations that are spatially and temporally local (Kausel, 1988). As a result, a large number of local ABCs were developed such as the viscous boundary condition (Lysmer and Kuhlemeyer, 1969) and the extrapolation boundary condition (Liao and Wong, 1984). In order to improve the accuracy of the boundary condition, high-order ABCs were proposed such as the paraxial boundary condition (Engquist and Majda, 1979) and the BGT boundary condition (Bayliss and Turkel, 1982) etc.

Even though high-order ABCs can increase the accuracy by increasing the order, they encounter difficulties in numerical implementation when the order is higher than two (Givoli, 2004). In recent years, local high-order ABCs have been proposed, for example, the Givoli-Neta ABC Givoli and Neta (2003), the Hagstrom-Warburton ABC Hagstrom and Warburton (2004). These high-order local ABCs are practically implementable for an arbitrarily order, based on the concept of using auxiliary variables originally proposed by Collino (1993).

Most of high-order ABCs are singly asymptotic at the high-frequency limit and appropriate for propagating waves. It has been shown in Chapter 6 that the singly asymptotic open boundary is not suitable for long-time analyses involved layered system since it cannot model evanescent waves below the cut-off frequencies. To improve the accuracy of the long-time behavior of ABCs, the inclusion of evanescent modes is necessary (Hagstrom *et al.*, 2008). The high-order doubly asymptotic open boundary condition constructed in Chapter 3 has been proposed for the modal equations of scalar waves in a semi-infinite layer. The open boundary condition is asymptotic at both high- and low-frequency limits. It has been shown that the doubly asymptotic boundary can model not only propagating waves but also evanescent waves.

For vector wave propagation problems, most of existing high-order ABCs are singly asymptotic at high-frequency limit, specifically developed for circular and spherical boundaries such as the high-order ABCs proposed by Clayton and Engquist (1977) and Randall (1988, 1989). However, in case of semi-infinite layers, it is rarely reported in literature, for example, the high-order ABC developed by Higdon (1992) and Guddati and Tassoulas (1999). From application point of view, it is necessary to develop a temporally local open boundary that is applicable to vector wave propagation in semi-infinite layers.

The objective of this chapter is to develop a doubly asymptotic open boundary for vector wave propagation in a homogeneous semi-infinite layer with a constant depth by extending the SBFEM. This chapter is organized as follows: in Section 7.2, the governing equation (the equation of the in-plane motion) of a homogeneous semi-infinite layer with a constant depth is derived for vector waves. In Section 7.3, the SBFEM equation in displacement of the semi-infinite layer is derived in the time domain. In Section 7.4, the SBFEM equation in dynamic stiffness of the semi-infinite layer is derived in the frequency domain. In Section 7.5, the derivation of the doubly asymptotic continued fraction solution is presented. In Section 7.6, the high-order doubly asymptotic open boundary condition is constructed in both frequency and time domains. In Section 7.7, numerical examples are demonstrated in the frequency and time domains. In Section 7.8, conclusions are presented.

## 7.2 Governing differential equation of vector waves

A semi-infinite layer with constant depth  $h$  is shown in Fig. 7.2.1(a). The semi-infinite layer is isotropic, homogeneous and elastic. The material constants are the mass density  $\rho$ , the Young's modulus  $E$  and the Poisson's ratio  $\nu$ . The in-plane motion ( $u = u(x, y, t)$  and  $v = v(x, y, t)$  in the  $x$  and  $y$  directions, respectively) of the semi-infinite layer in the Cartesian coordinates  $(x, y)$  and the plane strain condition are considered. For the boundary conditions, it is assumed that the vertical boundary  $\Gamma_V$  located at  $x = x_b$  is subjected to time-dependent in-plane normal and shear stresses. Free condition is imposed on the upper boundary  $\Gamma_U$ , and fixed boundary condition is imposed on the lower boundary.

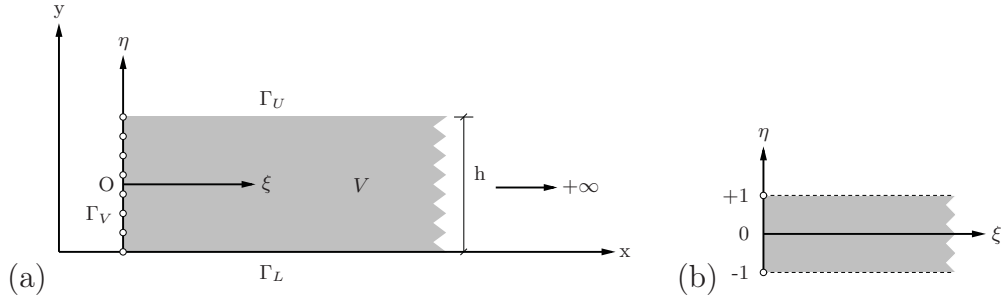


Figure 7.2.1: Homogeneous semi-infinite layer with constant depth: (a) geometry and semi-discretization and (b) typical element

Introducing the differential operator denoting the matrix of spatial derivatives in the Cartesian coordinates,

$$[L] = \begin{bmatrix} \frac{\partial}{\partial x} & 0 & \frac{\partial}{\partial y} \\ 0 & \frac{\partial}{\partial y} & \frac{\partial}{\partial x} \end{bmatrix}^T \quad (7.2.1)$$

The in-plane strains  $\{\varepsilon\} = [\varepsilon_x \quad \varepsilon_y \quad \gamma_{xy}]^T$  are expressed as

$$\{\varepsilon\} = [L]\{w\} \quad (7.2.2)$$

where the displacement vector  $\{w\}$  is defined as

$$\{w\} = [u \quad v]^T \quad (7.2.3)$$

$\varepsilon_x$  and  $\varepsilon_y$  are the normal strains in the  $x$  and  $y$  directions,  $\gamma_{xy}$  is the shear strain. The in-plane stresses  $\{\sigma\} = [\sigma_x \quad \sigma_y \quad \tau_{xy}]^T$  are equal to

$$\{\sigma\} = [D]\{\varepsilon\} \quad (7.2.4)$$

where  $\sigma_x$  and  $\sigma_y$  are the normal stresses in the  $x$  and  $y$  directions,  $\tau_{xy}$  is the shear stress,  $[D]$  is the elasticity matrix for plane strain condition,

$$[D] = \begin{bmatrix} \lambda + 2G & \lambda & & \\ \lambda & \lambda + 2G & & \\ & & & G \end{bmatrix} \quad (7.2.5)$$

where the Lamé constant  $\lambda$  and the shear modulus  $G$  are

$$\lambda = \frac{E\nu}{(1+\nu)(1-2\nu)} \quad (7.2.6)$$

$$G = \frac{E}{2(1+\nu)} \quad (7.2.7)$$

The governing equation of motion in the elastic medium is expressed as

$$[L]^T\{\sigma\} = \rho\{\ddot{w}\} \quad (7.2.8)$$

where  $\{\ddot{w}\} = [\ddot{u} \ \ddot{v}]^T$  is the acceleration vector.

Substituting Eqs. (7.2.3) and (7.2.4) into Eq. (7.2.8), using Eqs. (7.2.2) and (7.2.5), and rearranging the equation lead to

$$(\lambda + G)\phi_{,x} + G\nabla^2 u = \rho\ddot{u} \quad (7.2.9a)$$

$$(\lambda + G)\phi_{,y} + G\nabla^2 v = \rho\ddot{v} \quad (7.2.9b)$$

where the potential  $\phi$  is defined as

$$\phi = \varepsilon_x + \varepsilon_y \quad (7.2.10)$$

and the Laplace operator  $\nabla^2$  is defined as

$$\nabla^2 = \frac{\partial^2}{\partial x^2} + \frac{\partial^2}{\partial y^2} \quad (7.2.11)$$

Differentiating Eqs. (7.2.9a) and (7.2.9b) with respect to  $y$  and  $x$ , respectively, combining them, using Eq. (7.2.10), and rearranging the resulting equation lead to the equation of dilatational wave or  $P$ -wave formulated in two-dimensional Cartesian coordinates,

$$\nabla^2 \phi = \frac{1}{c_p^2} \ddot{\phi} \quad (7.2.12)$$

with the speed of  $P$ -wave  $c_p$ ,

$$c_p = \sqrt{\frac{(\lambda + 2G)}{\rho}} \quad (7.2.13)$$

Afterwards, differentiating Eqs. (7.2.9a) and (7.2.9b) with respect to  $y$  and  $x$ , respectively, subtracting the latter from the former, and rearranging the equation lead

to the equation of shear wave or  $S$ -wave formulated in two-dimensional Cartesian coordinates,

$$\nabla^2 \varphi = \frac{1}{c_s^2} \ddot{\varphi} \quad (7.2.14)$$

where the potential  $\varphi$  is defined as

$$\varphi = u_{,y} - v_{,x} \quad (7.2.15)$$

and  $c_s$  is the speed of  $S$ -wave,

$$c_s = \sqrt{\frac{G}{\rho}} \quad (7.2.16)$$

### 7.3 Scaled boundary finite element method of semi-infinite layer with constant depth

The scaled boundary finite element method (SBFEM) is a novel semi-analytical approach. It was first developed for modeling unbounded domains with arbitrary geometry and called the consistent infinitesimal finite-element cell method (Wolf and Song, 1996). The original derivation of the SBFEM for vector wave propagation was proposed by Wolf and Song (1995). In modeling of the semi-infinite layer with constant depth  $h$ , which is a special case (see Fig. 7.2.1(a)), the scaling center  $O$  is located at infinity, and thus the scaling corresponds to translating the vertical boundary  $\Gamma_V$  (Li *et al.*, 2005).

The vertical boundary  $\Gamma_V$  shown in Fig. 7.2.1(a) is discretized by one-dimensional line elements. A typical element is shown in Fig. 7.2.1(b). Its geometry can be expressed in the scaled boundary coordinates  $(\xi, \eta)$  as

$$x(\xi) = x_b + \xi \quad (7.3.1a)$$

$$y(\eta) = \{N(\eta)\}^T \{y_b\} \quad (7.3.1b)$$

where  $\xi$  is the horizontal coordinate that  $\xi \geq 0$ ,  $\eta$  the vertical coordinate that  $-1 \leq \eta \leq 1$ ,  $\{N(\eta)\}^T$  transpose of the shape function vector formulated in the coordinate  $\eta$ , and  $\{y_b\}$  the vertical coordinate vector of the nodes on the vertical boundary  $\Gamma_V$ .

The vector of spatial derivatives in the Cartesian coordinates  $[\frac{\partial}{\partial x} \quad \frac{\partial}{\partial y}]^T$  is related to those in the local coordinates  $[\frac{\partial}{\partial \xi} \quad \frac{\partial}{\partial \eta}]^T$  by

$$[\frac{\partial}{\partial x} \quad \frac{\partial}{\partial y}]^T = [J(\eta)]^{-1} [\frac{\partial}{\partial \xi} \quad \frac{\partial}{\partial \eta}]^T \quad (7.3.2)$$

where  $[J(\eta)]$  is the Jacobian matrix, which is expressed as

$$[J(\eta)] = \begin{bmatrix} x(\xi)_{,\xi} & y(\eta)_{,\xi} \\ x(\xi)_{,\eta} & y(\eta)_{,\eta} \end{bmatrix} = \begin{bmatrix} 1 & 0 \\ 0 & y(\eta)_{,\eta} \end{bmatrix} \quad (7.3.3)$$

Its inverse and determinant are

$$[J(\eta)]^{-1} = \frac{1}{|J(\eta)|} \begin{bmatrix} y(\eta)_{,\eta} & 0 \\ 0 & 1 \end{bmatrix} \quad (7.3.4)$$

$$|J(\eta)| = y(\eta)_{,\eta} = \{N(\eta)\}_{,\eta}^T \{y_b\} \quad (7.3.5)$$

respectively. By substituting Eq. (7.3.4) into Eq. (7.3.2), the spatial derivatives in the Cartesian coordinates are rewritten as

$$\frac{\partial}{\partial x} = \frac{\partial}{\partial \xi} \quad (7.3.6a)$$

$$\frac{\partial}{\partial y} = \frac{1}{|J(\eta)|} \frac{\partial}{\partial \eta} \quad (7.3.6b)$$

Substituting Eq. (7.3.6) into Eq. (7.2.1) and using Eq. (7.3.5) yield

$$[L] = [b^1] \frac{\partial}{\partial \xi} + [b^2(\eta)] \frac{\partial}{\partial \eta} \quad (7.3.7)$$

where  $[b^1]$  and  $[b^2(\eta)]$  are defined as

$$[b^1] = \begin{bmatrix} 1 & 0 & 0 \\ 0 & 0 & 1 \end{bmatrix}^T \quad (7.3.8a)$$

$$[b^2(\eta)] = \frac{1}{|J(\eta)|} \begin{bmatrix} 0 & 0 & 1 \\ 0 & 1 & 0 \end{bmatrix}^T \quad (7.3.8b)$$

The displacements along a horizontal line passing through a node on the boundary are represented by nodal displacement functions  $\{w(\xi)\}$ . The displacement fields are approximated by interpolating the nodal displacement function  $\{w(\xi)\}$

piecewisely,

$$w = w(\xi, \eta) = [N(\eta)]\{w(\xi)\} \quad (7.3.9)$$

where  $[N(\eta)]$  denotes the shape function matrix formulated in the coordinate  $\eta$ ,

$$[N(\eta)] = \begin{bmatrix} N_1(\eta) & 0 & N_2(\eta) & 0 & \dots \\ 0 & N_1(\eta) & 0 & N_2(\eta) & \dots \end{bmatrix} \quad (7.3.10)$$

Substituting Eqs. (7.3.7) and (7.3.9) into Eq. (7.2.2) yields

$$\{\varepsilon\} = [B^1(\eta)]\{w(\xi)\}_{,\xi} + [B^2(\eta)]\{w(\xi)\} \quad (7.3.11)$$

where  $[B^1(\eta)]$  and  $[B^2(\eta)]$  are defined as

$$[B^1(\eta)] = [b^1][N(\eta)] \quad (7.3.12a)$$

$$[B^2(\eta)] = [b^2(\eta)][N(\eta)]_{,\eta} \quad (7.3.12b)$$

Substituting Eq. (7.3.11) into Eq. (7.3.13) leads to

$$\{\sigma\} = [D]([B^1(\eta)]\{w(\xi)\}_{,\xi} + [B^2(\eta)]\{w(\xi)\}) \quad (7.3.13)$$

In the derivation of the scale boundary finite element equation in displacement, the virtual work principle

$$\int_V \{\varepsilon^*\}^T \{\sigma\} dV = \int_V w^*(\xi, \eta) \rho \ddot{u} dV + \int_{\Gamma_V} w^*(\xi, \eta) \tau_s d\Gamma_V \quad (7.3.14)$$

is employed (Wolf, 2003). The left-hand side of the equation represents the internal virtual work where the virtual strain vector  $\{\varepsilon^*\}$  corresponds to the strain vector in Eq. (7.3.11). The right-hand side is the external work of the inertial force and the surface traction  $\{t_s\}$  where the virtual displacements  $\{w^*\} = \{w^*(\xi, \eta)\}$  is approximated by

$$w^*(\xi, \eta) = [N(\eta)]\{w^*(\xi)\} = \{w^*(\xi)\}^T [N(\eta)]^T \quad (7.3.15)$$

using the same shape function as that in Eq. (7.3.9). For a two-dimensional problem, the third dimension is assumed to be a unit length. An infinitesimal area  $dV$  and

an infinitesimal boundary  $d\Gamma_V$  are defined as

$$dV = |J(\eta)|d\xi d\eta \quad (7.3.16a)$$

$$d\Gamma_V = |J(\eta)|d\eta \quad (7.3.16b)$$

respectively. For convenience, each term in Eq. (7.3.14) is considered individually. Using Eq. (7.3.11) for  $\{\varepsilon^*\}$  and substituting Eqs. (7.3.13) and (7.3.16a) into the single term on the left-hand side of Eq. (7.3.14) yield

$$\begin{aligned} \int_V \{\varepsilon^*\}^T \{\sigma\} dV &= \int_0^\infty \{w^*(\xi)\}_{,\xi}^T [E^0] \{w(\xi)\}_{,\xi} d\xi + \int_0^\infty \{w^*(\xi)\}_{,\xi}^T [E^1]^T \{w(\xi)\} d\xi \\ &+ \int_0^\infty \{w^*(\xi)\}^T [E^1] \{w(\xi)\}_{,\xi} d\xi + \int_0^\infty \{w^*(\xi)\}^T [E^2] \{w(\xi)\} d\xi \end{aligned} \quad (7.3.17)$$

where the coefficient matrices  $[E^0]$ ,  $[E^1]$  and  $[E^2]$  are defined as

$$[E^0] = \int_{-1}^{+1} [B^1(\eta)]^T [D] [B^1(\eta)] |J(\eta)| d\eta \quad (7.3.18a)$$

$$[E^1] = \int_{-1}^{+1} [B^2(\eta)]^T [D] [B^1(\eta)] |J(\eta)| d\eta \quad (7.3.18b)$$

$$[E^2] = \int_{-1}^{+1} [B^2(\eta)]^T [D] [B^2(\eta)] |J(\eta)| d\eta \quad (7.3.18c)$$

$[E^0]$  is symmetric and positive definite.  $[E^2]$  is also symmetric but semi-positive definite.

To eliminate the derivatives  $\{w^*(\xi)\}_{,\xi}^T$  in the first and second terms on the right-hand side of Eq. (7.3.17), integration by parts is applied. This results in

$$\begin{aligned} \int_0^\infty \{w^*(\xi)\}_{,\xi}^T [E^0] \{w(\xi)\}_{,\xi} d\xi &= \{w^*(\xi)\}^T [E^0] \{w(\xi)\}_{,\xi} \\ &- \int_0^\infty \{w^*(\xi)\}^T [E^0] \{w(\xi)\}_{,\xi\xi} d\xi \end{aligned} \quad (7.3.19)$$

for the first term, and

$$\begin{aligned} \int_0^\infty \{w^*(\xi)\}_{,\xi}^T [E^1]^T \{w(\xi)\} d\xi &= \{w^*(\xi)\}^T [E^1]^T \{w(\xi)\} \\ &- \int_0^\infty \{w^*(\xi)\}^T [E^1]^T \{w(\xi)\}_{,\xi} d\xi \end{aligned} \quad (7.3.20)$$

for the second term. Substituting Eqs. (7.3.19) and (7.3.20) back into Eq. (7.3.17) results in

$$\begin{aligned}
\int_V \{\varepsilon^*\}^T \{\sigma\} dV = & \{w^*(\xi)\}^T [E^0] \{w(\xi)\}_{,\xi} - \int_0^\infty \{w^*(\xi)\}^T [E^0] \{w(\xi)\}_{,\xi\xi} d\xi \\
& + \{w^*(\xi)\}^T [E^1]^T \{w(\xi)\} - \int_0^\infty \{w^*(\xi)\}^T [E^1]^T \{w(\xi)\}_{,\xi} d\xi \\
& + \int_0^\infty \{w^*(\xi)\}^T [E^1] \{w(\xi)\}_{,\xi} d\xi + \int_0^\infty \{w^*(\xi)\}^T [E^2] \{w(\xi)\} d\xi
\end{aligned} \tag{7.3.21}$$

Substituting Eqs. (7.3.9), (7.3.15) and (7.3.16a) into the first term on the right-hand side of Eq. (7.3.14) results in

$$\int_V w^*(\xi, \eta) \rho \ddot{w} dV = \int_0^\infty \{w^*(\xi)\}^T [M^0] \{\ddot{w}\} d\xi \tag{7.3.22}$$

where the coefficient matrix  $[M^0]$  is defined as

$$[M^0] = \int_{-1}^{+1} [N(\eta)]^T \rho [N(\eta)] |J(\eta)| d\eta \tag{7.3.23}$$

$[M^0]$  is also symmetric and positive definite. Substituting Eqs. (7.3.15) and (7.3.16a) into the last term on the right-hand side of Eq. (7.3.14) results in

$$\int_{\Gamma_V} w^*(\xi, \eta) \tau_s d\Gamma_V = \{w^*(\xi)\}^T \{Q\} \tag{7.3.24}$$

where the internal nodal force vector  $\{Q\}$  is defined as

$$\{Q\} = \int_{-1}^{+1} [N(\eta)]^T \tau_s |J(\eta)| d\eta \tag{7.3.25}$$

Substituting Eqs. (7.3.21), (7.3.22), and (7.3.24) into Eq. (7.3.14) leads to

$$\begin{aligned}
& \{w^*(\xi)\}^T [E^0] \{w(\xi)\}_{,\xi} + \{w^*(\xi)\}^T [E^1]^T \{w(\xi)\} - \{w^*(\xi)\}^T \{Q\} \\
& - \int_0^\infty (\{w^*(\xi)\}^T [E^0] \{w(\xi)\}_{,\xi\xi} + \{w^*(\xi)\}^T [E^1]^T \{w(\xi)\}_{,\xi} \\
& - \{w^*(\xi)\}^T [E^1] \{w(\xi)\}_{,\xi} - \{w^*(\xi)\}^T [E^2] \{w(\xi)\} \\
& - \{w^*(\xi)\}^T [M^0] \{\ddot{w}\}) d\xi = 0
\end{aligned} \tag{7.3.26}$$

Equation (7.3.26) is satisfied when

$$\{w^*(\xi)\}^T [E^0] \{w(\xi)\}_{,\xi} + \{w^*(\xi)\}^T [E^1]^T \{w(\xi)\} - \{w^*(\xi)\}^T \{Q\} = 0 \quad (7.3.27)$$

and the integrand of the integral over  $\xi$  becomes zero,

$$\begin{aligned} \{w^*(\xi)\}^T ([E^0] \{w(\xi)\}_{,\xi\xi} + [E^1]^T \{w(\xi)\}_{,\xi} - [E^1] \{w(\xi)\}_{,\xi} \\ - [E^2] \{w(\xi)\} - [M^0] \{\ddot{w}\}) = 0 \end{aligned} \quad (7.3.28)$$

Rearranging Eq. (7.3.27) and for arbitrary  $\{w^*(\xi)\}^T$  lead to

$$\{Q\} = [E^0] \{w(\xi)\}_{,\xi} + [E^1]^T \{w(\xi)\} \quad (7.3.29)$$

in the time domain, which is equivalent to

$$\{Q\} = [E^0] \{W(\xi)\}_{,\xi} + [E^1]^T \{W(\xi)\} \quad (7.3.30)$$

in the frequency domain, where  $\{W(\xi)\}$  denotes the nodal displacement amplitudes. Similarly, for arbitrary  $\{w^*(\xi)\}^T$ , Eq. (7.3.28) leads to the scaled boundary finite element equation in displacement formulated in the time domain,

$$[E^0] \{w(\xi)\}_{,\xi\xi} + ([E^1]^T - [E^1]) \{w(\xi)\}_{,\xi} - [E^2] \{w(\xi)\} - [M^0] \{\ddot{w}\} = 0 \quad (7.3.31)$$

The scaled boundary finite element equation in displacement formulated in the frequency domain is obtained from the Fourier transform of Eq. (7.3.31) as

$$[E^0] \{W(\xi)\}_{,\xi\xi} + ([E^1]^T - [E^1]) \{W(\xi)\}_{,\xi} - [E^2] \{W(\xi)\} + \omega^2 [M^0] \{W(\xi)\} = 0 \quad (7.3.32)$$

where  $\omega$  is the excitation frequency. Note that the coefficient matrices of the semi-infinite layer at the vertical boundary  $\Gamma_V$  are obtained from the assembly of the coefficient matrices  $[E^0]$ ,  $[E^1]$ ,  $[E^2]$  and  $[M^0]$  of individual elements. To simplify the nomenclature, the same symbols are used for the assembled coefficient matrices.

## 7.4 Dynamic stiffness matrix of semi-infinite layer with constant depth

In the frequency domain, the excitation force-displacement relationship with the corresponding displacements is expressed as

$$\{R\} = [S^\infty(\omega)]\{W(\xi)\} \quad (7.4.1)$$

where  $[S^\infty(\omega)]$  is the dynamic stiffness matrix of the semi-infinite layer, and  $\{R\}$  the interaction forces that relates to the internal nodal force vector  $\{Q\}$  by the following equation:

$$\{R\} = -\{Q\} \quad (7.4.2)$$

Substituting Eq. (7.4.2) into Eq. (7.4.1) and using Eq. (7.3.1a) yield

$$-[E^0]\{W(\xi)\}_{,\xi} - [E^1]^T\{W(\xi)\} = [S^\infty(\omega)]\{W(\xi)\} \quad (7.4.3)$$

Taking the derivative of Eq. (7.4.3) with respect to  $\xi$  and rearranging the equation result in

$$-[E^0]\{W(\xi)\}_{,\xi\xi} - [E^1]^T\{W(\xi)\}_{,\xi} - [S^\infty(\omega)]\{W(\xi)\}_{,\xi} = 0 \quad (7.4.4)$$

Combining Eq. (7.3.32) and Eq. (7.4.4) leads to

$$-[S^\infty(\omega)]\{W(\xi)\}_{,\xi} - [E^1]\{W(\xi)\}_{,\xi} - [E^2]\{W(\xi)\} + \omega^2[M^0]\{W(\xi)\} = 0 \quad (7.4.5)$$

Equation (7.4.3) is rearranged as

$$\{W(\xi)\}_{,\xi} = -[E^0]^{-1}[E^1]^T\{W(\xi)\} - [E^0]^{-1}[S^\infty(\omega)]\{W(\xi)\} \quad (7.4.6)$$

Substituting Eq. (7.4.6) back into Eq. (7.4.5) leads to the scaled boundary finite element equation in dynamic stiffness formulated in the frequency domain,

$$([S^\infty(\omega)] + [E^1])[E^0]^{-1}([S^\infty(\omega)] + [E^1]^T) - [E^2] + \omega^2[M^0] = 0 \quad (7.4.7)$$

as  $\{W(\xi)\}$  can be arbitrary.

A concise formulation results when the transformation based on the following eigenvalue problem is introduced

$$[M^0][\Phi] = [E^0][\Phi][\Lambda^2] \quad (7.4.8)$$

where  $[\Lambda^2]$  and  $[\Phi]$  denote the eigenvalues and eigenvectors, respectively. Since  $[E^0]$  and  $[M^0]$  are positive definite, the eigenvectors are orthogonal. They are normalized as

$$[\Phi]^T[E^0][\Phi] = [I] \quad (7.4.9a)$$

$$[\Phi]^T[M^0][\Phi] = [\Lambda^2] \quad (7.4.9b)$$

Pre- and post-multiplying Eq. (7.4.7) by  $[\Phi]^T$  and  $[\Phi]$ , respectively and using Eq. (7.4.9) result in

$$[s^\infty(\omega)]^2 + [e^1][s^\infty(\omega)] + [s^\infty(\omega)][e^1]^T + [e^1][e^1]^T - [e^2] + \omega^2[\Lambda^2] = 0 \quad (7.4.10)$$

where

$$[s^\infty(\omega)] = [\Phi]^T[S^\infty(\omega)][\Phi] \quad (7.4.11)$$

$$[e^1] = [\Phi]^T[E^1][\Phi] \quad (7.4.12)$$

$$[e^2] = [\Phi]^T[E^2][\Phi] \quad (7.4.13)$$

Equation (7.4.10) The solution for  $[s^\infty(\omega)]$  can be determined directly from

$$[s^\infty(\omega)] = [\Theta_{21}][\Theta_{11}]^{-1} \quad (7.4.14)$$

where  $[\Theta_{21}]$  and  $[\Theta_{11}]$  are obtained from the following eigen-decomposition:

$$[Z] = [\Theta][\Omega][\Theta]^{-1} \quad (7.4.15)$$

with the matrix  $[Z]$ , the eigenvectors  $[\Theta]$  and the eigenvalues  $[\Omega]$

$$[Z] = \begin{bmatrix} -[e^1]^T & -[I] \\ [e^1][e^1]^T - [e^2] + \omega^2[\Lambda^2] & [e^1] \end{bmatrix} \quad (7.4.16a)$$

$$[\Theta] = \begin{bmatrix} [\Theta_{11}] & [\Theta_{12}] \\ [\Theta_{21}] & [\Theta_{22}] \end{bmatrix} \quad (7.4.16b)$$

$$[\Omega] = \begin{bmatrix} [\Omega_{11}] & \\ & [\Omega_{22}] \end{bmatrix} \quad (7.4.16c)$$

$[\Omega]$  is arranged in such a way that the real parts of the eigenvalues of  $[\Omega_{11}]$  are negative and those of  $[\Omega_{22}]$  are positive, and  $[\Theta]$  is partitioned conformably with the eigenvalues (Wolf and Song, 1996).

## 7.5 Doubly asymptotic continued fraction solution for dynamic stiffness matrix

This section describes the solution of the scaled boundary finite element equation for dynamic stiffness matrix (Eq. (7.4.10)). The solution is sought as a doubly asymptotic continued fraction solution. Two steps are involved in the solution procedure. In the first step detailed in Section 7.5.1, a continued fraction solution is determined at the high-frequency limit recursively. In each recursion, the coefficient matrices of one term of the continued fractions is obtained, and an equation is established for the residual. In the second step detailed in Section 7.5.2, a continued fraction solution of the residual equation of the high-frequency solution is determined at the low-frequency limit recursively. The doubly asymptotic solution is obtained by joining the low-frequency solution to the last term of the high-frequency solution.

### 7.5.1 Continued fraction solution at high frequency

The continued fraction solution at the high-frequency limit ( $\omega \rightarrow \infty$ ) is written as

$$[s^\infty(\omega)] = [k_\infty] + (i\omega)[c_\infty] - [\psi^{(1)}][y^{(1)}(\omega)]^{-1}[\psi^{(1)}]^T \quad (7.5.1a)$$

$$[y^{(i)}(\omega)] = [y_0^{(i)}] + (i\omega)[y_1^{(i)}] - [\psi^{(i+1)}][y^{(i+1)}(\omega)]^{-1}[\psi^{(i+1)}]^T \quad (i = 1, 2, 3, \dots, M_H) \quad (7.5.1b)$$

where  $[k_\infty]$ ,  $[c_\infty]$ ,  $[y_0^{(i)}]$  and  $[y_1^{(i)}]$  are coefficient matrices to be determined recursively in the solution procedure. The additional factor matrices  $[\psi^{(1)}]$  and  $[\psi^{(i+1)}]$  are introduced in order to improve numerical stability of the solution. To maintain the symmetry of the coefficient matrices of the open boundary (Eq. (7.6.16) in Section 7.6), the factor matrices and the transposed factor matrices are used in the residual terms  $[\psi^{(1)}][y^{(1)}(\omega)]^{-1}[\psi^{(1)}]^T$  and  $[\psi^{(i+1)}][y^{(i+1)}(\omega)]^{-1}[\psi^{(i+1)}]^T$  are residual terms.  $M_H$  is the order of the continued fraction solution at high frequency.

The coefficient matrices  $[k_\infty]$  and  $[c_\infty]$  are determined by substituting Eq. (7.5.1a) into Eq. (7.4.10). This leads to an equation of a power series of  $(i\omega)$ , including the

following three terms:

$$\begin{aligned}
& (i\omega)^2([c_\infty]^2 - [\Lambda^2]) + (i\omega)([c_\infty][k_\infty] + [c_\infty][e^1]^T + [k_\infty][c_\infty] + [e^1][c_\infty]) \\
& \quad + (([k_\infty] + [e^1])([k_\infty] + [e^1]^T) - [e^2] - ((i\omega)[c_\infty] + [k_\infty] + [e^1])[\psi^{(1)}] \\
& \quad \times [y^{(1)}(\omega)]^{-1}[\psi^{(1)}]^T - [\psi^{(1)}][y^{(1)}(\omega)]^{-1}[\psi^{(1)}]^T((i\omega)[c_\infty] + [k_\infty] + [e^1]^T) + \\
& \quad \quad + [\psi^{(1)}][y^{(1)}(\omega)]^{-1}[\psi^{(1)}]^T[\psi^{(1)}][y^{(1)}(\omega)]^{-1}[\psi^{(1)}]^T) = 0 \quad (7.5.2)
\end{aligned}$$

This equation is satisfied by setting all the three terms equal to zero. Thus the solution for  $[c_\infty]$  that satisfies the radiation condition is obtained from the first term ( $(i\omega)^2$  term) by selecting the positive root of each element on the diagonal of  $[\Lambda^2]$ ,

$$[c_\infty] = [\Lambda] \quad (7.5.3)$$

Substituting Eq. (7.5.3) into the second term ( $(i\omega)$  term) in Eq. (7.5.2) leads to the Lyapunov equation of  $[k_\infty]$ ,

$$[\Lambda][k_\infty] + [k_\infty][\Lambda] = -[\Lambda][e^1]^T - [e^1][\Lambda] \quad (7.5.4)$$

which can be solved by the function “lyap” in MATLAB.  $[k_\infty]$  is symmetric as well as  $[c_\infty]$ .

The last term in Eq. (7.5.2) is an equation of  $[y^{(1)}(\omega)]^{-1}$ . After being pre- and post-multiplied by  $[\psi^{(1)}]^{-1}[y^{(1)}(\omega)]$  and  $[y^{(1)}(\omega)][\psi^{(1)}]^{-T}$ , respectively, it is expressed as the  $i = 1$  case of

$$\begin{aligned}
& [a^{(i)}] - [y^{(i)}(\omega)]([b_0^{(i)}]^T + (i\omega)[b_1^{(i)}]^T) - ([b_0^{(i)}] + (i\omega)[b_1^{(i)}])[y^{(i)}(\omega)] \\
& \quad \quad \quad + [y^{(i)}(\omega)][c^{(i)}][y^{(i)}(\omega)] = 0 \quad (7.5.5)
\end{aligned}$$

with the following coefficient matrices:

$$[a^{(1)}] = [\psi^{(1)}]^T[\psi^{(1)}] \quad (7.5.6a)$$

$$[b_0^{(1)}] = [\psi^{(1)}]^T([k_\infty] + [e^1]^T)[\psi^{(1)}]^{-T} \quad (7.5.6b)$$

$$[b_1^{(1)}] = [\psi^{(1)}]^T[c_\infty][\psi^{(1)}]^{-T} \quad (7.5.6c)$$

$$[c^{(1)}] = [\psi^{(1)}]^{-1}(([k_\infty] + [e^1])([k_\infty] + [e^1]^T) - [e^2])[\psi^{(1)}]^{-T} \quad (7.5.6d)$$

The factor matrix  $[\psi^{(1)}]$  is selected to improve the stability of the solution by avoiding the singularity in  $[c^{(1)}]$ . A good choice is

$$[\psi^{(1)}] = [\phi^{(1)}][|\lambda^{(1)}|]^{1/2} \quad (7.5.7)$$

where the eigenvectors  $[\phi^{(1)}]$  and the eigenvalues  $[\lambda^{(1)}]$  are obtained from the following eigen-decomposition:

$$([k_\infty] + [e^1])([k_\infty] + [e^1]^T) - [e^2] = [\phi^{(1)}][\lambda^{(1)}][\phi^{(1)}]^{-1} \quad (7.5.8)$$

Note that the eigenvectors are orthogonal i.e.  $[\phi^{(1)}]^T = [\phi^{(1)}]^{-1}$ . By using Eqs. (7.5.7) and (7.5.8), Eq. (7.5.6) is rewritten as

$$[a^{(1)}] = [|\lambda^{(1)}|] \quad (7.5.9a)$$

$$[b_0^{(1)}] = [|\lambda^{(1)}|]^{1/2} [\phi^{(1)}]^{-1} ([k_\infty] + [e^1]^T) [\phi^{(1)}] [|\lambda^{(1)}|]^{-1/2} \quad (7.5.9b)$$

$$[b_1^{(1)}] = [|\lambda^{(1)}|]^{1/2} [\phi^{(1)}]^{-1} [c_\infty] [\phi^{(1)}] [|\lambda^{(1)}|]^{-1/2} \quad (7.5.9c)$$

$$[c^{(1)}] = [sgn^{(1)}] \quad (7.5.9d)$$

$[sgn^{(1)}]$  is the sign matrix of  $[\lambda^{(1)}]$ . Its diagonal entries are equal to +1 or -1.

To begin the recursive procedure, Eq. (7.5.1b) is substituted into Eq. (7.5.5). This also results in an equation of a power series of  $(i\omega)$  grouped into the following three terms:

$$\begin{aligned} & (i\omega)^2 (-[y_1^{(i)}][b_1^{(i)}]^T - [b_1^{(i)}][y_1^{(i)}] + [y_1^{(i)}][c^{(i)}][y_1^{(i)}]) + (i\omega) \left( (-[b_1^{(i)}] + \right. \\ & \left. [y_1^{(i)}][c^{(i)}])[y_0^{(i)}] + [y_0^{(i)}](-[b_1^{(i)}]^T + [c^{(i)}][y_1^{(i)}]) - [b_0^{(i)}][y_1^{(i)}] - [y_1^{(i)}][b_0^{(i)}]^T \right) \\ & + \left( ([a^{(i)}] - [b_0^{(i)}][y_0^{(i)}] - [y_0^{(i)}][b_0^{(i)}]^T + [y_0^{(i)}][c^{(i)}][y_0^{(i)}]) - \left( (-[b_0^{(i)}] \right. \right. \\ & \left. \left. + [y_0^{(i)}][c^{(i)}]) + (i\omega)(-[b_1^{(i)}] + [y_1^{(i)}][c^{(i)}]) \right) [\psi^{(i+1)}][y^{(i+1)}(\omega)]^{-1} \right. \\ & \times [\psi^{(i+1)}]^T - [\psi^{(i+1)}][y^{(i+1)}(\omega)]^{-1} [\psi^{(i+1)}]^T \left( (-[b_0^{(i)}]^T + [c^{(i)}][y_0^{(i)}]) \right. \\ & \left. \left. + (i\omega)(-[b_1^{(i)}]^T + [c^{(i)}][y_1^{(i)}]) \right) + [\psi^{(i+1)}][y^{(i+1)}(\omega)]^{-1} [\psi^{(i+1)}]^T \right. \\ & \left. \times [c^{(i)}][\psi^{(i+1)}][y^{(i+1)}(\omega)]^{-1} [\psi^{(i+1)}]^T \right) = 0 \quad (7.5.10) \end{aligned}$$

Equation (7.5.10) is also satisfied by setting all the three terms equal to zero. Pre- and post-multiplying the first term  $((i\omega)^2$  term) by  $[y_1^{(i)}]^{-1}$  yield the Lyapunov equation of  $[y_1^{(i)}]^{-1}$ ,

$$[b_1^{(i)}]^T [y_1^{(i)}]^{-1} + [y_1^{(i)}]^{-1} [b_1^{(i)}] = [c^{(i)}] \quad (7.5.11)$$

which can be solved by the function “lyap” in MATLAB.  $[y_1^{(i)}]$  is obtained from the inverse of the solution of Eq. (7.5.11).  $[y_1^{(i)}]$  is symmetric as well as  $[b_1^{(i)}]$  and  $[c^{(i)}]$ .

The second term ( $i\omega$  term) in Eq. (7.5.10) is the Lyapunov equation of  $[y_0^{(i)}]$ ,

$$(-[b_1^{(i)}] + [y_1^{(i)}][c^{(i)}])[y_0^{(i)}] + [y_0^{(i)}](-[b_1^{(i)}]^T + [c^{(i)}][y_1^{(i)}]) = [b_0^{(i)}][y_1^{(i)}] + [y_1^{(i)}][b_0^{(i)}]^T \quad (7.5.12)$$

which can be solved by the function “lyap” in MATLAB.  $[y_0^{(i)}]$  is symmetric as well as  $[y_1^{(i)}]$ .

The last term in Eq. (7.5.10) is an equation of  $[y^{(i+1)}(\omega)]^{-1}$ . Pre- and post-multiplying the last term by  $[y^{(i+1)}(\omega)][\psi^{(i+1)}]^{-1}$  and  $[\psi^{(i+1)}]^{-T}[y^{(i+1)}(\omega)]$ , respectively lead to an equation in the same form as Eq. (7.5.5)

$$[a^{(i+1)}] - ([b_0^{(i+1)}] + i\omega[b_1^{(i+1)}])[y^{(i+1)}(\omega)] - [y^{(i+1)}(\omega)]([b_0^{(i+1)}]^T + i\omega[b_1^{(i+1)}]^T) + [y^{(i+1)}(\omega)][c^{(i+1)}][y^{(i+1)}(\omega)] = 0 \quad (7.5.13)$$

with the coefficient matrices

$$[a^{(i+1)}] = [\psi^{(i+1)}]^T [c^{(i)}] [\psi^{(i+1)}] \quad (7.5.14a)$$

$$[b_0^{(i+1)}] = [\psi^{(i+1)}]^T (-[b_0^{(i)}]^T + [c^{(i)}][y_0^{(i)}]) [\psi^{(i+1)}]^{-T} \quad (7.5.14b)$$

$$[b_1^{(i+1)}] = [\psi^{(i+1)}]^T (-[b_1^{(i)}]^T + [c^{(i)}][y_1^{(i)}]) [\psi^{(i+1)}]^{-T} \quad (7.5.14c)$$

$$[c^{(i+1)}] = [\psi^{(i+1)}]^{-1} ([a^{(i)}] - [b_0^{(i)}][y_0^{(i)}] - [y_0^{(i)}][b_0^{(i)}]^T + [y_0^{(i)}][c^{(i)}][y_0^{(i)}]) [\psi^{(i+1)}]^{-T} = [\text{sgn}^{(i+1)}] \quad (7.5.14d)$$

The factor matrix  $[\psi^{(i+1)}]$  is set equal to

$$[\psi^{(i+1)}] = [\phi^{(i+1)}][|\lambda^{(i+1)}|]^{1/2} \quad (7.5.15)$$

where the eigenvectors  $[\phi^{(i+1)}]$  and the eigenvalues  $[\lambda^{(i+1)}]$  are obtained from the following eigen-decomposition:

$$[a^{(i)}] - [b_0^{(i)}][y_0^{(i)}] - [y_0^{(i)}][b_0^{(i)}]^T + [y_0^{(i)}][c^{(i)}][y_0^{(i)}] = [\phi^{(i+1)}][\lambda^{(i+1)}][\phi^{(i+1)}]^{-1} \quad (7.5.16)$$

$[\text{sgn}^{(i+1)}]$  is the sign matrix of  $[\lambda^{(i+1)}]$  of which diagonal entries are  $\pm 1$ . The continued fraction solution is determined recursively using Eq. (7.5.11) where the coefficient matrices  $[a^{(1)}]$ ,  $[b_0^{(1)}]$ ,  $[b_1^{(1)}]$  and  $[c^{(1)}]$  are initialized by Eq. (7.5.9) and updated during the recursion with Eq. (7.5.14).

After an order  $M_H$  continued fraction solution is obtained at the high-frequency limit, the residual satisfies Eq. (7.5.13) with  $i = M_H$ .

## 7.5.2 Continued fraction solution at low frequency

The residual equation (Eq. (7.5.13)) of the high-frequency continued fraction solution is solved again by a continued fraction but at the low frequency limit ( $\omega \rightarrow 0$ ). For simplicity in notation, the residual is expressed as

$$[y_L(\omega)] = [y^{(M_H+1)}(\omega)] \quad (7.5.17)$$

and Eq. (7.5.18) is rewritten as

$$\begin{aligned} [a_L] - ([b_{L0}] + (i\omega)[b_{L1}])[y_L(\omega)] - [y_L(\omega)]([b_{L0}]^T + (i\omega)[b_{L1}]^T) \\ + [y_L(\omega)][c_L][y_L(\omega)] = 0 \end{aligned} \quad (7.5.18)$$

with the following matrices used at the low-frequency limit:

$$[a_L] = [a^{(M_H+1)}] = [\psi_L^{(0)}]^T [c^{(M_H)}] [\psi_L^{(0)}] \quad (7.5.19a)$$

$$[b_{L0}] = [b_0^{(M_H+1)}] = [\psi_L^{(0)}]^T (-[b_0^{(M_H)}]^T + [c^{(M_H)}][y_0^{(M_H)}]) [\psi_L^{(0)}]^{-T} \quad (7.5.19b)$$

$$[b_{L1}] = [b_1^{(M_H+1)}] = [\psi_L^{(0)}]^T (-[b_1^{(M_H)}]^T + [c^{(M_H)}][y_1^{(M_H)}]) [\psi_L^{(0)}]^{-T} \quad (7.5.19c)$$

$$[c_L] = [c^{(M_H+1)}] = [\psi_L^{(0)}]^{-1} [a^{(M_H)}] [\psi_L^{(0)}]^{-T} = [\text{sgn}_L^{(0)}] \quad (7.5.19d)$$

where

$$[\psi_L^{(0)}] = [\psi^{(M_H+1)}] \quad (7.5.20a)$$

$$[\text{sgn}_L^{(0)}] = [\text{sgn}^{(M_H+1)}] \quad (7.5.20b)$$

The continued fraction solution at the low-frequency limit is expressed as

$$[y_L(\omega)] = [y_{L0}^{(0)}] + (i\omega)[y_{L1}^{(0)}] - (i\omega)^2 [\psi_L^{(1)}] [y_L^{(1)}(\omega)]^{-1} [\psi_L^{(1)}]^T \quad (7.5.21a)$$

$$[y_L^{(i)}(\omega)] = [y_{L0}^{(i)}] + (i\omega)[y_{L1}^{(i)}] - (i\omega)^2 [\psi_L^{(i+1)}] [y_L^{(i+1)}(\omega)]^{-1} [\psi_L^{(i+1)}]^T \quad (i = 1, 2, \dots, M_L) \quad (7.5.21b)$$

where  $[y_{L0}^{(0)}]$ ,  $[y_{L1}^{(0)}]$ ,  $[y_{L0}^{(i)}]$  and  $[y_{L1}^{(i)}]$  are coefficient matrices to be determined recursively. The factor matrices  $[\psi_L^{(1)}]$  and  $[\psi_L^{(i+1)}]$  are introduced to improve numerical stability of the solution.  $(i\omega)^2 [\psi_L^{(1)}] [y_L^{(1)}(\omega)]^{-1} [\psi_L^{(1)}]^T$  and  $(i\omega)^2 [\psi_L^{(i+1)}] [y_L^{(i+1)}(\omega)]^{-1} [\psi_L^{(i+1)}]^T$  are residual terms.  $M_L$  is the order of the continued fraction solution at low frequency.

Substituting Eq. (7.5.21a) into Eq. (7.5.18) leads to an equation of a power series of  $(i\omega)$ ,

$$\begin{aligned}
& ([y_{L0}^{(0)}][c_L][y_{L0}^{(0)}] - [b_{L0}][y_{L0}^{(0)}] - [y_{L0}^{(0)}][b_{L0}]^T + [a_L]) + (i\omega) ((-[b_{L0}] \\
& + [y_{L0}^{(0)}][c_L])[y_{L1}^{(0)}] + [y_{L1}^{(0)}](-[b_{L0}]^T + [c_L][y_{L0}^{(0)}]) - [b_{L1}][y_{L0}^{(0)}] - [y_{L0}^{(0)}][b_{L1}]^T) \\
& + (i\omega)^2 \left( ([y_{L1}^{(0)}][c_L][y_{L1}^{(0)}] - [b_{L1}][y_{L1}^{(0)}] - [y_{L1}^{(0)}][b_{L1}]^T) - ((-[b_{L0}] \right. \\
& + [y_{L0}^{(0)}][c_L]) + (i\omega)(-[b_{L1}] + [y_{L1}^{(0)}][c_L]) \left. \right) [\psi_L^{(1)}][y_L^{(1)}(\omega)]^{-1}[\psi_L^{(1)}]^T \\
& - [\psi_L^{(1)}][y_L^{(1)}(\omega)]^{-1}[\psi_L^{(1)}]^T \left( (-[b_{L0}]^T + [c_L][y_{L0}^{(0)}]) + (i\omega)(-[b_{L1}]^T \right. \\
& \left. + [c_L][y_{L1}^{(0)}]) \right) + (i\omega)^2 [\psi_L^{(1)}][y_L^{(1)}(\omega)]^{-1}[\psi_L^{(1)}]^T \\
& \left. \times [c_L][\psi_L^{(1)}][y_L^{(1)}(\omega)]^{-1}[\psi_L^{(1)}]^T \right) = 0
\end{aligned} \tag{7.5.22}$$

Similarly, this equation is satisfied by setting each of the three terms equal to zero. The first term (the constant term independent of  $(i\omega)$ ) is in terms of the Riccati equation of  $[y_{L0}^{(0)}]$ ,

$$[y_{L0}^{(0)}][c_L][y_{L0}^{(0)}] - [b_{L0}][y_{L0}^{(0)}] - [y_{L0}^{(0)}][b_{L0}]^T + [a_L] = 0 \tag{7.5.23}$$

Instead of solving  $[y_{L0}^{(0)}]$  directly from Eq. (7.5.23), it can be determined from the static stiffness matrix in another way using Eqs. (7.5.17), (7.5.20a) and (7.5.21a) in Eq. (7.5.1). This results in

$$\begin{aligned}
[s^\infty(\omega)] &= [k_\infty] + (i\omega)[c_\infty] - [\psi^{(1)}]([y_0^{(1)}] + (i\omega)[y_1^{(1)}] - [\psi^{(2)}]([y_0^{(2)}] + (i\omega)[y_1^{(2)}] - \dots \\
& - [\psi^{(MH)}]([y_0^{(MH)}] + (i\omega)[y_1^{(MH)}] - [\psi_L^{(0)}]([y_{L0}^{(0)}] + (i\omega)[y_{L1}^{(0)}] \\
& - (i\omega)^2 [\psi_L^{(1)}][y_L^{(1)}(\omega)]^{-1}[\psi_L^{(1)}]^T)^{-1}[\psi_L^{(0)}]^T)^{-1}[\psi^{(MH)}]^T \\
& \dots)^{-1}[\psi^{(2)}]^T)^{-1}[\psi^{(1)}]^T
\end{aligned} \tag{7.5.24}$$

Setting  $\omega$  equal to zero and rearranging Eq. (7.5.24) reversely yield the solution for  $[y_{L0}^{(0)}]$ ,

$$\begin{aligned}
[y_{L0}^{(0)}] &= -[\psi_L^{(0)}]^T([y_0^{(MH)}] - [\psi^{(MH)}]^T([y_0^{(MH-1)}] - \dots - [\psi^{(2)}]^T([y_0^{(1)}] \\
& - [\psi^{(1)}]^T([k_\infty] - [s^\infty(\omega = 0)])^{-1}[\psi^{(1)}])^{-1}[\psi^{(2)}] \\
& \dots)^{-1}[\psi^{(MH)}])^{-1}[\psi_L^{(0)}]
\end{aligned} \tag{7.5.25}$$

where  $[s^\infty(\omega = 0)]$  is determined from Eq. (7.4.14) by setting  $\omega$  equal to zero.  $[y_{L0}^{(0)}]$  is symmetric as well as  $[s^\infty(\omega = 0)]$ . The second term ( $(i\omega)$  term) is the Lyapunov

equation of  $[y_{L1}^{(0)}]$ ,

$$(-[b_{L0}] + [y_{L0}^{(0)}][c_L])[y_{L1}^{(0)}] + [y_{L1}^{(0)}](-[b_{L0}]^T + [c_L][y_{L0}^{(0)}]) = [b_{L1}][y_{L0}^{(0)}] + [y_{L0}^{(0)}][b_{L1}]^T \quad (7.5.26)$$

which can be solved by the function “lyap” in MATLAB.  $[y_{L1}^{(0)}]$  is symmetric as well as  $[c_L]$  and  $[y_{L0}^{(0)}]$ .

The last term in Eq. (7.5.22) is an equation of  $[y_L^{(1)}(\omega)]^{-1}$ . Pre- and post-multiplying the last term by  $[y_L^{(1)}(\omega)][\psi_L^{(1)}]^{-1}$  and  $[\psi_L^{(1)}]^{-T}[y_L^{(1)}(\omega)]$ , respectively result in an equation of  $[y_L^{(i)}(\omega)]$ . It is expressed as the  $i = 1$  case of

$$(\mathrm{i}\omega)^2[a_L^{(i)}] - [y_L^{(i)}(\omega)]([b_{L0}^{(i)}]^T + (\mathrm{i}\omega)[b_{L1}^{(i)}]^T) - ([b_{L0}^{(i)}] + (\mathrm{i}\omega)[b_{L1}^{(i)}])[y_L^{(i)}(\omega)] + [y_L^{(i)}(\omega)][c_L^{(i)}][y_L^{(i)}(\omega)] = 0 \quad (7.5.27)$$

with the following matrices used at the low-frequency limit:

$$[a_L^{(1)}] = [\psi_L^{(1)}]^T [c_L] [\psi_L^{(1)}] \quad (7.5.28a)$$

$$[b_{L0}^{(1)}] = [\psi_L^{(1)}]^T (-[b_{L0}^{(0)}]^T + [c_L][y_{L0}^{(0)}]) [\psi_L^{(1)}]^{-T} \quad (7.5.28b)$$

$$[b_{L1}^{(1)}] = [\psi_L^{(1)}]^T (-[b_{L1}^{(0)}]^T + [c_L][y_{L1}^{(0)}]) [\psi_L^{(1)}]^{-T} \quad (7.5.28c)$$

$$[c_L^{(1)}] = [\psi_L^{(1)}]^{-1} (-[b_{L1}][y_{L1}^{(0)}] - [y_{L1}^{(0)}][b_{L1}]^T + [y_{L1}^{(0)}][c_L][y_{L1}^{(0)}]) [\psi_L^{(1)}]^{-T} = [\mathrm{sgn}_L^{(1)}] \quad (7.5.28d)$$

The factor matrix  $[\psi_L^{(1)}]$  is set equal to

$$[\psi_L^{(1)}] = [\phi_L^{(1)}][|\lambda_L^{(1)}|]^{1/2} \quad (7.5.29)$$

where the eigenvectors  $[\phi_L^{(1)}]$  and the eigenvalues  $[\lambda_L^{(1)}]$  are obtained from the following eigen-decomposition:

$$-[b_{L1}][y_{L1}^{(0)}] - [y_{L1}^{(0)}][b_{L1}]^T + [y_{L1}^{(0)}][c_L][y_{L1}^{(0)}] = [\phi_L^{(1)}][\lambda_L^{(1)}][\phi_L^{(1)}]^{-1} \quad (7.5.30)$$

$[\mathrm{sgn}_L^{(1)}]$  is the sign matrix of  $[\lambda_L^{(1)}]$  of which diagonal entries are  $\pm 1$ . Substituting the recursive equation of the low-frequency limit (Eq. (7.5.21b)) into Eq. (7.5.27)

and rearranging the equation lead to an equation of a power series of  $(i\omega)$ ,

$$\begin{aligned}
& (-[b_{L0}^{(i)}][y_{L0}^{(i)}] - [y_{L0}^{(i)}][b_{L0}^{(i)T} + [y_{L0}^{(i)}][c_L^{(i)}][y_{L0}^{(i)}]) + (i\omega) \left( (-[b_{L0}^{(i)}] + [y_{L0}^{(i)}][c_L^{(i)}])[y_{L1}^{(i)}] \right. \\
& \quad + [y_{L1}^{(i)}](-[b_{L0}^{(i)T} + [c_L^{(i)}][y_{L0}^{(i)}]) - [b_{L1}^{(i)}][y_{L0}^{(i)}] - [y_{L0}^{(i)}][b_{L1}^{(i)T}) + (i\omega)^2 \left( ([a_L^{(i)}] \right. \\
& \quad - [b_{L1}^{(i)}][y_{L1}^{(i)}] - [y_{L1}^{(i)}][b_{L1}^{(i)T} + [y_{L1}^{(i)}][c_L^{(i)}][y_{L1}^{(i)}]) - \left( (-[b_{L0}^{(i)}] + [y_{L0}^{(i)}][c_L^{(i)}]) \right. \\
& \quad \quad \left. + (i\omega)(-[b_{L1}^{(i)}] + [y_{L1}^{(i)}][c_L^{(i)}]) \right) [\psi_L^{(i+1)}][y_L^{(i+1)}(\omega)]^{-1}[\psi_L^{(i+1)}]^T \\
& \quad - [\psi_L^{(i+1)}][y_L^{(i+1)}(\omega)]^{-1}[\psi_L^{(i+1)}]^T \left( (-[b_{L0}^{(i)T} + [c_L^{(i)}][y_{L0}^{(i)}]) \right. \\
& \quad \left. + (i\omega)(-[b_{L1}^{(i)T} + [c_L^{(i)}][y_{L1}^{(i)}]) \right) + (i\omega)^2 [\psi_L^{(i+1)}][y_L^{(i+1)}(\omega)]^{-1} \\
& \quad \quad \times [\psi_L^{(i+1)}]^T [c_L^{(i)}][\psi_L^{(i+1)}][y_L^{(i+1)}(\omega)]^{-1}[\psi_L^{(i+1)}]^T = 0 \quad (7.5.31)
\end{aligned}$$

This equation is satisfied by setting each term equal to zero. Pre- and post-multiplying the first term (the constant term independent of  $(i\omega)$ ) by  $[y_{L0}^{(i)}]^{-1}$  lead to the Lyapunov equation of  $[y_{L0}^{(i)}]^{-1}$ ,

$$[b_{L0}^{(i)T}][y_{L0}^{(i)}]^{-1} + [y_{L0}^{(i)}]^{-1}[b_{L0}^{(i)}] = [c_L^{(i)}] \quad (7.5.32)$$

which can be solved by the function “lyap” in MATLAB.  $[y_{L0}^{(i)}]$  is obtained from the inverse of the solution of Eq. (7.5.32).  $[y_{L0}^{(i)}]$  is symmetric as well as  $[c_L^{(i)}]$ . The second term ( $(i\omega)$  term) in Eq. (7.5.31) is the Lyapunov equation of  $[y_{L1}^{(i)}]$ ,

$$(-[b_{L0}^{(i)}] + [y_{L0}^{(i)}][c_L^{(i)}])[y_{L1}^{(i)}] + [y_{L1}^{(i)}](-[b_{L0}^{(i)T} + [c_L^{(i)}][y_{L0}^{(i)}]) = [b_{L1}^{(i)}][y_{L0}^{(i)}] + [y_{L0}^{(i)}][b_{L1}^{(i)T}] \quad (7.5.33)$$

which can be solved by the function “lyap” in MATLAB.  $[y_{L1}^{(i)}]$  is symmetric as well as  $[y_{L0}^{(i)}]$ .

The last term in Eq. (7.5.31) is an equation of  $[y_L^{(i+1)}(\omega)]^{-1}$ . Pre- and post-multiplying the last term by  $[y_L^{(i+1)}(\omega)][\psi_L^{(i+1)}]^{-1}$  and  $[\psi_L^{(i+1)}]^{-T}[y_L^{(i+1)}(\omega)]$ , respectively yield the residual equation

$$\begin{aligned}
& (i\omega)^2 [a_L^{(i+1)}] - ([b_{L0}^{(i+1)}] + (i\omega)[b_{L1}^{(i+1)}])[y_L^{(i+1)}(\omega)] - [y_L^{(i+1)}(\omega)]([b_{L0}^{(i+1)T} \\
& \quad + (i\omega)[b_{L1}^{(i+1)T}]) + [y_L^{(i+1)}(\omega)][c_L^{(i+1)}][y_L^{(i+1)}(\omega)] = 0 \quad (7.5.34)
\end{aligned}$$

where the coefficient matrices used updated recursively by

$$[a_L^{(i+1)}] = [\psi_L^{(i+1)}]^T [c_L^{(i)}] [\psi_L^{(i+1)}] \quad (7.5.35a)$$

$$[b_{L0}^{(i+1)}] = [\psi_L^{(i+1)}]^T (-[b_{L0}^{(i)}]^T + [c_L^{(i)}][y_{L0}^{(i)}]) [\psi_L^{(i+1)}]^{-T} \quad (7.5.35b)$$

$$[b_{L1}^{(i+1)}] = [\psi_L^{(i+1)}]^T (-[b_{L1}^{(i)}]^T + [c_L^{(i)}][y_{L1}^{(i)}]) [\psi_L^{(i+1)}]^{-T} \quad (7.5.35c)$$

$$\begin{aligned} [c_L^{(i+1)}] &= [\psi_L^{(i+1)}]^{-1} ([a_L^{(i)}] - [b_{L1}^{(i)}][y_{L1}^{(i)}] - [y_{L1}^{(i)}][b_{L1}^{(i)}]^T + [y_{L1}^{(i)}][c_L^{(i)}][y_{L1}^{(i)}]) [\psi_L^{(i+1)}]^{-T} \\ &= [\text{sgn}_L^{(i+1)}] \end{aligned} \quad (7.5.35d)$$

The factor matrix  $[\psi_L^{(i+1)}]$  is set equal to

$$[\psi_L^{(i+1)}] = [\phi_L^{(i+1)}] [|\lambda_L^{(i+1)}|]^{1/2} \quad (7.5.36)$$

where the eigenvectors  $[\phi_L^{(i+1)}]$  and the eigenvalues  $[\lambda_L^{(i+1)}]$  are obtained from the following eigen-decomposition:

$$[a_L^{(i)}] - [b_{L1}^{(i)}][y_{L1}^{(i)}] - [y_{L1}^{(i)}][b_{L1}^{(i)}]^T + [y_{L1}^{(i)}][c_L^{(i)}][y_{L1}^{(i)}] = [\phi_L^{(i+1)}] [\lambda_L^{(i+1)}] [\phi_L^{(i+1)}]^{-1} \quad (7.5.37)$$

$[\text{sgn}_L^{(i+1)}]$  is the sign matrix of  $[\lambda_L^{(i+1)}]$  of which diagonal entries are  $\pm 1$ .

The continued fraction solution at low frequency is evaluated by using Eqs. (7.5.32) and (7.5.33) whereby the recursive coefficient matrices are initialized by Eq. (7.5.28) and updated by Eq. (7.5.35). The doubly asymptotic continued fraction solution is determined by combining the high-frequency continued fraction solution in Eq. (7.5.1) with the low-frequency continued fraction solution in Eq. (7.5.21) using  $[y^{(MH+1)}(\omega)] = [y_L(\omega)]$  (Eq. (7.5.17)). It is expressed as

$$\begin{aligned} [s^\infty(\omega)] &= [k_\infty] + (i\omega)[c_\infty] - [\psi^{(1)}]([y_0^{(1)}] + (i\omega)[y_1^{(1)}] - [\psi^{(2)}]([y_0^{(2)}] + (i\omega)[y_1^{(2)}] - \dots \\ &\quad - [\psi^{(MH)}]^{-T}([y_0^{(MH)}] + (i\omega)[y_1^{(MH)}] - [\psi_L^{(0)}]([y_{L0}^{(0)}] + (i\omega)[y_{L1}^{(0)}] \\ &\quad - (i\omega)^2[\psi_L^{(1)}]([y_{L0}^{(1)}] + (i\omega)[y_{L1}^{(1)}] - \dots - (i\omega)^2[\psi_L^{(ML)}]([y_{L0}^{(ML)}] \\ &\quad + (i\omega)[y_{L1}^{(ML)}])^{-1}[\psi_L^{(ML)}]^T \dots)^{-1}[\psi_L^{(1)}]^T)^{-1}[\psi_L^{(0)}]^T)^{-1}[\psi^{(MH)}]^T \\ &\quad \dots)^{-1}[\psi^{(2)}]^T)^{-1}[\psi^{(1)}]^T \end{aligned} \quad (7.5.38)$$

Note that the residual term  $(i\omega)^2[\psi_L^{(ML+1)}][y_L^{(ML+1)}(\omega)]^{-1}[\psi_L^{(ML+1)}]^T$  at the low-frequency limit is neglected.

## 7.6 Doubly asymptotic open boundary condition

The procedure of constructing the high-order doubly asymptotic open boundary condition described in this section is based on the one described in Chapter 3. The vertical boundary ( $\xi = 0$ ) is considered. With use of Eq. (7.4.11), Eq. (7.4.1) mentioned previously in Section 7.4 can be transformed into Eq. (7.6.1),

$$\{\tilde{R}\} = [s^\infty(\omega)]\{\tilde{U}\} \quad (7.6.1)$$

where

$$\{\tilde{R}\} = [\Phi]^T \{R\} \quad (7.6.2a)$$

$$\{\tilde{U}\} = [\Phi]^{-1} \{U\} \quad (7.6.2b)$$

where  $\{U\}$  denotes  $\{U(\xi = 0)\}$ . Substituting Eq. (7.5.1a) into Eq. (7.6.1) leads to

$$\{\tilde{R}\} = [k_\infty] + (i\omega)[c_\infty]\{\tilde{U}\} - [\psi^{(1)}]\{\tilde{U}^{(1)}\} \quad (7.6.3)$$

where the auxiliary variable  $\{\tilde{U}^{(1)}\}$  is defined as

$$\{\tilde{U}^{(1)}\} = [y^{(1)}(\omega)]^{-1}[\psi^{(1)}]^T \{\tilde{U}\} \quad (7.6.4)$$

and then reformulated as

$$[\psi^{(1)}]^T \{\tilde{U}\} = [y^{(1)}(\omega)]\{\tilde{U}^{(1)}\} \quad (7.6.5)$$

which is the same form as Eq. (7.6.1). Similarly, an auxiliary variable is introduced for each term of the continued fraction in Eq. (7.5.1b). This yields

$$[\psi^{(i+1)}]^T \{\tilde{U}^{(i)}\} = [y^{(i+1)}(\omega)]\{\tilde{U}^{(i+1)}\} \quad (i = 0, 1, 2, \dots, M_H) \quad (7.6.6)$$

where Eq. (7.6.5) is included as the  $i = 0$  case with  $\{\tilde{U}^{(0)}\} = \{\tilde{U}\}$ . Multiplying Eq. (7.5.1b) by  $\{\tilde{U}^{(i)}\}$  and using the definition of auxiliary variables in Eq. (7.6.6) with  $i - 1$  and  $i$  result in

$$[\psi^{(i)}]^T \{\tilde{U}^{(i-1)}\} = [y_0^{(i)}]\{\tilde{U}^{(i)}\} + (i\omega)[y_1^{(i)}]\{\tilde{U}^{(i)}\} - [\psi^{(i+1)}]\{\tilde{U}^{(i+1)}\} \quad (i = 1, 2, \dots, M_H) \quad (7.6.7)$$

The residual  $\{\tilde{U}^{(M_H+1)}\}$  of an order  $M_H$  high-frequency continued fraction solution is expressed in Eq. (7.6.6) with  $i = M_H$  as

$$[\psi^{(M_H)}]^T \{\tilde{U}^{(M_H)}\} = [y^{(M_H+1)}(\omega)] \{\tilde{U}^{(M_H+1)}\} \quad (7.6.8)$$

$[y^{(M_H+1)}(\omega)] = [y_L(\omega)]$  (Eq. (7.5.17)) is expressed in Eq. (7.5.21a) as a low-frequency continued fraction solution. Multiplying Eq. (7.5.21a) by  $\{\tilde{U}^{(M_H+1)}\}$  and using Eqs. (7.5.17) and (7.6.8) lead to

$$[\psi_L^{(0)}]^T \{\tilde{U}^{(M_H)}\} = [y_{L0}^{(0)}] \{\tilde{U}^{(M_H+1)}\} + (i\omega)[y_{L1}^{(0)}] \{\tilde{U}^{(M_H+1)}\} - (i\omega)[\psi_L^{(1)}] \{\tilde{U}_L^{(1)}\} \quad (7.6.9)$$

where the auxiliary variable  $\{\tilde{U}_L^{(1)}\}$  is defined in

$$(i\omega)[\psi_L^{(1)}]^T \{\tilde{U}^{(M_H+1)}\} = [y_L^{(1)}(\omega)] \{\tilde{U}_L^{(1)}\} \quad (7.6.10)$$

Again, an auxiliary variable is introduced for each term of the continued fraction in Eq. (7.5.21b). This results in

$$(i\omega)[\psi_L^{(i+1)}]^T \{\tilde{U}_L^{(i)}\} = [y_L^{(i+1)}(\omega)] \{\tilde{U}_L^{(i+1)}\} \quad (i = 0, 1, 2, \dots, M_L) \quad (7.6.11)$$

with  $\{\tilde{U}_L^{(0)}\} = \{\tilde{U}^{(M_H+1)}\}$ . Multiplying Eq. (7.5.21b) by  $\{\tilde{U}_L^{(i)}\}$  and using the definition of auxiliary variables in Eq. (7.6.11) with  $i - 1$  and  $i$  result in

$$\begin{aligned} (i\omega)[\psi_L^{(i)}]^T \{\tilde{U}_L^{(i-1)}\} &= [y_{L0}^{(i)}] \{\tilde{U}_L^{(i)}\} + (i\omega)[y_{L1}^{(i)}] \{\tilde{U}_L^{(i)}\} \\ &\quad - (i\omega)[\psi_L^{(i+1)}] \{\tilde{U}_L^{(i+1)}\} \quad (i = 1, 2, \dots, M_L) \end{aligned} \quad (7.6.12)$$

For the low-frequency solution with  $i = M_L$ , the approximation  $\{\tilde{U}_L^{(M_L+1)}\} = 0$  is introduced. Substituting Eqs. (7.6.2a) and (7.6.2b) back into Eq. (7.6.1) results in

$$\{R\} = [\Phi]^{-T} [k_\infty] [\Phi]^{-1} \{U\} + (i\omega)[\Phi]^{-T} [c_\infty] [\Phi]^{-1} \{U\} - [\Phi]^{-T} [\psi^{(1)}] \{\tilde{U}^{(1)}\} \quad (7.6.13)$$

Assembling Eqs. (7.6.13), (7.6.7), (7.6.9) and (7.6.12) leads to a system of linear equations,

$$([K_h] + (i\omega)[C_h]) \{Z\} = \{F\} \quad (7.6.14)$$

where  $\{Z\}$  contains the displacement amplitudes on the boundary  $\Gamma_V$  and the auxiliary variables,  $\{F\}$  the amplitude of the excitation forces applied on the vertical



Equation (7.6.17) represents the high-order doubly asymptotic open condition. It is temporally local. When the low-frequency terms are neglected, it becomes a high-order singly asymptotic boundary condition.

## 7.7 Numerical examples

In this section, a homogeneous semi-infinite with a constant depth in Fig. 7.7.1(a) is analyzed in the frequency and time domains. The ratio of  $G/\rho = 1$  and  $\nu = 0.25$  are used in the analysis, and the plane strain condition is considered.

When evaluating the accuracy of the continued fraction solutions, the equivalent dynamic coefficient expressed in Eq. (A.3.1) in Appendix A is computed. Two spatial motion patterns are used for the in-plane case:  $u$ -spatial motion (using only horizontal displacements) and  $v$ -spatial motion (using only vertical displacements). The equivalent dynamic stiffness coefficients are normalized by the shear modulus  $G$  and plotted with respect to the dimensionless frequency  $a_0$ , which is defined as

$$a_0 = \frac{\omega h}{c_s} \quad (7.7.1)$$

The solution in Eq. (7.4.14) serves as the reference solution.

In Section 7.7.1, the doubly asymptotic continued fraction solution with use of factor matrices (i.e. the improved procedure) is addressed and compared with the unimproved one and the improved singly asymptotic solution to illustrate the robustness of the improved procedure. In Sections 7.7.2, 7.7.3 and 7.7.4, the responses of the semi-infinite layer to surface tractions applied on the vertical boundary  $\Gamma_V$  are computed. Several directions of the surface tractions and time history are considered.

The Newmark's method with  $\gamma = 0.5$  and  $\beta = 0.25$  (average acceleration scheme) is adopted to integrate Eq. (7.6.17) (see Section A.2 in Appendix A). An extended finite element mesh is analyzed by using ABAQUS, a commercial finite element package, to provide a reference solution to verify the high-order singly and doubly asymptotic open boundaries. Eight-node isoparametric quadrilateral element (Q8) is selected for the extended mesh method.

Based on the highest frequency of interest  $\omega_h$ , the wave period  $T = 2\pi/\omega_h$  and the minimum wavelength  $\lambda_w = c_s T$  of each sublayer are calculated. The SBFEM and FEM meshes are divided in such a way that 1 wavelength is represented by at least 9 nodes. The size of the time step  $\Delta t$  is chosen as 1/8 of the shortest period.

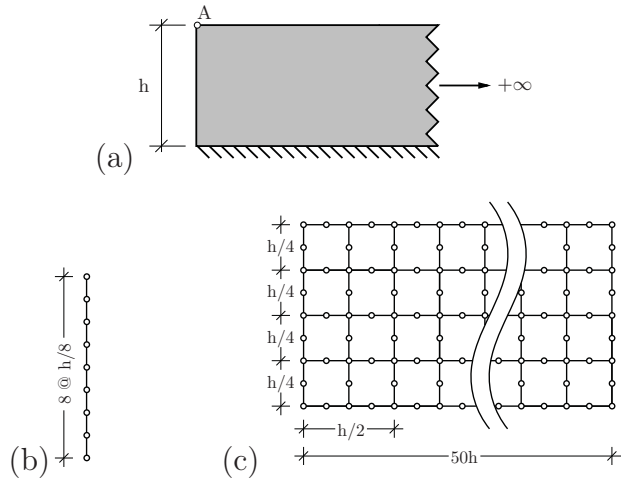
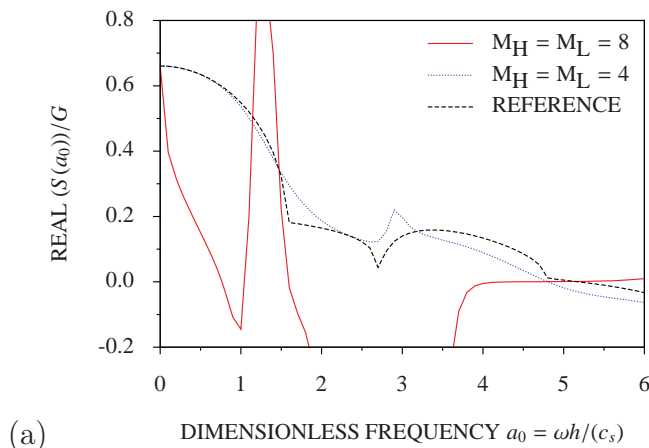


Figure 7.7.1: Semi-infinite layer: (a) geometry, (b) SBFEM mesh and (c) FE mesh

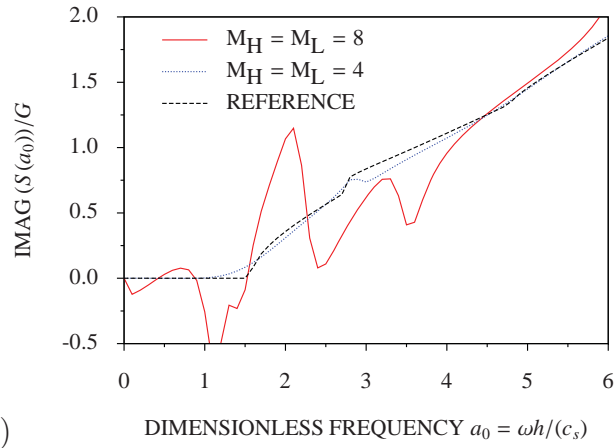
### 7.7.1 Illustration of robustness of doubly asymptotic open boundary for dynamic stiffness

The present open boundary based on the SBFEM is formulated directly on the the vertical boundary  $\Gamma_V$  of the layer. In the following sections, the boundary is discretized with 8 two-node elements in the SBFEM as shown in Fig. 7.7.1(b).

As mentioned in Section 7.5, the factor matrices are introduced to the doubly asymptotic continued fraction solution to improve the numerical stability of the solution. In case of vector wave propagation, the factor matrices are indeed necessary since the numerical stability of the solution deteriorates when the continued fraction order increases. As shown in Figs. 7.7.2 and 7.7.3 for the case of not using the factor matrices, the the order  $M_H = M_L = 4$  doubly asymptotic continued fraction solution agrees well with the reference solution, but when the order increases to  $M_H = M_L = 8$ , an error appears as the real and imaginary parts oscillate throughout the whole range of  $a_0$ .

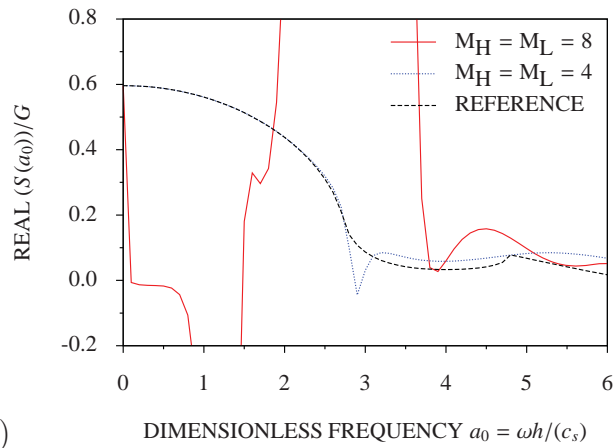


(a)

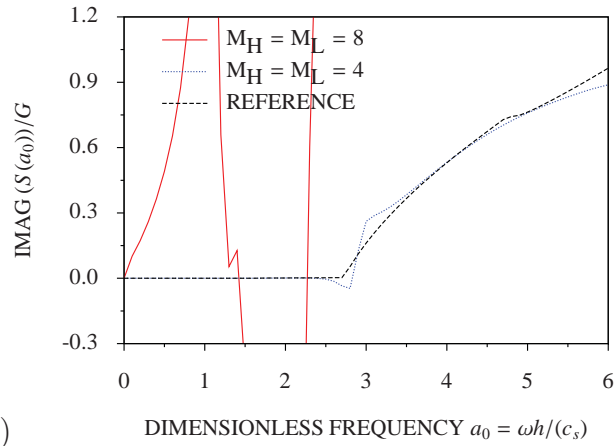


(b)

Figure 7.7.2: Equivalent dynamic stiffness coefficient of semi-infinite layer by doubly asymptotic continued fraction solution without improved numerical stability (using  $u$ -spatial motion): (a) real part and (b) imaginary part



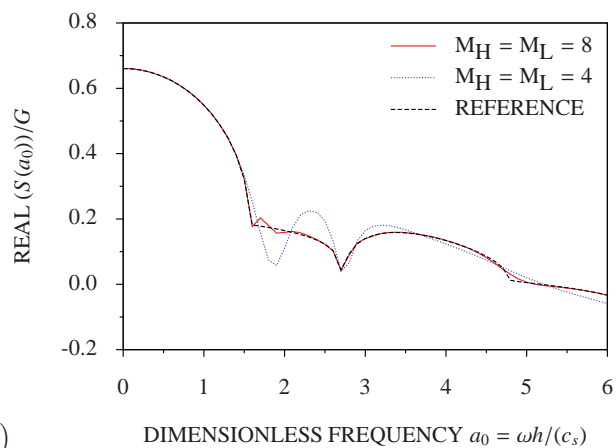
(a)



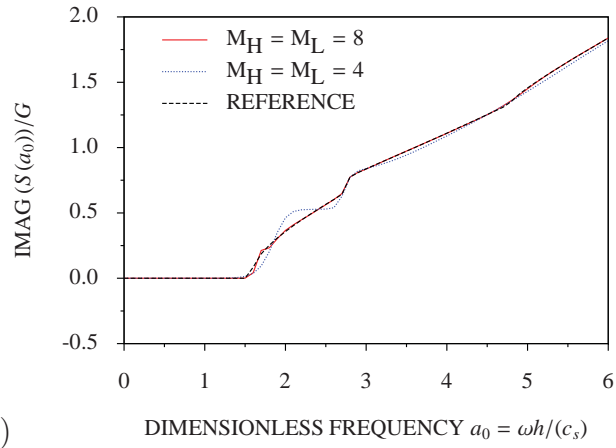
(b)

Figure 7.7.3: Equivalent dynamic stiffness coefficient of semi-infinite layer by doubly asymptotic continued fraction solution without improved numerical stability (using  $v$ -spatial motion): (a) real part, and (b) imaginary part

When the factor matrices are introduced, the results of the solution using the orders  $M_H = M_L = 4$  and  $M_H = M_L = 8$  are shown in Figs. 7.7.4 and 7.7.5. It can be seen that the real and imaginary parts of the results obtained from the order  $M_H = M_L = 4$  do not exhibit any oscillations and correspond to those of the reference solution. In addition, the accuracy of the results increases when the order is increased to  $M_H = M_L = 8$  as the real and imaginary parts converge to those of the reference solution. With use of the factor matrices, the doubly asymptotic solution can model evanescent waves the below cut-off frequencies accurately.

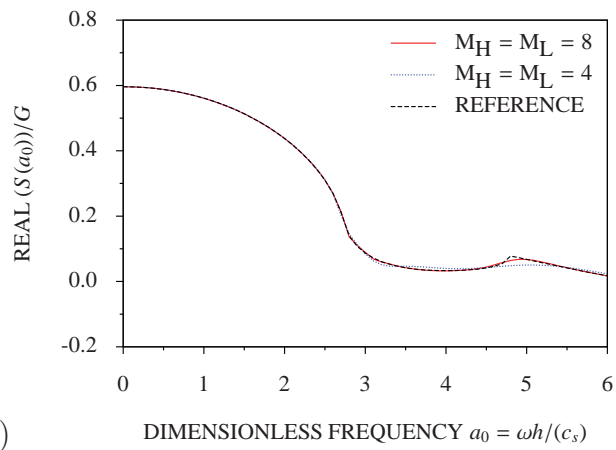


(a)

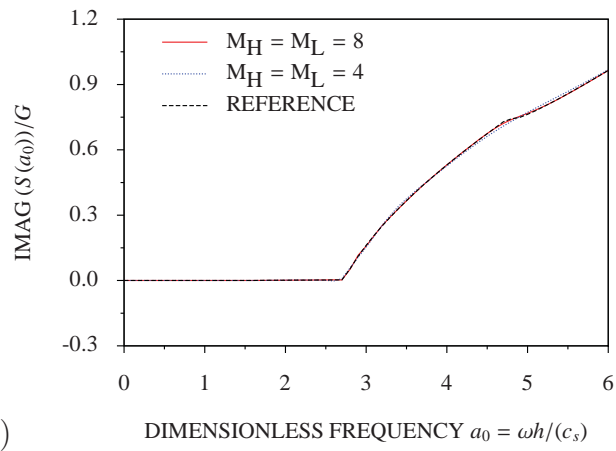


(b)

Figure 7.7.4: Equivalent dynamic stiffness coefficient of semi-infinite layer by doubly asymptotic continued fraction solution with improved numerical stability (using  $u$ -spatial motion): (a) real part and (b) imaginary part



(a)



(b)

Figure 7.7.5: Equivalent dynamic stiffness coefficient of semi-infinite layer by doubly asymptotic continued fraction solution with improved numerical stability (using  $v$ -spatial motion): (a) real part and (b) imaginary part

For the singly asymptotic solution with the same numbers of terms, its results are plotted in Figs. 7.7.6 and 7.7.5. The real parts of the result obtained from the order  $M_H = 9$  are always zero while the imaginary parts exhibit discontinuous points. This defect of the singly asymptotic solution is similar to the case of scalar wave propagation in semi-infinite layers i.e. it cannot model evanescent waves the below cut-off frequencies. The accuracy of the solution, however, deteriorates when the order is increased to  $M_H = 17$  as the oscillations appear in the real and imaginary parts. This is because the factor matrices of the high-frequency limit are not enough to improve the numerical stability of the solution.

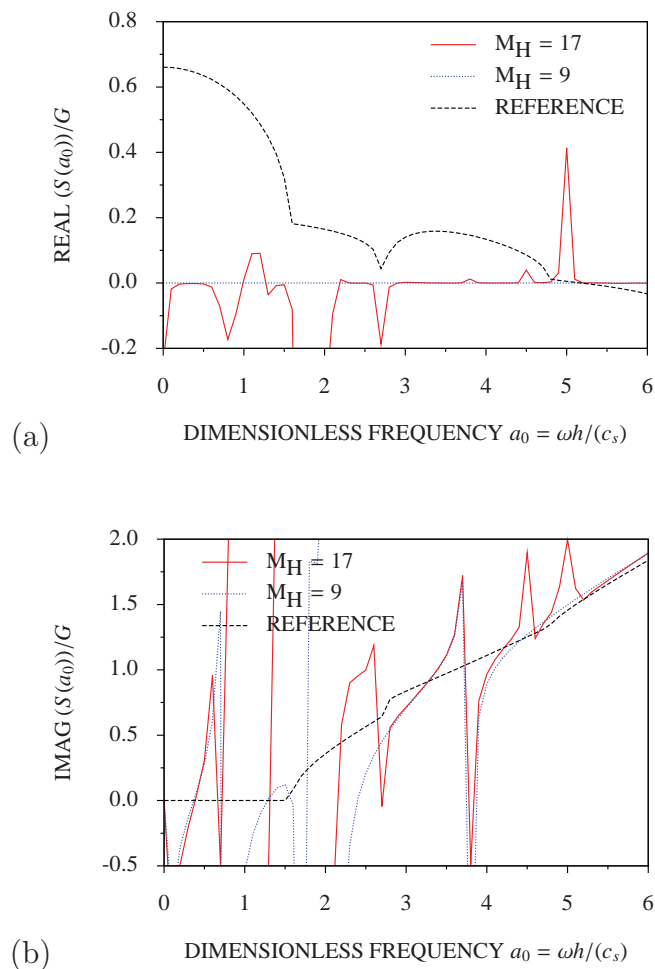


Figure 7.7.6: Equivalent dynamic stiffness coefficient of semi-infinite layer by singly asymptotic continued fraction solution with improved numerical stability (using  $u$ -spatial motion): (a) real part and (b) imaginary part

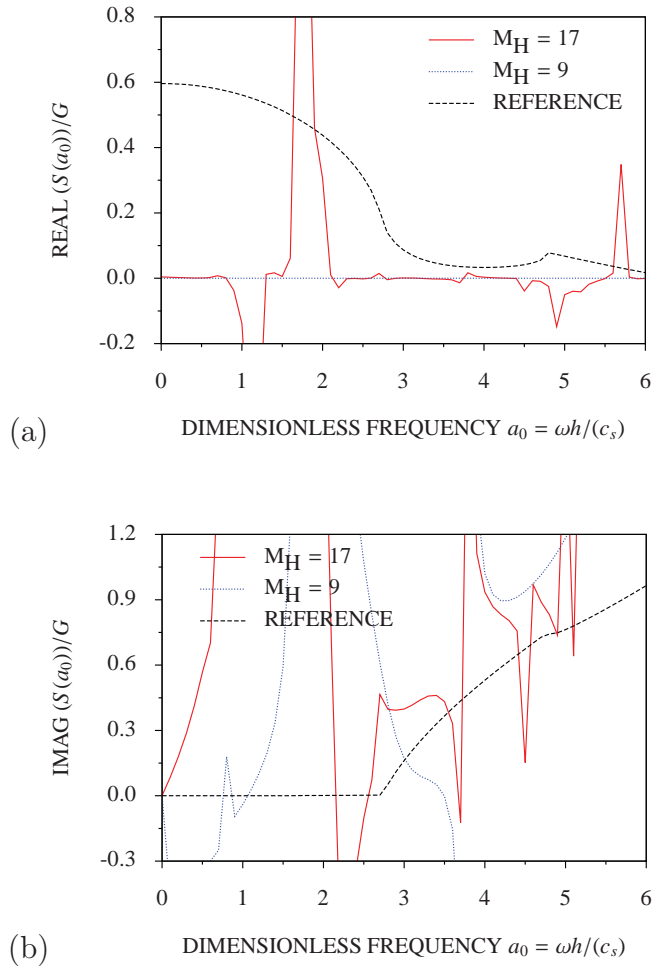


Figure 7.7.7: Equivalent dynamic stiffness coefficient of semi-infinite layer by singly asymptotic continued fraction solution with improved numerical stability (using  $v$ -spatial motion): (a) real part and (b) imaginary part

### 7.7.2 Semi-infinite layer subjected to horizontal surface traction

In this example, the transient response of the semi-infinite layer to a uniformly distributed surface traction  $p(t)$  on the vertical boundary  $\Gamma_V$  in the horizontal direction as illustrated in Fig. 7.7.8 is evaluated. The time-dependence of the surface traction  $p(t)$  is prescribed as a triangular function as plotted in Fig. 7.7.9(a) with respect to the dimensionless time  $\bar{t} = tc_s/h$ . The maximum surface traction is denoted as  $P_T$ . The Fourier transform of the function is also plotted in Fig. 7.7.9(b) with respect to the dimensionless frequency  $a_0$ . The highest dimensionless frequency  $a_h$  of interest is observed as 6.

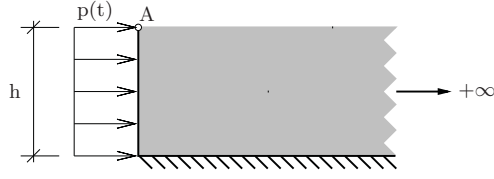


Figure 7.7.8: Semi-infinite layer subjected to horizontal surface traction

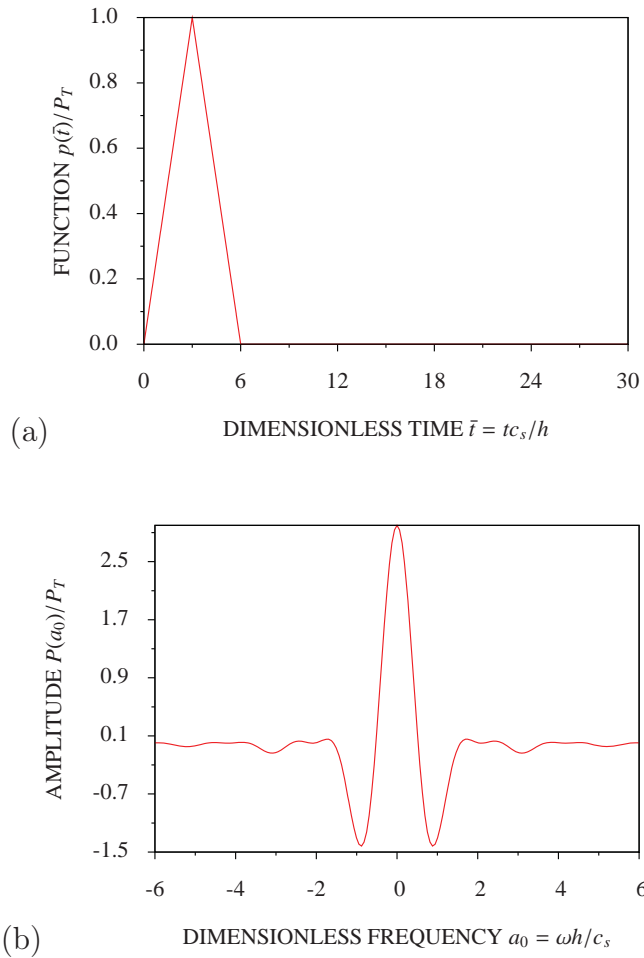
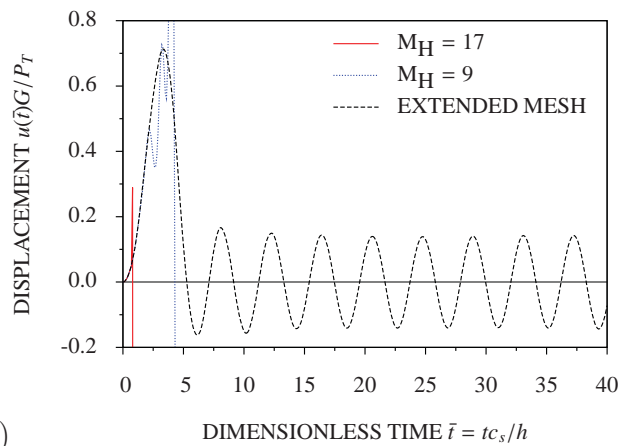


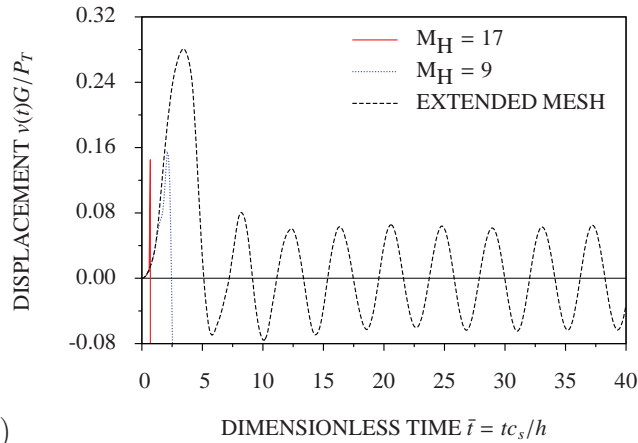
Figure 7.7.9: Triangular function: (a) time history and (b) Fourier transform

To obtain a reference solution, an extended finite element mesh as shown in Fig. 7.7.1(c) is analyzed. The number of nodes on the vertical boundary  $\Gamma_V$  is the same as that of the SBFEM. The length of the extended mesh is chosen as  $50h$  so that responses are not affected by the waves reflected at the truncated boundary. The total number of nodes in the extended finite element mesh is 2,809 while the scaled boundary finite element mesh has only 9 nodes. The dimensionless time step  $\Delta \tilde{t}$  of 0.1 is chosen for both the extended mesh and the open boundaries.

The displacement responses at Point  $A$  located at the top of the vertical boundary  $\Gamma_V$  (Fig. 7.7.1(a)) is chosen to evaluate the accuracy of the singly and doubly asymptotic open boundaries. The accuracy of the singly asymptotic open boundary is investigated first with the orders  $M_H = 9$  and  $M_H = 17$ . The responses of horizontal and vertical displacements of Point  $A$  are normalized by  $P_T/G$  and plotted with respect to the dimensionless time  $\bar{t}$  as shown in Fig. 7.7.10. At the order  $M_H = 9$ , the results are accurate at the early time ( $0 < \bar{t} < 1.5$ ). When  $\bar{t} > 1.5$ , the results start to deviate from those of the extended mesh method. In case of the order  $M_H = 17$ , its results are accurate only within the smaller range of  $0 < \bar{t} < 0.5$ . Even worse, its results deteriorate earlier than those of the order  $M_H = 9$  do. This indicates that the singly asymptotic open boundary is unable to transmit evanescent waves below cut-off frequencies. Thus it is impossible to use the singly asymptotic open boundary for a long-time analysis since the accuracy of the results deteriorates with increasing orders.



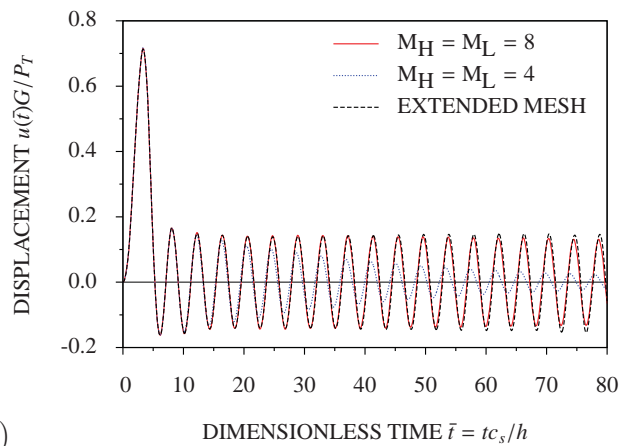
(a)



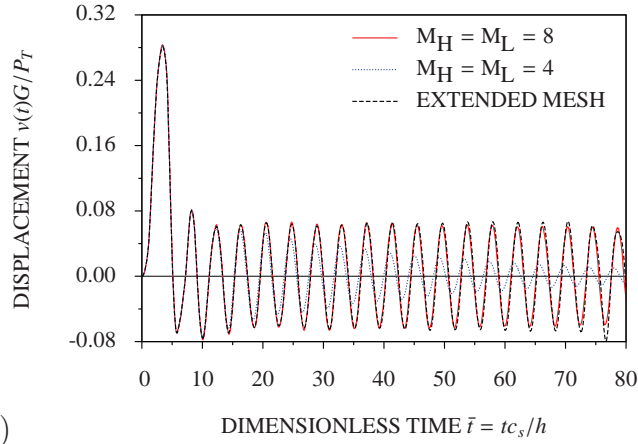
(b)

Figure 7.7.10: Displacement responses of Point *A* to horizontal surface traction by singly asymptotic open boundary: (a) horizontal displacement and (b) vertical displacement

The accuracy of the doubly asymptotic open boundary is then investigated with the orders  $M_H = M_L = 4$  and  $M_H = M_L = 8$ . The results of displacement responses of Point *A* are plotted in Fig. 7.7.11. At the order  $M_H = M_L = 4$ , the horizontal and the vertical displacements correspond to those of the extended mesh at the early time, attenuating continuously with time. At the order  $M_H = M_L = 8$ , the accuracy of the results at the late time increases as the results agree well with those of the extended mesh method. By comparing Figs. 7.7.10 and 7.7.11, the doubly asymptotic open boundary is much more accurate than the singly asymptotic open boundary with the same number of terms. Thus it is more suitable for a long-time analysis of the horizontal surface traction.



(a)



(b)

Figure 7.7.11: Displacement responses of Point  $A$  to horizontal surface traction by doubly asymptotic open boundary: (a) horizontal displacement and (b) vertical displacement

### 7.7.3 Semi-infinite layer subjected to vertical surface traction

The same uniform surface traction  $p(t)$  as in Section 7.7.2 is applied to the vertical boundary  $\Gamma_V$  but in the vertical direction as illustrated in Fig. 7.7.12.

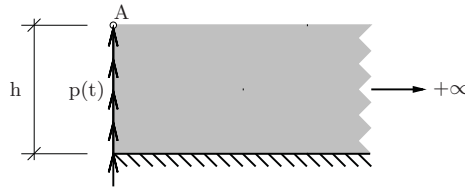


Figure 7.7.12: Semi-infinite layer subjected to vertical surface traction

A reference solution is obtained with the same extended mesh as in Section 7.7.2 (Fig. 7.7.1(c)).

The displacement responses at Point  $A$  by using the order  $M_H = 9$  and  $M_H = 17$  singly asymptotic open boundary are plotted in Fig. 7.7.13. At the very early time ( $0 < \bar{t} < 1.5$  for  $M_H = 9$  and  $0 < \bar{t} < 0.5$  for  $M_H = 17$ ), the results agree well with those of the extended mesh method. However, After  $\bar{t} > 1.5$  for  $M_H = 9$  and  $\bar{t} > 0.5$  for  $M_H = 17$ , the results are inaccurate. Similarly, the results obtained from the order  $M_H = 17$  diverge before those of the order  $M_H = 9$  do. This also indicates that the singly asymptotic open boundary is inappropriate for a long-time analysis since the results always diverge at the early time.

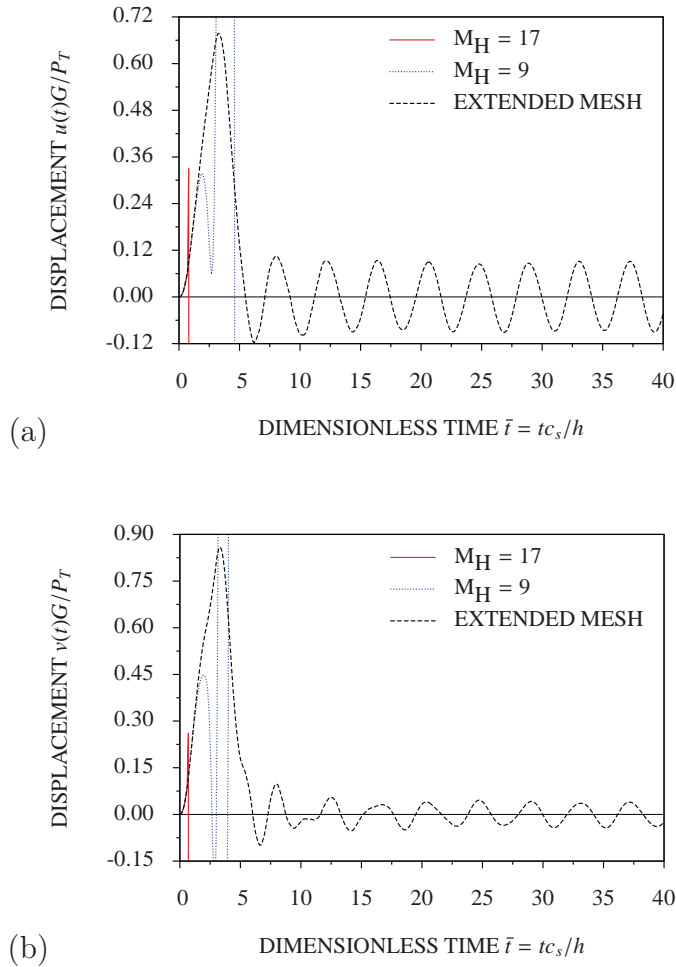


Figure 7.7.13: Displacement responses of Point *A* to vertical surface traction by singly asymptotic open boundary: (a) horizontal displacement and (b) vertical displacement

In contrast, the doubly asymptotic open boundary with the same numbers of terms yields the excellent results. The results obtained from the orders  $M_H = M_L = 4$  and  $M_H = M_L = 8$  are plotted in Fig. 7.7.14. All the results correspond to those of the extended mesh method, and no “fictitious reflection” is observed throughout the entire duration. The accuracy of the results at the late time increases when the order is increased to  $M_H = M_L = 8$ . Thus the doubly asymptotic open boundary is more suitable for a long-time analysis of the vertical surface traction.

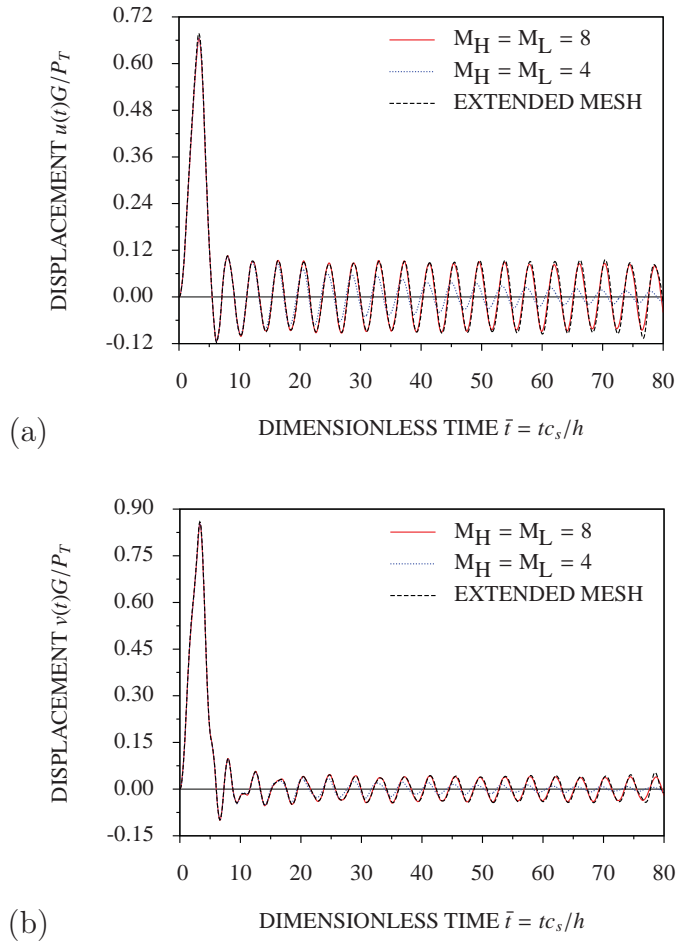


Figure 7.7.14: Displacement responses of Point *A* to vertical surface traction by doubly asymptotic open boundary: (a) horizontal displacement and (b) vertical displacement

### 7.7.4 Semi-infinite layer subjected to inclined surface traction

In the last example, the semi-infinite layer is subjected to uniformly distributed surface traction  $\tau_0(t)$  in the inclined direction as shown in Fig. 7.7.15.

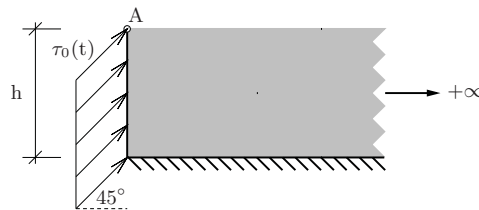


Figure 7.7.15: Semi-infinite layer subjected to inclined surface traction

The time history of  $\tau_0(t)$  is prescribed as a function of Ricker wavelet with  $t_s = 9$  and  $t_0 = 1.5$  (see Eqs. (A.1.1) and (A.1.2) in Appendix A). The time history is

plotted in Fig. 7.7.16(a) of which Fourier transform is shown in Fig. 7.7.16(b). The highest dimensionless frequency of interest  $a_h$  is observed as 6.

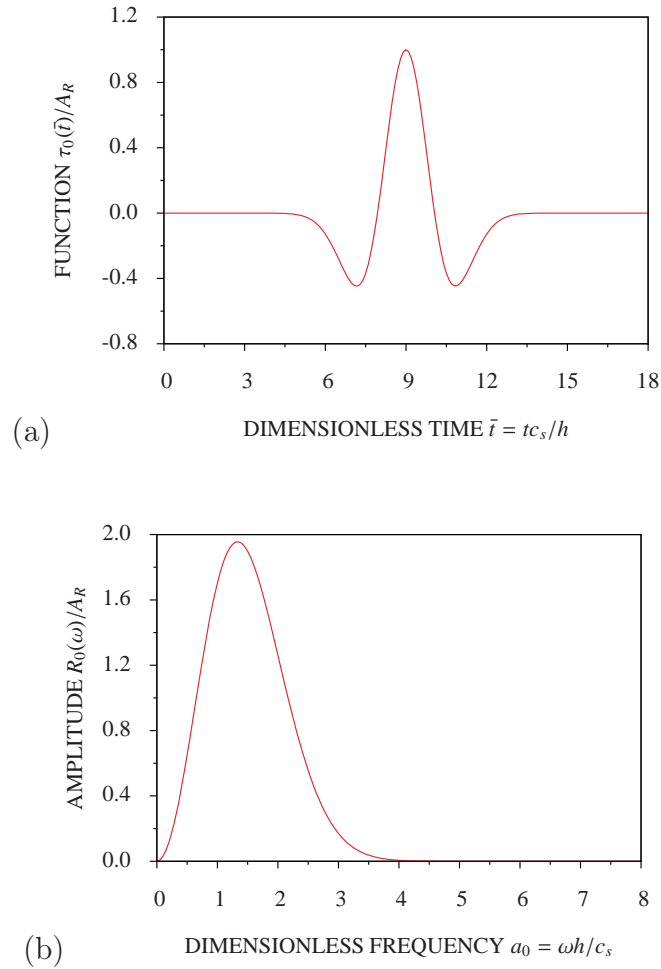
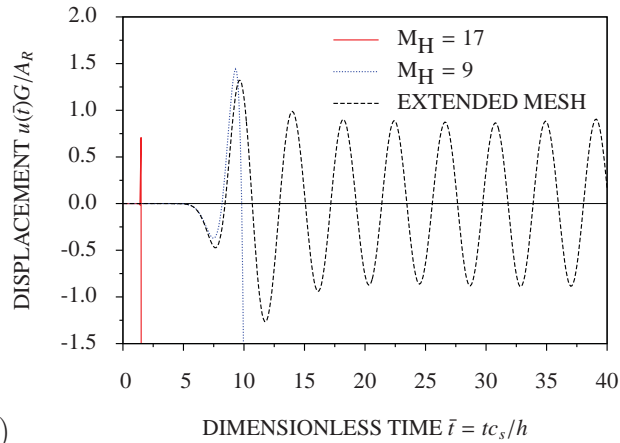


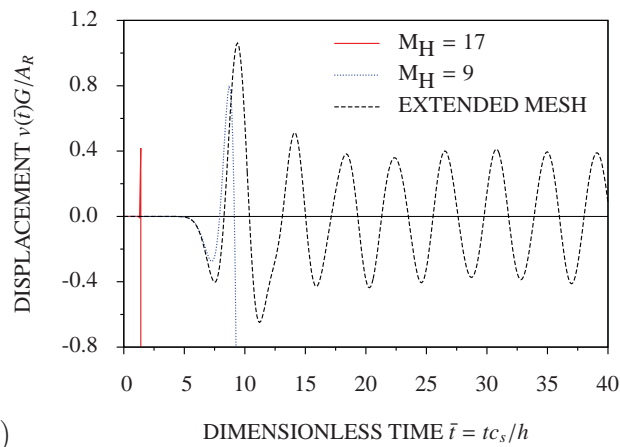
Figure 7.7.16: Ricker wavelet function: (a) time history and (b) Fourier transform

Again, a reference solution is obtained from the same extended mesh as in Section 7.7.2 (Fig. 7.7.1(c)).

The singly asymptotic open boundary is evaluated first. The displace responses Point *A* obtained from the orders  $M_H = 9$  and  $M_H = 17$  are plotted in Fig. 7.7.17. Again, the results are only accurate at the early time. At the order  $M_H = 9$ , the results are accurate until to  $\bar{t} = 6$ . After  $\bar{t} > 6$ , the differences between the results and those of the extended mesh method are noticed. Then the results suddenly diverge at about  $\bar{t} = 9$ . At the order  $M_H = 17$ , the results are accurate until to  $\bar{t} < 1.5$  and then suddenly diverge before those of the order  $M_H = 9$  do.



(a)



(b)

Figure 7.7.17: Displacement responses of Point A to to inclined surface traction by singly asymptotic open boundary: (a) horizontal displacement and (b) vertical displacement

The doubly asymptotic open boundary with the same numbers of terms is applied. The results are much more accurate as plotted in Fig. 7.7.18. The result obtained from using the order  $M_H = M_L = 4$  does not exhibit any “fictitious reflection” throughout the entire duration. Moreover, the accuracy of the result at the late time increases when the order is increased to  $M_H = M_L = 8$ . The result is almost the same as that of the extended mesh method, and no “fictitious reflection” is observed. Thus the doubly asymptotic open boundary is more suitable for a long-time analysis of the inclined surface traction.

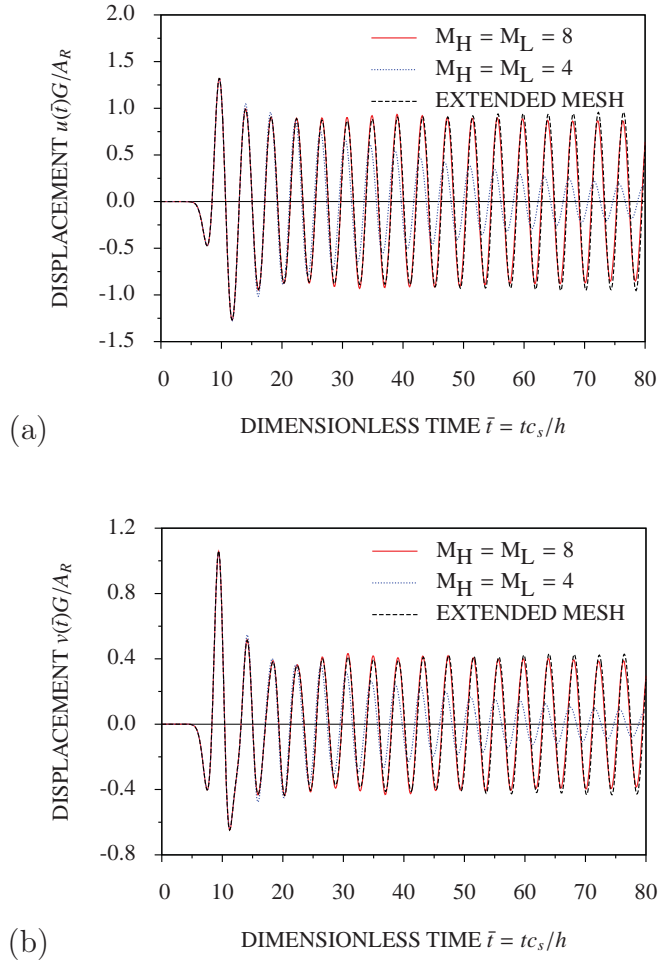


Figure 7.7.18: Displacement responses of Point *A* to inclined surface traction by doubly asymptotic open boundary: (a) horizontal displacement and (b) vertical displacement

## 7.8 Conclusions

A matrix solution for the scaled boundary finite element equation in dynamic stiffness is obtained for the modeling of vector wave propagation in a semi-infinite layer. The solution is expressed as high-order doubly asymptotic continued fraction in the frequency domain. It is formulated in the time domain as a high-order open boundary condition. From the analysis results obtained in the frequency and time domains, it can be concluded as follows:

1. In the frequency domain, due to the existence of the cut-off frequencies of the semi-infinite layer, the singly asymptotic continued fraction solution can only model propagating waves at high frequencies (i.e. above the cut-off frequencies), but cannot model evanescent waves at low frequencies (i.e. below the cut-off frequencies). The accuracy of the solution does not always increase

with increasing orders. In case of the doubly asymptotic continued fraction solution, it is more accurate and converges to the reference solution rapidly as the orders increase. It can model not only the propagating waves at the high frequencies, but also model the evanescent waves at low frequencies.

2. In the time domain, the accuracy of the doubly asymptotic open boundary rapidly increases with increasing orders, and is much higher than that of the singly asymptotic open boundary in comparison with the same number of terms. The displacement responses at the early time and the late time can be simulated accurately by the doubly asymptotic open boundary. On the contrary, the displacement responses obtained from the singly asymptotic open boundary often diverge at the early time, and the accuracy of the displacement responses does not always increase with increasing orders.
3. The high-order doubly asymptotic open boundary is indispensable to long-time analysis of vector wave propagation in homogeneous semi-infinite layers. The open boundary is temporally local. It is expressed as a system of first-order ordinary differential equation in time. The two time-independent coefficient matrices, the stiffness matrix  $[K_h]$  and the damping matrix  $[C_h]$  are banded and symmetric. Thus well-established time-stepping schemes in structural dynamics are directly applicable.

# Chapter 8

## Conclusions

### 8.1 Summary

The main objective of the research is to develop a reliable and efficient open boundaries for wave propagation problems in unbounded domains. The scaled boundary finite element method (SBFEM), a semi-analytical approach based on the finite element formulation, was adopted in the research as the theoretical framework. The advantages of the SBFEM is that no fundamental solution is required and the radiation condition at infinity is satisfied rigorously. Only the boundary of the computational domain is discretized, thereby reducing the spatial dimension by one. In addition, it can be coupled seamlessly with standard finite elements.

This research focuses on semi-infinite layered systems, which are frequently encountered in foundation engineering. This system is the most challenging one in the time-domain analysis of wave propagation due to the existence of the so-called cut-off frequency below which evanescent waves are present. This research is also extended to circular cavities embedded in full-planes. The proposed open boundary was a further development of the transmitting boundary proposed in Bazyar and Song (2008) by extending the singly asymptotic formulation to a doubly asymptotic formulation. This advance leads to significantly gain in accuracy and stability.

In Chapter 1, the introduction of the thesis was presented. The statement of problem was described. The background and motivation were explained. The objectives were presented and then followed by the outline of the research.

In Chapter 2, a detailed literature of existing approaches for wave propagation problems in unbounded domains was presented. The approaches were classified into two groups. The approaches in the first group are spatially and temporally global e.g. the boundary element method (BEM), the thin-layer method (TLM),

the SBFEM, exact non-reflecting boundaries, and also temporally local exact non-reflecting boundaries. The approaches in the second group are local procedures introducing approximations e.g. low-order absorbing boundary conditions (low-order ABCs), high-order ABCs, local high-order ABCs, the doubly asymptotic approximations (DAAs), infinite elements, and absorbing layers. The advantages and disadvantages of the approaches in such two groups were identified and reviewed.

In Chapter 3, the high-order doubly asymptotic open boundaries for the modal equations of scalar waves in a semi-infinite layer with constant depth and a circular cavity embedded in a full-plane were constructed. In the formulation, the method of separation of variables was applied to decompose a two-dimensional wave equation into a series of modal wave equations in one dimension. By combining these modal wave equations with the force-displacement relationship, the equations of modal dynamic stiffness coefficients were obtained in the frequency domain. The doubly asymptotic continued fraction solution of the modal dynamic stiffness coefficients was determined recursively. This doubly asymptotic continued fraction solution approaches to the exact solution at both high- and low-frequency limits. It was observed that the solution converged to the exact solution over the whole frequency range as the order of continued fractions increases. It was also demonstrated that many of existing transmitting boundaries could be regarded as singly asymptotic continued fraction solutions, which were special cases of the present doubly asymptotic solution. Numerical examples showed significant improvement in accuracy in comparison with the singly asymptotic continued fraction solution, especially in modeling evanescent waves below cut-off frequencies. By employing the continued fraction solution of the dynamic stiffness coefficients and introducing auxiliary variables, the force-displacement relationship in the frequency domain was expressed as a system of linear equations. It was written as a system of first-order ordinary differential equations representing a high-order doubly asymptotic open boundary condition in the time domain. Numerical examples of direct time-domain analysis demonstrated that the doubly asymptotic open boundaries yielded accurate results and exhibited no “fictitious reflections” at the late time while the singly asymptotic open boundaries were less accurate and always exhibited “fictitious reflections” at the late time.

In Chapter 4, the time-domain analysis of gravity dam-reservoir interaction was performed using the high-order doubly asymptotic open boundary developed in Chapter 3. The water in the reservoir was treated as acoustic fluid satisfying the scalar wave equation. The Dirichlet and the Neumann boundary conditions were applied on the top surface and at the base, respectively. By substituting the acceleration-pressure relationship of acoustic fluid (derived in the scaled boundary

coordinates) into the Galerkin's weighted residual method, the scaled boundary finite element (SBFE) equation in pressure with the coefficient matrices was formulated. The eigenvectors obtained from the eigen-decomposition of two coefficient matrices  $[E^0]$  and  $[E^2]$  of the SBFEM were used for the SBFE equation in pressure. This led to a system of decoupled equations for individual modes which was a function of the dimensionless frequency. Since the acceleration-pressure relationship of acoustic fluid was equivalent to the stress-strain relationship in Chapter 3, the modal dynamic stiffness coefficients were equivalently defined in the relationship between the force-pressure relationship. Therefore, the doubly asymptotic continued fraction solution for the modal dynamic stiffness coefficients could be determined by following the derivation in Chapter 3 as mentioned earlier. The doubly asymptotic open boundary condition in the time domain were also formulated by following the derivation in Chapter 3, but using the force-pressure relationship and including the continued fraction solutions of all the modes. As numerical examples, a rigid dam and a flexible dam were investigated. For the rigid dam, the doubly asymptotic open boundary was applied directly on the upstream face of the dam. The hydrodynamic pressure obtained from the doubly asymptotic open boundary were more accurate and no "fictitious reflections" occurred compared to those obtained from the singly asymptotic open boundary. The measured computer time of the doubly asymptotic open boundary increased linearly with the order of the open boundary and the numbers of time steps. For the flexible dam, the dam body and the irregular near-field of the reservoir were modeled by finite elements using ABAQUS, a commercial finite element package. The open boundary was applied on the truncated boundary to represent the regular far field of the reservoir. In the numerical implementation, the finite element equations of the near field and the open boundary conditions of the far field were solved by a sequential staggered implicit-implicit partitioned procedure. Based on the restart function in ABAQUS, a two-way data-exchange sequential coupling scheme was established. The results of the hydrodynamic pressure at the dam heel and the displacement responses at the dam crest obtained from the doubly asymptotic open boundary were accurate and stable. The accuracy of the results increased rapidly with increasing orders.

In Chapter 5, the high-order doubly asymptotic open boundary for scalar wave propagation in a full-plane with a circular cavity was developed by extending the SBFEM. The full-plane was assumed to be homogeneous and the circular boundary was subjected to time-dependent out-of-plane shear stresses. By employing either the virtual work method or the Galerkin's weighted residual method with the stress-strain relationship in an out-of-plane problem (derived in the scaled boundary coordinates), the scaled boundary finite element (SBFE) equation in displacement

was formulated with the coefficient matrices  $[E^0]$  and  $[E^2]$ . The scaled boundary finite element equation was decomposed by the eigenvectors of  $[E^0]$  and  $[E^2]$ . This led to a series of equations for individual modes which were similar to the modal equation of scalar waves obtained by the method of separation of variables in Chapter 3. The modal equations of dynamic stiffness coefficients were, therefore, determined by following the derivation in Chapter 3. However, the doubly asymptotic continued fraction solution for modal dynamic stiffness coefficients proposed in Chapter 3 could break down at certain modal eigenvalues. This problem occurred when the denominators of the coefficients of the continued fractions became zero. Hence, in Chapter 5, the factor coefficients were introduced to the formulation of the continued fraction to handle such a problem. All denominators of the coefficients in the improved formulation turned into sign functions which were equal to  $\pm 1$ . The high-order open boundary condition in the time domain was formulated in the same way as that in Chapter 4. In the frequency-domain analysis, the doubly asymptotic and the singly asymptotic continued fraction solutions were compared. The results indicated that the rate of convergence of the doubly asymptotic continued fraction solution was much higher, especially at high modes. In the time-domain analysis, the doubly asymptotic open boundary yielded more accurate results and faster convergence than the singly asymptotic open boundaries, especially in the area where the pressure was applied.

In Chapter 6, the high-order doubly asymptotic open boundary for scalar wave propagation in semi-infinite layered systems was constructed by extending the SBFEM. The material constants were assumed to be constant throughout each sublayer and could be different from those of the other sublayers. The Neumann and the Dirichlet boundary conditions were applied on the top surface and at the base, respectively. The translated boundary coordinate system was used in the SBFEM. By using the stress-strain relationship of an out-of-plane problem (derived in the scaled boundary coordinates) and the virtual work method, the SBFEM equation in displacement was formulated. The SBFEM equation in displacement was then used for deriving the SBFEM equation in dynamic stiffness. The SBFEM equation for this case cannot be decoupled. A continued fraction solution was sought in matrix form. To determine the coefficient and factor matrices of the doubly asymptotic continued fraction solution, the continued fraction was substituted in the SBFEM equation in dynamic stiffness, starting from the high-frequency limit and then followed by the low-frequency one. The recursive procedures at the high- and low-frequency limits were performed, depending on the orders of continued fraction. The factor matrices were set equal to the lower triangular matrices obtained from  $LDL^T$  decomposition. By following the derivation in Chapter 3, the the high-order open boundary condition in the time

domain was also expressed as a system of first-order ordinary differential equations. In the frequency-domain analysis, the results of the singly and doubly asymptotic continued fraction solutions were plotted as equivalent dynamic stiffness coefficients for convenience in comparison. The results indicated that the doubly asymptotic continued fraction solution was able to model evanescent waves below the cut-off frequencies in the layered systems while the singly asymptotic continued fraction solution was not. In the time-domain analysis, the singly and doubly asymptotic open boundaries were applied on the vertical boundaries of the layered systems. The open boundaries were compared with each other. The accuracy of the results obtained from the singly asymptotic open boundary could be improved with the increasing orders but in a very low rate. Moreover, the “fictitious reflections” always occurred. In contrast, the doubly asymptotic open boundary yielded more accurate results and the accuracy rapidly increased with the increasing orders. No “fictitious reflections” were observed.

In Chapter 7, the high-order doubly asymptotic open boundary for vector wave propagation in a homogeneous semi-infinite layer was constructed by extending the SBFEM. The Neumann and the Dirichlet boundary conditions were applied on the top surface and at the base, respectively. The translated boundary coordinate system was used in the SBFEM. By using the stress-strain relationship of an in-plane problem (derived in the scaled boundary coordinates) and the virtual work principle, the scaled boundary finite element (SBFE) equation in displacement was formulated. The SBFE equation in displacement was then used for deriving the SBFE equation in dynamic stiffness. The coefficient and factor matrices of the doubly asymptotic continued fraction solution was determined recursively. By following the derivation in Chapter 3, the the high-order open boundary condition in the time domain was expressed as a system of first-order ordinary differential equations. In the frequency-domain analysis, the results indicated that the doubly asymptotic continued fraction solution was able to model evanescent waves below the cut-off frequencies in the layer while the singly asymptotic continued fraction solution was not. In the time-domain analysis, the singly and doubly asymptotic open boundaries were applied on the vertical boundary of the semi-infinite layer. The accuracy of the singly asymptotic open boundary was very low accurate even at the early times. In contrast, the doubly asymptotic open boundary yielded accurate results without any “fictitious reflections” and the accuracy rapidly improved as the order increases.

## 8.2 Recommendations for future research

- In Chapter 5, the high-order doubly asymptotic open boundary was constructed for the scalar wave propagation in a full-plane with a circular cavity. It is of interest to extend the open boundary to acoustic wave propagation for underwater shock analysis. And also the coupling scheme with standard finite elements should be developed for the open boundary.
- In Chapter 5, only scalar wave propagation in a full-plane with a circular cavity was considered. The next study should extend to vector wave propagation focusing on a homogeneous full-plane first and then on a non-homogeneous full-plane if possible.
- In Chapter 6, the semi-infinite layered systems were considered for scalar waves. The next study should focus on non-homogeneous semi-infinite layers with the shear modulus varying as a power function of depth.
- In Chapter 7, the high-order doubly asymptotic open boundary for vector wave propagation in a semi-infinite layer with a constant depth was proposed. However, only the homogeneous layer was considered. In the future research, semi-infinite layered systems and non-homogeneous semi-infinite layer with the modulus of elasticity varying as a power function of depth should be considered.
- The geometry of the high-order doubly asymptotic open boundaries developed in this research are restricted to a vertical line for a semi-infinite layer with a constant depth and a circle for a circular cavity embedded in a full-plane. In the future research, the high-order doubly asymptotic open boundary should be developed for arbitrary geometry.
- Stability of the high-order doubly asymptotic open boundary in the time domain should be extensively studied. This includes the cases of scalar and vector wave propagation in a semi-infinite layer with a constant depth, a circular cavity embedded in a full-plane and also arbitrary geometry.
- In the time-domain analysis in Chapter 4 in case of the flexible dam the rigid foundation was only considered, the high-order doubly asymptotic open boundary was applied only on the truncated boundary of the near-field water. However, in reality, the foundation is not all rigid and the material constants vary with depth. Hence, it is of great interest if the flexible foundation is taken

into account. Thus the high-order open boundary should also be applied on the truncated boundary of the flexible foundation.

# Appendix A

## Summary of Equations

### A.1 Ricker wavelet function

The Ricker wavelet function is given as

$$\tau_0(t) = A_R \left( 1 - 2 \left( \frac{t - t_s}{t_0} \right)^2 \right) \exp \left( - \left( \frac{t - t_s}{t_0} \right)^2 \right) \quad (\text{A.1.1})$$

where  $t_s$  is the time when the wavelet reaches its maximum,  $2/t_0$  is the dominant frequency  $\omega_p$ , and  $A_R$  is the amplitude of the wavelet. The Fourier transform of the Ricker wavelet is expressed as

$$R_0(\omega) = 0.5\sqrt{\pi}A_R t_0 (\omega t_0)^2 \exp(-0.25(\omega t_0)^2) \quad (\text{A.1.2})$$

where  $\omega$  denotes the excitation frequency.

### A.2 Newmark's method

The Newmark's method can be employed by following these steps (Huge and Belytschko, 1983): first, determine the predictors from

$$\{\tilde{u}\}_{n+1} = \{u\}_n + (\Delta t)\{\dot{u}\}_n + (0.5 - \beta)(\Delta t)^2\{\ddot{u}\}_n \quad (\text{A.2.1a})$$

$$\{\dot{\tilde{u}}\}_{n+1} = \{\dot{u}\}_n + (1 - \gamma)(\Delta t)\{\ddot{u}\}_n \quad (\text{A.2.1b})$$

where  $\beta$  and  $\gamma$  are chosen parameters and  $\Delta t$  is time step. Next, solve for  $\{\ddot{u}_{t+\Delta t}\}$  from

$$\{\ddot{u}\}_{n+1} = ([M] + \gamma(\Delta t)[C] + \beta(\Delta t)^2[K])^{-1}(\{F_{n+1}\} - [C]\{\dot{\tilde{u}}\}_{n+1} - [K]\{\tilde{u}\}_{n+1}) \quad (\text{A.2.2})$$

where  $[K]$  is the stiffness matrix,  $[C]$  is the damping matrix and  $[M]$  is the mass matrix. Then, determine the correctors from

$$\{u\}_{n+1} = \{\tilde{u}\}_{n+1} + \beta(\Delta t)^2\{\ddot{u}\}_{n+1} \quad (\text{A.2.3a})$$

$$\{\dot{u}\}_{n+1} = \{\dot{\tilde{u}}\}_{n+1} + \gamma(\Delta t)\{\ddot{u}\}_{n+1} \quad (\text{A.2.3b})$$

### A.3 Equivalent dynamic stiffness coefficient

The equivalent dynamic stiffness coefficient is expressed as

$$S(\omega) = \{\varphi\}^T [S^\infty(\omega)] \{\varphi\} \quad (\text{A.3.1})$$

where  $[S^\infty(\omega)]$  is the dynamic stiffness matrix, and  $\{\varphi\}$  denotes the linear spatial motion pattern of the nodes on the discretized boundary which does not vary with time (Wolf and Song, 1996).

# References

- ABAQUS (2004). *ABAQUS Version 6.5 Documentation*. ABAQUS, Inc, U.S.A.
- Abarbanel, S. and Gottlieb, D. (1997). A mathematical analysis of the PML method. *Journal of Computational Physics*, 134:357–363.
- Abarbanel, S. and Gottlieb, D. (1998). On the construction and analysis of absorbing layers in CEM. *Applied Numerical Mathematics*, 27:331–340.
- Akiyoshi, T. (1978). Compatible viscous boundary for discrete models. *Journal of the Engineering Mechanics Division*, 104:1253–1266.
- Akiyoshi, T., Fuchida, K., and Fang, H. L. (1994). Absorbing boundary conditions for dynamic analysis of fluid-saturated porous media. *Soil Dynamics and Earthquake Engineering*, 13:387–397.
- Akiyoshi, T., Sun, X., and Fuchida, K. (1998). General absorbing boundary conditions for dynamic analysis of fluid-saturated porous media. *Soil Dynamics and Earthquake Engineering*, 17:397–406.
- Alpert, B., Greengard, L., and Hagstrom, T. (2000). Rapid evaluation of nonreflecting boundary kernels for time-domain wave propagation. *SIAM Journal on Numerical Analysis*, 37:1138–1164.
- Alpert, B., Greengard, L., and Hagstrom, T. (2002). Nonreflecting boundary conditions for the time-dependent wave equation. *Journal of Computational Physics*, 180:270–296.
- ANSYS (2009a). Fluid analysis guide. *Release 12.0, SAS IP, Inc.* (<http://www.ansys.com>).
- ANSYS (2009b). High-frequency electromagnetic analysis guide. *Release 12.0, SAS IP, Inc.* (<http://www.ansys.com>).

- Astley, R. J. (1983). Wave envelope and infinite elements for acoustical radiation. *International Journal for Numerical Methods in Fluids*, 3:507–526.
- Astley, R. J. (1996). Transient wave envelope elements for wave problems. *Journal of Sound and Vibration*, 192:245–261.
- Astley, R. J. (1998a). Mapped spheroidal wave-envelope elements for unbounded wave problems. *International Journal for Numerical Methods in Engineering*, 41:1235–1254.
- Astley, R. J. (1998b). Transient spheroidal elements for unbounded wave problems. *Computer Methods in Applied Mechanics and Engineering*, 164:3–15.
- Astley, R. J. (2000). Infinite elements for wave problems: a review of current formulations and an assessment of accuracy. *International Journal for Numerical Methods in Engineering*, 49:951–976.
- Astley, R. J. and Coyette, J. P. (2001a). Conditioning of infinite elements schemes for wave problems. *Communications in Numerical Methods in Engineering*, 17:31–41.
- Astley, R. J. and Coyette, J. P. (2001b). The performance of spheroidal infinite elements. *International Journal for Numerical Methods in Engineering*, 52:1379–1396.
- Astley, R. J. and Eversman, W. (1983). Finite element formulations for acoustical radiation. *Journal of Sound and Vibration*, 88:47–64.
- Astley, R. J. and Hamilton, J. A. (2006). The stability of infinite element schemes for transient wave problems. *Computer Methods in Applied Mechanics and Engineering*, 195:3553–3571.
- Astley, R. J., Macaulay, G. J., and Coyette, J. P. (1994). Mapped wave envelope elements for acoustical radiation and scattering. *Journal of Sound and Vibration*, 170:97–118.
- Aydinoğlu, M. N. (1993). Consistent formulation of direct and substructure methods in nonlinear soil-structure interaction. *Soil Dynamics and Earthquake Engineering*, 12:403–410.
- Bécache, E., Fauqueux, S., and Joly, P. (2003). Stability of perfectly matched layers, group velocities and anisotropic waves. *Journal of Computational Physics*, 188:399–433.

- Bécache, E., Givoli, D., and Hagstrom, T. (2010). High-order absorbing boundary conditions for anisotropic and convective wave equations. *Journal of Computational Physics*, 229:1099–1129.
- Baker, G. A. and Graves-Morris, P. (1996). *Padé Approximants*. Cambridge University Press, New York.
- Banerjee, P. K. and Butterfield, R. (1977). *Boundary element methods in geomechanics*, 529–570. *Finite Elements in Geomechanics*. John Wiley & Sons, New York.
- Basu, U. and Chopra, A. K. (2003). Perfectly matched layers for time-harmonic elastodynamics of unbounded domains: theory and finite-element implementation. *Computer Methods in Applied Mechanics and Engineering*, 192:1337–1375.
- Basu, U. and Chopra, A. K. (2004). Perfectly matched layers for transient elastodynamics of unbounded domains. *International Journal for Numerical Methods in Engineering*, 59:1039–1074.
- Bayliss, A., Gunzburger, M., and Turkel, E. (1982). Boundary Conditions for the Numerical Solution of Elliptic Equations in Exterior Regions. *SIAM Journal on Applied Mathematics*, 42:430–451.
- Bayliss, A. and Turkel, E. (1980). Radiation boundary conditions for wave-like equations. *Communications on Pure and Applied Mathematics*, 33:707–725.
- Bayliss, A. and Turkel, E. (1982). Far field boundary conditions for compressible flows. *Journal of Computational Physics*, 48:182–199.
- Bayraktar, A., Hance, E., and Akköse, M. (2005). Influence of base-rock characteristics on the stochastic dynamic response of dam-reservoir-foundation systems. *Engineering Structures*, 27:1498–1508.
- Baziar, M. H. and Song, C. (2006a). Time-harmonic response of non-homogeneous elastic unbounded domains using the scaled boundary finite-element method. *Earthquake Engineering and Structural Dynamics*, 35:357–383.
- Baziar, M. H. and Song, C. (2006b). Transient analysis of wave propagation in non-homogeneous elastic unbounded domains by using the scaled boundary finite-element method. *Earthquake Engineering and Structural Dynamics*, 35:1787–1806.

- Bazyar, M. H. and Song, C. (2008). A continued-fraction-based high-order transmitting boundary for wave propagation in unbounded domains of arbitrary geometry. *International Journal for Numerical Methods in Engineering*, 74:209–237.
- Bennett, A. F. (1976). Open boundary conditions for dispersive waves. *Journal of the Atmospheric Sciences*, 33:176–182.
- Berenger, J. P. (1994). A perfectly matched layer for the absorption of electromagnetic waves. *Journal of Computational Physics*, 114:185–200.
- Berenger, J. P. (1996). Three-dimensional perfectly matched layer for the absorption of electromagnetic waves. *Journal of Computational Physics*, 127:363–379.
- Beskos, D. E. (1987). Boundary element methods in dynamic analysis. *Applied Mechanics Reviews (ASME)*, 40:1–23.
- Beskos, D. E. (1997). Boundary element methods in dynamic analysis: Part II (1986-1996). *Applied Mechanics Reviews (ASME)*, 50:149–197.
- Bettess, P. (1977). Infinite elements. *International Journal for Numerical Methods in Engineering*, 11:53–64.
- Bettess, P. and Zienkiewicz, O. C. (1977). Diffraction and refraction of surface waves using finite and infinite elements. *International Journal for Numerical Methods in Engineering*, 11:1271–1290.
- Betti, E. (1873). Teoria della elasticita'. *Il Nuovo Cimento*, 10:58–84.
- Birk, C. and Ruge, P. (2007). Representation of radiation damping in a dam-reservoir interaction analysis based on a rational stiffness approximation. *Computers and Structures*, 85:1152–1163.
- Bouchon, M., Schultz, C. A., and Toksoz, M. N. (1995). A fast implementation of boundary integral equation methods to calculate the propagation of seismic waves in laterally varying layered media. *Bulletin of the Seismological Society of America*, 85:1679–1687.
- Brebbia, C. A. (1978). *The Boundary Element Method for Engineers*. Pentech Press/Halstead Press, London/New York.
- Brebbia, C. A. and Dominguez, J. (1977). Boundary element methods for potential problems. *Applied Mathematical Modelling*, 1:372–378.

- Burnett, D. S. (1994). A three-dimensional acoustic infinite element based on a prolate spheroidal multipole expansion. *The Journal of the Acoustical Society of America*, 96:2798–2816.
- Burnett, D. S. and Holford, R. L. (1998). Prolate and oblate spheroidal acoustic infinite elements. *Computer Methods in Applied Mechanics and Engineering*, 158:117–141.
- Camara, R. J. (2000). A method for coupled arch dam-foundation-reservoir seismic behaviour analysis. *Earthquake Engineering and Structural Dynamics*, 29:441–460.
- Chakrabarti, P. and Chopra, A. K. (1973). Earthquake analysis of gravity dams including hydrodynamic interaction. *Earthquake Engineering and Structural Dynamics*, 2:143–160.
- Chakraborty, A., Gopalakrishnan, S., and Kausel, E. (2005). Wave propagation analysis in inhomogeneous piezo-composite layer by the thin-layer method. *International Journal for Numerical Methods in Engineering*, 64:567–598.
- Chew, W. C. and Liu, Q. (1996). Perfectly matched layers for elastodynamics: a new absorbing boundary condition. *Journal of Computational Acoustics*, 4:341–359.
- Chew, W. C. and Weedon, W. H. (1994). A 3d perfectly matched medium from modified Maxwell’s equations with stretched coordinates. *Microwave and Optical Technology Letters*, 7:599–604.
- Chopra, A. K. (1967). Hydrodynamic pressures on dams during earthquakes. *Journal of the Engineering Mechanics Division*, 93:205–223.
- Chopra, A. K. (1968). Earthquake behavior of reservoir-dam systems. *Journal of the Engineering Mechanics Division*, 94:1475–1500.
- Chopra, A. K. (1970). Earthquake response of concrete gravity dams. *Journal of the Engineering Mechanics Division*, 96:443–454.
- Chopra, A. K. and Chakrabarti, P. (1972). The earthquake experience at Koyna dam and stresses in concrete gravity dams. *Earthquake Engineering and Structural Dynamics*, 1:151–164.
- Chopra, A. K. and Chakrabarti, P. (1981). Earthquake analysis of concrete gravity dams including dam-water-foundation rock interaction. *Earthquake Engineering and Structural Dynamics*, 9:363–383.

- Chwang, A. T. (1978). Hydrodynamic pressures on sloping dams during earthquakes. Part 2. Exact theory. *Journal of Fluid Mechanics*, 87:343–348.
- Chwang, A. T. and Housner, G. W. (1978). Hydrodynamic pressures on sloping dams during earthquakes. Part 1. Momentum method. *Journal of Fluid Mechanics*, 87:335–341.
- Clayton, R. and Engquist, B. (1977). Absorbing boundary conditions for acoustic and elastic wave equations. *Bulletin of the Seismological Society of America*, 67:1529–1540.
- Collino, F. (1993). High order absorbing boundary conditions for wave propagation models: straight line boundary and corner cases. In *Proceedings of the Second International Conference on Mathematical and Numerical Aspects of Wave Propagation*, 161–171, Newark. Delaware.
- Collino, F. and Tsogka, C. (2001). Application of the perfectly matched absorbing layer model to the linear elastodynamic problem in anisotropic heterogeneous media. *Geophysics*, 66:294–307.
- Cruse, T. A. (1968). A direct formulation and numerical solution of the general transient elastodynamic problem. II. *Journal of Mathematical Analysis and Applications*, 22:341–355.
- Cruse, T. A. (1969). Numerical solutions in three dimensional elastostatics. *International Journal of Solids and Structures*, 5:1259–1274.
- Cruse, T. A. and Rizzo, F. J. (1968). A direct formulation and numerical solution of the general transient elastodynamic problem. I. *Journal of Mathematical Analysis and Applications*, 22:244–259.
- Czygan, O. and von Estorff, O. (2002). Fluid-structure interaction by coupling BEM and nonlinear FEM. *Engineering Analysis with Boundary Elements*, 26:773–779.
- Deek, A. J. and Wolf, J. P. (2002a). Semi-analytical elastostatic analysis of unbounded two-dimensional domains. *International Journal for Numerical and Analytical Methods in Geomechanics*, 26:1031–1057.
- Deek, A. J. and Wolf, J. P. (2002b). A virtual work derivation of the scaled boundary finite-element method for elastostatics. *Computation Mechanics*, 28:489–504.
- Deek, A. J. and Wolf, J. P. (2003). Semi-analytical solution of Laplace’s equation in non-equilibrating unbounded problems. *Computers and Structures*, 81:1525–1537.

- Demkowicz, L. and Gerdes, K. (1998). Convergence of the infinite element methods for the Helmholtz equation in separable domains. *Numerische Mathematik*, 79:11–42.
- Doherty, J. P. and Deeks, A. J. (2003a). Elastic response of circular footings embedded in a non-homogeneous half-space. *Géotechnique*, 53:703–714.
- Doherty, J. P. and Deeks, A. J. (2003b). Scaled boundary finite-element analysis of a non-homogeneous axisymmetric domain subjected to general loading. *International Journal for Numerical and Analytical Methods in Geomechanics*, 27:329–355.
- Doherty, J. P. and Deeks, A. J. (2003c). Scaled boundary finite-element analysis of a non-homogeneous elastic half-space. *International Journal for Numerical Methods in Engineering*, 57:955–973.
- Dominguez, J. (1977). *Stress Analysis Around Anchor Plates: a Boundary Element Method Application*. PhD thesis, Universidad de Sevilla.
- Dominguez, J. (1993). *Boundary Element in Dynamics*. Computational Mechanics, Southampton.
- Engquist, B. and Majda, A. (1977). Absorbing boundary conditions for the numerical simulation of waves. *Mathematics of Computation*, 31:629–651.
- Engquist, B. and Majda, A. (1979). Radiation boundary conditions for acoustic and elastic wave calculations. *Communications on Pure and Applied Mathematics*, 32:313–357.
- Eringen, A. C. and Suhubi, E. S. (1975). *Elastodynamics-Vol. II, Linear Theory*. Academic Press, New York.
- Fan, S. C. and Li, S. M. (2008). Boundary finite-element method coupling finite-element method for steady-state analyses of dam-reservoir systems. *Journal of Engineering Mechanics*, 134:133–142.
- Felippa, C. A. (1980). A family of early-time approximations for fluid structure interaction. *Journal of Applied Mechanics*, 47:703–708.
- Feltrin, G. (1997). Absorbing boundaries for the time-domain analysis of dam-reservoir-foundation systems. Technical report, Institute of Structural Engineering, Swiss Federal Institute of Technology Zurich, Zurich, Switzerland.

- Fu, L. Y. (2002). Seismogram synthesis for piecewise heterogeneous media. *Geophysical Journal International*, 150:800–808.
- Fu, L. Y. and Bouchon, M. (2004). Discrete wavenumber solutions to numerical wave propagation in piecewise heterogeneous-I. theory of two-dimensional SH case. *Geophysical Journal International*, 157:481–498.
- Ge, Z. and Chen, X. (2007). Wave propagation in irregularly layered elastic models: a boundary element approach with a global reflection/transmission matrix propagator. *Bulletin of the Seismological Society of America*, 97:1025–1031.
- Ge, Z. and Chen, X. (2008). An efficient approach for simulating wave propagation with the boundary element method in multilayered media with irregular interfaces. *Bulletin of the Seismological Society of America*, 98:3007–3016.
- Geers, T. L. (1969). Excitation of an elastic cylindrical shell by a transient acoustic wave. *Journal of Applied Mechanics*, 36:459–469.
- Geers, T. L. (1971). Residual potential and approximate methods for three-dimensional fluid-structure interaction problems. *The Journal of the Acoustical Society of America*, 49:1505–1510.
- Geers, T. L. (1972). Scattering of a transient acoustic wave by an elastic cylindrical shell. *The Journal of the Acoustical Society of America*, 51:1640–1651.
- Geers, T. L. (1974). Shock response analysis of submerged structures. *Shock and Vibration Bulletin*, 44:17–32.
- Geers, T. L. (1978). Doubly asymptotic approximations for transient motions of submerged structures. *The Journal of the Acoustical Society of America*, 64:1500–1508.
- Geers, T. L. (1991). *A fully consistent formulation of early-time approximations for acoustic media*, 521–528. *The Finite Element Method in the 1990's*. Springer-Verlag, Berlin.
- Geers, T. L. (1998). Singly and doubly asymptotic computational boundaries. In Geer, T. L., editor, *Proceedings of the IUTAM Symposium on Computational Methods for Unbounded Domains*, 135–141, Dordrecht.
- Geers, T. L. and Felippa, C. A. (1983). Doubly asymptotic approximations for vibration analysis of submerged structures. *The Journal of the Acoustical Society of America*, 73:1152–1159.

- Geers, T. L. and Lewis, B. A. (1997). Doubly asymptotic approximations for transient elastodynamics. *International Journal of Solids and Structures*, 34:1293–1305.
- Geers, T. L. and Sprague, M. A. (2010). A residual-potential boundary for time-dependent, infinite-domain problems in computational acoustics. *The Journal of the Acoustical Society of America*, 127:675–682.
- Geers, T. L. and Tothaker, B. J. (2000). Third-order doubly asymptotic approximations for computational acoustics. *Journal of Computational Acoustics*, 8:101–120.
- Geers, T. L. and Zhang, P. (1988). *Doubly asymptotic approximations for electromagnetic scattering problems*, 357–369. Boundary Element Methods in Applied Mechanics. Peramon Press.
- Geers, T. L. and Zhang, P. (1994). Doubly asymptotic approximations for submerged structures with internal fluid volumes. *Journal of Applied Mechanics*, 61:893–906.
- Gerdes, K. (1998). The conjugated vs. the unconjugated infinite element method for the Helmholtz equation in exterior domains. *Computer Methods in Applied Mechanics and Engineering*, 152:125–145.
- Givoli, D. (1991). Non-reflecting boundary conditions: a review. *Journal of Computational Physics*, 94:1–29.
- Givoli, D. (1992a). *Numerical Methods for Problems in Infinite Domains*. Elsevier, Amsterdam.
- Givoli, D. (1992b). A spatially exact non-reflecting boundary condition for time dependent problems. *Computer Methods in Applied Mechanics and Engineering*, 95:97–113.
- Givoli, D. (1999). Recent advances in the DtN FE method. *Archives of Computational Methods in Engineering*, 6:71–116.
- Givoli, D. (2004). High-order local non-reflecting boundary conditions: a review. *Wave Motion*, 39:319–326.
- Givoli, D. and Cohen, D. (1995). Nonreflecting boundary conditions based on Kirchhoff-type formulae. *Journal of Computational Physics*, 117:102–113.
- Givoli, D., Hagstrom, T., and Patlashenko, I. (2006). Finite element formulation with high-order absorbing boundary conditions for time-dependent waves. *Computer Methods in Applied Mechanics and Engineering*, 195:3666–3690.

- Givoli, D. and Keller, J. B. (1989). A finite element method for large domains. *Computer Methods in Applied Mechanics and Engineering*, 76:41–66.
- Givoli, D. and Neta, B. (2003). High-order non-reflecting boundary scheme for time-dependent waves. *Journal of Computational Physics*, 186:24–46.
- Givoli, D., Neta, B., and Patlashenko, I. (2003). Finite element analysis of time-dependent semi-infinite wave-guides with high-order boundary treatment. *International Journal for Numerical Methods in Engineering*, 58:1955–1983.
- Green, G. (1828). *An essay on the application of mathematical analysis to the theories of electricity and magnetism*. T. Wheelhouse, Nottingham.
- Grote, M. J. (2006). Local nonreflecting boundary condition for Maxwell’s equations. *Computer Methods in Applied Mechanics and Engineering*, 195:3691–3708.
- Grote, M. J. and Keller, J. B. (1995a). Exact nonreflecting boundary conditions for the time dependent wave equation. *SIAM Journal on Applied Mathematics*, 55:280–297.
- Grote, M. J. and Keller, J. B. (1995b). On nonreflecting boundary conditions. *Journal of Computational Physics*, 122:231–243.
- Grote, M. J. and Keller, J. B. (1996). Nonreflecting boundary conditions for time-dependent scattering. *Journal of Computational Physics*, 127:52–65.
- Grote, M. J. and Keller, J. B. (1998). Nonreflecting boundary conditions for Maxwell’s equations. *Journal of Computational Physics*, 139:327–342.
- Grote, M. J. and Keller, J. B. (2000). Exact nonreflecting boundary condition for elastic waves. *SIAM Journal on Applied Mathematics*, 60:803–819.
- Guddati, M. N. and Tassoulas, J. L. (1998a). Characteristics methods for transient analysis of wave propagation in unbounded media. *Computer Methods in Applied Mechanics and Engineering*, 164:187–206.
- Guddati, M. N. and Tassoulas, J. L. (1998b). An efficient numerical algorithm for transient analysis of exterior scalar wave propagation in a homogeneous layer. *Computer Methods in Applied Mechanics and Engineering*, 167:261–273.
- Guddati, M. N. and Tassoulas, J. L. (1999). Space-time finite elements for the analysis of transient wave propagation in unbounded layered media. *International Journal of Solids and Structures*, 36:4699–4723.

- Guddati, M. N. and Tassoulas, J. L. (2000). Continued-fraction absorbing boundary conditions for the wave equation. *Journal of Computational Acoustics*, 8:139–156.
- Guiggiani, M. and Gigante, A. (1990). A general algorithm for multidimensional Cauchy principal value integrals in the boundary element method. *Journal of Applied Mechanics*, 57:906–915.
- Ha-Duong, T. and Joly, P. (1994). On the stability analysis of boundary conditions for the wave equation by energy methods. Part I: the homogeneous case. *Mathematics of Computation*, 62:539–563.
- Hagstrom, T., De Castro, M. L., Givoli, D., and Tzemach, D. (2007). Local high-order absorbing boundary conditions for time-dependent waves in guides. *Journal of Computational Acoustics*, 15:1–22.
- Hagstrom, T. and Hariharan, S. I. (1998). A formulation of asymptotic and exact boundary conditions using local operators. *Applied numerical mathematics*, 27:403–416.
- Hagstrom, T., Mar-Or, A., and Givoli, D. (2008). High-order local absorbing conditions for the wave equation: extensions and improvements. *Journal of Computational Physics*, 227:3322–3357.
- Hagstrom, T. and Warburton, T. (2004). A new auxiliary variable formulation of high-order local radiation boundary conditions: corner compatibility conditions and extensions to first-order systems. *Wave Motion*, 39:327–338.
- Hall, J. F. and Chopra, A. K. (1982). Two-dimensional dynamic analysis of concrete gravity and embankment dams including hydrodynamic effects. *Earthquake Engineering and Structural Dynamics*, 10:305–332.
- Hall, W. S. and Oliveto, G. (2003). *Boundary Element Methods for Soil-Structure Interaction*. Kluwer Academic Publishers, Dordrecht.
- Harari, I. and Albocher, U. (2006). Studies of FE/PML for exterior problems of time-harmonic elastic waves. *Computer Methods in Applied Mechanics and Engineering*, 195:3854–3879.
- Harari, I. and Djellouli, R. (2004). Analytical study of the effect of wave number on the performance of local absorbing boundary conditions for acoustic scattering. *Applied Numerical Mathematics*, 50:15–47.

- Harari, I. and Hughes, T. J. R. (1992a). Analysis of continuous formulations underlying the computation of time-harmonic acoustics in exterior domains. *Computer Methods in Applied Mechanics and Engineering*, 97:103–124.
- Harari, I. and Hughes, T. J. R. (1992b). Galerkin/least-squares finite element methods for the reduced wave equation with non-reflecting boundary conditions in unbounded domains. *Computer Methods in Applied Mechanics and Engineering*, 98:411–454.
- Harari, I., Patlashenko, I., and D, G. (1998). Dirichlet-to-Neumann maps for unbounded wave guides. *Journal of Computational Physics*, 227:3322–3357.
- Hasting, F. D., Schneider, J. B., and L, B. S. (1996). Application of the perfectly matched layer (PML) absorbing boundary condition to elastic wave propagation. *The Journal of the Acoustical Society of America*, 100:3061–3069.
- Higdon, R. L. (1986). Absorbing boundary conditions for difference approximations to the multi-dimensional wave equation. *Mathematics of Computation*, 47:437–459.
- Higdon, R. L. (1987). Numerical absorbing boundary conditions for the wave equation. *Mathematics of Computation*, 49:65–90.
- Higdon, R. L. (1992). Absorbing boundary conditions for acoustic and elastic waves in stratified media. *Journal of Computational Physics*, 101:386–418.
- Higdon, R. L. (1994). Radiation boundary conditions for dispersive waves. *SIAM Journal on Numerical Analysis*, 31:64–100.
- Hu, F. Q. (1996). On absorbing boundary conditions for linearized Euler equations by a perfectly matched layer. *Journal of Computational Physics*, 129:201–219.
- Huge, T. J. and Belytschko, T. (1983). A precis of developments in computational methods for transient analysis. *Journal of Applied Mechanics*, 50:1033–1041.
- Jaswon, M. A. (1963). Integral equation methods in potential theory. I. *Proceedings of the Royal Society A: Mathematical, Physical & Engineering Sciences*, 275:23–32.
- Jaswon, M. A. and Ponter, A. R. (1963). An integral equation solution of the torsion problem. *Proceedings of the Royal Society A: Mathematical, Physical & Engineering Sciences*, 273:237–246.

- Kausel, E. (1981). An explicit solution for the Green's functions for dynamic loads in layered media. *MIT Research Report R81-13*, MA 02139.
- Kausel, E. (1986). Wave propagation in anisotropic layered media. *International Journal for Numerical Methods in Engineering*, 23:1567–1578.
- Kausel, E. (1988). Local transmitting boundaries. *Journal of Engineering Mechanics*, 114:1011–1027.
- Kausel, E. (1994). Thin-layer method: formulation in the time domain. *International Journal for Numerical Methods in Engineering*, 37:927–941.
- Kausel, E. (1999). Dynamic point sources in laminated media via the thin-layer method. *International Journal of Solids and Structures*, 36:4725–4742.
- Kausel, E. and Park, J. (2006). Response of layered half-space obtained directly in the time domain, part II: SV-P and three-dimensional sources. *Bulletin of the Seismological Society of America*, 96:1810–1826.
- Kausel, E. and Peek, R. (1982a). Boundary integral method for stratified soils. *MIT Research Report R82-50*, MA 02139.
- Kausel, E. and Peek, R. (1982b). Dynamic loads in the interior of a layered stratum: an explicit solution. *Bulletin of the Seismological Society of America*, 72:1459–1481.
- Kausel, E. and Roesset, J. M. (1977). Semianalytic hyperelement for layered strata. *Journal of the Engineering Mechanics Division*, 103:569–588.
- Keller, J. B. and Givoli, D. (1989). Exact non-reflecting boundary conditions. *Journal of Computational Physics*, 82:172–192.
- Kellogg, O. D. (1929). *Foundations of Potential Theory*. Verlag Vong Julius Springer, Berlin.
- Komatitsch, D. and Tromp, J. (2003). A perfectly matched layer absorbing boundary condition for the second-order seismic wave equation. *Geophysical Journal International*, 154:146–153.
- Kreiss, H. O. (1970). Initial boundary value problems for hyperbolic systems. *Communications on Pure and Applied Mathematics*, 23:277–298.
- Krenk, S. (2002). Unified formulation of radiation conditions for the wave equation. *International Journal for Numerical Methods in Engineering*, 53:275–295.

- Kupradze, V. D. (1963). *Potential Methods in the Theory of Elasticity*. Fizmatgiz, Moscow.
- Lachat, J. C. and Watson, J. O. (1976). Effective numerical treatment of boundary integral equations: a formulation for three-dimensional elastostatics. *International Journal for Numerical Methods in Engineering*, 10:991–1005.
- Leis, R. (1986). *Initial-boundary Value Problems in Mathematical Physics*. B.G. Teubner, Stuttgart.
- Li, B., Cheng, L., and Deeks, A. J. (2005). A modified scaled boundary finite-element method for problems with parallel side-faces. Part I. Theoretical developments. *Applied Ocean Research*, 27:216–223.
- Liao, Z. P. (1996). Extrapolation non-reflecting boundary conditions. *Wave Motion*, 24:117–138.
- Liao, Z. P. and Wong, H. L. (1984). A transmitting boundary for the numerical simulation of elastic wave propagation. *Soil Dynamics and Earthquake Engineering*, 3:174–183.
- Lindman, E. L. (1975). "Free-space" boundary conditions for the time dependent wave equation. *Journal of Computational Physics*, 18:66–78.
- Liu, Q. H. (1999). Perfectly matched layers for elastic waves in cylindrical and spherical coordinates. *The Journal of the Acoustical Society of America*, 105:2075–2084.
- Luco, J. E. (1982). Linear soil-structure interaction: a review. *In Earthquake Ground Motion and Its Effects on Structures*, (AMD)53:41–57.
- Lysmer, J. (1970). Lumped mass method for Rayleigh waves. *Bulletin of the Seismological Society of America*, 60:89–104.
- Lysmer, J. and Kuhlemeyer, R. L. (1969). Finite dynamic model for infinite media. *Journal of the Engineering Mechanics Division*, 95:859–877.
- Lysmer, J., Udaka, T., Tsai, C. F., and Seed, H. B. (1975). Flush: a computer program for approximate 3-D analysis of soil-structure interaction problems. Technical Report Report No. EERC 75-30, Earthquake Engineering Research Center, University of California, Berkeley.

- Lysmer, J. and Waas, G. (1972). Shear waves in plane infinite structures. *Journal of the Engineering Mechanics Division*, 98:85–105.
- Mathews, I. C. and Geers, T. L. (1987). A doubly asymptotic, nonreflecting boundary for ground shock analysis. *Journal of Applied Mechanics*, 54:489–497.
- Nicolas-Vullierme, B. (1991). A contribution to doubly asymptotic approximations: an operator top-down derivation. *Journal of Vibration and Acoustics*, 113:409–415.
- Nielsen, A. H. (2009). Boundary conditions for seismic analysis. *SECED Newsletter*, 21:7–11.
- Olson, L. G. and Bathe, K. J. (1985). An infinite element for analysis of transient fluid-structure interactions. *Engineering Computations*, 2:319–329.
- Papoulis, A. (1957). A new method of inversion of the Laplace transform. *Quarterly of Applied Mathematics*, 14:405–414.
- Park, J. and Kausel, E. (2004). Numerical dispersion in the thin-layer method. *Computers & Structures*, 82:607–625.
- Park, J. and Kausel, E. (2006). Response of layered half-space obtained directly in the time domain, part I: SH sources. *Bulletin of the Seismological Society of America*, 96:1795–1809.
- Park, K. C. (1980). Partitioned transient analysis procedures for coupled-field problems: stability analysis. *Journal of Applied Mechanics*, 47:370–376.
- Park, K. C. and Felippa, C. A. (1980). Partitioned transient analysis procedures for coupled-field problems: accuracy analysis. *Journal of Applied Mechanics*, 47:919–926.
- Paronesso, A. and Wolf, J. P. (1995). Global lumped-parameter model with physical representation for unbounded medium. *Earthquake Engineering and Structural Dynamics*, 24:637–654.
- Paronesso, A. and Wolf, J. P. (1998). Recursive evaluation of interaction forces and property matrices from unit-impulse response functions of unbounded medium based on balancing approximation. *Earthquake Engineering and Structural Dynamics*, 27:609–618.

- Qi, Q. and Geers, T. L. (1997). Doubly asymptotic approximations for transient poroelastodynamics. *The Journal of the Acoustical Society of America*, 102:1361–1371.
- Ramshaw, C. L., Selby, A. R., and Bettess, P. (1998). *Computation of the transmission of waves from pile driving*, 115–128. Ground Dynamics and Man Made Processes. Thomas Telford Publications, London.
- Randall, C. L. (1988). Absorbing boundary condition for the elastic wave equation. *Geophysics*, 53:611–624.
- Randall, C. L. (1989). Absorbing boundary condition for the elastic wave equation: velocity-stress formulation. *Geophysics*, 54:1141–1152.
- Rizzo, F. J. (1967). An integral equation approach to boundary value problems of classical elastostatics. *Quarterly of Applied Mathematics*, 25:83–95.
- Ruge, P., Trinks, C., and Witte, S. (2001). Time-domain analysis of unbounded media using mixed-variable. *Earthquake Engineering and Structural Dynamics*, 30:899–925.
- Sacks, Z. S., Kingsland, D. M., Lee, R., and Lee, J. F. (1995). A perfectly matched anisotropic absorber for use as an absorbing boundary condition. *IEEE Transactions on Antennas and Propagation*, 43:1460–1463.
- Saini, S. S., Bettess, P., and Zienkiewicz, O. C. (1978). Coupled hydrodynamic response of concrete gravity dams using finite and infinite elements. *Earthquake Engineering and Structural Dynamics*, 6:363–374.
- Shirron, J. J. and Babuska, I. (1998). A comparison of approximate boundary conditions and infinite element methods for exterior Helmholtz problems. *Computer Methods in Applied Mechanics and Engineering*, 164:121–139.
- Smith, W. D. (1974). A nonreflecting plane boundary for wave propagation problems. *Journal of Computational Physics*, 15:492–503.
- Sofronov, I. L. (1998). Artificial boundary conditions of absolute transparency for two- and three-dimensional external time-dependent scattering problems. *European Journal of Applied Mathematics*, 9:561–588.
- Somigliana, C. (1885). Sopra l’equilibrio di un corpo elastico isotropo. *Il Nuovo Cimento*, 17:140–148.

- Sommerfeld, A. (1949). *Partial Differential Equations in Physics*. Academic Press, New York.
- Song, C. (2004a). A matrix function solution for the scaled boundary finite-element equation in statics. *Computer Methods in Applied Mechanics and Engineering*, 193:2325–2356.
- Song, C. (2004b). Weighted block-orthogonal base functions for static analysis of unbounded domains. In *Proceedings of the Sixth World Congress on Computational Mechanics*, 615–620, Beijing, China.
- Song, C. (2006). Dynamic analysis of unbounded domains by a reduced set of base functions. *Computer Methods in Applied Mechanics and Engineering*, 195:4075–4094.
- Song, C. and Bazyar, M. H. (2007). A boundary condition in Padé series for frequency-domain solution of wave propagation in unbounded domains. *International Journal for Numerical Methods in Engineering*, 69:2330–2358.
- Song, C. and Bazyar, M. H. (2008). Development of a fundamental-solution-less boundary element method for exterior wave problems. *Communications in Numerical Methods in Engineering*, 24:257–279.
- Song, C. and Wolf, J. P. (1995). Consistent infinitesimal finite-element–cell method: out-of-plane motion. *Journal of Engineering Mechanics*, 121:613–619.
- Song, C. and Wolf, J. P. (1996). Consistent infinitesimal finite-element cell method: three-dimensional vector wave equation. *International Journal for Numerical Methods in Engineering*, 39:2189–2208.
- Song, C. and Wolf, J. P. (1997). The scaled boundary finite-element method – alias consistent infinitesimal finite-element cell method – for elastodynamics. *Computer Methods in Applied Mechanics and Engineering*, 147:813–835.
- Song, C. and Wolf, J. P. (1999). Body loads in scaled boundary finite-element method. *Computer Methods in Applied Mechanics and Engineering*, 180:117–135.
- Stokes, G. G. (1849). On the dynamical theory of diffraction. *Cambridge Philosophical Transactions*, 9:1–62.
- Sullivan, D. (1997). An unsplit step 3-D PML for use with the FDTD method. *IEEE Microwave and Guided Wave Letters*, 7:184–186.

- Symm, G. T. (1963). Integral equation methods in potential theory. II. *Proceedings of the Royal Society A: Mathematical, Physical & Engineering Sciences*, 275:33–46.
- Taflove, A. and Hagness, S. C. (2000). *Computational Electrodynamics: The Finite-Difference Time-Domain Method (2nd edition)*. Artech House, Boston, London.
- Tajimi, H. (1980). A contribution to theoretical prediction of dynamic stiffness of surface foundations. In *Proceedings of 7th World Conference on Earthquake Engineering*, 105–112, Istanbul, Turkey.
- Tan, H. and Chopra, A. K. (1996). Dam-foundation rock interaction effects in earthquake response of arch dams. *Journal of Structural Engineering*, 122:528–538.
- Teixeira, F. L. and Chew, W. C. (1997). PML-FDTD in cylindrical and spherical grids. *IEEE Microwave and Guided Wave Letters*, 7:285–287.
- Thompson, L. L., Huan, R., and He, D. (2001). Accurate radiation boundary conditions for the two-dimensional wave equation on unbounded domains. *Computer Methods in Applied Mechanics and Engineering*, 191:311–351.
- Thomson, W. (1848). Note on the integration of the equations of equilibrium of an elastic solid. *Cambridge and Dublin Mathematical Journal*, 3:87–89.
- Ting, L. and Miksis, M. J. (1986). Exact boundary conditions for scattering problems. *The Journal of the Acoustical Society of America*, 80:1825–1827.
- Touhei, T. and Ohmachi, T. (1993). A FE-BE method for dynamic analysis of dam foundation reservoir systems in the time domain. *Earthquake Engineering and Structural Dynamics*, 22:195–209.
- Tsai, C. S. and Lee, G. C. (1991). Time-domain analyses of dam-reservoir system II: substructure method. *Journal of Engineering Mechanics*, 117:2007–2026.
- Tsai, C. S., Lee, G. C., and Ketter, R. L. (1990). A semi-analytical method for time-domain analyses of dam-reservoir interactions. *International Journal for Numerical Methods in Engineering*, 9:913–933.
- Tsynkov, S. V. (1998). Numerical solution of problems on unbounded domains. A review. *Applied Numerical Mathematics*, 27:465–532.

- Ucci, M., Camata, G., and Spacone, E. (2010). Nonlinear soil-structure interaction of a curved bridge located on the Italian Tollway A25. *SPRING 2010 - DIANA ELEMENTS*, 12–14.
- Underwood, P. and Geers, T. L. (1981). Doubly asymptotic, boundary-element analysis of dynamic soil-structure interaction. *International Journal of Solids and Structures*, 17:687–697.
- Vu, T. and Deeks, A. J. (2006). Use of higher-order shape functions in the scaled boundary finite-element method. *International Journal for Numerical Methods in Engineering*, 65:1714–1733.
- Waas, G. (1972). *Linear Two-Dimensional Analysis of Soil Dynamics Problems in Semi-Infinite Layered Media*. PhD thesis, University of California, Berkeley, CA.
- Waas, G. (1980). Dynamisch belastete Fundamente auf geschichtetem Baugrund. *VDI Berichte*, 381:185–189 (in German).
- Waas, G. and Hartmann, H. G. (1988). Damping and stiffness of foundations on inhomogeneous media. In *Proceedings of Ninth World Conference on Earthquake Engineering*, III, 343–348, Tokyo-Kyoto, Japan.
- Westergaard, H. M. (1933). Water pressure on dams during earthquakes. *Transactions of the American Society of Civil Engineering*, 98:418–472.
- White, W., Valliapan, S., and Lee, I. K. (1977). Unified boundary for finite dynamic models. *Journal of the Engineering Mechanics Division*, 103:949–964.
- Wolf, J. P. (1985). *Dynamic Soil-Structure Interaction*. Prentice-Hall, Englewood Cliffs, NJ.
- Wolf, J. P. (1988). *Soil-Structure Interaction Analysis in Time Domain*. Prentice-Hall, Englewood Cliffs, NJ.
- Wolf, J. P. (1991). Consistent lumped-parameter models for unbounded soil: physical representation. *Earthquake Engineering and Structural Dynamics*, 20:11–32.
- Wolf, J. P. (2003). *The Scaled Boundary Finite Element Method*. John Wiley & Sons, Chichester.
- Wolf, J. P. and Song, C. (1995). Consistent infinitesimal finite-element cell method: in-plane motion. *Computer Methods in Applied Mechanics and Engineering*, 123:355–370.

- Wolf, J. P. and Song, C. (1996). *Finite-Element Modelling of Unbounded Media*. John Wiley & Sons, Chichester.
- Wolf, J. P. and Song, C. (2000). The scaled boundary finite-element method - a primer: derivations. *Computers & Structures*, 78:191–210.
- Yang, R., Tsai, C. S., and Lee, G. C. (1993). Explicit time-domain transmitting boundary for dam-reservoir interaction analysis. *International Journal for Numerical Methods in Engineering*, 36:1789–1804.
- Yu, T., Zhou, B., and Chen, B. (2003). An unsplit formulation of the Berenger’s PML absorbing boundary condition for FDTD meshes. *IEEE Microwave and Guided Wave Letters*, 13:384–350.
- Zhao, L. and Cangellaris, A. C. (1996). A general approach for the development of unsplit-field time-domain implementations of perfectly matched layers for FDTD grid truncation. *IEEE Microwave and Guided Wave Letters*, 6:209–211.
- Zienkiewicz, O. C. and Bettess, P. (1978). Fluid-structure dynamic interaction and wave forces: an introduction to numerical treatment. *International Journal for Numerical Methods in Engineering*, 13:1–16.
- Zienkiewicz, O. C., Emson, C., and Bettess, P. (1983). A novel boundary infinite element. *International Journal for Numerical Methods in Engineering*, 19:393–404.